Application of Energy Dispersive X-Ray Diffraction (EDXRD) in the detection of fat nodules in liver disease and plaques in the blood vessels of the heart

Chukwuneke Sid Abuchi

University College London

2018

Submitted for the degree of Doctor of Philosophy

University College London

Declaration

I, Chukwuneke Sid Abuchi, confirm that the work presented in this PhD thesis is my own. Where any information has been derived from other sources, I confirm that this has been indicated in the bibliography of the thesis.

Acknowledgement:

I would like to immensely thank Professor Robert D Speller my Main/Principal supervisor, Joel Professor of Medical Physics and Deputy Head of Department of Medical Physics & Bioengineering. Robert as popularly called has been such a great motivator and a respectable academic of great virtue and excellent humility, generally offering systematic and guided advice, encouragement and overall support to all and especially to me. I will ever remember him. I also thank Professor Gary J Royle my second supervisor for his ever-ready-to-help stance in every need. They are both great academicians and problem solvers. I am also very grateful to Professor Tom D. Fearn , who generated the analytic tool for this work and for his selfless attention, advice, suggestions and encouragement. I must also thank Dr Marco Federighi, the Vice Dean and Faculty Tutor of the Faculty of Engineering Sciences for his advice, encouragement and assistance. I need to thank our current HOD, Professor Jem Hebden. I admired the special qualities in him. I need to thank Drs. Daniel T. O'Flynn and Robert Moss and Nick Calvert for making useful suggestions, Nick Calvert for assistance with Monte Carlo simulations and also Dennis Tsang who made sure that our computers are in perfect working order. Special thanks to Ms Karen J. Cardy, the Departmental Administrator for her excellent administration and care of the students, particularly the foreign research students. I also wish to specially thank Ms Mohini Nair for resilience and efficiently doing a great job of departmental teaching support. Mohini, Karen and Andy O'Reilly were very nice and kind. I thank my special friends, Dr Wole Oyekoya (UCL, Computer Science Dept.), Ms Manu Davies (Life & Medical Sciences), Dr Dalhatu Sarki Tafida (Nigerian Ambassador in UK) and Gwen White (Royal Commonwealth Society) for powerful inspiration, moral support and encouragement.

It is mandatory that I acknowledge the sponsorship of the Federal Government of Nigeria through her agency, Tertiary Education Tax Fund (TETFUND). I am grateful to Nnamdi Azikiwe University and particularly the then Vice Chancellor, Professor Boniface C Egboka and the then Deputy Vice Chancellor, Academic, Professor Sam Omenyi for their magnanimity, tremendous support and cooperation with all the needed approvals. I thank all my friends and colleagues in the Faculty of Medicine, Faculty of Health Sciences & Technology and Faculty of Basic Medical Sciences,

Nnamdi Azikiwe University, Nnewi Campus particularly, Professors Adinma, Ikpeze, Igwegbe, Eleh, Ezechukwu, Ikechebelu, Chianakwana, Nwosu, Meludu, Dioka, Unekwe and Ahaneku (current Vice Chancellor) and Drs Anyabolu, Osuji, Okpala (Radiology) and Afiadigwe and lastly, my friend in deed, Innocent Okika and Ven. Prof Israel Okoye plus others I cannot list.

I owe a lot of gratitude to my children, Ifechukwu, Chukwunonso and Uzoma who missed the essential fatherly love, care and attention all these tempestuous years and most essentially for their constant prayers and unparalleled patience. I am also grateful to two fantastic ladies, Chinelo Okoli and my sister Ginikachukwu, particularly for their timely support and rapid responses in times of critical needs and financial challenges in the UK.

Most importantly, I really have to thank God Almighty for his special grace and mercy and for all the people connected with this research work.

Title: Application of Energy Dispersive X-Ray Diffraction (EDXRD) in the detection of fat nodules in liver disease and plaques in the blood vessels of the heart

Abstract

Fat deposits in tissue or organs are a major health problem. Assessment of fat nodules in the liver (particularly prior to a liver transplant) or plaques in coronary arteries are important investigations that are undertaken in hospitals throughout the world. Many of the current techniques for investigation, e.g., computed tomography coronary angiography (CTCA), lead to high radiation doses or carry significant risks (catheter angiography) and hence new, quantitative tests are required. This thesis looks at using localised X-ray diffraction measurements as an alternative approach to quantifying the fat content of blood vessels or liver tissue.

Energy dispersive X-ray diffraction (EDXRD) has been used to study the diffraction profiles of specially designed tissue phantoms. Phantoms have been built to represent a fatty-liver and a diseased heart where the size of the fatty inclusion can be varied. Combinations of tissue equivalent materials and real tissues have been used in each phantom. Diffraction profiles have been measured on these phantoms for a range of fat inclusions. All measurements were made on a fixed geometry diffractometer using a nominal scattering angle of 6^0, a High Purity Germanium (HPGe) detector system and a tungsten target X-ray source.

The diffraction data has been subjected to different analysis procedures. The results on the phantoms have shown that the minimum detectable levels of fat inclusions are clinically relevant. These results have then been used to scale up the measured diffraction data to patient-sized objects. Although these estimates demonstrate that doses need to be increased they also indicate that useful clinical data could be obtained at acceptable dose levels.

Contents

CHAPTER 1

Introduction and the background to the involvement of fat in the liver and heart

CHAPTER 2

Design and development of tissue EDXRD SYSTEM

CHAPTER 3

Experimental determination of the detectability of fat nodule in the liver and plaques in the blood vessels of the heart using EDXRD on small size phantoms/tissues

CHAPTER 4

Liver and heart tissue diffraction spectra analysis

CHAPTER 6

Conclusions and Future Work with Recommendations

LIST OF FIGURES

Chapter 1

Chapter 2

Chapter 3

Chapter 4

Chapter 5

LIST OF TABLES

Chapter 1

Chapter 2

Chapter 3

Chapter 5

Chapter 1

Introduction and the background to the involvement of fat in the liver and heart disease

1.0 Introduction

This study is focused on the energy dispersive x-ray diffraction (EDXRD) technique of investigation of two major issues. The number one issue is to detect fat deposits or nodule in the liver and number two, to detect the plaques in the blood vessels of the heart.

The experiments will be carried out with fatty liver samples and simulated fatty heart. X-ray diffraction spectral patterns will be obtained, studied and analysed critically for the detection of the issues stated. The EDXRD experimental approach will be preceded with a radiation transport Monte Carlo simulation with predictive capability for the X-ray diffraction system detection applications. Monte Carlo simulations will provide a comprehensive evaluation, design, and optimization of proposed investigation systems. The Monte Carlo simulation will be discussed later in this chapter. The information obtained will guide on any needed considerations or improvements in evaluated data and measurements, and may contribute towards having results that can usefully validate the data and development of EDXRD as a viable state-of-the-art detection technique.

The most important aspect will be the detection of the unusual presence of fat deposits in the tissue samples. Such early detection and accurate diagnosis of the disease will lead to prompt and specific treatment before it progresses to cause irreversible damage. Consequently, our goal is to achieve valuable detection of the fat deposits at the early stage of accumulation of the fat and plaque deposits in these tissues.

Heart disease, coronary or ischaemic (CHD or IHD), is arguably the UK's biggest killer (BHF, 2012), number 1 in the USA (Hoyert and Xu, 2012) and in the world, table 1.1 (WHO, 2011). CHD develops when the blood supply to the muscles and tissues of the heart becomes obstructed by the build-up of fatty and thick substances inside the walls

of the coronary artery. These substances are formed from cholesterol and are called plaques (figure 1.8b). This medical condition is known as atherosclerosis. This heart condition is one of the two investigations in this study of the heart and liver disease.

On the other hand, liver cancer is one of the most common forms of cancer in the world. Liver cancers 75% - 90% of which are hepatocellular carcinoma (HCC), are the third most common causes of cancer deaths among men and the sixth most common among women (London and McGlynn, 2006, 2009; Chuang et al, 2009) and among the top ten in the world, table 1.2 (Chan, 2010).There is a little controversy in the given statistics due to uncorrelated research figures. According to Wei et al (2012), liver cancer is the fifth most common cancer in men and the seventh in women world- wide. For example, about 50% of patients diagnosed with cirrhosis die within five years unless they receive surgical liver transplant [www.mayoclinic.org]. The potential risk factors for liver cancer include hepatitis B virus (HBV), hepatitis C virus (HBC), body fatness, diabetes and insulin resistance and the oral contraceptives (Chuang et al, 2009). Liver Disorders/Diseases include, hepatitis – inflammation of liver, often caused by viral infection transmitted enterically (HVA) or through blood (HVB, HVC, HVD). The blood-borne viruses are linked to chronic hepatitis and cirrhosis, characterized by growth of scar tissue.

This first chapter will look at the development and magnitude of liver and heart problems and describe the basic outline of their anatomy, physiology and pathology. Also, brief overview of some of the techniques that are currently used to investigate the problems and their limitations will be discussed. The expected advantage EDXRD can offer above the current techniques will also be discussed.

Table 1.1: The top 10 causes of death

WHO: Fact sheet N°310.Updated June 2011

The 10 leading causes of death by broad income group (2008)

Middle-income countries	Deaths in millions	% of deaths
Ischaemic heart disease	5.27	13.7%
Stroke and other cerebrovascular disease	4.91	12.8%
Chronic obstructive pulmonary disease	2.79	7.2%
Lower respiratory infections	2.07	5.4%
Diarrhoeal diseases	1.68	4.4%
HIV/AIDS	1.03	2.7%
Road traffic accidents	0.94	2.4%
Tuberculosis	0.93	2.4%
Diabetes mellitus	0.87	2.3%
Hypertensive heart disease	0.83	2.2%

High-income countries	Deaths in millions	% of deaths
Ischaemic heart disease	1.42	15.6%
Stroke and other cerebrovascular disease	0.79	8.7%
Trachea, bronchus, lung cancers	0.54	5.9%
Alzheimer and other dementias	0.37	4.1%
Lower respiratory infections	0.35	3.8%
Chronic obstructive pulmonary disease	0.32	3.5%
Colon and rectum cancers	0.30	3.3%
Diabetes mellitus	0.24	2.6%
Hypertensive heart disease	0.21	2.3%
Breast cancer	0.17	1.9%

World	Deaths in millions	% of deaths
Ischaemic heart disease	7.25	12.8%
Stroke and other cerebrovascular disease	6.15	10.8%
Lower respiratory infections	3.46	6.1%
Chronic obstructive pulmonary disease	3.28	5.8%
Diarrhoeal diseases	2.46	4.3%
HIV/AIDS	1.78	3.1%
Trachea, bronchus, lung cancers	1.39	2.4%
Tuberculosis	1.34	2.4%
Diabetes mellitus	1.26	2.2%
Road traffic accidents	1.21	2.1%

Table 1.2: The top 10 deadliest cancers

The top 10 deadliest cancers in the world (Chan, 2010)	
1	Lung and bronchial cancer
2	Colon and rectal cancer
3	Breast cancer
4	Pancreatic cancer
5	Prostate
6	Leukaemia
7	Non-Hodgkin lymphoma
8	Liver and intrahepatic duct cancer
9	Ovarian cancer.
10	Oesophageal cancer.

Figure 1.1 of the liver shows the right and left lobes. The inset is the anatomical arrangement /position in the body. The heart figure 1.2 and liver, figure 1.3, partner together to ensure blood circulates healthfully throughout the body. However, research on atherosclerosis confirms a tight connection between liver and heart pathology. Physiologically, blood and bile intimately tie liver and heart health together.

With the above health information on liver cancers and cardiovascular diseases, it becomes a challenge to seek for more and better ways to provide improved affordable

detection and diagnostic systems or modes for these major health problems. This leads to the idea of undertaking X-ray diffraction investigations of the liver and heart tissues with a view to detect the plaques in the blood vessels of the heart and fat deposits in the liver.

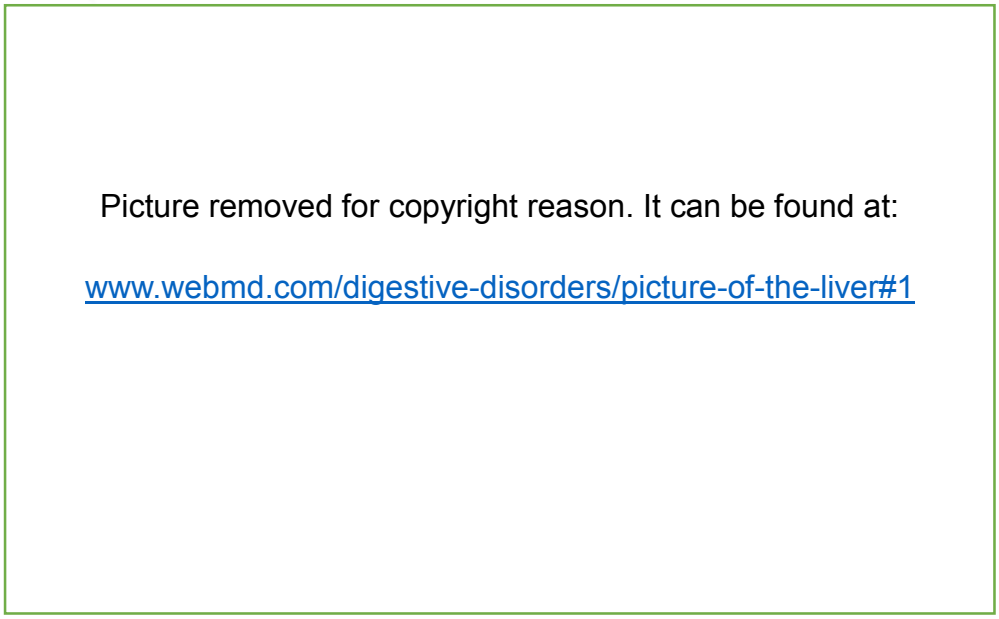

Figure 1.1: The liver showing the right and left lobes. The inset is the anatomical arrangement /position in the body.[1]

[1] [WEBMD.LLC- www.webmd.com/digestive-disorders/picture-of-the-liver#1

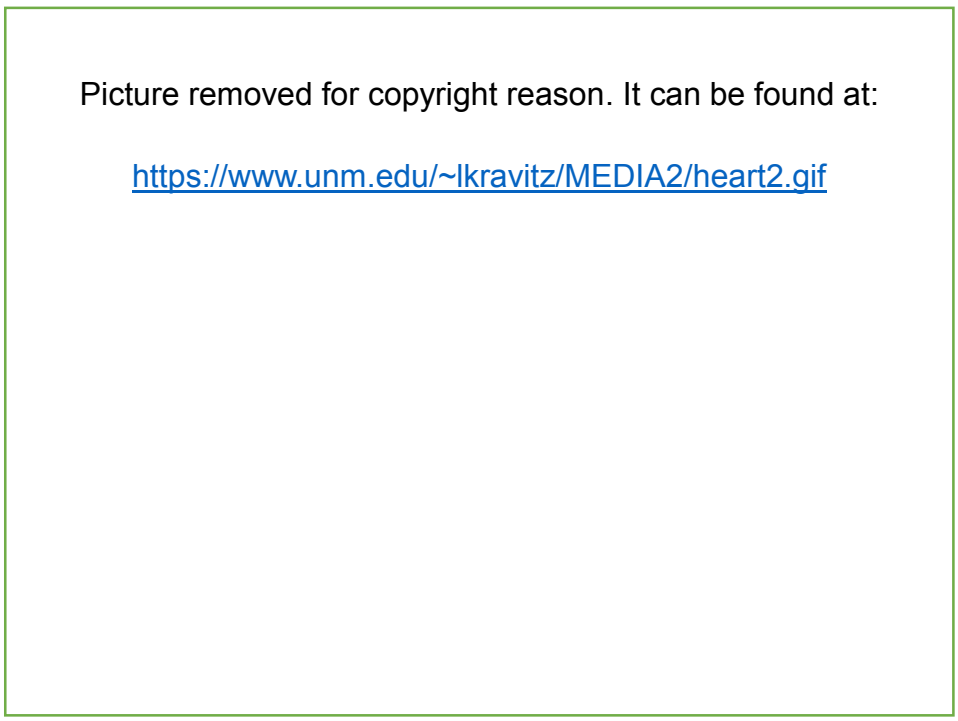

Figure 1.2: A pictorial view of the heart showing the major parts.

1.1 Anatomy, Physiology and pathology of the Liver

The liver is the largest organ or gland in the body and weighs between 1.2 to 1.6 kilograms, with 1/6 of the entire liver mass on the left lobe and 5/6 to the right lobe, separated by the falciform ligament which divides the right and the left liver (as in figure 1.2) and suspends the liver from the diaphragm and the anterior abdominal wall. The ligamentum teres is the remnant of the umbilical vein. The liver has a double blood supply from the hepatic artery and the portal vein (shown in Figure 1.3). The hepatic artery receives the blood from the artery, aorta (Ao), while the hepatic portal vein receives nutrient-rich venous blood from the stomach, pancreas, spleen and the intestines.

Figure 1.3: Schematic diagram of the liver with the hepatic blood supply routes showing the arterial and venous supply (Quiroga et al, 2001).

The liver cells [hepatocytes] within the walls of the sinusoids carry out the functions of the liver. Other major inter-linked flows are from the gastro-duodenal artery [GDA], superior mesenteric vein (SMV) which carries blood through the portal vein to the liver and the inferior mesenteric vein (IMV) which is the vein of the spleen.

The liver performs many functions, the most fundamental of which is homeostasis (the tendency to maintain, or the maintenance of, normal, internal stability in an organism by coordinated responses of the organ systems that automatically compensate for environmental changes) and blood sugar regulation.
Some essential regulatory functions include:
Regulation of the blood sugar: Normal blood sugar level is about 0.1%. Any excess from the gut is stored as glycogen. The hormone insulin which is secreted from the pancreas also turns the excess glucose into glycogen.
Regulation of amino acids: The amino acids in the blood are maintained at normal level. The useful amino acids are converted to useful carbohydrates. The extra amino acids are converted into urea, a waste product, transported to the kidney and excreted from the body as urine.
Bile formation: The bile contains salt and excretory pigments that help to speed up the digestion of lipids.

Lipid regulation: Lipids are extracted from the blood and get converted to carbohydrates for immediate use or stored for future use.
Blood storage: Expands to accommodate large blood inflow. The blood is released into the blood circulatory system as needed.
Toxin and hormone regulation: The liver extracts harmful substances from the blood and sends them to the bile and kidney for their removal from the body.
Heat regulation: The physical activity of the liver produces heat, which circulates in the blood and provides the necessary heat for some less-active organs.
Cholesterol, plasma proteins (fibrinogen, prothrombin, albumens and globulins), vitamins (A, made in the liver from carotene & B12, stored in the liver) and heparin (blood clotting preventing substance) formation and use are regulated.
When the liver fails to function efficiently, it leads to disorders like biliary calculi (gallstones), due to the crystallization of cholesterol resulting from excess cholesterol or too little bile salts. Also, blood-borne viruses, liver inflammation and scar tissue growth may arise as a consequence of the liver malfunction.

1.2 Anatomy, Physiology and Pathology of the heart

The heart [figures 1.4 and 1.5] is a hollow muscular organ with four chambers [2 atria and 2 ventricles] found in the chest between the lungs and weighs about 300 grams.
The core functions of the heart are to generate blood pressure, route the blood, separate pulmonary and systemic circulation, regulate the blood supply and provide enough blood flow to maintain normal metabolism in the body. The heart valves enforce unidirectional blood flow through the heart.

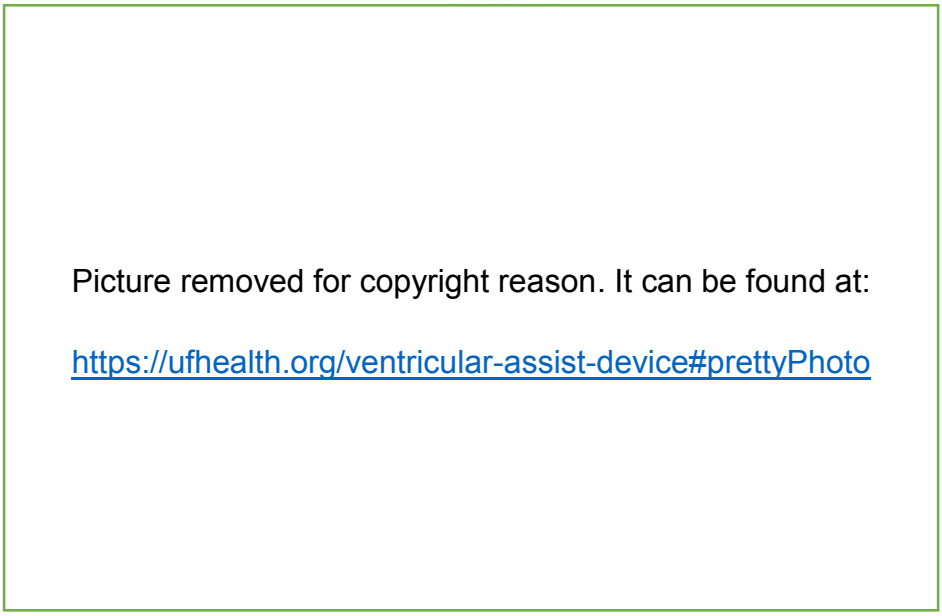

Figure 1.4: Pictorial diagram of a dissected heart showing the four chambers, the blood and the major relevant blood vessels (White PW, 2006)

The key features relevant to this study are the blood vessels. The blood vessels are the arteries (the vessels that carry away the oxygenated blood from the heart), the veins (the vessels that return deoxygenated blood to the heart) and the capillaries (the small vessels that allow diffusion of gases, nutrients and wastes between plasma and interstitial fluid). The aorta is the largest artery. The blood vessels that transport the blood through the body parts from the left ventricle and back to the right atrium are called systemic vessels and those that transport the blood from the right ventricle through the lungs and back to the left atrium are the pulmonary vessels.

1.3 Normal and diseased liver

A healthy or normal liver, figure 1.6a, is a large, dark-red organ located in the cranial portion of the abdomen, just behind the diaphragm. It stores and filters blood, secretes bile, detoxes the body system of noxious substances, converts sugars into glycogen, synthesizes and breaks down fats while temporarily stores fatty acids and synthesizes serum proteins which helps regulate blood volume, and fibrinogen and prothrombin, which are essential blood clotting factors.

On the other hand, fatty or diseased liver, figure 1.6b, is one manifested with accumulation of triglycerides in the liver or affected with infiltration of fat and fatty acids in large drops beyond the level which is normally encountered. This may be as a result of a normal physiological response to increased peripheral lipolysis, obesity or the action of hepatotoxinslets. The liver can store up to 20 per cent of its weight in glycogen and up to 40 per cent of its weight in fats. Another type of fat present in the liver is the steatosis, which together with the triglycerides may increase the liver size up to 3 times. Lard is a pork-based product and a major culprit in raising cholesterol levels. It contains high amounts of saturated fats. The computed tomography (CT) and magnetic resonance imaging (MRI) scans of fatty or diseased liver are shown in figures 1.7a and 1.7b respectively.

Picture removed for copyright reason. It can be found at:

http://library.med.utah.edu/WebPath/LIVEHTML/LIVER002.html

Figure 1.5a: Normal liver. This is the external surface of a normal liver. The colour is brown and the surface is smooth. A normal liver is about 1200 to 1600 grams[2].

[2] http://library.med.utah.edu/WebPath/LIVEHTML/LIVER002.html

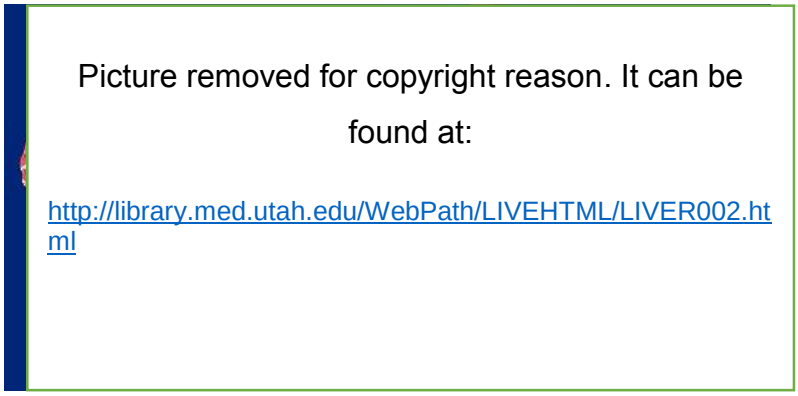

Figure 1.5b: Diseased liver. On-going liver damage with liver cell necrosis followed by fibrosis and hepatocyte regeneration results in cirrhosis. This produces a nodular, firm liver. The nodules seen here are larger than 3 mm and, hence, this is an example of "macro-nodular" cirrhosis[3].

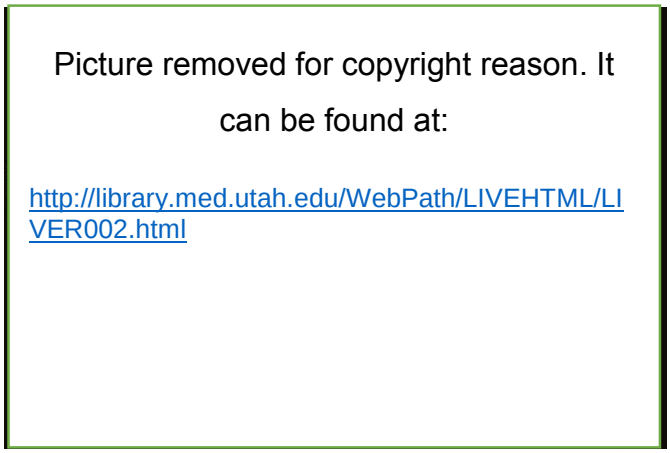

Figure 1.5c: Diseased liver with macronodular cirrhosis. This is Viral hepatitis (B or C), the most common cause for macronodular cirrhosis[4].

[3] http://library.med.utah.edu/WebPath/LIVEHTML/LIVER002.html
[4] http://library.med.utah.edu/WebPath/LIVEHTML/LIVER002.html

Picture removed for copyright reason. It can be found at:

http://library.med.utah.edu/WebPath/LIVEHTML/LIVER002.html

Figure 1.5d: Fatty liver. This liver is slightly enlarged and has a pale yellow appearance, seen both on the capsule and cut surface. This uniform change is consistent with fatty metamorphosis (fatty change)[5].

Picture removed for copyright reason. It can be found at:

http://journals.sagepub.com/doi/pdf/10.1177/107327481001700202

Figure 1.6a: CT scan of diseased liver. (A) CT before contrast shows the tumour mass with a thin pseudo-capsule (arrow). (B) Arterial-phase enhanced image shows two enhancing masses (arrows), indicating a hepatic arterial supply. (C) Delayed image shows washout of contrast, i.e., the tumours (arrows) are enhancing less than the liver. (Source: Cancer control, 2010. H. Lee Moffitt Cancer Centre and Research Institute Inc. USA)

[5] http://library.med.utah.edu/WebPath/LIVEHTML/LIVER002.html

Picture removed for copyright reason. It can be found at:

http://journals.sagepub.com/doi/pdf/10.1177/107327481001700202

Figure1.6b. MRI of HCC. (A) T1-weighted in-phase image shows the tumour in segment II of the liver (arrow). (B) Opposed phase image shows lower signal in the tumour (arrow), indicating steatosis. (C) Arterial-phase image after contrast injection shows enhancement of the tumour, a sign of neovascularity and arterial supply (arrow). (D) Delayed image shows washout of enhancement (arrow). (Source: Cancer control, 2010. H. Lee Moffitt Cancer Centre and Research Institute Inc. USA)

1.4. **Normal and diseased heart**

A normal heart, figure 1.7, is one without any physical impairment to its normal functions. Its atria receive venous blood from the veins, while the ventricles pump blood into the arteries and maintain normal blood and nutrients circulation, with these blood vessels intact.

Heart disease originates when the blood vessels of the heart are no longer intact and consequently, the heart malfunctions. Occlusion of the blood vessels or more importantly the artery may result as fatty deposits accumulate to form a fatty plaque, figures 1.8a and 1.8b. The plaque protrudes into the lumen of the artery, narrowing it down and reducing the amount of blood flow in the artery. Severe narrowing can lead to angina, ischemia and infarction.

Picture removed for copyright reason. It can be found at:

http://www.sharonrn.com/heartant.html

Figure1.7: External appearance of normal heart. The epicardial surface is smooth and glistening and the amount of epicardial fat is usual or normal.

Picture removed for copyright reason. It may be found at:

http://www.biosbcc.net/b100cardio/htm/heartdis.htm

Figure 1.8a: A section of the arterial blood vessel showing the narrowed down lumen of the artery with fatty plaque

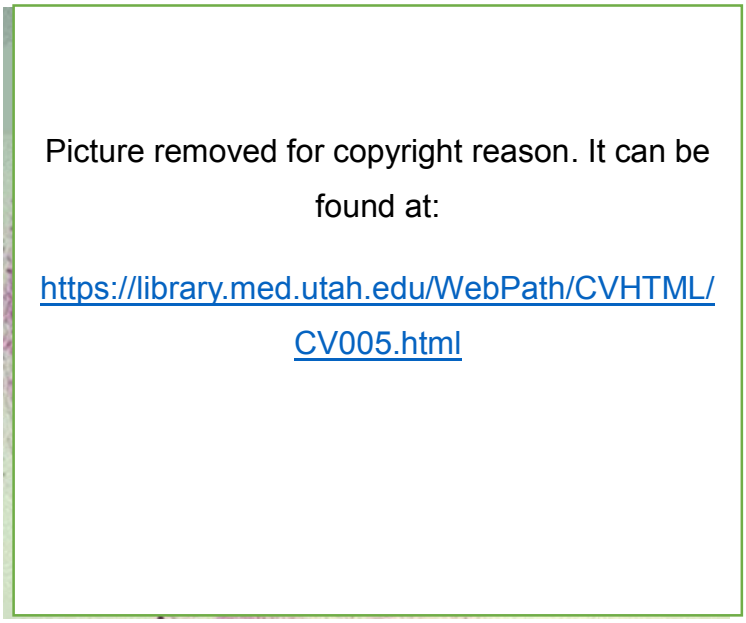

Figure 1.8b: Diseased heart. The coronary artery shown here has narrowing of the lumen due to build-up of athero-sclerotic plaques.

1.5 Types of liver cancer

Types of liver cancer [table 1.3] that can result from fat build-up include hepatocellular carcinoma (HCC), main liver cancer (that leads to DNA damage) and hepato-blastoma, cholangio-sarcoma, bile duct cancer, angio-sarcoma and hemangio-sarcoma. This is caused by HBV and HBC and also alcoholic cirrhosis (Chuang et al, 2009).

Hepatoblastoma is the most common hepatic tumour. It represents 1% of malignancies in children (London and Mcglynn, 2006).

Cholagiocarcinoma is the second most important and frequent type of adult liver cancer and accounts for 3% of gastrointestinal cancers worldwide (Khan et al, 2005).

Angiosarcoma is a rare mesenchymal tumour of the liver which usually presents in elderly men (Rademaker et al, 2000).

Table 1.3: Types of liver cancer

	Cancer type	Description	Origin	Age affected	Prevalence
1	Hepatocellular carcinoma	Main liver cancer	Hepatocytes [main liver cells]	Adults	75%
2	Hepato-blastoma	Primary malignant tumour	Hepatic cells	Children	1%
3	Cholangio-sarcoma	Malignant tumour	Intrahepatic bile duct epithelial cells	Adults	3%
4	Angiosasarcoma & Hemangiosarcoma	Malignant tumour	Blood vessels	Adult & Elderly	-
5	Bile duct cancer	Bile duct tumour	Bile duct	Adults	10 - 20%

1.6 Fat in the liver and heart diseases

A liver is considered fatty if the fat content is greater than 10 percent of the liver. Non-alcoholic fatty liver disease (NAFLD) represents the most common form of liver disease. Within the degrees and types of NAFLD, simple fatty accumulation (hepatic steatosis) can lead to weight excess and diabetes. The more severe form of fatty liver known as non-alcoholic steato-hepatitis (NASH) may progress to a permanent scar called cirrhosis and eventually result in liver failure. Fatty liver can cause inflammation, which also leads to permanent scarring (cirrhosis). Fatty liver can also develop into conditions that compromise the liver's ability to break down fats, for example as in obesity and high triglycerides. Since fatty liver typically has no symptoms, people are often diagnosed during tests for some other conditions. Unfortunately, permanent liver damage may occur before a diagnosis is made.

Liver problems do affect the heart. The passive venous congestion of the liver may result in heart failure, constrictive pericarditis and hepatic venous outflow obstruction. Also inhomogeneous, mottled, reticulated-mosaic pattern of parenchyma and periportal low attenuation may appear on contrast enhanced CT [Gore et al, 1994].

MRI demonstrated periportal hyper-intensity, secondary to perivascular lymph-edema [Tani et al, 2000]. Growing evidence has suggested that inflammation plays a strong

role in developing cardiovascular disease, especially atherosclerosis, or hardening of the arteries [NIH, 2009].

Science Daily [Aug. 24, 2009] highlighted the new findings from researchers at Washington University School of Medicine in St. Louis which suggest that it is not the fat stored in the belly that affects metabolic risk factors for diabetes, high blood triglycerides and cardiovascular disease, but its collection in the liver.

The liver is one of the most important organs to be involved with metastatic disease, which arises most frequently from primary sites in the colon, breast, breast, lung, pancreas and stomach [Ackerman et al, 1969].

Atherosclerosis, a health condition that causes high blood pressure and heart disease contribute to some liver diseases. The study of both, undoubtedly demonstrates the interconnectivity between liver and heart health. When deposits of fatty substances, cholesterol, cellular waste products, calcium and other substances build up in the inner lining of an artery, it can grow large enough to significantly reduce the blood's flow, in addition to the danger of it breaking off and throwing a blood clot into circulation.

1.7 The current methods of diagnosis and disease detection

In medicine the currently acceptable and common modes of detection, classification and diagnosis of tissue conditions are Histopathology, Medical Ultrasound, Magnetic Resonance Imaging, Biopsy, Computed Tomography and Medical Radiography. Pathological investigation is achieved by the use of direct tissue sample either surgically extracted or obtained through biopsy (an invasive technique of extraction) or the use of urine, blood or specific samples as in chemical pathology. The essential expectations or requirement for in vivo and non in vivo investigation are the system reliability and accuracy with respect to specificity, sensitivity and resolution in addition to being readily available, affordable, little discomfort to the patient and with minimum risk.

Fatty liver or heart is a common imaging finding, with a prevalence of 15%–95%, depending on the population [Willian et al. 2011; RACGP, 2011; Sattar, 2014]. The diagnostic standard of reference is biopsy with histologic analysis, but fat deposition

in the liver or heart may be diagnosed noninvasively with US or MR imaging if established criteria are applied.

1.7.1 Histopathology

Histopathology is a laboratory based diagnosis and study of disease via microscopic examination of tissues for proper medical interpretation of the cells and tissue samples. Tissue samples are excised from the main body surgically or through biopsy. A histopathologist determines the cause of death by performing autopsies. However, histopathology is invasive, applies to the dead and cannot be done in real time.

1.7.2 Medical Radiography

X-ray imaging is a transmission-based technique in which X-rays from a source pass through the patient and are detected on the opposite side of the body. Contrast in the images of different types of tissues arises from attenuation of X-rays in the body. For example, X-ray attenuation is particularly efficient in bone, but less so in soft tissues. In planar X-ray radiography, the image produced is simply a two-dimensional projection of the tissues lying between the X-ray source and the film. Planar X-ray radiography is used for a number of different purposes.
Although Planar X-ray imaging is most popular due to low cost and availability, its inefficiency in imaging soft tissues makes it unpopular for advanced investigation of soft tissues.

1.7.3 Ultrasound

Ultrasound deals with sound frequencies above the limits of human hearing, that is, sound with frequency greater than 20,000 cycles per second (20 kHz). The frequencies emitted are in the range of 2-15MHz. Audible sound sensed by the human ear is in the range of 20Hz to 20 kHz.

Ultrasound can be generated by transforming electrical energy to sound energy. This can happen either by via magnetostriction generator or reciprocal piezoelectric

generator. A magnetostriction generator can produce ultrasonic waves of comparatively low frequency. For generating high frequency ultrasonic waves, piezoelectric generator is used and is more *relevant.* An ultrasound wave is generated when an electric field is applied to an array of piezoelectric crystals located on the transducer surface. Electrical stimulation causes mechanical distortion of the crystals resulting in vibration and production of sound waves (i.e. mechanical energy). The conversion of electrical to mechanical (sound) energy is called the converse (reciprocal) piezoelectric effect (Gabriel Lippman1881).

Each piezoelectric crystal produces an ultrasound wave. The summation of all waves generated by the piezoelectric crystals forms the ultrasound beam. Ultrasound waves are generated in pulses (intermittent trains of pressure waves) and each pulse commonly consists of 2 or 3 sound cycles of the same frequency.

Ultrasound can be directed as a beam. It obeys the laws of reflection and refraction and is reflected by objects of small size. It is not invasive and can be done real-time. The image is formed by the reverse of the process used to create the sound waves. The echoes returning to the transducer are converted by the piezoelectric (quartz) crystals into electrical signals and are then processed to form the image.

Highly reflective interfaces give rise to a strong echo which is represented on the screen as a bright spot, whilst the opposite is true of weakly reflective interfaces. Areas without acoustic interfaces such as the lumen of vessels and other cavities containing liquid (blood, bile, ascites or urine) give no reflection and no spot on the screen, this, results in a black pixels in the image. If the waves hit gases or solids the density difference is so great that most of the acoustic energy is reflected and it becomes impossible to see deeper. To form an image, an ultrasound machine needs to determine the direction of the echo, how strong the echo was and how long it took the echo to be received from when the sound was transmitted. Once the ultrasound scanner determines these three things, it can locate which pixel in the image to light up and to what intensity. The speed of sound is different in different materials, and is dependent on the acoustical impedance of the material. However, the ultrasound scanner assumes that the acoustic velocity is constant at 1540 m/s. An effect of this

assumption is that in a real body with non-uniform tissues, the beam becomes de-focused and image resolution is reduced [Rajagopal, 2009].

1.7.3.1 The limitation of ultrasound

Ultrasound propagates poorly through a gaseous medium but excels in watery or fluidic compartments. Ultrasound results may be inaccurate due to poor resolution. It is more qualitative than quantitative.

1.7.4 Computed Tomography

Computerised tomography (CT) scan uses X-rays and a computer to create detailed images of the inside of a body. Each scan or slice when put together, form a 3-D picture of the body. A CT scan offers detailed views of different tissue types including lungs, bones, soft tissues and blood vessels.

CT scans are commonly performed on the head and abdomen. CT scans involve exposure to radiation in the form of X-rays. A head or spine examination should take less than 30 minutes including patient set up and data acquisition. A scan of the chest, abdomen and/or pelvis may take longer. The procedure is painless. For some scans, an injection or a drink of a contrast agent (a radio-opaque dye) is given to make it easy to see the parts of the body more clearly. The scan time depends on the scan area and the organ. The pictures of a CT scan are more detailed than a typical transmission X-ray.

CT offers very good spatial resolution [about 0.5mm-1mm, Speller, 2014, personal communication] and the ability to study the entire liver in a single breath-hold. The performance of CT scanners has further been improved in terms of speed of acquisition, resolution, and the ability to image the liver during various phases of contrast enhancement more precisely than was previously possible [Silverman, 1995].

Intravenous iodinated contrast media are routinely used in the imaging of the liver to improve the contrast-to-noise ratio between liver lesions and normal liver. They also

help to characterize liver lesions, based on the enhancement patterns of liver lesions during various phases of contrast circulation in the liver [Paulson et al, 1998].

CT fluoroscopy is a new tool that assists in performing biopsies of liver lesions. Current multi-slice CT fluoroscopy systems allow real-time monitoring of the needle during biopsies and may increase the yield and decrease the time required for the biopsy, with an acceptable radiation dose [Kuszyk et al, 1996].However, its limitations include the need for a high radiation dose and it has a low sensitivity for the detection and characterization of lesions smaller than 1 cm [Garden, 2009].

1.7.5 Biopsy

This is a process where a small piece of tissue or fluid is taken out from the organ of interest for pathological investigations. A fine needle may be used for aspiration of the fluid, as in fine needle biopsy. A special biopsy (cupped) needle may also be used to cut out sample from the inner organ. Liver biopsy and histologic analysis is considered the diagnostic reference standard for the assessment of fatty liver [Williams et al, 2011].

1.7.6 Magnetic Resonance Imaging

Magnetic resonance imaging (MRI), or Nuclear magnetic resonance imaging (NMRI), is a medical imaging technique most commonly used in radiology to visualize the structure and function of the body. It provides detailed images of the body in any plane. MRI provides much greater contrast between the different soft tissues of the body than computed tomography (CT), making it especially useful in neurological (brain), musculoskeletal, cardiovascular, and oncological (cancer) imaging.

Unlike CT, it does not use ionizing radiation, but uses a magnetic field to align the nuclear magnetization of (usually) hydrogen atoms in water in the body. Radiofrequency fields are used to systematically alter the alignment of this magnetization, causing the hydrogen nuclei to produce a rotating magnetic field detectable by the scanner. This signal can be manipulated by additional magnetic fields to build up enough information to construct an image of the body.

MRI is a relatively new technology, which has been in use for little more than 40 years (compared with over 110 years for X-ray radiography). The first MR Image was published in 1973 and the first study performed on a human took place on July 3, 1977.

1.7.7 Positron Emission Tomography

Positron emission tomography is nuclear medicine imaging technique that provides a three-dimensional image of the liver and its related structures. Isotopes such as, C-11, N-13, O-15, F-18, Cu-64 and I-124 are used as positron emitters. . PET is often used in conjunction with CT to produce more accurate and detailed images. The basic process employed in PET is the annihilation of a positron and an electron that results in two almost collinear γ photons, each having energy of 511 keV. When these are detected in coincidence by a pair of detectors placed in a ring (or a set of rings) around the body, one can infer that the annihilation occurred at some place along a line (not taking into account the finite size of the detectors) joining the centres of the two detectors. By registering many coincidence events from different detector pairs one obtains a transformed image of the spatial density ρ(r) of the positron-emitting nuclide [Kacperski and Spyrou, 2004].

The PET/ MRI combination is technically a difficult procedure and its clinical role is uncertain besides being invasive and very expensive [Cherry, 2009].

1.7.8 Endoscopy

Endoscopy plays an important role in diagnosing and managing liver disease. Endoscopy uses a narrow, illuminated tube with a fiber-optic camera at the end, to visualize the liver and associated structures. However, the procedure is invasive and qualitative [Greenberger et al, 2009; Gershman, 2012].

1.7.9 The summary of the techniques

Histopathology and Biopsy are both laboratory based with high accuracy but they are invasive and the former applies to the dead while both cannot be done real time.

Planar X-ray imaging is most popular due to low cost and availability, yet, its inefficiency in imaging soft tissues makes it unpopular for advanced investigation of soft tissues.

Ultrasound propagates poorly through a gaseous medium but excels in watery or fluidic compartments. Ultrasound results may be inaccurate due to poor resolution and the ability of the operator analysis. It is not invasive and can be done real-time but it is more qualitative than quantitative.

CT offers very good contrast resolution and hence has the ability to study soft tissues but CT, though quantitative, is expensive and invasive and poses a high radiation dose problem.

Magnetic resonance imaging (MRI), or Nuclear magnetic resonance imaging (NMRI), is primarily a medical imaging technique most commonly used to visualize the structure and function of the body and has advantage of better contrast over CT, US and X-Ray but MRI is very expensive and cannot be widely used.

1.8 The need for alternative imaging techniques

A study of the four most generally used imaging modalities, Medical Ultrasound, Computed Tomography, Magnetic Resonance Imaging and the traditional X-ray Imaging has shown various levels of accuracies, sensitivity, specificity and consistency. Ideally, perfectly working imaging equipment will be 100% sensitive, specific and accurate. Sensitivity in this case is defined as the equipment's ability to detect a problem in patient (example, tumour) all the time. Specificity means the ability to reject all manifestations that are true negatives and accept all manifestations that are true positives. Accuracy is the ability to maintain specificity (to the point of discerning false positives and false negatives) and sensitivity.

Vanviliet et al, 2007, did an extensive study of 569 oesophageal or gastric cardiac cancer patients who had undergone neck/thorax/abdomen CT, abdomen US, neck endoscopic ultrasonography and/or chest X-ray for staging. The sensitivity and specificity were first determined at an organ level (results of investigations, i.e., CT, US abdomen, US neck, EUS, and chest X-ray, per organ), and then at a patient level (results for combinations of investigations), considering that the detection of distant metastases is a contraindication to surgery. They compared three strategies for each organ: CT alone, CT plus another investigation if CT was negative for metastases (one-positive scenario), and CT plus another investigation if CT was positive, but requiring that both were positive for a final positive result (two-positive scenario). CT showed sensitivities for detecting metastases in celiac lymph nodes, liver and lung of 69, 73, and 90%, respectively, which was higher than the sensitivities of abdomen US (44% for celiac lymph nodes and 65% for liver metastases), EUS (38% for celiac lymph nodes), and chest X-ray (68% for lung metastases). In contrast, neck US showed a higher sensitivity for the detection of malignant supraclavicular lymph nodes than CT (85 vs 28%). At a patient level, sensitivity for detecting distant metastases was 66% and specificity was 95% if only CT was performed. A higher sensitivity (86%) was achieved when neck US was added to CT (one-positive scenario), at the same specificity (95%). Slightly higher specificities (97–99%) were achieved if liver and/or lung metastases found on CT, were confirmed by US abdomen or chest X-ray, respectively (two-positive scenario).

The combination of neck/thorax/abdomen CT and neck US was most cost-effective for the detection of metastases in patients with oesophageal or gastric cardiac cancer, whereas the performance of CT only had a lower sensitivity for metastases detection and higher costs.

Chandawarkar et al (1996), calculated the accuracy, sensitivity, and specificity of each radiological investigation for each anatomic group of nodes for CT, US and MRI and showed that EUS is more accurate and significantly more sensitive ($P<0.01$) for lymph nodes along the right recurrent laryngeal nerve and those in the upper and mid-periesophageal, infracarinal locations. Paratracheal and lower paraesophageal nodes are assessed better using CT whereas MRI is better for mid-paraesophageal and infra-aortic nodes. US is most accurate and sensitive for evaluation of cervical and abdominal nodes ($P < 0.01$, that is, the chance of observing the result).

Tschammler (1998), pointed out the inaccuracies in the article published by Chandarwarkar et al,[1996] faulting their EUS results for the lymph nodes, for a system with 80% specificity, 20% sensitivity and 95% accuracy, to be false and unrealistic. He agreed with the MRI accuracy and specificity at 94% respectively with a sensitivity of 50% and also the CT accuracy, specificity and sensitivity of 92%, 94% and 75% respectively.

Finally, Chandarwarkar et al [1996] also concluded that US is the most accurate method to evaluate cervical and abdominal nodes but did not give the criteria for their conclusions nor the criteria they used to differentiate between benign and malignant lymph nodes.

The above findings simply confirm that the sensitivity, accuracy and specificity of these modalities are dependent on the particular anatomy, its stage of health and position. Data on accuracy, specificity and sensitivity are influenced by the prevalence of pathological findings. A tabulated summary of findings by some researchers on MRI, CT and US regarding the system sensitivity, specificity of detection and accuracy is shown on in table 1.4a and table 1.4b shows a comparative assessment of the four major modalities.

Table 1.4a: MRI, CT and US; Sensitivity, Specificity and Accuracy of detection assessment. The dash [-] in the table represents a 'value not stated'.[Griffiths, 2005]

Author/ Modality	Sensitivity (%)	Specificity (%)	Accuracy (%)
Chandawarkar et al, 1996. MRI US CT	 50 20 94	 94 80 75	 94 95 92
Hendrick, 2005 ;Griffiths, 2005 MRI	>90	37-90	-
Houssami, 200; Griffiths, 2005 . US	81.7	88	-

Upadhyaya et al, 2006. US CT MRI	 - - -	 - - -	 83.5 85.71 95.45
Van villiet et al, 2007. CT US CT +US CT+ US + X-ray	 69 lymph node 73 liver 90 lung - - -	 44 65 - 85 86 97 -99	 - - - - - -

Table 1.4b: MRI, CT, US and X-Ray: Modality Comparison in tissue imaging (Abuchi, C. S. 2013. Personal compilation)

Factors of Consideration	**MRI**	**CT**	**US**	**X-Ray**
Detection accuracy	Highest accuracy	Lower in sensitivity & specificity than MRI	Investigator's skill dependent	Excellent for bony tissue
Radiation Exposure	None	Exposure to radiation	None	Exposure to radiation
Planar or Multi-planar	Excellent multi-planar	Multi-planar	Multi-planar	Planar
2-D or 3-D possibility	3-D enabled	3-D enabled	3-D enabled	2-D enabled
Use of Contrast agent	Safe contrast agent [Gadolinium]	Contrast agent [Iodine]	No contrast	No contrast except for special investigation
Invasive or Non-invasive	Non-Invasive	Invasive	Non-invasive	Invasive
Cost	Higher [higher than CT]	High	Moderate [higher than X-ray]	Low
Availability	Not widely available	More available than MRI	Versatile & widely available	Most available and common
Quantitative or Qualitative	Quantitative	Quantitative	Qualitative	Qualitative
Image acquisition Time	Time consuming	Short [15s-120s after injection of	10 – 15 mins.	5 – 15 mins. [Acquisition

		contrast agent]		time = few secs.]
Combination with other modality	Stand-alone	CT & US	CT& US	CT & US
Resolution	Spatial =3-4mm; Contrast: Best of the four.	Spatial = 1-2mm; Contrast: next to MRI	Spatial=2-3mm; Contrast: next to CT	Spatial=1mm; Contrast: Poor
Comment	Great impact in liver evaluation [Hamer et al., 2005].Very sensitive & specific for soft tissue lesions.	CT & US combined are most cost effective for metastasis detection.	Best for cervical & abdominal scan [Chandarwarkar et al., 1999]	Good for bones and other calcified objects .

1.9 Interaction of x-ray photons with matter

When x-rays photons pass through material, some of them interact with the material. Some are attenuated or stopped and some pass through. Possible interactions are:

Photoelectric absorption (photoelectric effect, PE)

Compton / Incoherent / Inelastic Scattering (CE) (Incoh.)

Coherent (Raleigh) Scattering (Coh.)

Pair Production (PP). This is not relevant in diagnostics and in this study because of the energy level of > 1.02 MeV photons involved. Therefore, PP will not be discussed further.

All these interactions result in attenuation of the incident beam and the relationship is given as equation 1.0

$$I_x = I_o e^{-ux} \qquad 1.0$$

Where, I_x = detected/measured (final) intensity

I_o = original intensity

μ = linear attenuation coefficient

x = the distance of travel of the beam within the sample

The equation expresses the exponential relationship between the incident primary photons and the transmitted photons for the beam with respect to the thickness of the absorber and so can be used to calculate the attenuation by any thickness of material. Linear and mass attenuation coefficients are the coefficients used most often.
Because mass attenuation is usually given, the equation can be written as:

$$I_x = I_o e^{-\rho (\mu/\rho)x} \quad \ldots\ldots\ldots\ldots \quad 1.1$$

Where, ρ = density of the sample and
(μ/ρ) = the mass attenuation of the sample

For monoenergetic beam, the number of incident photons (N_o) and the number of emerging photons (N_x) are related by the equation given below:

$$N_x = N_o e^{-\mu x} \quad \ldots\ldots\ldots\ldots \quad 1.2$$

or

$$N_x = N_o e^{-\rho (\mu/\rho)x} \quad \ldots\ldots\ldots\ldots \quad 1.3$$

The interactions of importance are the scattering (coherent and incoherent) and photoelectric absorption / effect (PE). Both contribute to (μ_{total})

$$\mu_{total} = \mu_{pe} + \mu_{coh} + \mu_{Incoh} + \mu_{pp} \quad \ldots\ldots\ldots\ldots \quad 1.4$$

Where μ_{pe} = attenuation due to photoelectric effect

μ_{pe} = attenuation due to coherent scattering

μ_{pe} = attenuation due to incoherent scattering

μ_{pe} = attenuation due to pair production

1.9.1 Photoelectric Absorption (PE)

When an x-ray photon interacts with the bound electron in an atom, the electron in an inner shell may be knocked out of its shell and an outer electron takes its position, an Auger electron or a characteristic x-ray is emitted (x-ray fluorescence) and the electrons in the shells are rearranged. It may be possible for the characteristic x-ray produced this way to be detected as a scattered x-ray which it is not. The photoelectric

absorption cross-section, σ_{pe} depends on atomic number Z, of the sample and the energy of the incident photon. The relation is as given below:
For high energy (>5 MeV) photon beam:

$$\sigma_{pe} \propto Z^5/ (h\nu)^2 \quad \ldots\ldots\ldots\ldots \quad 1.5$$

For low energy (<100 keV) photon beam, PE is likely to occur with a high Z scatter:

$$\sigma_{pe} \propto Z^4/(h\nu)^3 \quad \ldots\ldots\ldots\ldots \quad 1.6$$

Where, h = Planks constant and ν = frequency of the photon

1.9.2 Compton (Incoherent /Inelastic) Scattering

Compton scattering occurs when a photon interacts with a loosely bound electron in an atom and transfers part of its energy to the electron, causing the photon to change direction and energy. Compton scattering is independent of Z and the probability of interaction decreases with increase in energy. Compton is not included in this study as the study is focussed on coherent /elastic scattering.

1.9.3 Coherent scattering

Coherent scattering results in no energy loss of the incident x-ray photon and has been described by two models, Thompson and Rayleigh. The Thompson model involves one single electron and the Rayleigh model involves all the electrons in an atom.

Coherent scattering occurs when the incident photon beam strikes the atom and interacts with its tightly bound electrons which vibrate momentarily while the atom itself remains unexcited and unionized. The oscillating electrons emit radiation of the same wavelength as the incident photon. The scattered radiation emitted by the electrons, combine constructively with each other to form a coherent scattering. This is the Rayleigh scattering and is the most important interaction mechanism in tissue or tissue-like materials (Johns and Cunningham, 1983).

The Thompson's coherent scattering is a classical model which presents a situation where the incident beam passes near an electron and makes the electron accelerate

momentarily (due to the beam's electric field) and radiate energy. In the Thompson's model, no energy is given to the electron. In the Rayleigh process, the wavelength of the scattered radiation is the same as the incident photon beam.

The scattering gives the atomic form factor. Thompson scatter which relates to the Rayleigh is therefore defined by very useful equations relevant to EDXRD. The scattering cross section is defined as:

$$\delta\sigma_T/\delta\Omega = r^2/2\,(1+\cos^2\theta) \quad \ldots\ldots\ldots\ldots\ldots\ldots\ldots\ldots\ldots\ldots \quad 1.7$$

Where, $\delta\sigma / \delta\Omega$ = differential scattering cross section, T= Thompson

r = radius of an electron (2.818×10^{-15} m)

θ = angle of scatter

The interest and usefulness of coherently scattered photons in medical diagnosis was first highlighted by Speller and Horrocks (1991) and applied in tissue studies by Speller (1999).

Coherently scattered signal is subject to various degrading effects, such as self-elastic) scattering and incoherent (Compton or inelastic) scattering.

Coherent x-ray photon scatter show interesting peaks and valleys at diagnostic energies (Johns and Yaffe, 1983). These scattered photons in EDXRD studies can demonstrate diffraction patterns more efficiently.

The linear differential scattering cross section for many electrons is given the formula,

$$\frac{\delta\sigma_{coherent}}{\delta\Omega} = \frac{r_e^2}{2}(1+\cos^2\theta)\,[F_m(\boldsymbol{X}, Z)]^2 \quad 1.8$$

Where, θ is the scattering angle and r_e the electron radius, $F_m(\boldsymbol{X}, Z)$ is the molecular form factor and Z is the atomic number (Harding et al 1987). $F_m(\chi,Z)$ is given in terms of the momentum transferred to the photon, X, which in turn accounts for the dependence of scatter distribution on the scatter angle and energy and symbolizes the momentum transfer. The momentum transfer is given by the formula:

$$X = \frac{E}{hc}\frac{\sin\theta}{2} = \frac{1}{\lambda}\frac{sin\theta}{2} \quad 1.9$$

Where h is the Planck's constant (6.626 x 10^{-34} J s); c is the speed of light (3 x 10^{8} m/s); E is the photon energy (in keV) and λ is the wavelength of the incident beam. Coherent scattering can be constructive when in phase (thus reinforced) or destructive when out of phase as shown in figure 1.9a.

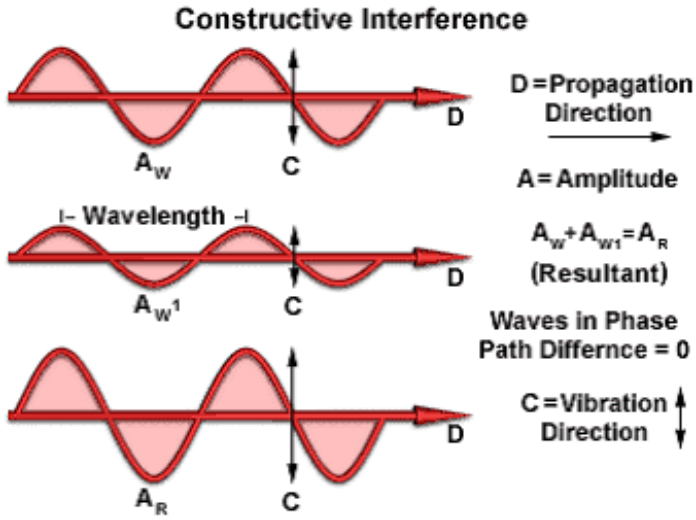

Figure 1.9a: Constructive interference[6]

Peak position depends upon the structure of the material and the positions and the intensities of the peaks, provide a unique diffraction pattern that can specifically identify the material.

[6] [http://web.pdx.edu/~pmoeck/phy381/Topic5a-XRD.pdf

The Intensity of diffraction peak from a flat rectangular sample of phase α in a diffractometer with a fixed receiving slit (neglecting air absorption), may be described as:

$$I_{(hkl)\alpha} = \frac{K_e K_{(hkl)\alpha} v_\alpha}{\mu_s}$$

Here K_e is a constant for a particular experimental system:

$$K_e = \frac{I_o \lambda^3}{64\pi r}\left(\frac{e^2}{m_e c^2}\right)^2$$

where:

- I_0 = incident beam intensity
- r = distance from the specimen to the detector
- λ = wavelength of the X-radiation
- $(e^2/m_e c^2)^2$ is the square of the classical electron radius
- μ_s = linear attenuation coefficient of the specimen
- v_α = volume fraction of phase α in specimen

Also, $K_{(hkl)\alpha}$ is a constant for each diffraction reflection *hkl* from the crystal structure of phase α:

$$K_{(hkl)\alpha} = \frac{M_{hkl}}{V_\alpha^2}\left|F_{(hkl)\alpha}\right|^2\left(\frac{1+\cos^2(2\theta)\cos^2(2\theta_m)}{\sin^2\theta\cos\theta}\right)_{hkl}$$

where:

- M_{hkl} = multiplicity for reflection *hkl* of phase α
- V_α = volume of the unit cell of phase α
- the fraction in parentheses equals the Lorentz and polarization corrections for the diffractometer $(Lp)_{hkl}$, including a correction for the diffracted beam monochromator
- $2\theta_m$ = the diffraction angle of the monochromator
- $F_{(hkl)\alpha}$ = the structure factor for reflection *hkl* including anomalous scattering and temperature effects

The UCL X-ray diffraction system has a tungsten target source which produces poly-energetic beam. A high purity germanium detector with good energy resolution is used to acquire the diffraction profile of the samples under investigation at a fixed diffraction angle. The benefits of using coherently scattered x-rays in place of transmitted x-rays are in the imaging of materials with very similar atomic numbers [Podgorsak, 2010]. The transmission x-ray images can clearly distinguish between materials of high and low Z, but cannot distinguish between materials of the same Z, for example, the fibro-glandular breast tissue and breast carcinoma due to very low contrast.

1.10 X-ray Diffraction and the Bragg's Law

X-ray diffraction is a very versatile, quantitative, non-destructive and non-invasive analytical technique. Earlier studies with X-ray diffraction investigated materials at molecular level, identified the position of atoms in crystals [Hukins, 1981]. The theory and methodology of X-ray powder diffraction as applied to the crystalline materials are similarly applied to semi-crystalline, non-crystalline and amorphous materials. When an X-ray beam hits a sample, it diffracts according to Bragg's law.

$$n\lambda = 2d \sin \theta \qquad 1.10$$

Where, n is the order of diffraction, λ is the photon wavelength, d is the spacing between the scattering planes and θ is the scattering angle [figure 1.9a]. Diffraction can easily be observed in crystalline materials. If the atoms of a crystal are rigidly fixed to one another in a crystal lattice, the phase relationship between the radiation emitted by the electrons within different atoms are constant and will result in constructive interference at a well-defined angle in agreement with the Bragg's law

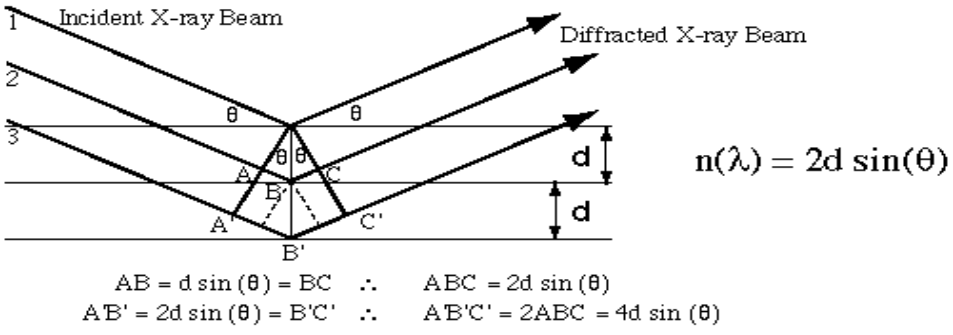

Figure 1.9b: Bragg's law illustrated.

If the path difference (ABC) between the diffracted rays 1 and 2 (path difference is the difference in path traversed by two waves, measured in terms of wavelength of the associated wave) is exactly one wavelength then they will reinforce each other by constructive interference. Under these same conditions the path difference A'B'C') between rays 1 and 3 will be two wavelengths and they also will constructively interfere.

For a given material, there will be a set of planes, each having a specific angle usually called the Bragg angle that satisfies Bragg's law, resulting in a diffraction pattern with a number of peaks at the angle corresponding to a particular plane. Crystallographers use the set of well-defined angles for a particular material to determine the crystal structure of the material or to identify the material. The intensity of a given interference from a given set of planes depends on a number of factors which include atomic form factor and the crystal structure [Kidane, 2001].

1.11 X-Ray Diffraction and scatter in biological tissues

A lot of studies have used X-ray diffraction to differentiate between healthy and diseased tissue and also applied the technique in the investigation of tissue structure at the onset or progress of disease. Studies vary from the use of small angle x-ray scattering [SAXS], wide angle x-ray scattering [WAXS], diffraction enhanced imaging [DEI], angle dispersive x-ray diffraction [ADXRD] and energy dispersive x-ray diffraction [EDXRD].

In a topical review by Theodorakou and Farquharson, [2008], they described the techniques used by various researchers and showed the interesting results obtained from the different x-ray techniques including the x-ray diffraction studies on the brain, breast, fat, kidney, muscle and uterus. The technique of interest in this work is the diffraction technique.

Amorphous materials produce diffraction spectra (diffraction profiles or scatter signatures specific to the material) with one or two broad peaks due to their short range molecular order. The peak as well as the shape, intensity, and the peak width identifies the materials, [Jian and Hejing, 2003]. These values therefore have caused X-ray diffraction to be targeted at diagnostic applications as several investigators found significant differences between the diffraction profiles of healthy and diseased tissue in the bone [Harding et al, 1987; Royle and Speller, 1990], breast [Rogers et al, 1999], water, plastic and beef muscle [Kosannetzky et al, 1987; Peplow and Verghese, 1998; Johns and Wismayer, 2004].

The scatter signatures are derived from momentum transfer argument which is a function of photon energy and the angle of scatter. The signatures are obtained from

a measure of the angular dispersion of a monochromatic source as in ADXRD or a measure of the energy dispersion of a polychromatic X-ray source at a fixed angle as in EDXRD.

Other investigators [Nakano et al, 1999; Lewis et al, 2000; Fernandez et al, 2002, 2005; Amenta et al, 2003; Gelse et al, 2003; Siu etal, 2005; Round et al, 2005; Falzon et al, 2006] used the SAXS technique to distinguish between normal and abnormal tissue, categorizing them into healthy, benign and cancerous tissues for the range of organs studied and with particular interest in collagen pattern.

The X-ray beam from this ADXRD arrangement is of inherently low energy, 8keV, resulting from the k_{α} lines of copper and penetration depth is severely limited thus restricting the sample to a very small size [Esbrand, 2009].

The success story with diffraction, especially EDXRD, set the pace for further experimentation and investigation with biological materials and tissues. All these results have been quantitatively processed with statistical details, hence its usefulness in tissue characterization.

1.12 Animal tissue components

About 96% of the body mass is made up by 4 primary elements, oxygen (60%), carbon (23%), hydrogen (10%), and nitrogen (2.5%). Other major elements are calcium (1.4%), phosphorous (1.1%), sulphur (0.2%), potassium (0.2%), sodium (0.14%), chlorine (0.14%), and magnesium (0.03%) (Emsley, 1998).

Mattsson and Thomas (2006) listed the body composition at atomic level as consisting of the elements quoted by Emsley (1998) above. At the molecular level, the constituents include the minerals (of the bone and soft tissue), carbon, hydrogen and oxygen and at the cellular level, extracellular solids and fluids and cells (adipocytes) (Wang et al, 1992; 2002; 2005).

The six major types of molecules in the human body are water, lipids, proteins, carbohydrates, bone and soft tissue minerals.

The organ-tissue mixture can be classified into bony tissue, visceral organs (heart, lung, liver and kidney), skeletal muscle, real bone and adipose tissue.

The visceral organs fall into one category and have nearly the same contents with a few differences. The bone stands out on its own. The components affect the way the tissues diffract and attenuate and the production of diffraction spectra (profiles). Bone can be easily differentiated but not the visceral tissues. They require advanced imaging to distinguish one from the other.

1.13 Animal tissue samples

The pig's tissue is the animal tissue substitute of choice for human tissue. Amongst the large animals available, pig featured in studies of involving the heart, lung, liver, kidney, muscle, brain and bone with satisfactory results. Therefore, pig appears to be the most widely used and the most suitable animal due to its physiological and anatomical compatibility with the human tissue and its ability to breed large numbers of animals rapidly, which ensures regular supply of the porcine tissues.

Tissues from different animals had been used for cardiovascular studies as shown on table 1.6, with preference given to pig for human suitability, compatibility and satisfactory results. Baboon was the best but not readily available for use (Rashid et al, 2004).

Table 1.5: Researchers and the animal tissues they used in cardiovascular studies for over three decades (Rashid et al, 2004).

Researcher (main)	**Animal used**	Remark
Clowes et al (1986)	Baboon	Not easily available
Zilla et al (1994)	Baboon	
Panetta et al (2002)	Pig	Available
Robotin-Johnson et al (1998)	Pig	
Niklason et al (1999)	Pig	

Elkins et al (2001)	Sheep	Available
Dohmen et al (2001)	Sheep	
Shum-Tim et al (1999)	Lamb	Available
Watanabe et al (2001)	Dog	Not easily available
Conklin et al (2002)	Dog	
Clarke et al (2001)	Dog	
Lantz et al (1990, 2001)	Dog	
Shindo et al (1987)	Dog	
Matsuda et al (1993, 1994, 1995, 1996)	Dog	
Miwa et al (1994)	Dog	
Seifalian et al (2003)	Dog	
Niu et al (1993)	Dog	
Noishiki et al (1998, 2001)	Dog	
L'Heureux et al (1998)	Dog	
Tsukagoshi et al (1999)	Rabbit	Readily available
Sparks et al (2002)	Rabbit	
KUO et al (1998)	Rabbit	
Campbell et al (1999)	Rabbit and Rat	
Yue et al (1989)	Rat	
Liu et al (2000)	Rat	
Kobayashi et al (1992)	Rat	
Nathan et al (1995)	Rat	
Shimizu et al (2002)	Rat	
Eschenhagen et al (2002)	Rat	
Okamura et al (2002)	Mouse	Readily available

1.14 Energy Dispersive X-Ray Diffraction

Here the issue is the use of scattered radiation, which is seen as a problem in medicine (Speller, 1999) in that it is alleged to reduce the image quality and prevents abnormality detection. Reasonable attempts have been made to exploit the scattered radiation to give useful information that can be used for characterisation and structural analysis (Johns and Yaffe, 1982; Hukins, 1983; Kosanetzky et al, 1987; Speller, 1999).

The production of coherent scattering has been discussed in section 1.9.3. The merit of it is in its use in various XRD imaging including EDXRD, ADXRD, the low and small angle x-ray scattering (LAXS / SAXS), energy dispersive x-ray fluorescence (EDXRF) and X-ray refraction. These studies produce useful results as seen from the diffraction profiles obtained. It has been shown in the studies that different arrangements of the molecules in a sample produce different diffraction patterns. EDXRD and ADXRD are most popular. Generally, XRD has been widely applied and particularly the Rietveld Method (Rietveld, 1966) termed then as 'gold standard' for structural quantitative analysis with accuracies in the range of 99% is generally accepted as the preferred tool. It has been applied in different studies that include forensic analysis, study of contaminants, mineral assays, pharmaceutical analysis, quantitative phase analysis, amorphous and crystalline contents of materials and fibre analysis. Other interesting studies that have been done with XRD are residual stress analysis in industries, texture analysis, particle size determination and crystal orientation. All these point to XRD as a good and promising area of research for better applications.

The aspects of ADXRD and EDXRD are directed to biological materials and their analysis due to their material specific signature production. The energy level applied to the methods at diagnostic levels is about 100KeV or less, usually from 30KeV to 100KeV and at low scattering angles. Energy can be made lower than 30KeV depending on the tissue sample.

ADXRD uses low energy mono-energetic beam at varying angles, whereas, EDXRD uses a high energy resolution detector at a fixed angle, poly-energetic beam. Therefore scatter in ADXRD is a function of angle as angles are varied, but in EDXRD, the scatter is a function of energy as energy is varied.

In the review by Theodoraku and Farquharson (2008), they referred to ADXRD as most conventional method to obtain x-ray signatures. They went further to say that ADXRD is more accurate than EDXRD because, according to them momentum is only limited by the angular resolution of the experimental set up in ADXRD while EDXRD is limited by the resolution of the detecting system and the polychromatic spectrum. The use of high purity germanium (HPGe) detector addressed the resolution and the energy problem, making EDXRD a more convenient and preferable because of fast data acquisition. The main purpose of the HPGe detector is to convert gamma rays into electrical impulses which can be used, with suitable signal processing, to determine their energy and intensity. Further details of the HPGe will be treated in Chapter 2, where the design and development of tissue EDXRED system will be treated. In EDXRD, the spectrometer system, the scattering angle and the photon energy are complementary towards the momentum transfers result. EDXRD measures both coherent and incoherent scattering at low angles less than 10 degrees.

In conclusion EDXRD method needs to be optimised for use in clinical application. Experimental measurements are time consuming and expensive compared to simulation and modelling, yet it is more reliable and realistic. An alternative but theoretical method to the experimental measurement is the Monte Carlo Simulation. Monte Carlo Simulations aim to simulate each individual x-ray photon and their interactions, in an effort to replicate the results seen in experimentation. If accurate, the simulations provide more information about the properties of the objects under inspection (by the x-rays) than might be possible with experimentation.

However, Chaparian (2009) stated that Monte Carlo Simulation lacks a satisfactory physical model for Coherent or Rayleigh scattering effects. Following the argument in this concluding part, the study of EDXRD appears promising and worthwhile. If the result comes out very satisfactory the future work will be on transforming EDXRD to real time diagnostic imaging modality.

1.15 Previous XRD works

A lot of work has been done over the years using EDXRD for a variety of applications in medicine, security and industry. A summary of some of the studies is given on table 1.8.

Table 1.6: Previous studies of X- ray diffraction of biological tissues

Tissue type	Mode of investigation	Researchers/ Year of study	Results / Remarks
Kidney	XRF	Grinyer et al 2006	Identified mercury
Bone	LAXS	Royle and Speller, 1990 and 1995	Determined mineral bone density. Diffraction spectra of dry bone and bone equivalent (animal fat) with values: Dry bone, 1.7nm^{-1}; fat, 1.9nm^{-1}
Bone & muscle (tissue equivalent)	Goniometer with NaI detector	Poletti et al, 2004	Measured scatter signatures
Bone & Breast(human)	Microbeam SXRF	Geraki et al, 2008	Identified metals. Classification of breast into: Healthy/invasive duct carcinoma
Heart & muscle (animal)	XRD	Matsubara and Millman, 2008	Diffraction patterns
Liver (human)	ADXRD	Theodoraku and Faquharson, 2009	Normal & abnormal classification
Muscle, blood, liver, bone & brain	XRD	Kosanetzky et al, 1987	Obtained the differential pattern for each
Breast(human) Kidney & bone	XRD with CMOS sensor	Bohndiek et al, 2008	Obtained the scatter signatures for each
Breast & bone (human)	XRD	Royle et al, 1999	Differentiated between normal and abnormal breast tissue.
Breast(human)	SAXS	Suhonen et al, 2005	Identified collagen
Breast(human)	XRD & DEI	Fernandez et al, 2002, 2005	Identified healthy /cancerous/mixed tissue
Breast(human)	XRD & DEI	Lewis et al, 2000, 2005	Identified healthy /cancerous/mixed tissue

Breast(human)	XRD & DEI	Falzon et al, 2000	Classified the breast tissue into: healthy /cancerous/mixed tissue
Breast(human)	XRDCT	Kosanetzky et al, 1987	Classified breast tissue into: healthy /cancerous/mixed tissue
Breast(human)	XRDCT	Harding et al, 1987	Classified the breast tissue into: healthy /cancerous/mixed tissue
Breast(human)	XRDCT	Evans et al, 1991	Classification into adipose/fibro-glandular/benign/carcinoma/fibrocystic disease
Breast(human)	XRDCT	Johns and Yaffe, 1987	Classified the tissue into: Normal / abnormal/fibrous/infiltrating duct carcinoma/fibro-adenoma/fibrocystic
Breast(human)	XRDCT	Kidane et al, 1999, 2001	Classification into: adipose/fibro-glandular/fibro-adenoma/ benign/carcinoma/fibrocystic change
Breast(human)	XRDCT	Poletti et al, 2002	Classification into: Adipose and glandular
Breast(human)	XRDCT	Castro et al, 2004,2005	Classification into: healthy/connective/adipose/infiltrating duct carcinoma
Breast(human)	XRDCT	Ryan and Faquharson, 2004	Classification into: Adipose/fibro-adenoma/invasive duct carcinoma
Breast(human)	XRDCT	Grifiths et al, 2003, 2007	Discrimination and analysis of breast tissue into: fat, tumour and connective tissue
Breast(human)	XRDCT	Pani et al, 2006, 2010	Characterization of the breast tissue into: Adipose/fibrosis/well differentiated cancer/poorly differentiated cancer/benign
Breast(human)	XRDCT	Peplow and Verghese, 1998	Measured form factors via calculation. Identified normal and neo-plastic breast tissue
Breast (human)	XRDCT	Kleuker et al, 1998	Classification into: Healthy and cancerous tissue
Breast(human)	XRD	Harris et al,2003	Identified diffraction image of cancerous inclusion in healthy breast tissue
Breast(human)	XRD	Changizi et al, 2003 and 2005	Classification into: adipose, 1.09nm^{-1}; fibro-glandular, 1.25nm^{-1}; benign fibrocystic change, 1.38nm^{-1}; carcinoma, 1.53nm^{-1}

The work done above demonstrated the ability of XRD to differentiate between normal fibrocystic changes (benign) and carcinoma (malignant) breast tissues and the inability to differentiate between different types of carcinoma [Changizi et al, 2008].

The system needs to be optimized, to reduce the time for data acquisition, increase sensitivity, spatial resolution and momentum transfer resolution with good system geometrical set-up for accuracy of results and potential clinical application [Chaparian et al, 2010].

From the list of works as listed in the reviews by Theodorarkou and Farquharson (2008; 2010) and till now, it can be deduced that most of the research was on the breast, with a few on the liver and none specifically on the heart.

1.16 Focus of this work [EDXRD of the liver and heart]

This study is focused on the EDXRD investigation of two major issues. Issue number one, is to detect fat deposits or nodule in the liver and number two, to detect the plaques in the blood vessels of the heart. Some experiments are carried out with fatty liver and fatty heart. Spectral patterns are obtained and studied critically. EDXRD is solely used for the investigations. The most important aspect will be the detection of the unusual presence of fat deposits in the tissue samples. Such early detection and accurate diagnosis of disease will lead to prompt and specific treatment before it progresses to cause irreversible damage. As stated earlier, about 50% of patients diagnosed with cirrhosis die within five years unless they receive surgical liver transplant [www.mayoclinic.org]. Consequently, our goal is to achieve valuable detection on time.

1.17 Summary and the scope of this PhD work

The work covers the EDXRD investigations of some biological materials with focus on the liver and the heart. EDXRD has been used to detect the fat nodules in the liver and should extend to the detection of the fat deposits and plaques in the blood vessels of the heart. This is with a view to come to the conclusions for the authenticity of

EDXRD as a useful tool for detection and diagnosis of fatty problems and related issues associated with the liver and the heart.

The first chapter dwelt on the purpose of the research, the health problems involving the liger and the heart, the motivation and what I intend to achieve and the possible contribution to knowledge and in diagnostic radiology and an overview of the basic anatomy and physiology of the liver and heart. The involvement of fat in the liver and the heart, with diseases and problems are listed. The available imaging techniques are briefly discussed and how they are currently used and their limitations. The need for alternative imaging techniques and the basic physics of x-ray photon interactions are discussed. X-ray diffraction and the Bragg's law, and photon scattering in biological tissues are also looked at. The usefulness of EDXRD as a non-invasive and quantitative tool for improved investigations and its effectiveness in detection of fatty tissue are discussed. Fat as a health hazard is also discussed. The basic principles of X-ray diffraction and its application to tissue discussed. Tissues from different animals have been used but porcine has been chosen as most suitable for investigations.

Chapter 2 discusses the design and development of a tissue diffraction system. It covers the calculation needed to set up the system, the alignment techniques, positioning and selection of the collimators and the determination of the scattering volume and the checks for performance of the system.

Chapter 3 discusses the experiments performed to determine the detectability of the fat nodules in liver disease and the plaques in the blood vessels of the heart using the EDXRD technique on small size phantoms/tissues. The data are acquired and processed for analysis.

Chapter 4 shows the results and analysis of the three main experimental works with the EDXRD system in the liver and heart investigation for the small sized phantoms. This chapter has the overall liver and heart data obtained and evaluated with statistical analyses, with the aim of finding the most robust approach to the detection of early disease.

A multivariate analytical software and procedure will be expertly developed and used. The main software will be Matlab and the main explanatory form of analysis is the principal component analysis (PCA), which finds the linear combinations of the

underlying variables with maximal variance. This can be used to assess the detectability and sensitivity of the system from the analysed data.

Chapter 5 shows the translation of the output of the results from small-sized phantom/tissue to patient/life-sized tissues of the liver and the heart. The needed geometrical modifications and adjustments of the EDXRD system for the life-size tissues are critically taken into account. The estimates of likely dose to patients are made to ensure conformity to the norms and standards of radiation protection and the ALARA principles. The results or the conclusions show the feasibility of the system to fit into clinical application.

Chapter 6 has the conclusions derived from the work and discussion on the results and the conclusions. The results or the conclusions are indicators of the feasibility of the EDXRD system and its ability to fit into clinical application. Suggestions for future research work for the development and production of an EDXRD diagnostic system/equipment that can be used in a clinical environment.

Chapter 2

Design and the development of tissue EDXRD system

2.1 Introduction

Having seen the problems and diseases associated with the presence of fat in the liver and the heart, the application of EDXRD and the systematic approach in the investigation becomes important. The choice of equipment and the entire system design are carefully processed.

This chapter describes all the major components of the EDXRD equipment and the system set-up. The system alignment techniques used, selection of detectors, positioning of the collimators, calculation and identification of the sensitive scattering volume are detailed in the following sections.

2.2 Materials and instrumentation

The system components include a Philips AGO industrial X-ray set and brass collimators. A high purity germanium detector [HPGe] with a planar crystal of 26mm diameter and depth of 10mm (model number, GLP16/95/16PS, manufactured by EG & G Ortec, Oakridge, Tennessee, USA) together with a multi-channel analyser [Dspect Junior, ORTEC] were used to analyse the diffraction spectra. The schematic diagram of the set-up is shown in figure 2.1a. Also shown is the photograph of the setup in figure 2.1b.

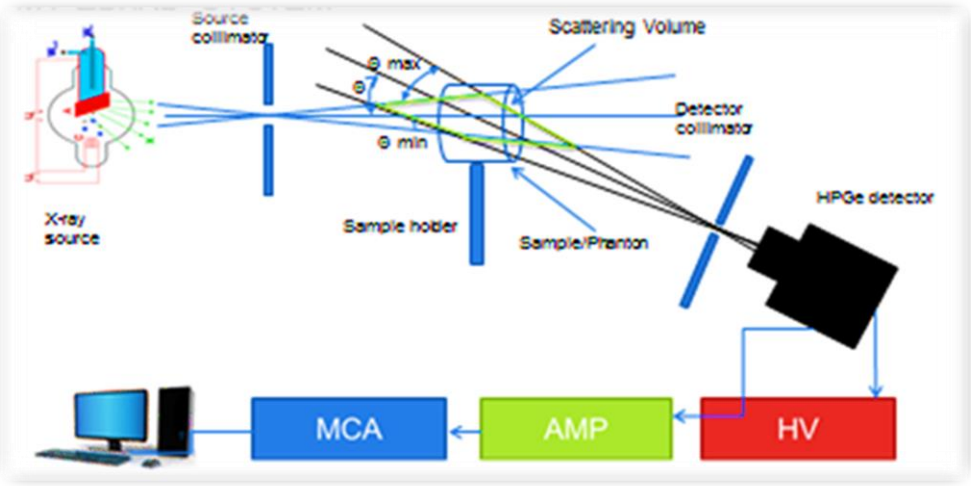

Figure 2.1a: The schematic diagram of the complete EDXRD set-up showing the associated electronics, the high voltage (HV) supply, amplifier (AMP), the multi-channel analyser (MCA) and the computer for data acquisition and processing. The colour used for the identification of the instruments here has no added meaning.

Figure 2.1b: The photograph of the system set-up. The X-ray source is shown in the distance with the HPGe detector in the foreground. The close-up shows the two brass collimators and the sample stage.

2.2.1 EDXRD system set up

The x-ray tube, source collimator [SC], sample, detector collimator [DC] and the detector need to be carefully aligned and this procedure is described in section 2.4. The choice of the components used in these experiments is given in the following sub-sections.

2.2.2 X-ray source

The x-ray source is a tungsten (W) target industrial x-ray tube [Philips AGO installation model] of high-power and water-cooled. The source spectrum is polychromatic and the beam has an inherent filtration of approximately 0.5mm Al. There are two settings for the focal spot size of the X-ray source. One has a dimension of 3mm x 3mm and the other 1mm x 1mm. The focal spot was set at the 1mm x 1mm slot and was reasonable for the collimators employed and ideally suitable to the X-ray beam. The tube has a maximum operational output potential and current of 160kVp and 30mA respectively. For the investigations, the operating parameters used ranged between 40kVp, 2mA, up to 70kVp, 6mA.

2.2.3 Detector choices for EDXRD investigations

Detectors for EDXRD need to have good energy resolution and either HPGe or CZT/CdTe are used. Some of the important properties of these materials are summarised in Table 2.1.

High purity germanium (HPGe) detectors are commonly used for x-ray spectroscopy due to their extremely high energy resolution capabilities, which is generally quoted by the manufacturers as better than 500eV at 122 keV. A major disadvantage in HPGe is the small energy gap of 0.7 eV between the valence and the conduction band (see table 2.1), compared to the others. Consequently, it requires a cooling to liquid nitrogen temperatures and the sensor must be enclosed in a cryostat [Knoll, 1999]. Germanium offers good detection efficiency, especially at low E, due to its atomic number, Z (= 32). Pani et al (2009) suggested replacing HPGe detectors with CZT (Cadmium Zinc Telluride) detectors in EDXRD systems to reduce cost and allow the system to operate

at room temperature. CZT, due to its higher w-value (mean energy required to produce an ion pair) has lower energy resolution of 5-6% at 60keV (Bertolucci et al, 1998) and poorer charge mobility leading to some degree of charge trapping. Therefore, the use of CdTe or CZT might only be justified in systems with poor geometrical resolution and where high energy resolution cannot salvage the overall spectral resolution.

In the UCL EDXRD system HPGe has been chosen and the system is computer controlled. The excellent energy resolution of these detectors means that the achievable momentum transfer resolution of an energy dispersive diffraction system becomes limited purely by the angular resolution of the system collimation. The HPGe is therefore the detector of choice and most suitable for the EDXRD studies. The detector used in these experiments is a planar design of diameter 26mm and depth 10mm, model number, GLP16/95/16PS, from EG & G Ortec, USA. This detector has a nominal energy resolution of better than 440eV at 122 keV. Maestro software from EG & G Ortec was used to assign photon intensity to a specific related channel amongst the 512 channels. The Maestro output is a '.chn' format which was converted using IDL code to a format suitable for import to Excel. The detector system was calibrated using Americium-241 and the energy resolution evaluated as the ratio of full-width-at-half-maximum [FWHM] to the maximum energy at the peak position and expressed as a percentage.

$$\text{Energy resolution} = \frac{FWHM}{Energy\ (max.)\ @peak}\ x\ 100\% \qquad 2.1$$

Table 2.1: Table of some of the relevant properties of Ge, CdTe and CZT that affect their suitability as detectors in an EDXRD system (Baciak et al 2002; Sakellaris et al 2010).

material	**Density ($g.cm^{-3}$)**	**μ at 140 keV (cm^{-1})**	**Energy gap (eV)**	**w-value (eV)**	**Mobility life time ($cm^2.V^{-1}$)**	
					electron	hole
Ge	5.32	0.72	o.7	2.98	0.72	0.84
CdTe	5.85	3.22	1.5	4.43	$3x10^{-3}$	$5x10^{-4}$
CZT	5.82	3.07	1.7	~5	$3x10^{-3}$	$5x10^{-5}$

2.2.4 The System collimators

There is a primary collimator in front of the x-ray source to reduce the beam diameter and two further collimators that define the scattering geometry of the diffraction system. The collimator positions are shown in Fig 2.1a. The collimators are made of brass blocks 75 x 60 mm and are 20 mm thick. The collimators bodies are drilled to hold collimator plugs that define the beam shape. A collection of 13 brass collimation plugs with circular apertures of different diameters ranging from 0.5mm to 2mm are available to provide different diameter pencil beams. All collimators plugs were 20mm thick.

The diffraction cell consists of the two collimators with the detector collimator adjusted angularly to provide a nominal scattering angle of 6^0. The primary collimator which is 80mm from the source is referred to as the source collimator [SC]. The other collimator is close to the detector and is referred to as detector collimator [DC]. The gap between these two collimators is ~180mm. The collimation arrangement is shown in figure 2.2

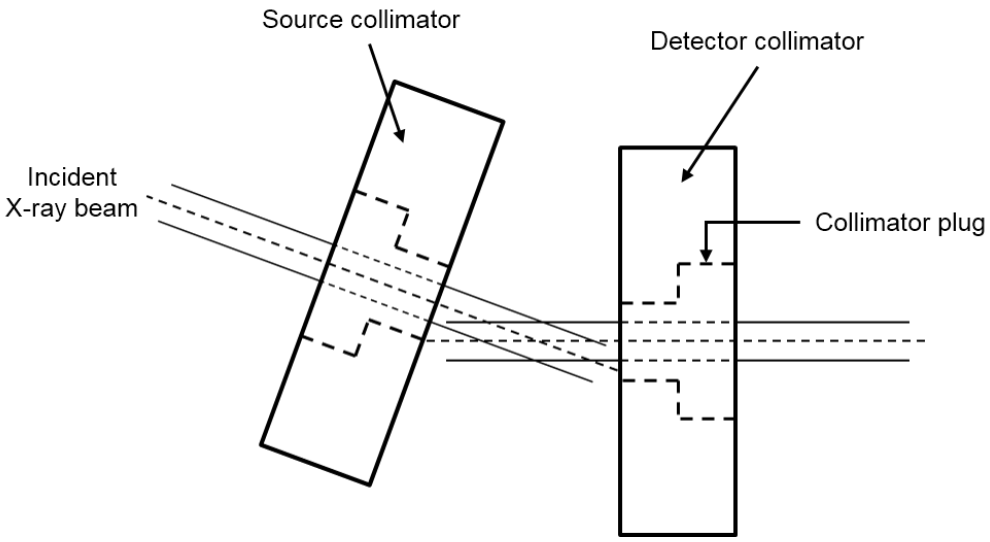

Figure 2.2: Collimator arrangement showing the collimator plugs and the nominal scattering volume.

Collimation defines the effective volume from which scatter can be collected and the angular resolution [Eqn.6] of the EDXRD system:

$$\text{Angular resolution} = \frac{\Delta\theta}{\theta} = \frac{\theta \max - \theta min}{\theta} \qquad 2.2$$

Where θ is the nominal scatter angle, θ_{max} and θ_{min} are the maximum and minimum angles at which an x-ray photon can scatter within the sample scattering volume and also be detected.

2.2.5 The multi-channel analyser (MCA)

The MCA analyses the detector pulses. The system used on the diffraction system uses digital signal processing and includes a pulse shaping amplifier. Different parameters of the amplifier are controlled by the user but the system also includes a 'self-optimisation' option. With this option detector pulses are recorded and adjustments made to the amplifier settings to give the best MCA performance. This option was chosen for all diffraction experiments. For the experiments, the number of channels was set to 512 as the energy resolution of the detector (~500eV) and energy range (~10 – 70 keV) did not require extra channels. The time for data acquisition ranged from 1 – 300seconds in live time mode and was adjusted to provide better than

1% for the maximum of any diffraction spectrum. This implied that the measurements were obtained with about 99% confidence level with values at a considered precision of 99% or more and with an error of 1% or less for every diffraction spectrum acquired.

2.2.6 The cooling system for the detector

The major drawback of germanium detectors is that they must be cooled to liquid nitrogen temperatures to produce spectroscopic data. At higher temperatures, the electrons can easily cross the band gap in the crystal and reach the conduction band, where they are free to respond to the electric field, producing too much electrical noise or dark current. Cooling the detector to liquid nitrogen temperature (77 K) reduces thermal excitations of valence electrons so that only a gamma ray interaction can give an electron the energy necessary to cross the band gap and reach the conduction band.

For the detector used in these experiments the crystal was electrically cooled using an X-COOLER II (MMR Technologies Inc.) and CryoSecure (compressor power controller) both supplied by Ortec.

2.2.7 The computer interface and sample translation

Some experiments required the phantom/sample to be scanned and consequently had to move through the scattering volume between the source and detector collimators. This was achieved using a single 200 mm linear stage by Zaber Technology. A serial interface was supplied with this unit that was controlled by the same computer used to acquire the diffraction spectra.

2.3 Diffraction imaging system geometry and alignment procedures

The geometrical positioning of the x-ray source, the two collimators (SC and DC) and the detector is such that the values of the distances between the various components of the EDXRD system must be optimized for good diffraction patterns of the tissues. Figure 2.3 show the general layout and the parameters that could be altered to optimize the scattering geometry.

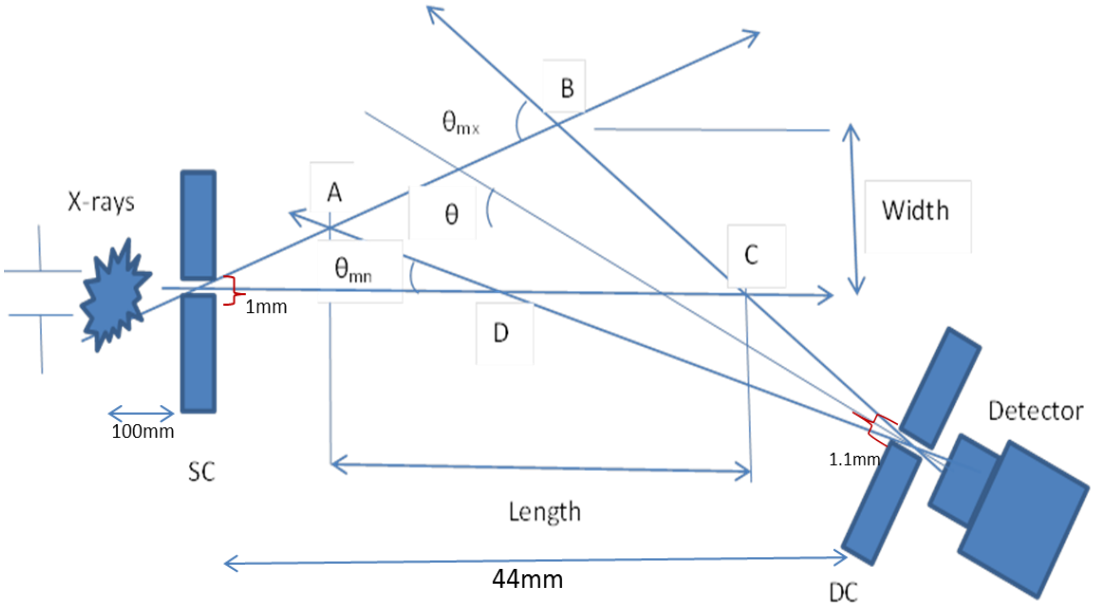

Figure 2.3: Schematic diagram of the geometrical direction of the x-ray beam through the two collimators, the source collimator (SC), detector collimator (DC) and to the detector (diagram is not to scale).

Alignment of the system to obtain a given scattering geometry is a four stage process and is done with the aid of a flat panel detector, in this case a Flash Scan 30 (Varian, USA). The components to be aligned are the x-ray beam from the source, the collimators and the HPGe detector. Firstly, the optical bench and the x-ray beam central axis must be made co-planar. Secondly, the source collimator is put in place and adjusted for maximum transmitted intensity with the correct beam profile. Thirdly,

the detector collimator is put in place and aligned at a nominal scattering angle of 0^0. At this stage maximum transmitted intensity between the two collimators with an optimum beam profile are essential. Finally, the detector collimator is adjusted to a required scattering angle and the detector placed in the correct position.

Alignment stage1: X-ray beam central axis and the optical table surface - This alignment that ensures that the x-ray beam central axis is co-planar with the optical table. A flat panel pixelated detector [Flash Scan 30, Varian, USA;] 2304 x 3200 pixels @ 127 micron pitch] was fixed 1.5m from the x-ray source. The flat panel was calibrated using flat fields and dark images. The source is housed within a lead lined enclosure which has a 5mm diameter exit window. The centre height of the exit window was determined above the surface of the optical table (260 mm). X-ray images were taken and the vertical position of the source was adjusted until the centre of the recorded image was at the same height. Once this condition was obtained the position of the centre of the circular image was marked with a cross wire.

Alignment stage 2: Source Collimator [SC] aligned with the central axis of the x-ray beam - The source collimator was mounted on rotation and translation stages (figure 2.7) to allow the position of the collimator to be adjusted. Initially the central collimator plug was removed to provide a 5mm hole which made alignment easier. The collimator position was adjusted until the image of the collimated beam was circular and centred on the position of the central axis as shown by the cross wire. The collimator plug was inserted and further adjustments made to bring the collimated beam image into alignment with the cross wires

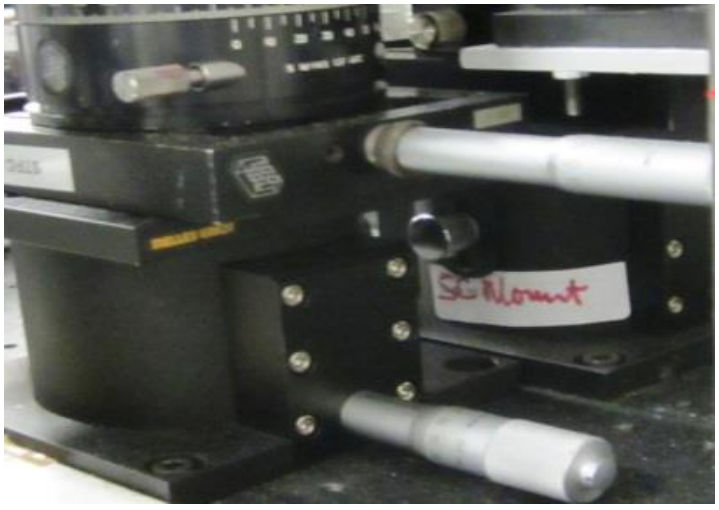

Figure 2.4: Photograph of the manual translation stage for the alignment, adjustment and mounting of the source collimator

Alignment stage 3: Detector collimator (DC) mounted and aligned with the central axis

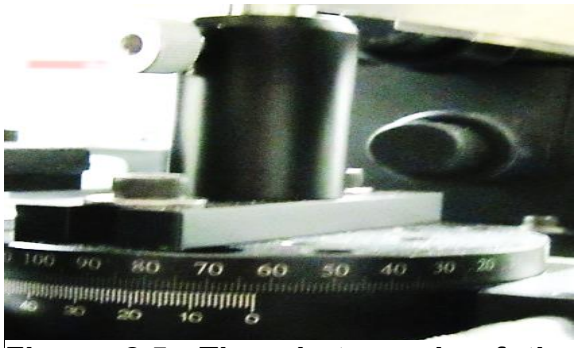

Figure 2.5: The photograph of the manual translation stage for DC mount, adjustment and alignment.

- Initially the detector collimator was aligned with the central axis of the X-ray beam, i.e., at an effective scattering angle of 0^0.

The alignment of the detector collimator was achieved in the same way as the source collimator. Firstly, without the collimator plug and then with the plug inserted. At this stage all collimators were aligned co-axially along the central axis of the beam (see images in figure 2.6).

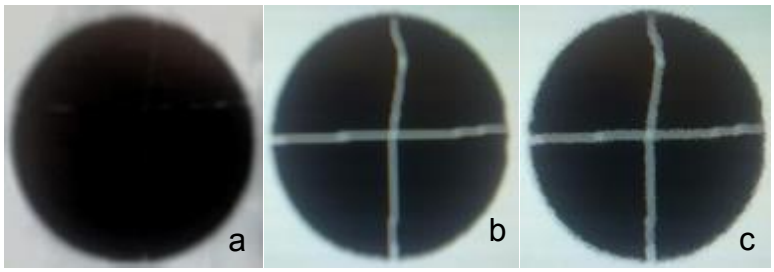

Figure 2.6: The x-ray beam images. (a) The X-ray beam image without any mounted collimators. (b) The X-ray beam image with the crosswire after aligning the SC. (c) The X-ray beam image after aligning the DC with the SC.

In figure 2.6, the first figure marked ‘a’ demonstrates the appearance of an image of the X-ray beam from the tungsten source which was first aligned parallel to the optical bench using a flat pixelated detector, ‘Dpix’ (2304 x 3200 pixels) positioned 2 meters away from the source and at a height that accommodated the circular beam, first without collimation and collected using the software, ViVA by Varian Medical System Incorporated, Carlifornia, USA. The centre of the circular beam was identified with a code written in IDL. Two straight wires are used to form a crosswire and carefully placed on the pixelated detector with their point of intersection depicting the centre of the beam. The ‘b’ part of the figure shows the X-ray image of the crosswire with the source collimator mounted and aligned with the source, whereas the ‘c’ part of the

figure shows the image with the crosswire with the detector collimator mounted and aligned with the source collimator.

Alignment stage 4:

Rotation of detector collimator for the setting of the required scatter angle – With all collimators co-axially aligned along the central axis the detector collimator was rotated by 6^0. A scattering angle of 6^0 was chosen based on the work by Kidane, 2001 and Griffiths, 2005 which demonstrated then to be the optimum scattering angle for the beam conditions and tissues to be studied. To check this scattering angle a sample of material with a known structure (and hence spectrum) was used. Caffeine was chosen to generate a diffraction profile (see figure 2.7). Minor adjustment of the detector collimator was used to bring the features in the diffraction profile to the known positions for a 6^0 scattering angle.

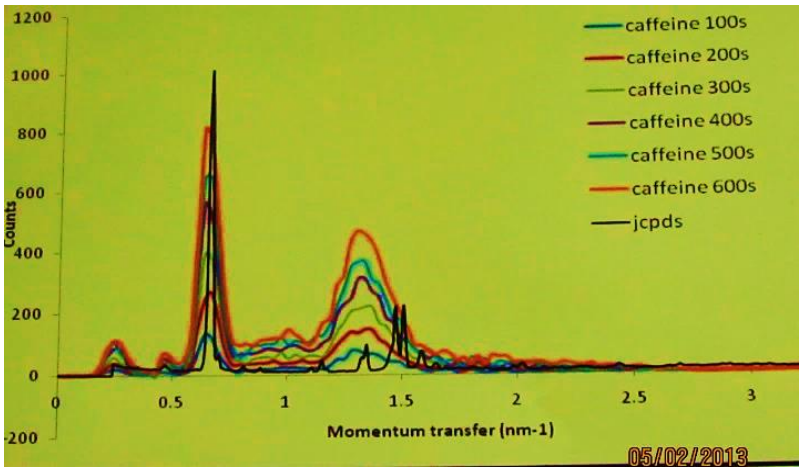

Figure 2.7: Caffeine sample spectra expressed in units of momentum transfer with the JCPDS caffeine

To understand the effect of sample positioning in the region from where scatter originates the sensitivity map of the scattering volume needs to be determined and will be discussed in section 3.4.2.

2.4 System checks for correct operation

2.4.1 Energy calibration

Before starting a series of diffraction measurements the HPGe detector was calibrated using Am-241. The amplifier settings were adjusted until the main photo-peak corresponding to the 59.5 keV line of the spectrum occurred in channel 400. Using the main peak along with two lower energies (14keV and 18keV) Maestro assigned the

appropriate energy to each channel. The detected, calibrated spectrum is shown in figure 2.8, with other peaks at lower energies of 14 keV and 18 keV. The energy resolution of the system (defined in section 2.2.4) was calculated to be 0.48keV at 59.5keV.

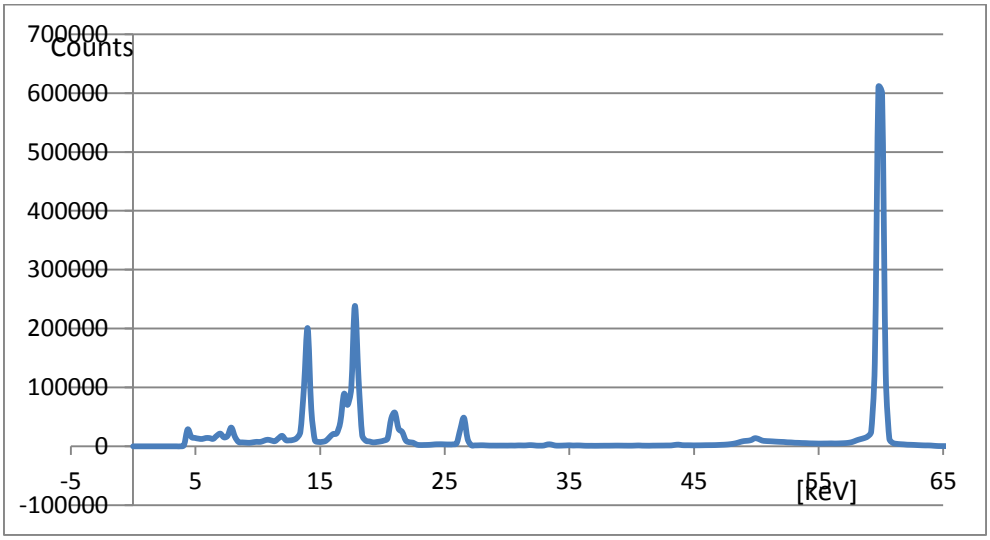

Figure 2.8: Am-241 spectrum used for calibration of HPGe detector.

2.4.2 Scattering volume calculation/mapping

The scattering volume is a geometrical space within which relevant scatter and hence the X-ray diffraction signal is created. The volume has been geometrically calculated and measured as a sensitivity map.

Scattering volume (SV) by geometrical calculation - The scattering volume was geometrically calculated using the system spatial dimensions given in table 2.2 and in figure 2.9.

Table 2.2: Table of the distances used in scattering volume determination.

Descriptor	Values (mm)
X-ray source to exit window	100
Exit window to source collimator	180
Detector to to detector collimator	25
Source collimator diameter	1.1

Detector collimator diameter	1.0
Detector collimator length	20
Detector collimator length	20
Source to sample distance	302
Source to collimator distance	280
Distance between source collimator and the detector collimator	44
Distance between the detector/source collimator and sample	22

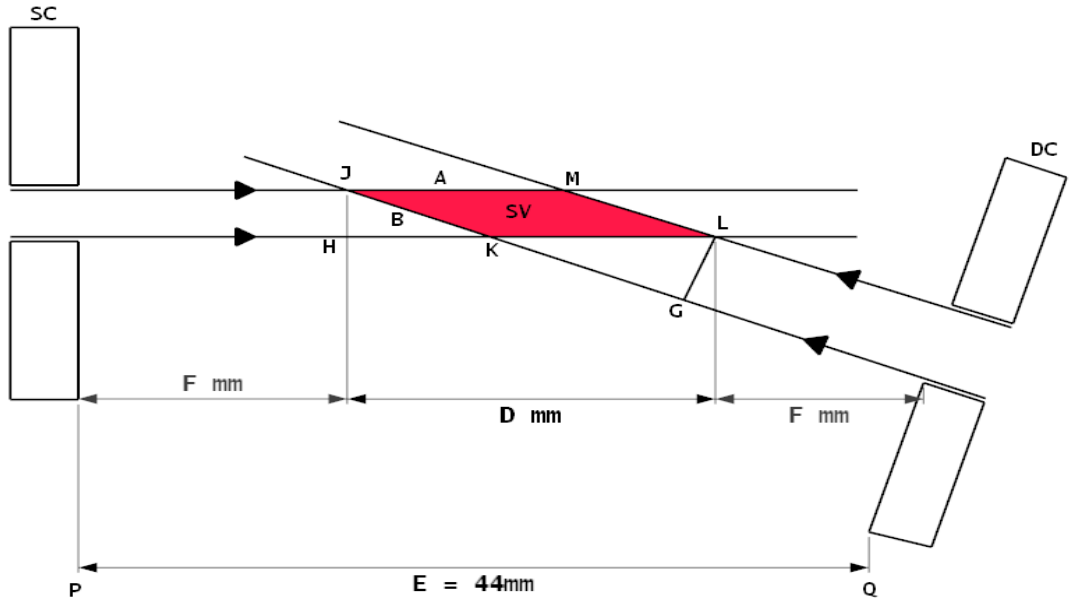

Figure 2.9: Scattering volume by geometrical calculation where the diameters of the two collimators are of equal aperture.

In figure 2.9, *KLMJ* is the scattering volume [SV]. *D* = horizontal length of SV. D = HK + KL; SC = source collimator; DC= detector collimator; JH = vertical width of SV. A and B are the two sides of the SV, while JH and LG represent the SC and DC collimator width/diameter respectively. PQ = horizontal distance between SC & DC. F & D are measurable distances. E is known. Different scattering volumes, SV, are obtained for the different collimator plug aperture combinations (see the Matlab code for the calculation in Appendix B). SV is the area of maximum intensity and scatter.

2.4.3 Diffraction profile test with known sample

A test of the system performance was made with a small pack of caffeine powder of 2mm thickness. The sample holder was made from 2mm thick cardboard within which a square of 25mm x 25mm was removed (figure 2.10). One side of the cardboard was sealed with transparent tape and the cavity was then filled with caffeine and the other side sealed. The caffeine sample was mounted on a manual translation stage that allowed the sample to be moved between the detector and source collimators along the central axis of the diffraction system. In this way any point or region of interest within the scattering volume could be investigated or repeated. Exposure factors of 70kV and 6mA were used and the diffraction signature was acquired for 100s.The raw data was converted from an energy spectrum to one expressed in values of momentum transfer assuming a scattering angle of 6^0. Figure 2.11 shows the diffraction signature (uncorrected for the shape of the incident x-ray spectrum) on the Joint committee on Powder Diffraction Standards (JCPDS) data. From the plots of this investigation, a measured momentum transfer value of 0.708nm^{-1} was obtained for the first peak in the data. This value is in good agreement with the standard caffeine MT value of 0.7nm^{-1} from the data of the Joint committee on Powder Diffraction Standards (JCPDS) MT values as shown in figure 2.7 and a good indication that the system is correctly set at 6^0.

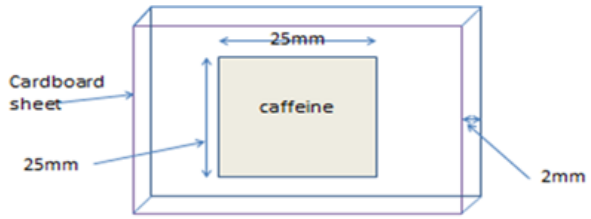

Figure 2.10: Schematic diagram of the caffeine sample enclosed in a 25mm x 25mm x 2mm cardboard holder

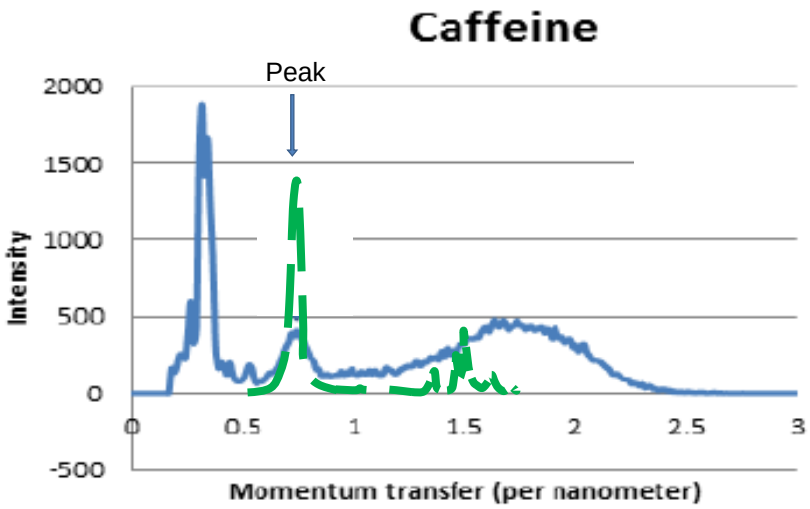

Figure 2.11: Diffraction pattern of Caffeine experimentally obtained with the corresponding JCPDS caffeine data shown as the dotted line in green

2.4.4 Tissue sample holder and in-built test sample

All tissue samples were to be held in 40mm diameter tubes (see Chapter 3) and required to be scanned across the central axis of the diffraction system. A holder was as shown in Figure 2.12. The holder and in-built test sample of caffeine were mounted on a single translation stage. With appropriate computer control measurements of unknown samples could be taken. But before the measurement the in-built test sample of caffeine could be presented to the system as a check for the system's optimum performance.

Figure 2.12: Caffeine sample mounted on a translation stage

2.5 Summary

In this chapter, the design and the set-up of the EDXRD system for use in the investigation of the fat in the liver and heart have been described. Philips AGO Industrial X-ray set with a tungsten (W) source was chosen. Tungsten was chosen for its K_α energy. The focal spot of 1mmx 1mm chosen was commensurate with the collimation as chosen and the incident x-ray beam from the x-ray tube with maximum operational output potential of 160kVp and current of 30mA.

High purity Germanium detector was the detector of choice and commonly used for x-ray spectroscopy due to their extremely high energy resolution capabilities (~ 1% FWHM at 60 keV or 500eV at 122keV). The main disadvantage of HPGe detectors is their small energy band gap of 0.7 eV, meaning that the detectors have to be cooled with an attached cooling system. In this case the cooling was electro-mechanical the X- cooler II (NMR Technologies) and the CryoSecure both supplied by Ortec Inc. USA.

With all the instruments for the EDXRD connected as shown in figures 2.1a and 2.1b, three major components (the x-ray beam, the collimators and the HPGe detector) of the system were aligned in four stages (the central x-ray beam axis alignment with the optical bench surface, the central x-ray beam with the mounted source collimator, the central x-ray beam aligned with the mounted detector collimator and the rotation of the detector collimator for the setting of the scatter angle) using the Flash Scan 30 (by Varian , USA). The system check was done. Energy calibration was done using the Americium-241. Scattering volume mapping and diffraction profile check accomplished with a test sample, caffeine. These checks established that the system

was in working order. Following the development of this diffraction system described in this chapter the system was used to investigate in-vitro the application of tissue diffraction to two major clinical problems namely, fatty deposits in the liver and plaques in the blood vessels of the heart. These two sets of experiments are described in Chapter 3.

Chapter 3

Experimental determination of the detectability of fat nodules in the liver and plaques in the blood vessels of the heart using EDXRD on phantoms/tissues

3.1 Introduction

Chapter 2 discussed the design, building and testing of an EDXRD system to look at tissue samples. The following chapters look at the application of that system to look at two major clinical problems (fat in liver and plaques in the blood vessels) as discussed in chapter 1.

This chapter describes experiments carried out on small sized tissue phantoms. Chapter 4 looks at the tools used to analyse these data and chapter 5 considers the case of human sized objects/phantoms.

3.2 Experimental set up

The experimental set up was discussed in Chapter 2 and the parameters used in the experiments to be presented in this Chapter are given in table 3.1.

Table 3.1: Diffractometer parameters used in the experiments described in Chapter 3.

Parameter	Value
The focal spot size of the x-ray tube	1.0mm
Source collimator diameter (SCD)	1.1mm
Detector collimator diameter (DCD)	1.0mm
Distance between focal spot and X-ray tube window	100mm
Distance between source collimator and the X-ray tube exit window	180mm

Range of collimator separation	44mm-57mm
Sample to source collimator distance	22mm
Nominal scatter angle	6^0
X-ray tube voltage	70kV
X-ray tube current	6mA

Thirteen different collimator plugs of diameters ranging from 0.5mm – 2mm were available. A previous study (Maini, S.K, 2012) showed optimum angular resolution of 0.53^0 for the combination of 1.1mm and 1.0mm for SCD and DCD respectively.

3.3 Fatty liver tissue phantoms used in the experiments

Phantoms were designed to mimic the clinical problem on a small scale. The idea was to establish the viability of the technique in a small scale and then scale the phantoms up to represent human sized objects.

Phantoms were constructed from thin walled Perspex tube. The tube outside diameter was 50mm, with a wall thickness of 5mm. 30mm lengths were used, filled with tissue and positioned so that the axis of the tube was parallel with the incident X-ray beam (see Figure 3.1). Two types of phantom were prepared – single tissue phantoms and those containing small, variable diameter inserts within the bulk tissue. The latter were to mimic disease conditions and were prepared by drilling holes across the central diameter as shown in Figure 3.1. These holes were used to insert the ‘fat nodules’.

The procedure was to fill the sample holder with animal liver. Real fresh, porcine liver was used for these experiments for the reasons stated in section 1.13. The fresh liver was carefully squeezed into the sample holders trimmed to fit and wrapped with cling film to ensure no loss of blood. Those samples that required holes to be bored in them were put in the freezer. Cork borers of appropriate diameters (8mm, 6.5mm, 6mm, 5mm, 4.5mm and 3mm) were then used to remove liver from the sample where the cross-diameter holes had been previously drilled. These holes were then filled with liquefied fat using hypodermic syringes.

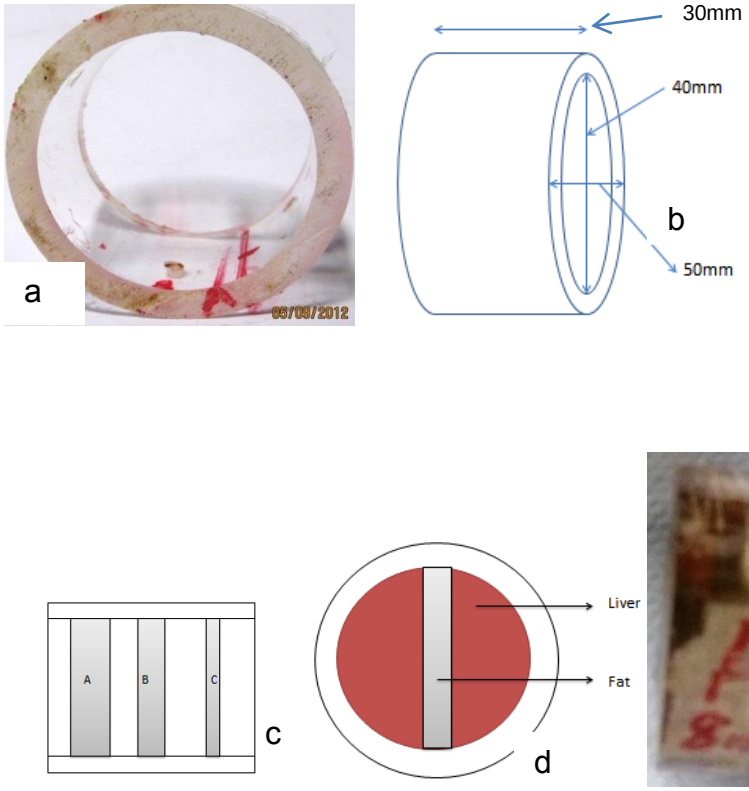

Figure 3.1: This figure shows the different stages in the preparation of the phantoms. ‘a’ & ‘b’ show the unfilled sample holder made out of Perspex tube. ‘c’, ‘d’ and ‘e’ show the cross-diameter holes and the phantom filled with liver and fat. A=6mm, B=5mm and C=3mm.

3.3.1 Lard as fat substitute

Lard was used as a fat substitute as it is a product of pork fat. Some other materials were tried as a fat substitute, namely gel and agar but lard was found to maintain its physical properties and usability for longer periods. To prevent loss of material during the experiments cling film was used to seal the phantom (see Figure 3.2).

Figure 3.2: single tissue phantoms containing lard. These were used to test the suitability of using lard to create fat nodules in the two-tissue phantoms.

3.4 The source and detector collimators adjustment

The source collimator is the first to shape the x-ray beam by restricting the diameter of the beam incident on the samples. Correctly set-up, the collimator allows only those photons that travel directly along the axis of its hole to pass. The collimators have interchangeable inserts with varying inside diameters of hole ranging from 0.5mm to 2.0mm and the distance between the source collimator (SC) and detector collimator (DC) was adjusted according to the required geometry of the diffraction cell. In this case the SC to DC distances between both their front and back inside edges ends differ due to the angular adjustment. The diffraction cells are shown in figure 3.3. This arrangement accommodated the current phantoms of width 30mm. Investigations under this geometry formed the first phase. A human-sized liver/heart sample would require an SC to DC distance of at least 30cm.

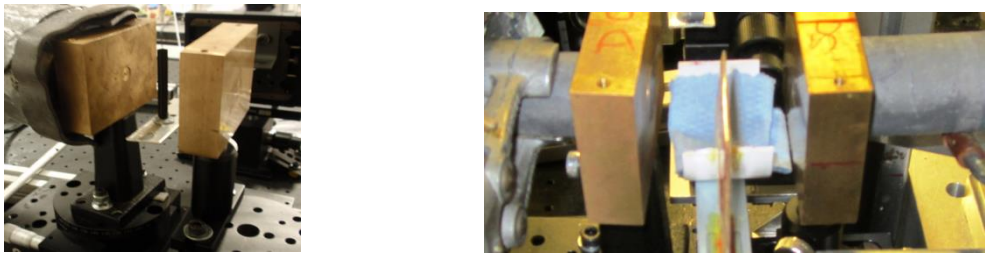

Figure 3.3: Photographs showing the arrangement of the diffraction cell. The non-parallel arrangement of the two collimator blocks (SC & DC) ensures a scattering angle of six degrees. In the RH image the caffeine test sample can be seen mounted on the horizontal translation slide.

3.4.1 Translation stages

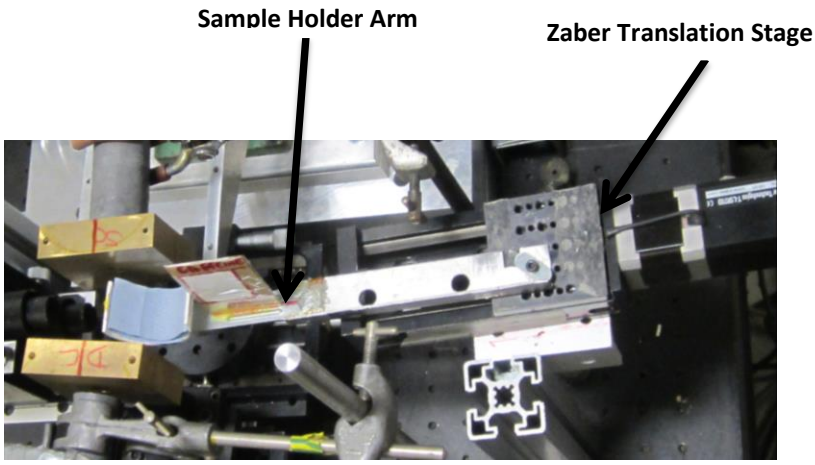

Figure 3.4: The short Zaber translation slide, T-LSR 075 in the set-up. The two collimator blocks can be seen in the LH side of the photograph. The sample holder and caffeine test sample are mounted together on the translation slide. Activating the slide moves the samples through the X-ray beam so that measurements can be made at different points across the sample.

Zaber translation stages/slides (figure 3.4) are computer-controlled and were used to position the sample. The translation stage was mounted in the setup as shown in figures 3.3 and 3.4. Initial positioning of the sample was made using the translation slide in manual mode. Once correctly positioned for the start of the experiments the computer control mode was enabled.

3.4.2 Measurement of the scattering volume

Before diffraction measurements on samples could be taken the scattering volume, i.e., the region from where the diffraction signal arises, needed to be determined. With this knowledge the sample holder had to be correctly positioned in the diffraction cell for optimum performance.

This measurement was undertaken by suspending a 3mm diameter Perspex ball from a thin wire support. The wire support was mounted above the diffractometer on

crossed x-y translation slides (Zaber T-LSR 075) so that the ball could be positioned accurately over the volume between the two collimators of the diffractometer. The height of the ball was adjusted so that it moved in the central plane of the scattering volume and at each position the scattered photon spectrum was recorded. From each spectrum the total integrated signal was calculated. In total the ball was moved over a 10 x 20 matrix of positions each point separated by 500μm. This matrix of intensity values is shown in Figure 3.5.

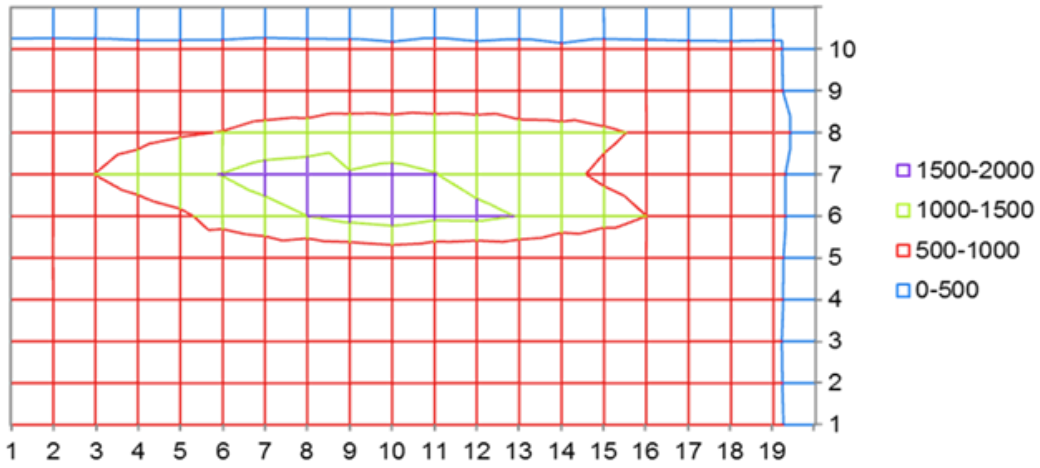

Figure 3.5: A contour plot of the scattered intensity recorded from a 3.00mm diameter Perspex ball moved throughout the scattering volume. The ball was positioned in the plane containing the two central axes of the collimator holes.

It can be seen that the most intense region of the scattering volume is approximately 0.5mm wide but extends over a length of ~3.0mm. The central point of this region, shown as (9.5, 6.5) in Figure 3.5, occurred at 20.0mm from the source collimator.

3.5 General experimental procedure

The general procedure followed throughout the experiments on tissue samples was to undertake the following five tasks:

Calibrate the detector using americium-241 (Am-241) source held in front of the lead detector shield.

The shield was in place to prevent multiple scattered photons reaching the germanium crystal. At the entrance face to the detector a 10mm hole was present to allow the collimated and coherently scattered photons to enter the detector. For calibration purposes the radioactive isotope was placed close to this aperture. At 10cm, a typical example of the recorded spectrum is shown in Figure 3.6. Using this spectrum the channel/energy calibration of the multi-channel analyser (MCA) was checked and by estimating the full width at half maximum (FWHM) of the primary 59.5 keV line in the spectrum the energy resolution was determined. Throughout the experiments the FWHM was 480±10 eV.

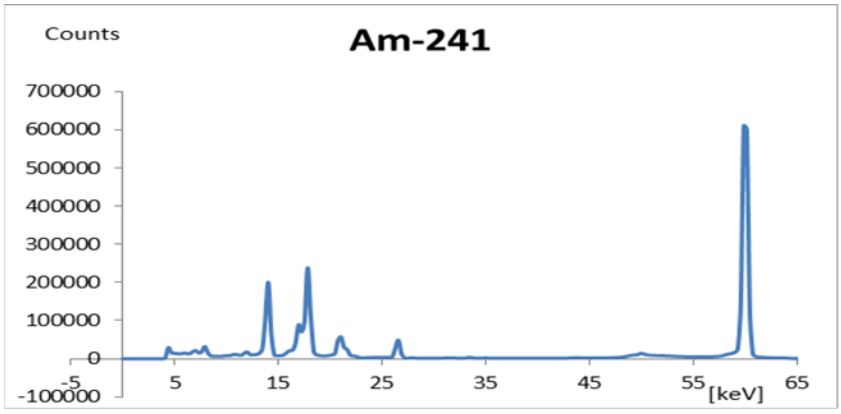

Figure 3.6: Typical spectrum recorded during the calibration procedure for the detector.

Warm-up the X-ray source following the procedure set down in the X-ray source manual.

This involved increasing the kV and mA in steps 10kV and 1mA respectively during a series of 2 minute exposures.

Measure the diffraction profile from a test standard.

For all the experiments described in this thesis the test standard used was a caffeine sample 15 x 15 x 2mm. This sample was permanently mounted on the sample holder (see Figure 3.4) and could be moved into position using the translation stage. This

measurement was made at the start and end of each measurement cycle. A typical set of these measurements in shown in Figure 3.7. The similarity in the figures and measurements indicate that the system operated under the same conditions without any distortion and gives credence to results as they are both in agreement with the standards as obtained from the JCPDS data.

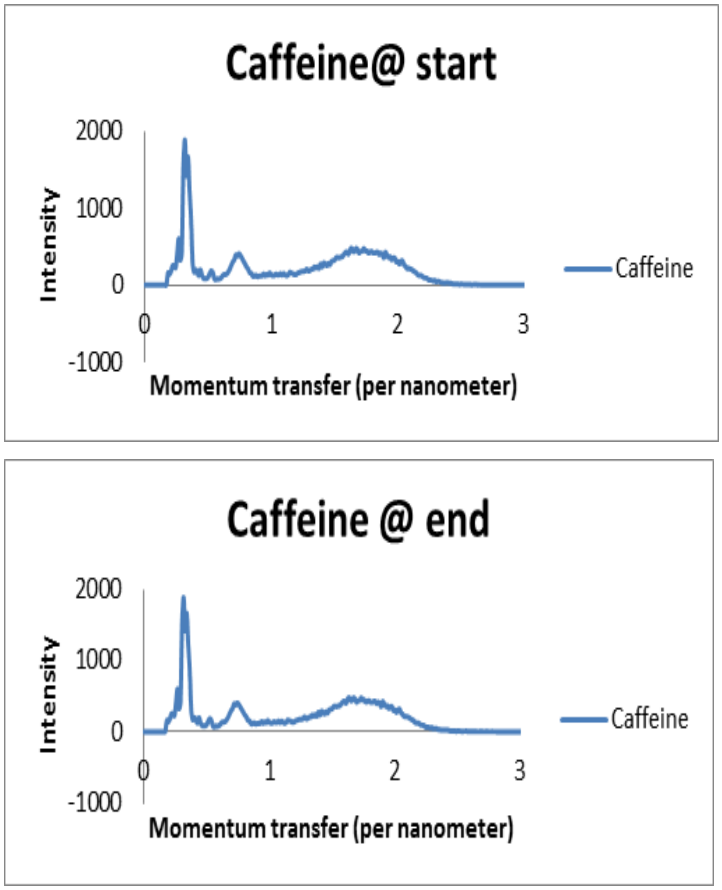

Figure 3.7: Diffraction profiles of the test standard (caffeine) measured at the start and end of the experimental cycle.

Measure the background from an empty sample holder.

An empty sample holder was mounted and the background spectrum recorded using the same exposure factors that were to be used in this cycle of experiments.

Measure the diffraction profiles from the samples.

Each sample was mounted in the sample holder and using the translation slide was positioned such that the radiation

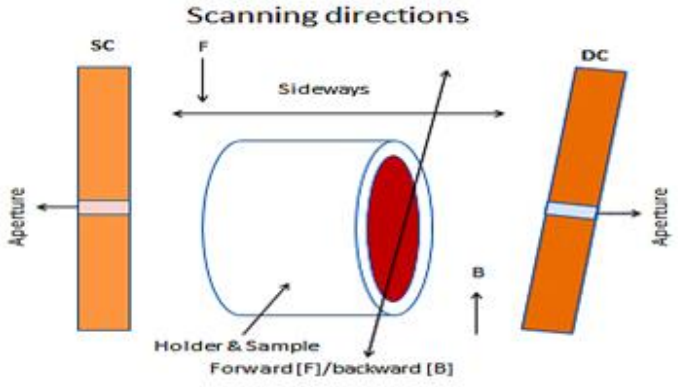

Figure 3.8: Schematic diagram of the scanning directions used during the experiments. Positioned between the detector and source collimators the sample is scanned across horizontally and perpendicularly to the beam axis.

beam passed through one extreme of the sample diameter. The diffraction profile was measured for this position and the sample then moved to the next position across the sample diameter (see Figure 3.8). These processes of positioning, recording and then positioning were under computer control and were repeated until the full diameter of the sample had been investigated.

3.5.1 Measurements using liver/fat phantoms

Table 3.2 summarizes the three major experiments that were carried out on the fatty-liver phantoms. All phantoms consist of a transparent cylindrical Perspex tube of outside diameter of 50mm, inside diameter of 40mm and thickness of 5mm.

The inside diameter of 40mm is the space allowance for the sample contents and the length (distance along the 40mm) of scan to be carried out.

For the liver samples, the thickness of the sample, their positions and for multiple inserts their distances apart were the major considerations in the choice of scan distance (or scan length). Room was made within the pure liver portion before the fat insert and after the fat insert. It was for this reason that the scan length was chosen. The length was more or less the minimum. The length could be more but the longer the more time it consumed. For the thirty-one spectra obtained from one liver sample with three different thicknesses (5mm. 6mm and 4mm, a total of 15mm) of fat inserts, there was a spacing of 5mm between them. This meant a total of 25mm distance from the back end of 5mm fat insert to the front end of the 4mm fat insert, living 7.5mm of

pure liver before the 5mm fat and 7.5mm after the 4mm fat, within a sample holder of 40mm diameter. This explained the geometry behind the choice of scan length of 31mm and implied that only 6mm each of liver at both ends (3mm before 5mm insert and 3mm after the 4mm) was part of the scan length.

For the heart samples, in taking the decision to limit these distances to 17mm, 16mm and 17mm respectively, the factors considered include:

- the position where the heart tissue represented by the beeswax (starting scan points from the beeswax area)
- the position of the blood vessel with the fat insert (the middle and area of interest) and
- the other position of the heart tissue representing the beeswax (end scan points in the beeswax area at the other end).

For the voltage settings, the acceptable diagnostic potential for tissue studies is in the range of 30kVp –100kVp with the corresponding maximum energy of 100keV.

As for timing, the acquisition time of 50s was taken after series of trials runs in the experiment to ensure that useful spectra of good quality were obtained without change except for the increase in intensity which is directly proportional to time. Also as radiation dose is controlled by current and time it means that shorter exposure time has the advantage of dose reduction.

In addition, the measuring time of 50 seconds also reduces the running time of the EDXRD system, as prolonged time can damage the system. For example, the power cables may burn out. It happened before and was repaired. Reoccurrence could be costly in money and time and can hinder the investigation. However, the reduction in time did not affect the quality and shape of the spectra.

Table 3.2: The Experiments and the conditions used in the fatty-liver experiments. Note all the liver experiments were carried out at 70 kV and 6mA. Scan step size was 1mm in all cases

Experiment number	Sample	Fat insert diameter (mm)	Scan length (mm)
1. Scanned Liver Samples with five thicknesses of fat	A	8.5	12
	B	6.5	12
	C	4.5	12
	D	3.0	8
	E	3.0	8
2 Scanned liver samples with 3 different thicknesses		5 6 4	31
3 Scanned Heart		0 2 3	17

3.5.2 Typical spectra

Following recording of the raw data the spectra were corrected using the background measurements made with an empty phantom. Typical spectra are shown in Figure 3.9.

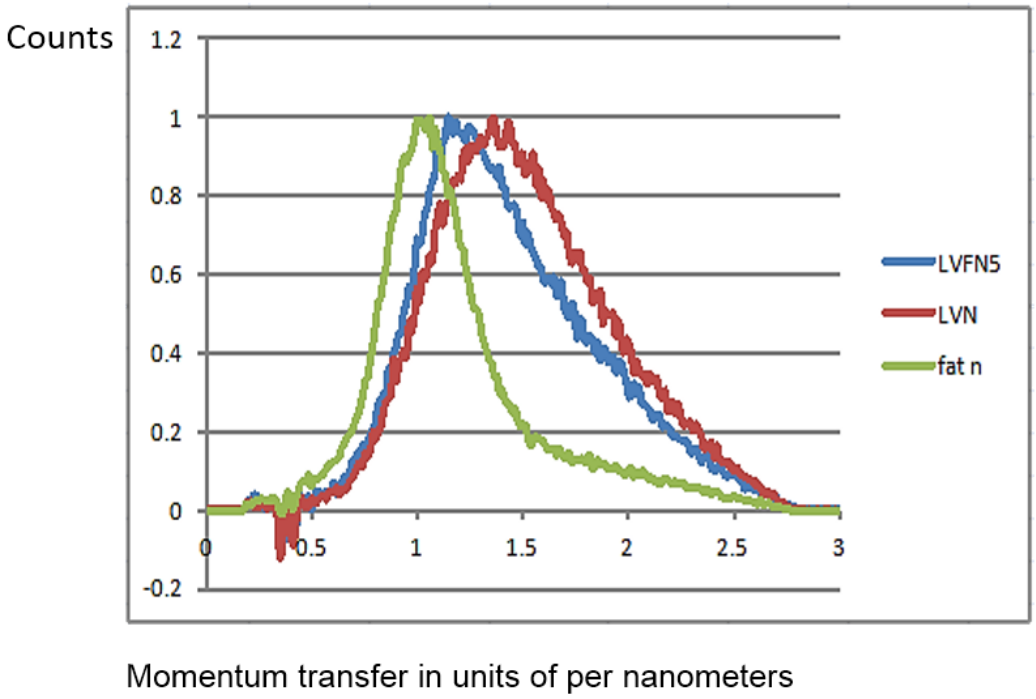

Figure 3.9: Normalised liver (LVN), normalised fat (fat n) and one of the normalised fat-liver (LVFN5) spectra. The 5 in LVFN5 meant that spectrum here was a result from 5 samples.

Two effects can be seen in these spectra. Firstly the removal of background counts creates an artefact at around 0.4 nm^{-1}. This is due to the fact that the attenuation created by the phantom is not recorded in the background spectrum. Secondly the effect of mixing the two base materials creates a spectrum whose shape fits or represents a mixture of the two materials in question.

3.6 Heart disease phantoms

This phantom was a more complex structure. The same plastic cylindrical material used for the fabrication of the liver phantom was used in the heart phantom. Flexible plastic tube, the brand normally used for blood transfusion, was used as a substitute for the blood vessels. Water was used as a substitute for blood, while beeswax was used as a substitute for the heart tissue (see Figure 3.10). Real porcine fat was used in this investigation to create plaques. Different sized blood vessels were created using different diameter tubes and these ranged from 6mm to 9mm. Plaques of different thicknesses (1.0mm to 6.0mm) were introduced into the ‘blood vessels’ before the ‘blood’ was added and the tubes sealed with silicone.

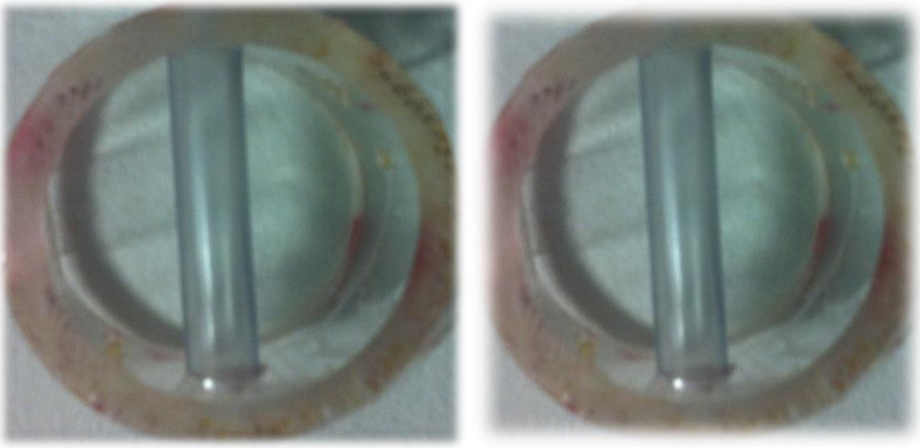

Figure 3.10: Heart phantoms made using plastic tubes as a substitute for the major vessels supplying blood to the heart. These were surrounded by muscle tissue (wax) and the tubes filled with water (blood). Plaques of different sizes were added to the blood 'vessels'.

The experimental procedure, data generation and processing of the data were the same as for the liver tissue phantoms (see table 3.2). A typical set of normalised heart and fat spectra are shown in Figure 3.11.

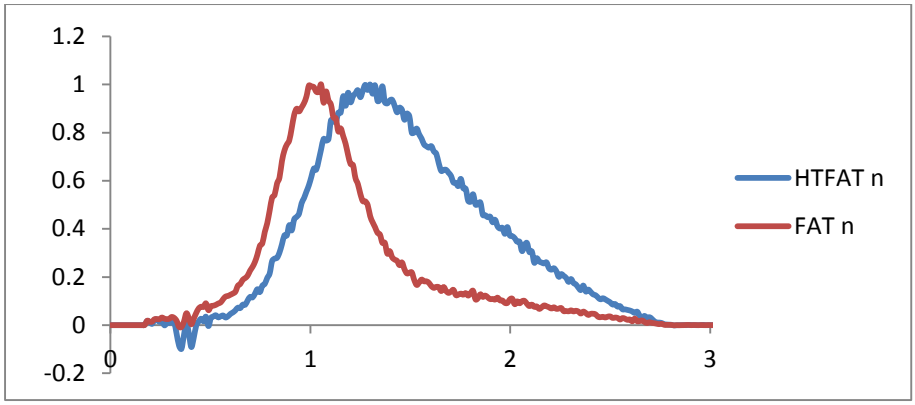

Figure 3.11: Typical spectra taken from the heart disease phantoms following background correction. These spectra have been normalised (HTFATn = normalised fattyheart and FATn = normalised fat).

Having generated and processed the data from the two scanned liver, one with the five samples and the other with three fat inserts and the heart phantom, their analysis with respect to assessment of the detectability of the problems and how far the system was able to do it is the subject of chapter 4. The analysis will show if the system detected the fat nodules in the liver and the fat inserts in the heart phantom and to what extent, under the operating conditions. The result of the analysis will show if the system as set up has the potential for clinical application.

3.7 Summary

In this chapter, the enumeration and the full description of the experiments carried out on the tissue substitute phantoms prepared to simulate these disease conditions have been made.

The experimental application of the EDXRD system in two major clinical problems (fat nodules in the liver tissue and plaques in the blood vessels of the heart tissue) was carried out. The diffractometer parameter values and geometrical settings were stated. Of the two focal spot sizes (1mm x 1mm and 3mm x 3mm) in the x-ray set, 1mm x 1mm was chosen to provide a pencil beam fit for the collimation diameter chosen (i.e. SCD,1mm and DCD,1.1mm). Also the collimation separation of 44mm – 57mm meant

that the sample to be of lower value of thickness or with to be contained in the sample space. The 57mm value of the collimation separation at the front end and the 44mm at the back end (as shown in figure3.8), was due to the adjustment of the detector collimator (DC) to the scatter angle of 6 (6^0) degree, which in turn was due to the energy range (70keV) in the experiment.

The sample holder was made out of transparent Perspex tube and prepared with the tissue sample fixed as described in section 3.3. Pure porcine liver tissue was used. Lard was used as fat. With the EDXRD system ready for experimentation, a Zaber translation stage was added to move the sample across the length and breadth of the sample space between the two collimators (SC and DC). Caffeine test sample mounted on the translation stage was used to plot the scattered intensity and the mapping out the scattering volume.

The experimental procedure followed five main tasks. All operations are computer controlled except the positioning. The first was the calibration of the HPGe detector, using americium-241, to ensure proper quality and standard and accuracy of output. The second task was warming up of the x-ray source following a standard but routine procedure for both current and voltage timed increment. Thirdly, a caffeine sample of 15mm x15mm x 2mm in dimension was used as a test standard. The diffraction profile for caffeine is well established and so the profile match and its reproducibility was assuring and confirmatory. The fourth task was the exposure of the empty sample holder and the background measurement of radiation from the empty sample holder. Finally the live and heart samples were exposed and the measurements from their diffraction profiles taken.

The liver samples were of two sets. One was scanned liver with five (5) samples with fat inserts of different thicknesses and the other one sample with three (3) fat inserts of different thicknesses (as shown in table 3.2). The scan length, as applied here, was the distance traversed within the sample and was chosen depending on the thickness of the liver insert. The value of this distance covered some thicknesses of the liver before the fat insert, the fat insert and part of the liver after the fat insert. The heart samples were three (3) in number with zero, 2mm and 3mm fat inserts. Water represented blood, beeswax represented the heart, transparent blood transfusion rubber tube was used as the blood vessel and real porcine fat for the fat inserts. The

diffraction data were generated from all the samples and were processed producing diffraction images which were further analysed with multivariate analytical tool. Their analysis which are covered in the next chapter are with respect to assess the detectability of the fat inserts in the liver samples and the plaques (fat inserts) in the heart samples.

Chapter 4

Liver and heart tissue diffraction spectra analysis

4.1 Introduction

As said in the closing remark in chapter 3, the motive behind this work is to explore the possibility of applying EDXRD to disease detection and medical diagnosis. Special emphasis is on detecting the fat nodules in the liver and the plaques in the blood vessels of the heart. Chapter three described the experiments carried out on the tissue substitute Phantoms prepared to simulate these disease conditions. This chapter looks at the overall liver and heart data obtained and evaluates them with statistical analyses with the aim of finding the most robust approach to the detection of early disease.

The analytical software and the procedure were expertly developed by Professor Tom Fearn (UCL). The Matlab programs (Codes) are in the Appendix. The main software used is Matlab and the main explanatory form of analysis is the principal component analysis (PCA), which finds the linear combinations of the underlying variables with maximal variance. This can be used to assess the detectability and sensitivity of the system from the analysed data. Therefore this is an appropriate technique for data description and explorative data structure modelling of any generic (n, p) – dimensional data matrix (i.e. p-dimensional characterization of n samples). The details are to be described in the section that follows.

4.2 The Principal Component Analysis (PCA)

4.2.1 Introduction

PCA may be used in the analysis of data sets with few variables and one with large number of variables. It is more useful when dealing with large variables by using it to reduce the large variables to a manageable size and for ease of analysis. The main idea of the PCA is to replace a complex multidimensional data set by a simpler one with fewer dimensions which can still fit the original data very close enough to be

considered as a very good approximation. It is an important analytical tool in chemometrics and particularly in spectroscopy (Davies and Fearn, 2005).

4.2.2 Principles and Procedures

Large data tables like the data sets obtained from diffraction profiles under consideration here have got rows in the range of 8 to 31, which represent the samples (scores) and a maximum of 512 columns (number of diffraction channels), which represent the variables (loadings). This contains a large amount of information with some partly hidden due to the complexity of its interpretation. PCA is therefore a projection method that can help us see the information contained in such data set. It will enable the following:

- ⇒ The easiness in finding how one sample varies from another.
- ⇒ Show which variables contribute most to the difference seen
- ⇒ Show if the variables have similar contributions
- ⇒ Show if the variables contribute independent of each other
- ⇒ The detection of sample patterns
- ⇒ Quantification of the amount of useful information contained in a dataset

Obtaining these information from a dataset means trying to find out what makes one sample either similar to or different from another sample. In a PCA analysis, two samples can be said to be similar if the following conditions exist:

- ⇒ Samples have close or same value for most variables (in this case, the number of Photon counts obtained in each channel). Otherwise, the samples are different. This scenario represents a close picture of close coordinates of sample values in a multidimensional space.

The principle behind PCA is primarily to find the direction in space (with an arrow-head line drawn to show), where the distance between data points is the largest. This means indicating the linear combination of the variables that result in the samples differences.

The directions and combinations signify the Principal Components (PCs). The PCs when computed and graded, give the following information:

⇒ The first PC i.e. PC1 has the most information. It has the direction that explains the most significant variance (highest variation).

⇒ The second PC, PC2 and the subsequent PCs must be orthogonal to PC1 with the maximum amount of the remaining variability (number of residuals) which PC1 did not take into consideration.

⇒ The number of PCs may vary as the number of variables

Building up and using a PCA involves three major steps. These are:

⇒ Selection and application of appropriate pre-processing methods
⇒ Running a PCA, choosing the number of components and diagnosing the model
⇒ Interpretation of the loadings (values of peaks in the coordinate system) and scores (the values of the spectra in the coordinate system) plot

i. Pre-processing –

Pre-processing can be used to eliminate the effect of background, different variances in variables and reduce the noise introduced by some of these effects. The most usual pre-processing method are centering and weighting.

Centering involves the subtraction of the average from each of the variables. This is referred to as mean-centering. Doing this ensures that all the results obtained can be interpreted in terms of the variation around the mean.

Weighting can be applied in projection methods such as the principal component analysis (PCA) based on finding the direction of maximum variation. PCA is explained further in the next sub-section. They all depend on the relative variance of the variables and depending on the required information, weights based on the standard deviation (SD) of the variables (i.e. the square root of the variance which expresses the variance in the same unit as the original value) are used.

In this case, the common weightings applied are:

⇒ 1, which represents no weighting and all calculations are based on the raw variables.

⇒ 1/SD, which represents standardization and which gives the variables the same variance. This gives the variables the same chance to influence the estimation of the components.

⇒ Constant, which can be used to set the weighting for each variable.

ii. Running the PCA, choosing the number of components and diagnosing the model

This has to be done and most probably repeated several times, before the loadings and scores can be interpreted in a manner that the result can be reliable and acceptable.

Diagnosing a PCA model means, checking the variances to determine how many components to include and to assess how much information the selected number of components can account for and to identify the sample that do not fit (outliers) and then exclude them from the investigation. Small number of PCs will result in less accurate model. Large number of PCs will introduce only noise which will also lead to inaccurate model. The PCA is therefore primarily applied to the EDXRD spectral data to obtain the required information with respect to their shapes, variability, detectability and sensitivity of the system.

4.2.3 Basic approach to the analysis of the EDXRD spectra

Most of the experiments that have been undertaken result in a set of spectra where each spectrum relates to a different position of the X-ray beam with respect to the Phantom. As can be seen from table 3.2 the major series of experiments had 5 samples A-E. Each sample was liver with fat inserted where the sizes of the inserts are given in table 3.2. Within each set of spectra relating to a given insert the X-ray beam will have moved across the sample firstly recording spectra from pure (or mostly pure) liver, through the fat nodule embedded in liver, back to pure liver (see Figure 4.1).

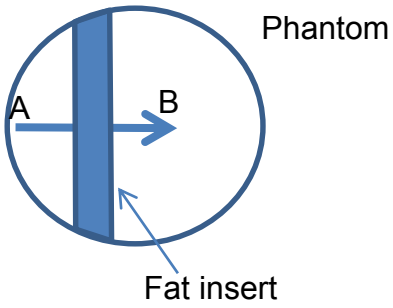

Figure 4.1: Schematic representation of the scans made across inserts in the fatty-liver Phantoms. The scan shown as the arrow A to B was made up of 12 or 8 points at which diffraction profiles are collected.

The analysis is broken down into three steps:

Step 1:- Assuming the case where each spectrum relates to a different position across the scan, if there are 31 spectra from the scan of the fatty-liver Phantom and these are averaged, the mean spectrum looks as shown in Figure 4.2.

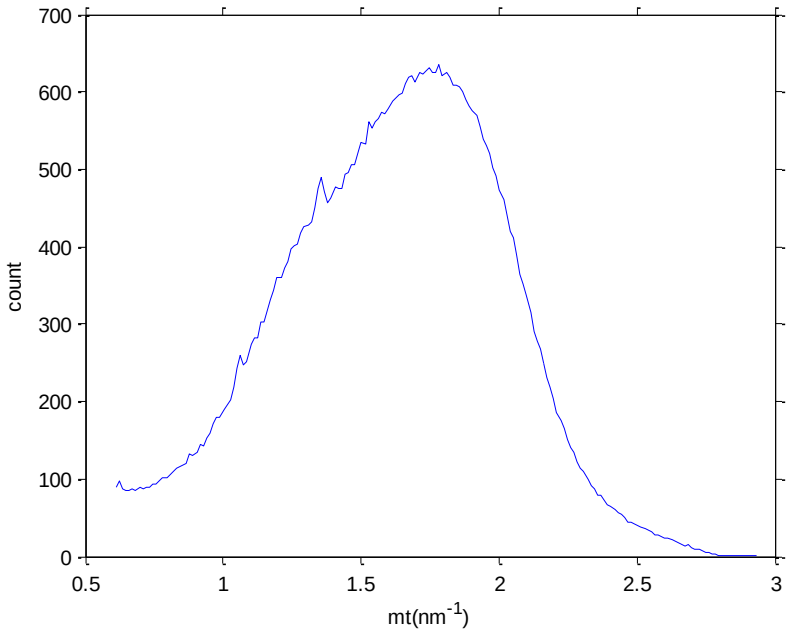

Figure 4.2: The averaged spectrum from 31 different spectra where each spectrum corresponds to a different position in the scan. In this case a scan corresponds to the X-ray beam passing through three fat nodules of different diameter embedded in liver tissue.

Step 2:- Subtracting this mean spectrum from each of the 31 spectra gives the residuals which are shown in Figure 4.3.

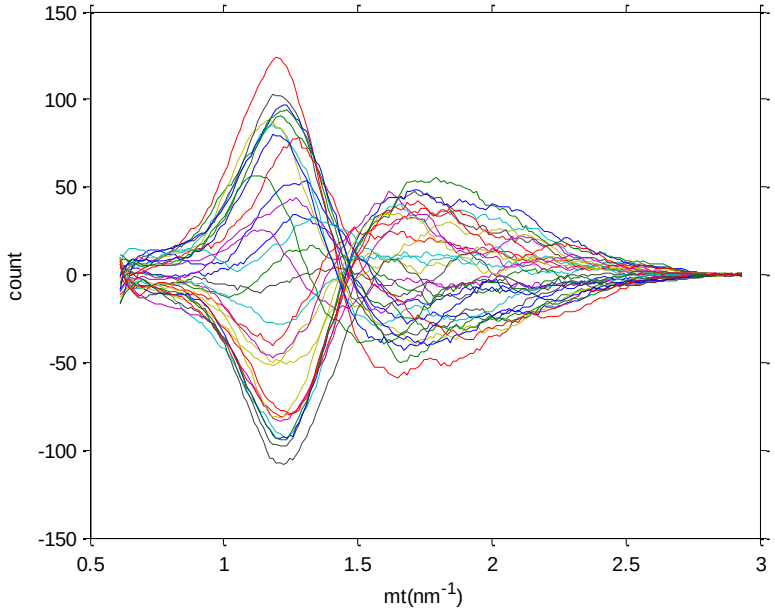

Figure 4.3: A plot of the residual count left after subtraction of the mean spectrum shown in Figure 4.2 from each individual spectrum. These spectra have been smoothed for display purposes but any further analysis uses the raw data.

On inspection of Figure 4.3 it can be seen that generally the curves have the same shape and only differ in their scales. This is exactly an expected result in a two-component (component 1 and component 2) mixture where the spectra are additive. In additive case:

Two-component mixture = component 1 + component 2. 4.1

(Spectrum of component 1 = sp1; spectrum of component 2 = sp2)

The function (f) of a two component spectra = f (sp1 + sp2). 4.2

$$f(sp1 + sp2) = f(sp1) + f(sp2) \quad 4.3$$

Where sp1 represents the function (f) of individual component of the two-component spectra f (sp1) + f (sp2). The spectral shape in Figure 4.3 corresponds to the difference between the spectra of the two components, and the scale provides information about the relative proportions of the two components in the mixture.

When Principal Component Analysis (PCA) models the data by a single factor it estimates both the shape of the common curve (this is the *loading vector* from the PCA) and the multiples of that curve present in each of the spectra (referred to as the *scores*). Figure 4.4 shows this common curve found from PCA multiplied by the appropriate factor for each of the 31 cases.

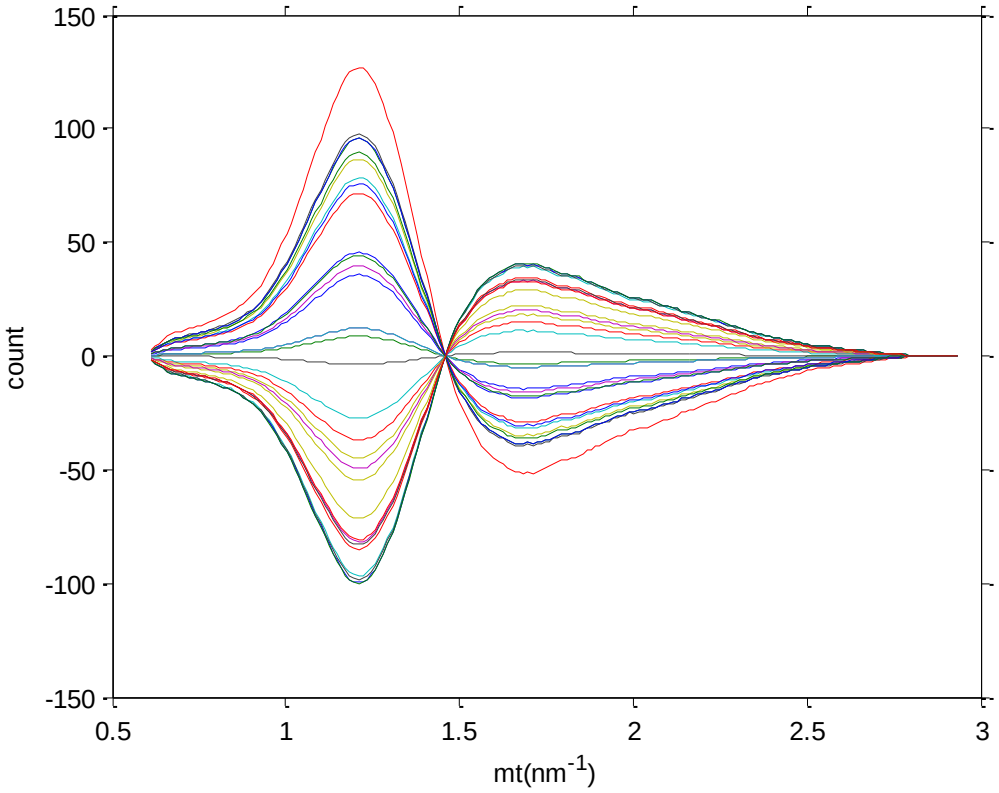

Figure 4.4: The loading vector multiplied by the scaling factor required to fit each of the individual spectra.

Step 3:- Adding the mean spectrum on to these factors generates a fitted curve that can be compared with each of the original spectra. Furthermore, these factors allow the fraction of fat that is present in each spectrum to be calculated and this can be estimated for each point in the scan.

In total there are three sets of data that have undergone the analysis outlined above. They are:

Fatty-liver scanned (1) – a set of 52 spectra where each spectrum refers to a different position across the Phantom (see Figure 4.1). Five Phantoms were used each

containing a single fat nodule. This was designed as an experiment to look at the sensitivity of the technique for finding small fat nodules. The acquisition time was fixed at 50s at 70 kV, 6mA.
The acquisition time of 50s was taken after a series of trials runs in the experiment which ensured that useful spectra of good quality and shape were obtained. It is worthy to note that for diagnostic imaging in Radiology the typical voltage is in the range of 40kVp – 80kVp (Dowsett et al, 2006).

Fatty-liver scanned (2) – a set where each spectrum refers to a different position across the Phantom (see Figure 4.1). A single Phantom containing three fat nodules was used. This was designed as an experiment to look at the sensitivity of the technique for finding small fat nodules in a pattern of fat and liver. The acquisition time was fixed at 50s at 70 kV, 6mA.

Heart disease scanned (3) – a set where each spectrum refers to a different position across the Phantom (see Figure 4.1). Three Phantoms were used each containing a different sized plaque. This was designed as an experiment to look at the sensitivity of the technique for finding small plaques in blood vessels. The acquisition time was 50s and the operating potential was chosen to be 40 kV, 2mA. The time of 50s did not affect the quality of the result. The increase in time only affected the number of photons produced and not the structure and shape. The voltage of 40kVp was to be the starting voltage. The range of voltage for this type of study is between 40kVp and 70kVp. The choice of voltage was influenced by the energy requirement. The maximum energy range for this experiment was 70keV. The plan for the heart experiment was to start with low voltage (40kVp) and then increase in steps of 10kVp to higher voltage (70kVp). The plan did not work out due to the breakdown of the x-ray system caused by the burnt power cables. All the experiments could have been done under the same parametric conditions. The experiments were very time consuming but for research information voltage, current and time variation was useful with respect to energy and radiation dose outcomes

4.2.4 The 'fatty- liver scanned' analysis – data set 1.

The spectra for the different sized fat samples were analysed together. The momentum transfer range was taken from 0.61nm^{-1} to 1.99nm^{-1}. Values outside this region were not used in the analysis for two probable reasons. The first was the unusual large characteristic peak probably due to tungsten of the X-ray tube target (lower bound) and secondly because there was little variation in the diffraction profile (upper bound). No smoothing was done.

The method of analysis, as outlined above, is based on the assumption that the system is approximately linear and additive. By this assumption a typical spectrum of a 60/40 mixture of liver and fat could be found by multiplying the taking spectrum of pure liver by a factor 0.6 and the spectrum of pure fat by a factor of 0.4. Essentially the system will be one-dimensional, in the sense that all the spectra can be approximated closely by a mean spectrum (M) + some scalar multiple (s) of this difference spectrum (D) (see section 4.2). 'D' was estimated by carrying out PCA on the mean-centred spectra and saving the first principal component only. The result was an estimate of D (the loading vector for the first principal component) and the scalar multiples, s (the scores of the samples on this component). Fitted spectra were constructed as ($M + s \times D$). These were compared with the measured spectra (Figures 4.5- 4.9) to examine how good the fits are and indirectly, how reasonable the assumption, that it is a one-dimensional system.

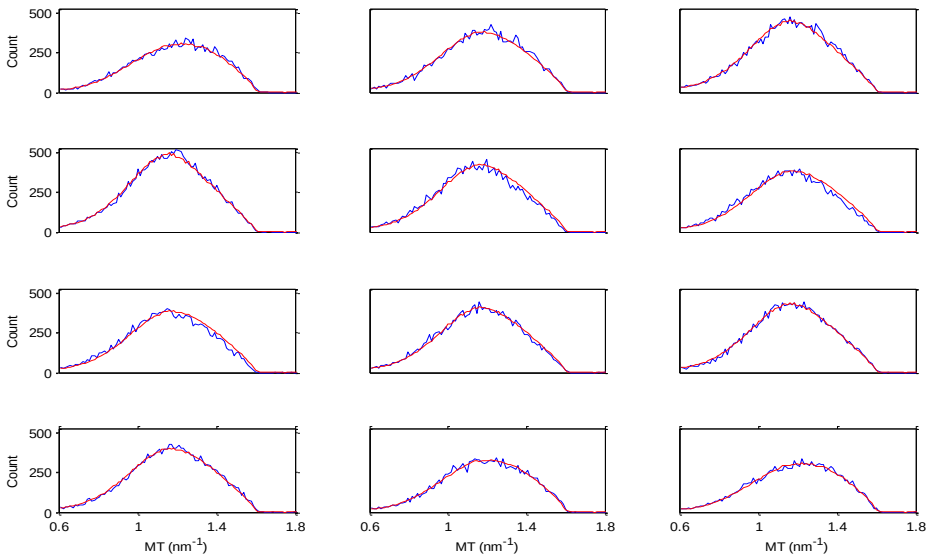

Figure 4.5: Observed (blue) and fitted (red) spectra for sample A. The 12 graphs represent different scanned positions across the sample. From Figure 4.1 position 'A' in the scan is given by the top left hand profile and position 'B' (the end of the profile) is given by the bottom the right hand graph.

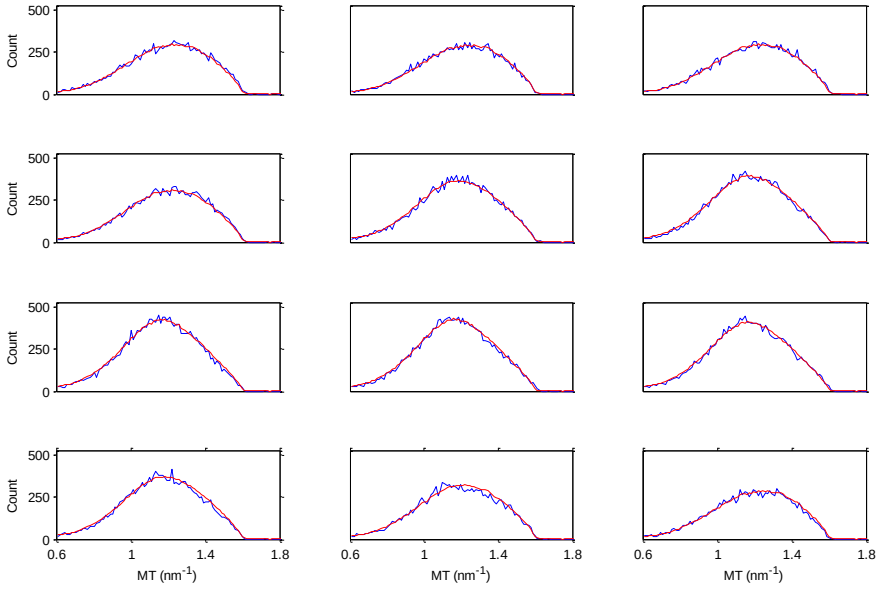

Figure 4.6: Observed (blue) and fitted (red) spectra for sample B. The 12 graphs represent different scanned positions across the sample. From Figure 4.1 position 'A' in the scan is given by the top LH profile and the end of the profile (position 'B') is given by the bottom RH graph.

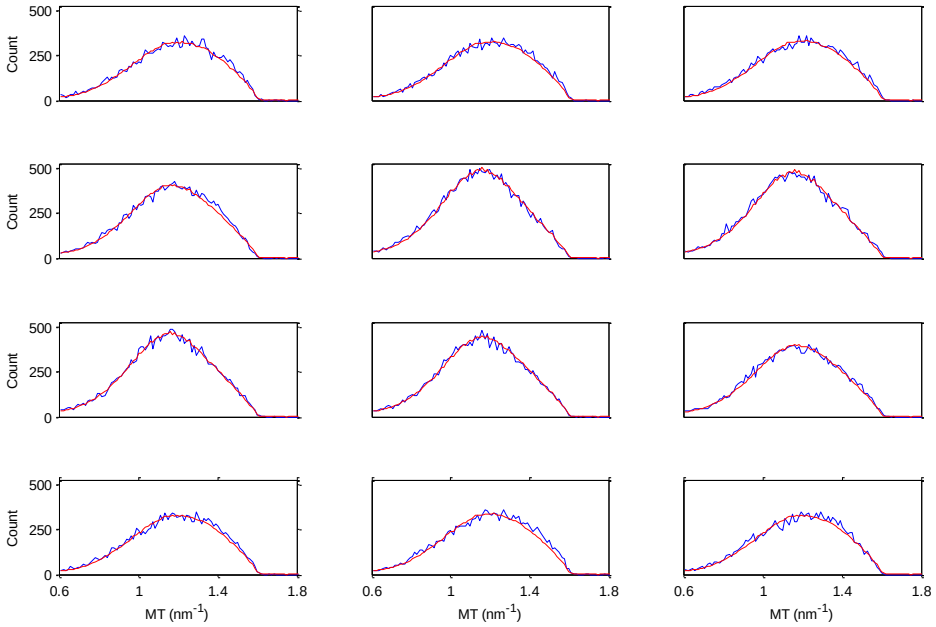

Figure 4.7: Observed (blue) and fitted (red) spectra for sample C. The 12 graphs represent different scanned positions across the sample. From Figure 4.1 position 'A' in the scan is given by the top LH profile and the end of the profile (position 'B') is given by the bottom RH graph.

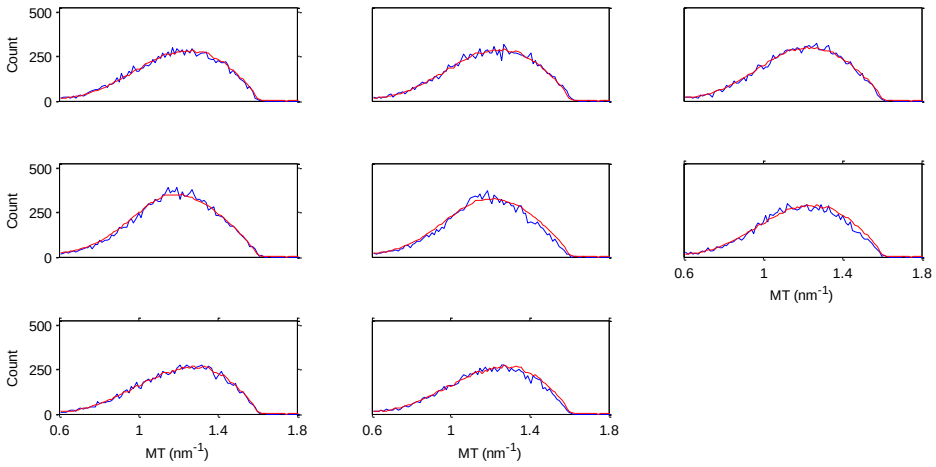

Figure 4.8: Observed (blue) and fitted (red) spectra for sample D. The 8 graphs represent different scanned positions across the sample. From Figure 4.1 position 'A' in the scan is given by the top LH profile and the end of the profile (position 'B') is given by the bottom RH graph.

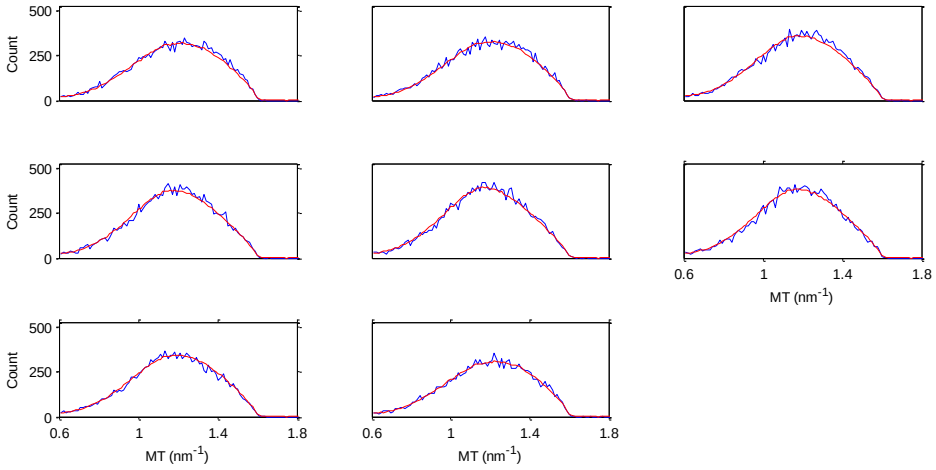

Figure 4.9: Observed (blue) and fitted (red) spectra for sample E. The 8 graphs represent different scanned positions across the sample. From Figure 4.1 position 'A' in the scan is given by the top left hand (LH) profile and the end of the profile (position 'B') is the bottom right hand (RH) graph.

In order to get rid of some arbitrary scaling in's' and *'D'*, it is also assumed that the set of spectra contains at least one pure fat and at least one pure liver. If this is true, these will be the spectra that have the extreme values of 's'. Thus the fitted spectra corresponding to the extreme values of 's' were taken as estimates of the two pure components (see Figure 4.10). The value, *'s'* is rescaled so that its values run from 0 to 100%, thus giving estimates of the concentration of component 2 (in this case fat) in each spectrum.

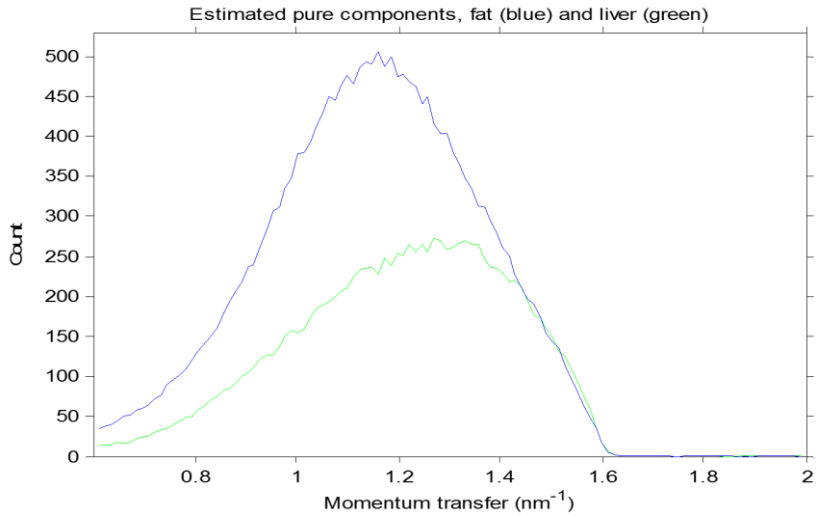

Figure 4.10: Fitted spectra for the two extreme values of the factor 's'.

Thus the fitted spectra in Figures 4.5 – 4.9 can be interpreted as weighted averages of the spectra in Figure 4.10, with the weights for the fat spectra being the '*s*' values given in Figure 4.11. Discussion of these results will be left until section 4.3.

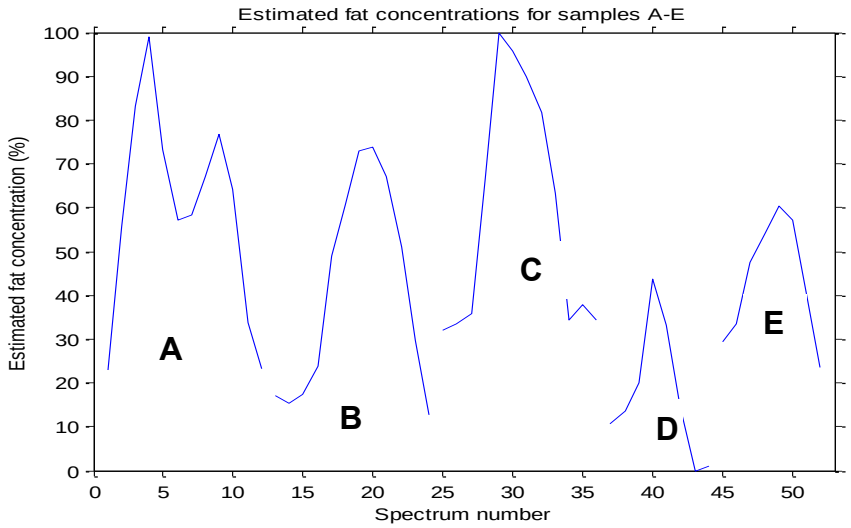

Figure 4.11: Estimated fat concentrations in the 5 Phantoms, A-E, of different thicknesses are shown from left to right

4.2.5 The 'fatty- liver scanned' analysis – data set 2.

In this case a single Phantom was used with three different fat nodule diameters included in the one Phantom. Scanning the Phantom created 31 points at which diffraction profiles were collected and the results from the analysis described in section 4.2 are given in Figures 4.12, 4.13 and 4.14.

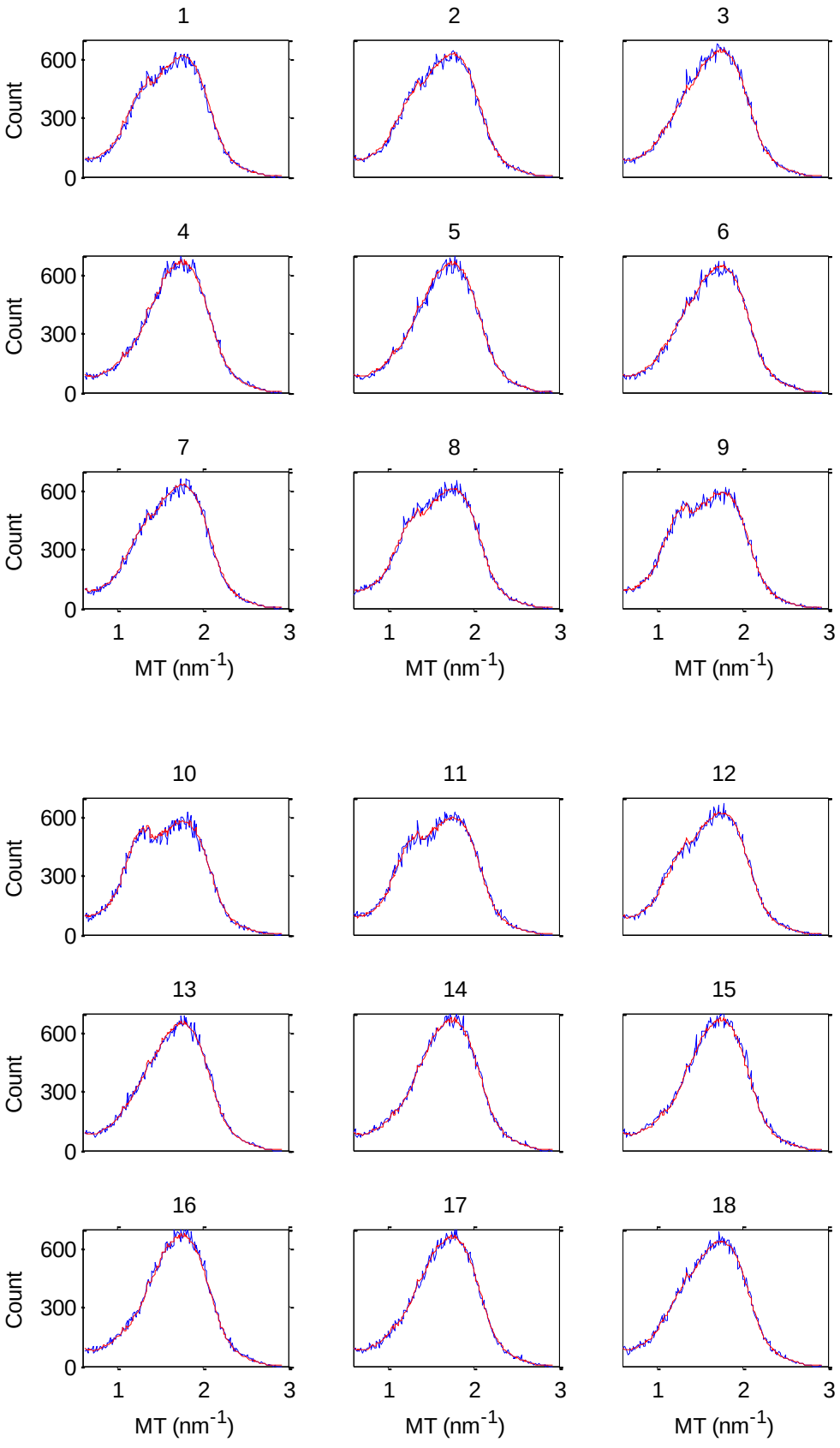
1
2
3
4
5
6
7
8
9
10
11
12
13
14
15
16
17
18
Count
600
300
0
1
2
3
MT (nm-1)

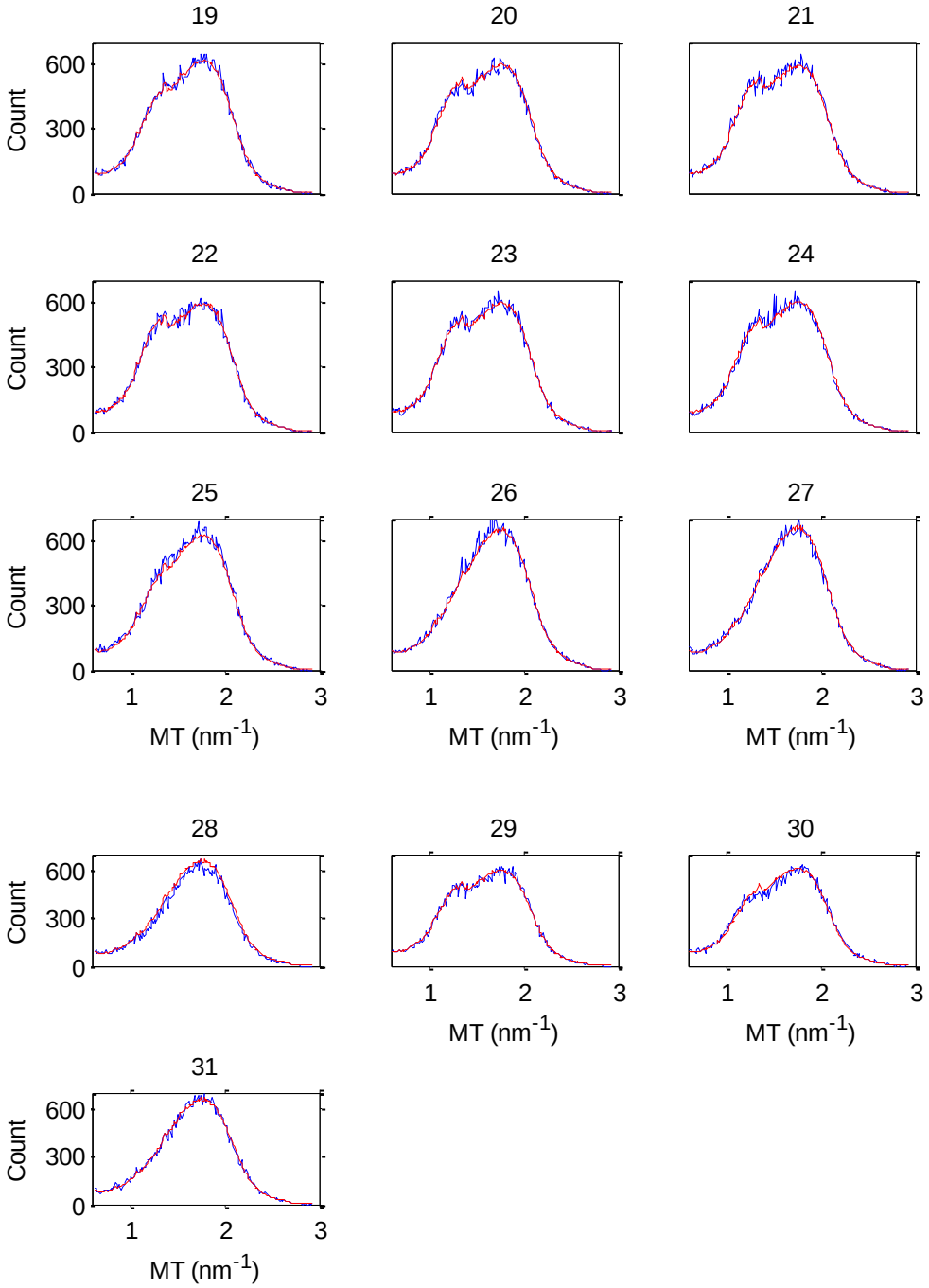

Figure 4.12: Observed (blue) and fitted (red) spectra for the sample with 3 different inserts. The 31 graphs represent different scanned positions across the sample. From Figure 4.1 position 'A' in the scan is given by the top left hand (LH) profile, number 1 and the end of the profile (position 'B') is the bottom right hand (RH) graph, number 31.

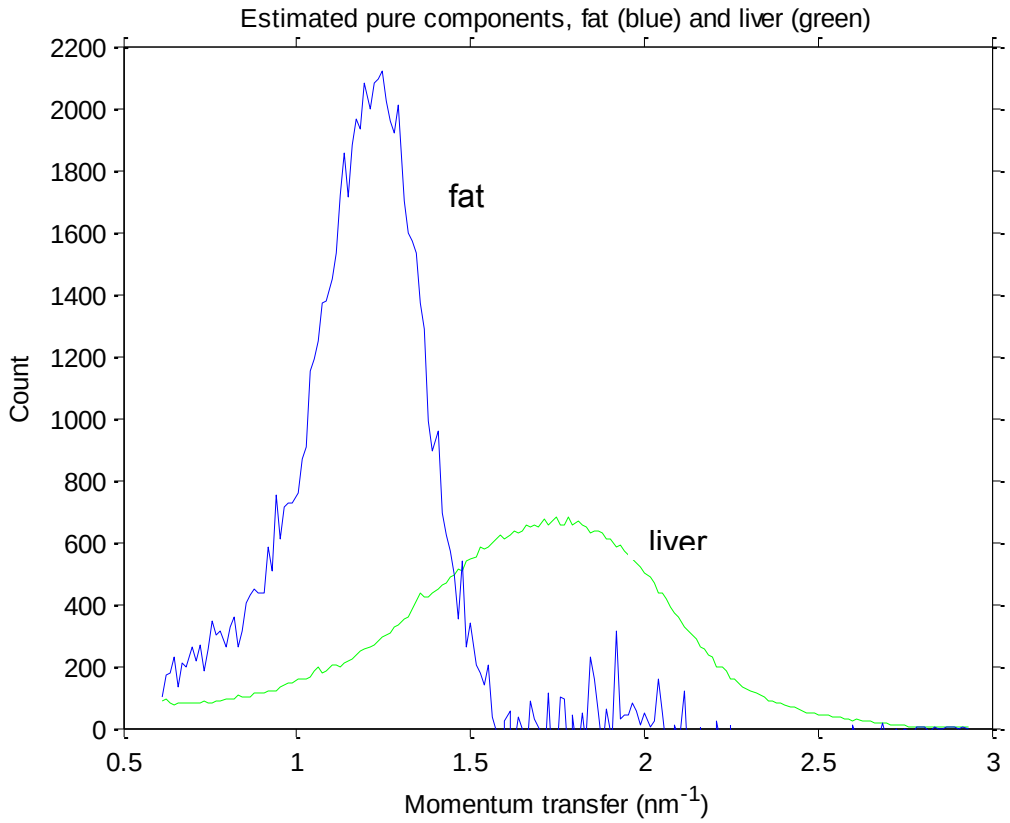

Figure 4.13: The estimated pure components of fat (blue) and the liver (green)

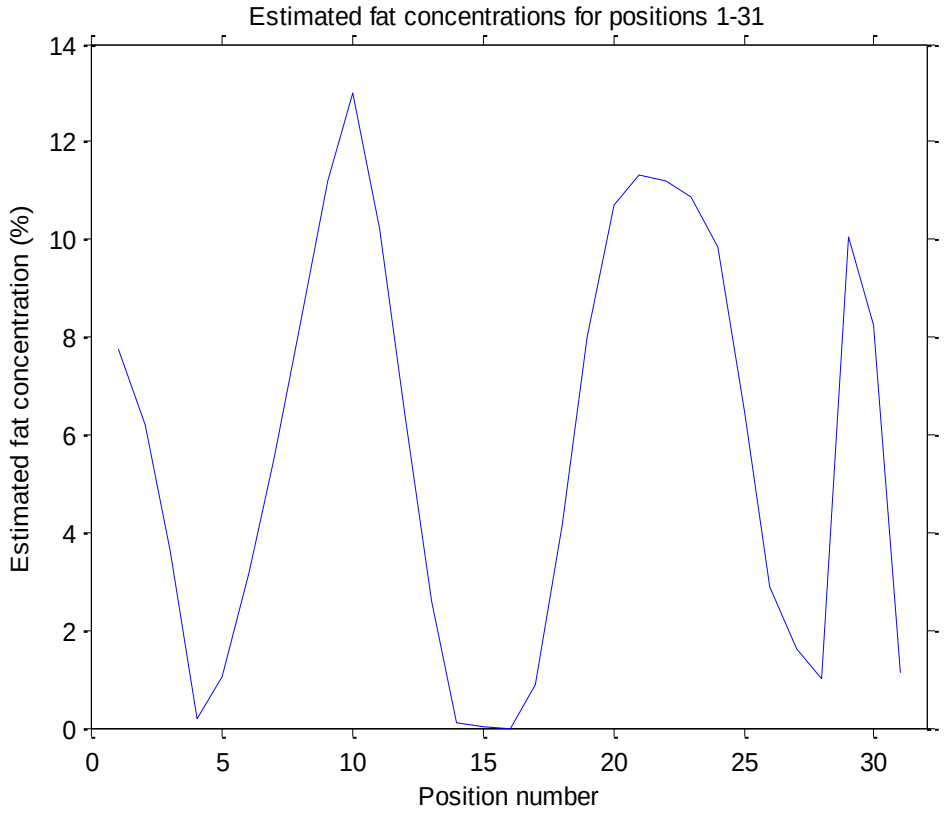

Figure 4.14: The estimated fat concentrations for the scanned positions number 1 to 31.

4.2.6 The 'heart disease scanned' analysis – data set 3.

Three different Phantoms as described in Chapter three were used in these experiments. In the first Phantom the 'blood vessel' contained only 'blood' with no fat present. In the other two Phantoms 2mm and 3mm of fat were present in the 'blood vessel' with the remaining part of the volume filled with 'blood'. The vessel had an internal diameter of 6mm. Either 16 or 17 positions were used to record diffraction profiles at points across the 'blood vessel'. The analysis procedure followed was as described in section 4.2 and led to three forms of output for each analysis – the estimated spectra for pure components, fitted spectra at each point in the scan and finally a plot of the estimated contribution of a given component.

As this Phantom contains several components (beeswax as heart muscle substitute, plastic tube as the blood vessel, fat as a plaque and water as blood) and the analysis procedure considers the problem to be a two component Phantom the vessel, fat and

water have been grouped together. This is because beeswax is the only component in the Phantom that will give rise to genuine pure spectrum due to the position of the scan points.

For no fat present in the blood vessel (0mm fat) the two component spectra are shown in Figure 4.15.

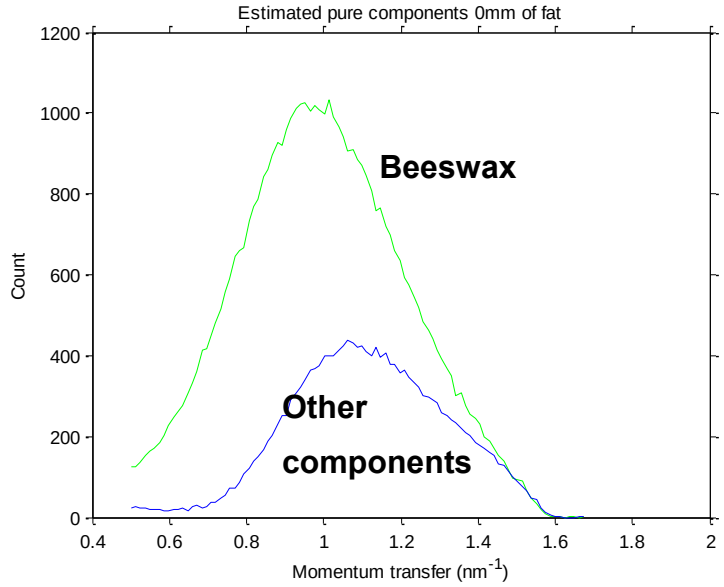

Figure 4.15: The estimated spectra of the pure components, beeswax and others (blood + the blood vessel).

The fitted spectra are shown in Figure 4.16.

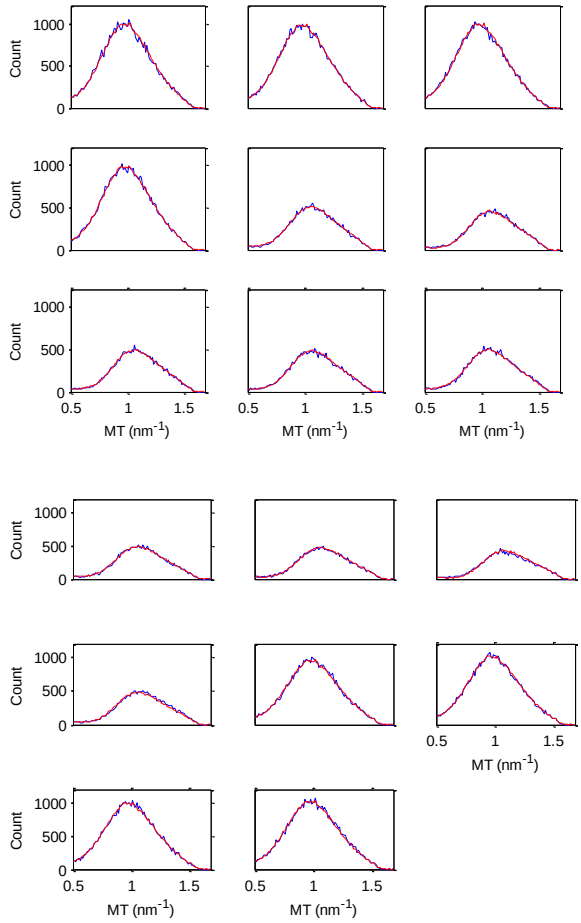

Figure 4.16: The observed and fitted spectra for the 17 scanned positions for 0mm fat in the blood vessel

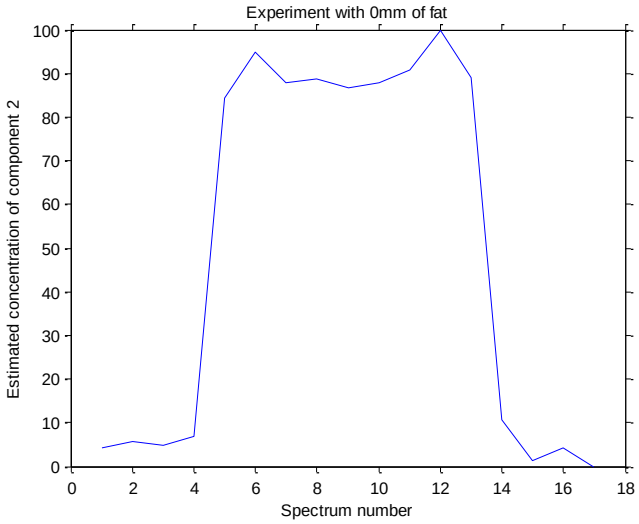

Figure 4.17: The estimated concentration of non-beeswax in the blood vessel for the 17 scanned positions for 0mm fat in the blood (water)

From Figure 4.17 it can be seen that as the beam scans across the Phantom the edges of the blood vessel and its contents are recorded. Note the central region is related to the blood/fat combination in the centre of the vessel. For the other two Phantoms that were used, the equivalent results to Figure 4.17 are Figures 4.18 and 4.19. It appeared that figure 4.18 missed the feature common to figures 4.17 and 4.19, due to inadequate scanned positions. Whereas figures 4.17 and 4.19 had 17 scanned positions, figure 4.18 had 16 scanned positions and conseqently the loss of feature.

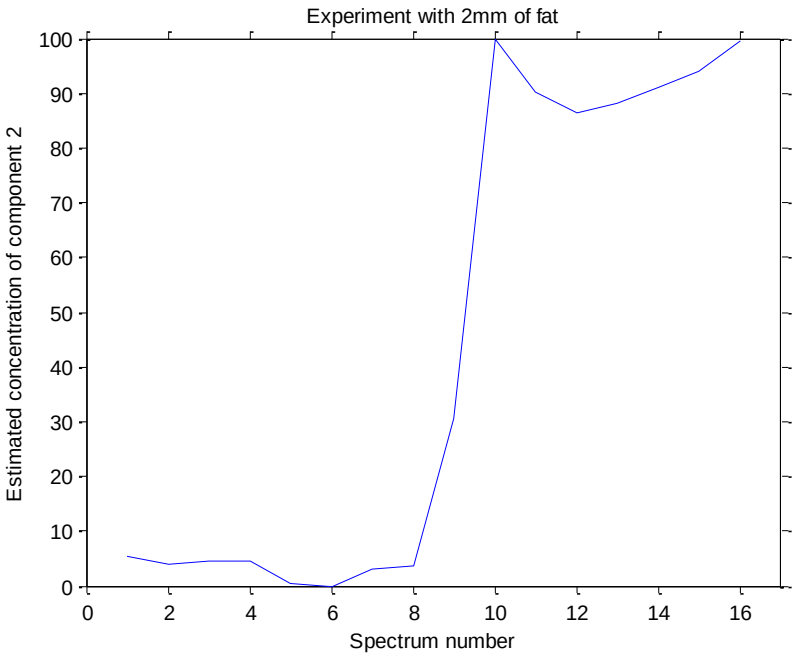

Figure 4.18: The estimated concentration of non-beeswax in the blood vessel for the 16 scanned positions for 2mm fat in the blood (water)

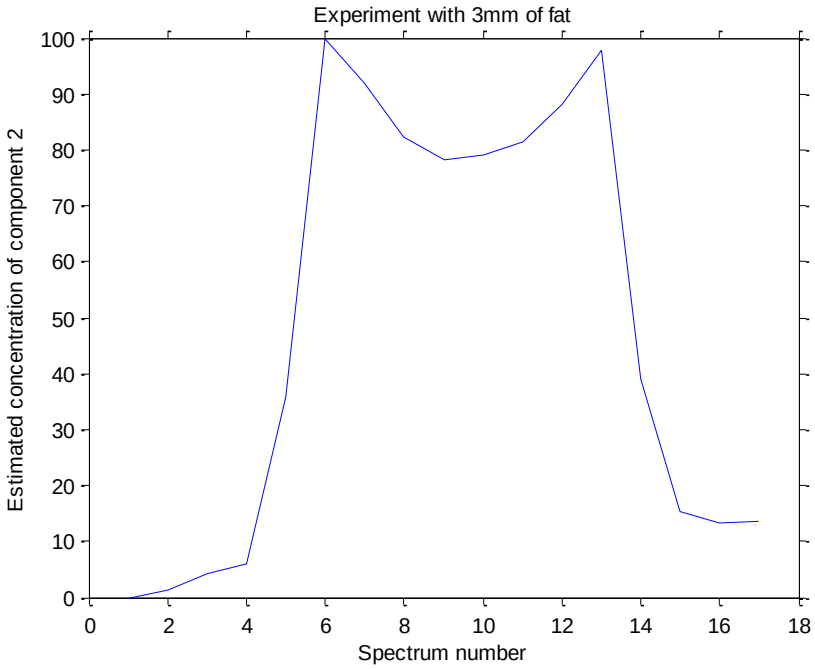

Figure 4.19: The estimated concentration of non-beeswax in the blood vessel for the 17 scanned positions for 3mm fat in the blood (water)

Plotting the estimated pure components from the three runs together on the same graph resulted in the figure 4.20 shown below.

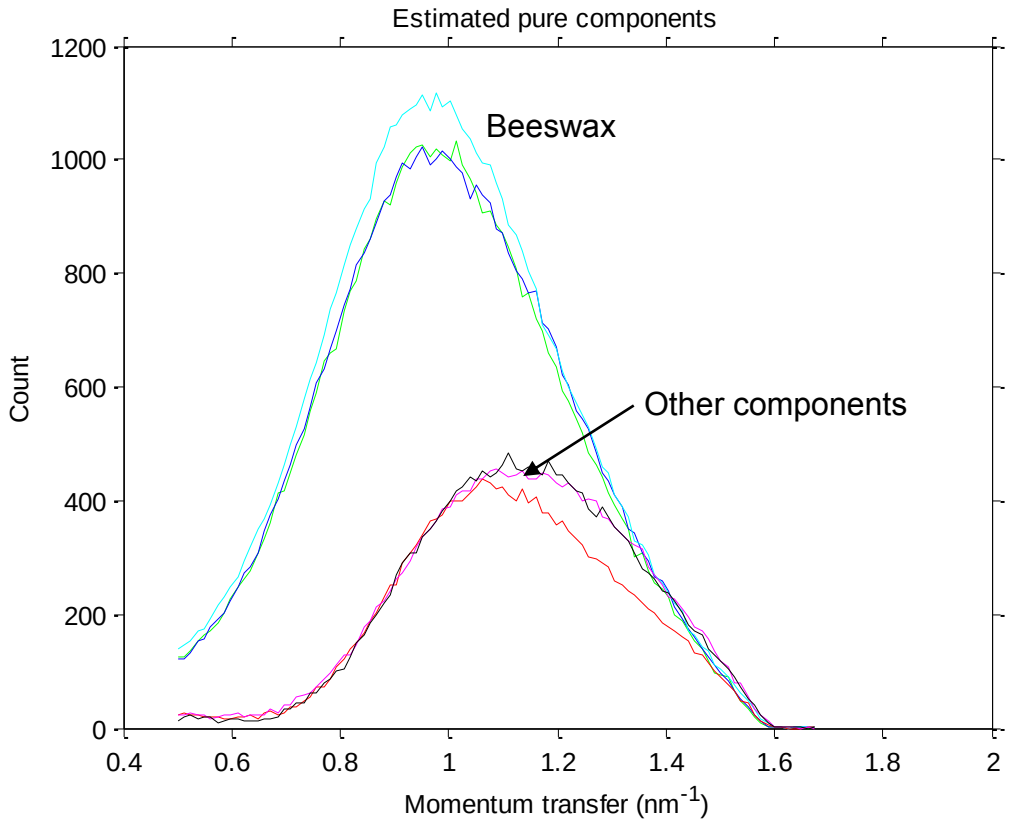

Figure 4.20: The estimated spectra of the pure components (all the 3 together)

The colour coding for the big peak which is the spectra for beeswax is green=0mm, blue=2mm, cyan=3mm fat. The colour coding for the smaller one is red=0mm, magenta=2mm, black=3mm. The 0mm curve should be a water spectrum and the 2mm and 3mm curves should be for two different mixtures of water and fat. Their shapes should have been different from each other and as well slightly different from the shape of the water only spectrum. It is possible that within the particular part of the tube where measurements are being made the amounts of fat could be similar (same thickness).

4.2.6.1 PCA of the heart disease scanned analysis – data set 3 and four extra spectra of 0mm, 2mm, 4mm, 6mm of fat inserts.

The data for the analysis of the heart investigation were obtained from the experiment with three different heart Phantoms as described in chapter three. In this experiment two of the Phantoms had in them different thicknesses of fat insert of 2mm and 3mm each, where as one had no fat insert (0mm). From these Phantoms, 50 spectra were obtained.

The Phantom with no fat (0mm) insert had17 spectra. The Phantom with 2mm fat inset had 16 spectra while that with 3mm fat insert hat 17 spectra. Each of the spectra represented 1mm of the distance covered by scanning across the Phantom. In taking the decision to limit these distances to 17mm, 16mm and 17mm respectively, the factors considered include:

- the position where the heart tissue represented by the beeswax (starting scan points from the beeswax area)
- the position of the blood vessel with the fat insert (the middle and area of interest)
- the next position of the heart tissue representing the beeswax (end scan points in the beeswax area at the other end)
- the measuring time was 50 seconds .

In the analysis 54 spectra were used and these include the 50 spectra from the three Phantoms from the three experiments with the heart Phantom with the fat inserts of 0, 2 and 3mm fat in the “blood vessel” of the heart. In addition to the 50 spectra, 4 extra spectra were taken from a similar experiment with a timing of 100seconds measurements selected from the experiment. In this 4 extra spectra experiment (to be referred to as the “four spectra extract”), a range of measuring times was used on heart Phantom with 0, 2, 4, 6mm fat inserts. The four spectra extract is shown in Figure 4.29. This four spectra extract experiment was done with all the data measured and documented but not listed in the major experiments on table 3.2, as its detailed analysis is not required, safe for minor comparison.

The scores (samples/observations) and loading (variables/patterns) plots for a PCA of these 54 spectra are shown in Figures 4.21 and 4.22. The two principal components shown explain 98.7% of the total variation in the spectra, where the first principal component, PC1 explains 97.6% of the total variation in the spectra and the second principal component, PC2 only 1.1%, while the third principal component, PC3, explains only 0.2% with very noisy loadings. PC1 and PC2 can be said to be noise free. The noise in the experiment is made manifest in PC3 which accounts for only 0.2% of the total variation in the spectra. Therefore, consideration of any further PCs (from PC4 onwards) is no longer necessary because they will yield comparatively very insignificant values.

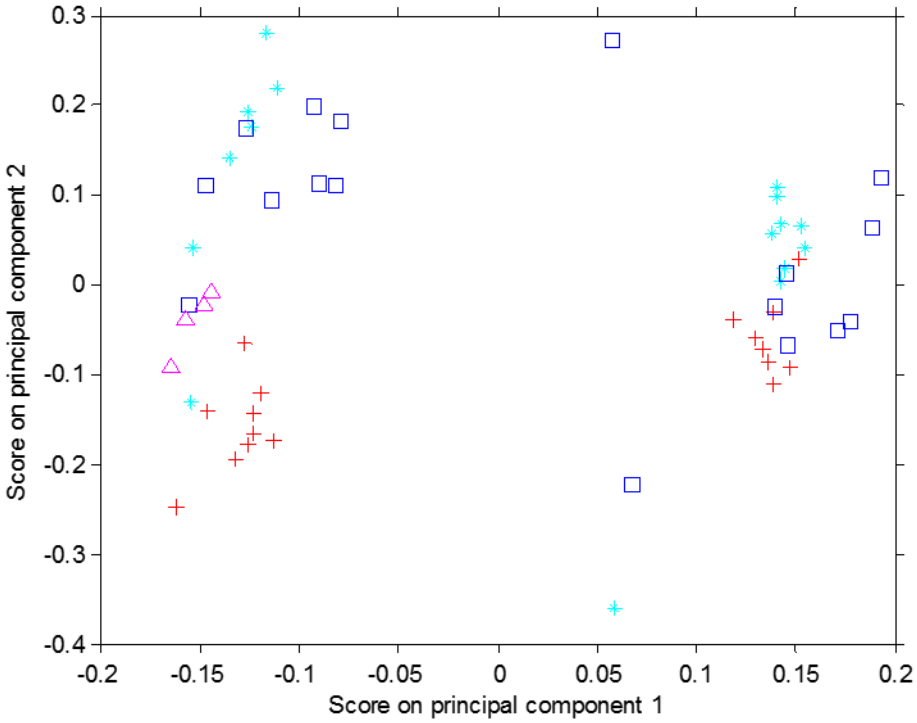

Figure 4.21. Scores plot for PCA of 54 heart spectra. Key to symbols: The red plus represents 0mm fat, green star represents 2mm fat, the blue square for the 3mm fat, while the triangle are the 4 measurements from the measuring time experiment.

Figure 4.21 is a scores plot for the PCA of the 54 heart spectra. The symbols, plus (+). Star (*), square (□), and triangle (Δ), represent 0mm fat sample, 2mm fat sample, 3mm fat sample and the four measurements (0mm, 2mm, 4mm and 6mm fat) in the four spectra experiment, Figure 4.29. In the plot there are two clusters of points, one on

the left hand side and the other on the right hand side and a few intermediate points, shifted more to the right hand side. The two clusters correspond to the measurements from the ends of the scans (cluster number 1, the right hand cluster in the plot) and the measurements from the middle of the scans (cluster number 2, the left hand cluster in the plot), where the blood vessel is situated. All the measurements from the four spectra group (the triangles) fit into the left hand cluster (cluster number 2). This is expected because these measurements were taken on the part of the Phantom with the blood vessel.

Figure 4.22 shows the loadings plot (loadings versus momentum transfer) from the PCA of the 54 heart spectra. The red curve shows the loadings for PC1 and the blue curve shows the loadings for PC2. The mean spectra for the two clusters as shown in Figure 4.21, are shown in Figure 4.23. The three intermediate points as shown in the middle of the plot (two squares and a star in Figure 4.21) were not included in these means plot (Figure 4.23) of the two clusters. Only the two main clusters are considered. Therefore on the left hand side of Figure 4.21 (negative scores on PC1) we have spectra that are represented by the blue curve in Figure 4.23.

Similarly on the right hand side of Figure 4.21, that is, going forward and to the right along the x-axis, more and more of the loading curve for PC1 as represented by the red curve in Figure 4.22 is added to this blue spectrum, representing the loading curve for PC2, thereby increasing the count and shifting the peak towards lower MT values, as can be seen in Figure 4.23, until eventually, just like on the right hand side on Figure 4.21, the spectra of the blue curve can also be seen like the red curve in Figure 4.23. Thus PC1 is describing the difference between spectra from the ends of the scan, the position of the beeswax and the spectra from the points of the middle measurements where the blood vessel and its contents are situated. The physical positions in the scans of the three intermediate points of the two squares and the star in Figure 4.21. Their positions are on the boundary between two ends and middle position. It is likely to be that they are the off-shoot from part of the blood vessel included in the measurement.

The PC2 can ideally be identified as clearly linked to the amount of fat in the blood vessel. The relationship is apparent not minding the imperfection of the correlation. Figure 4.24 shows the mean spectra for the measurements from the middle of each

of the three scans, that is, the measurements that appear in the cluster on the left of Figure 4.21(cluster number 2) but excluding the four spectra of Figure 4.29. In Figure 4.24, red colour represents the mean for 0mm of fat, the cyan 2mm and the blue the 3mm of fat. In both Figures 4.21 and 4.24, there is good separation between the 0mm fat and 3mm fat measurements, with the 3mm fat having higher scores on PC2 in Figure 4.21 (vide the positions of the blue squares compared with red pluses). The 3mm fat in Figure 4.24 has a mean spectrum whose peak is shifted towards higher MT levels and also a higher photon count.

The mean spectra of the 2mm fat plot in the picture has an anomaly, by not being clearly intermediate between 0 and 3 either in Figure 4.21 or Figure 4.24. The differences in Figure 4.24 are perhaps clearer in Figure 4.25, where the 0mm fat (red) spectrum in Figure 4.24 has been subtracted from both, the 2mm and 3mm fat in the same Figure 4.24. Here, the pattern obtained is nearly the same as that of the loading for PC2 in Figure 4.22.

The second unusual feature is that the 0, 2, 4, 6mm pattern from the four extra spectra should, have shown a much wider spread than the points from the scans, since the y-axis of Figure 4.22 is fat. As a matter of fact there is no noticeable spread in these points at all. Looking at the difference spectra does not reveal any pattern that stands out from the noise. The reason for so little variability in these spectra in the PC2 direction is not clear. This fact can then create room for some doubt on the interpretation of the PC2 axis as fat. Another feature is the amount of spread on the PC2 axis in the right cluster (cluster number 2) of Figure 4.21. If this cluster is the spectra of beeswax, there will be little or no variation along the PC2 axis. The fact that there is quite a lot, maybe half as much as in the cluster on the left (cluster number 1), must cast doubt on the simple interpretation of the PC2 axis as fat. The measured and fitted spectra using the two PC model are shown in Figures 4.26 - 4.29 and a plot of the scores on PC1 for each of the scans and the four spectra extract in Figure 4.30.

4.2.6.2 Conclusion

The conclusion is that there is a clear spectral difference between the two ends of the scans and their middle portions. Also the spectral difference showed a decreased

count and a shift in the peak towards higher MT values in the middle portions. It is therefore reasonable to say that all of these represent a difference between the beeswax at the ends and the blood vessel and its contents in the middle portions.

There are also spectral differences, mainly a peak shift further in the direction of higher MT, but this may not be taken to be strongly associated but rather weakly to the amount of fat in the blood vessel. However, it can be taken as a better provisional conclusion until a further research gives a better, additional and more concrete information. Ideally, the point of change in spectra would have been at the point where the blood vessel is located. There must be a technique to use to properly predetermine or designate geometrically, the positions of the contents in the sample for ease of conclusions and for accuracy. In summary, the scan can detect the blood vessel, and it can detect the fat to some extent.

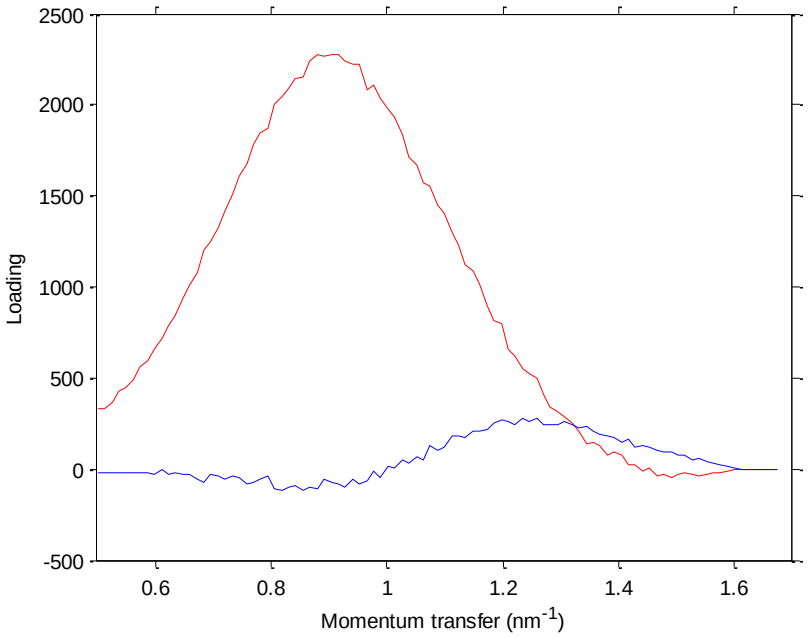

Figure 4.22. Loadings from PCA of 54 heart spectra. The red curve shows the loadings for PC1, the blue curve the loadings for PC2.

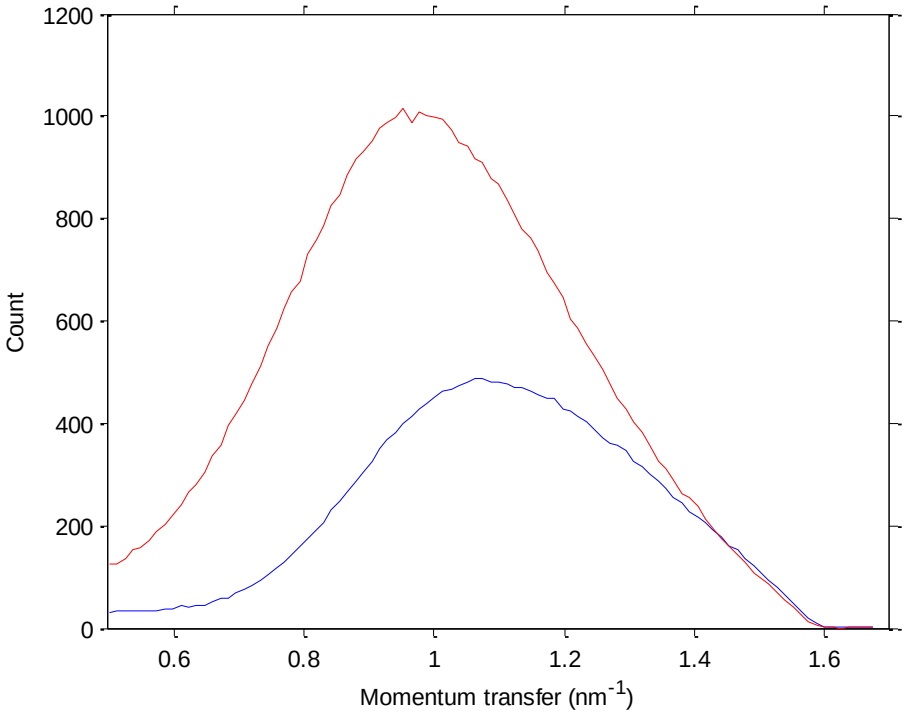

Figure 4.23. Mean spectra for the two main clusters in the scores plot (Figure 4.21). The blue curve is the mean spectrum of the left hand cluster, the red curve is the mean spectrum of the right hand cluster.

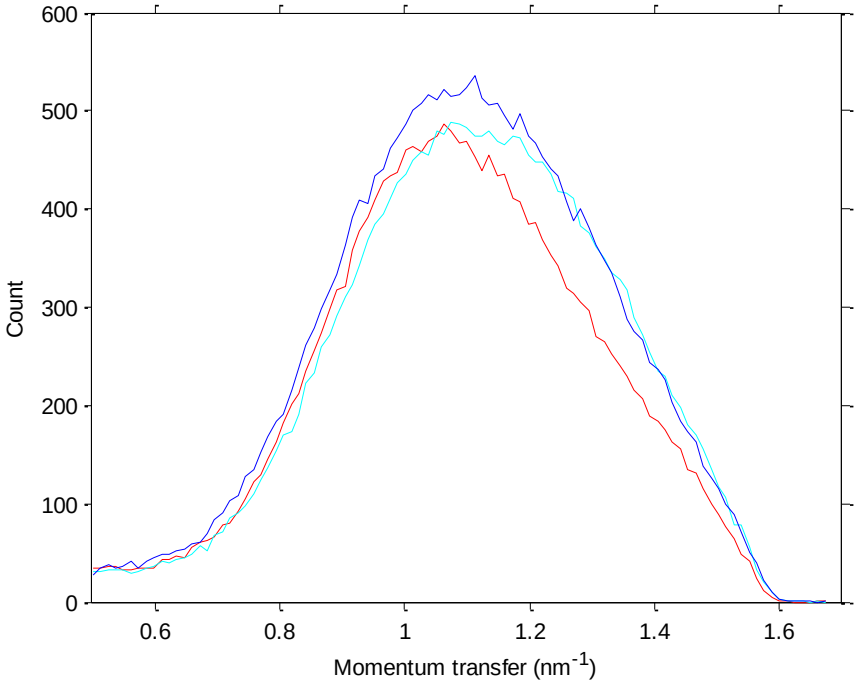

Figure 4.24. Mean spectra from the middle part of the scans of the heart phantom with 0mm (red), 2mm (cyan) and 3mm (dark blue) of fat.

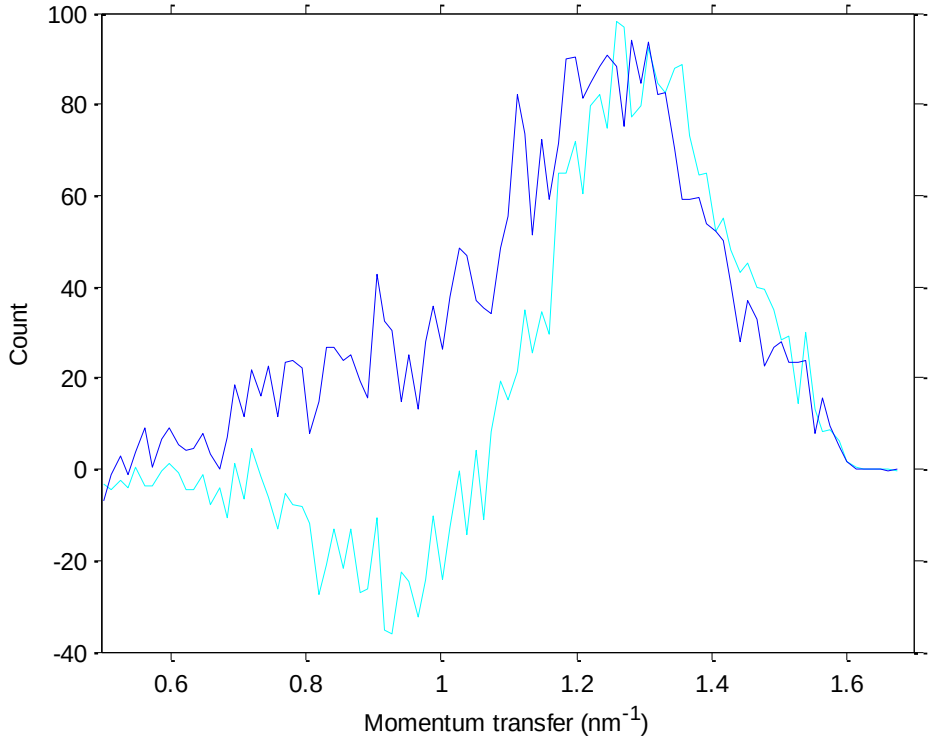

Figure 4.25. Differences between the mean spectra in Figure 4.23. Cyan: 2mm - 0mm. Dark blue: 3mm – 0mm.

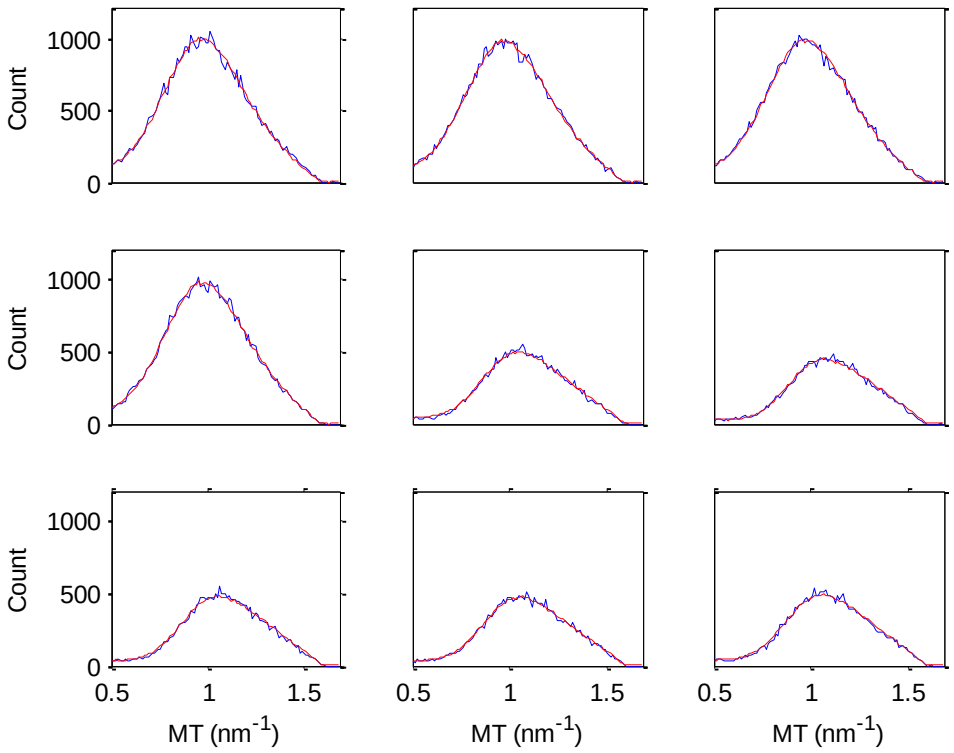

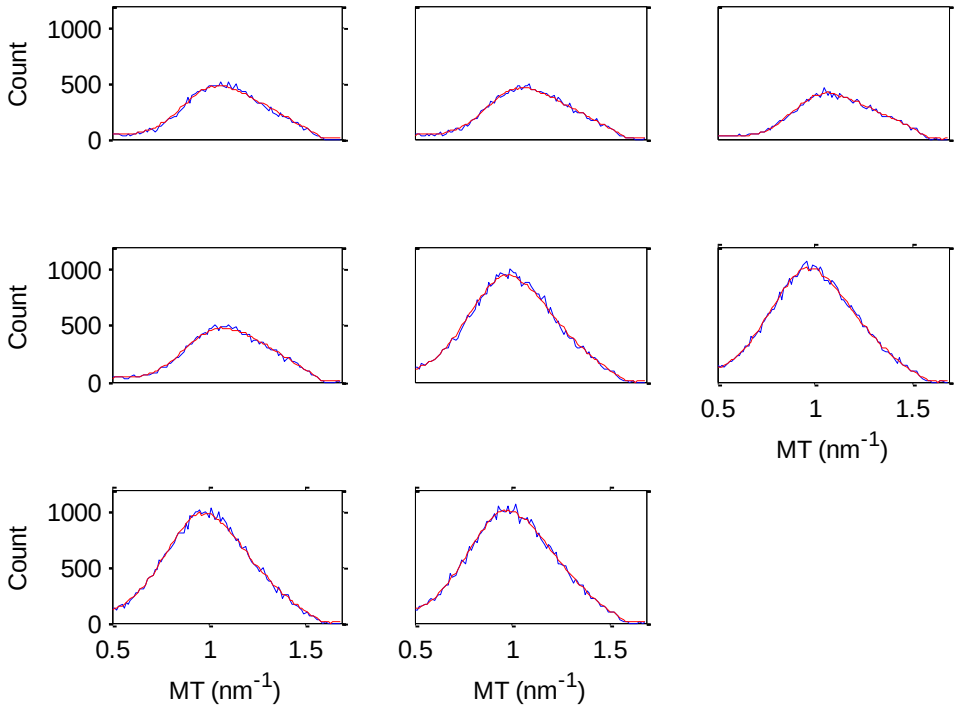

Fig 4.26. Measured spectra and fits from two PC model, scan of 0mm Phantom. Measurement points from 1-17 counting across rows

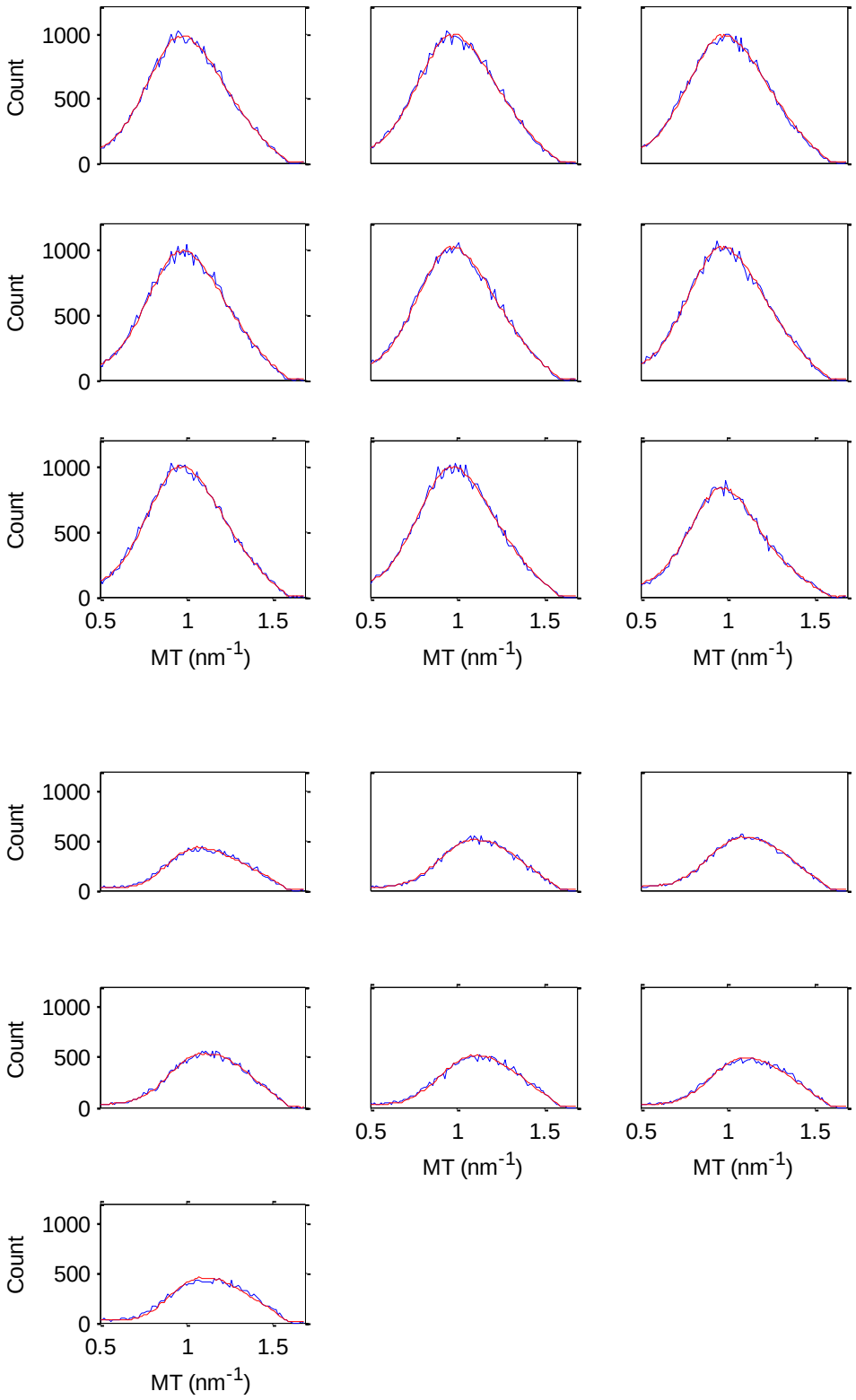

Fig 4.27. Measured spectra and fits from two PC model, scan of 2mm Phantom

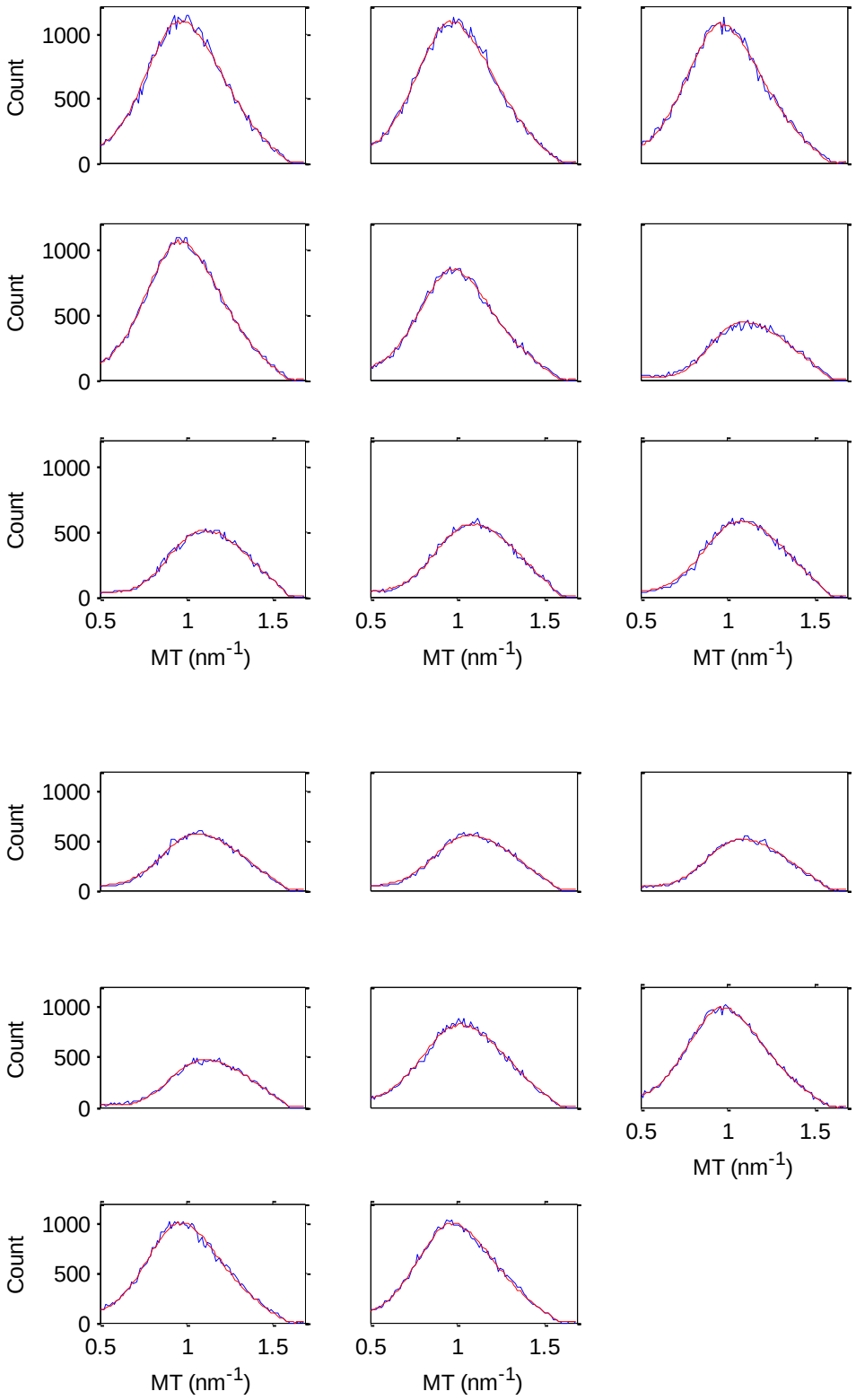

Fig 4.28. Measured spectra and fits from two PC model, scan of 3mm Phantom

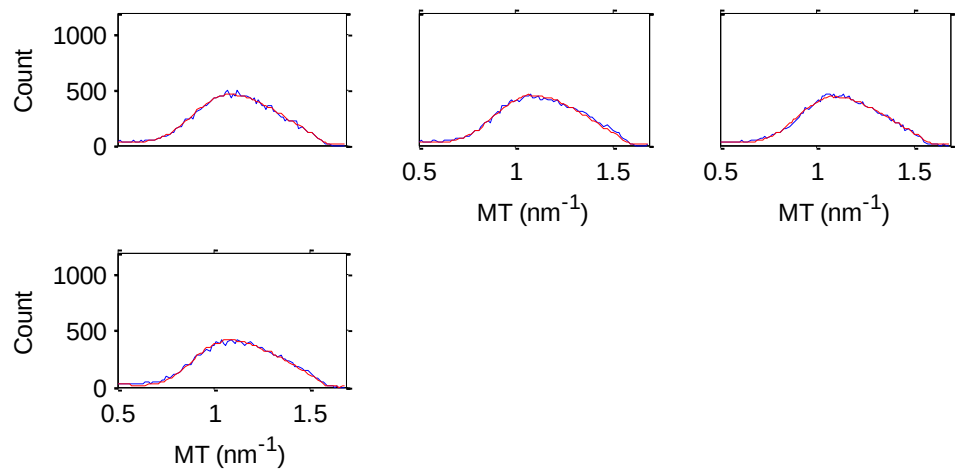

Figure 4.29. Measured spectra and fits from two PC model, 0, 2, 4, 6mm (across rows) measurements from the four spectra extract.

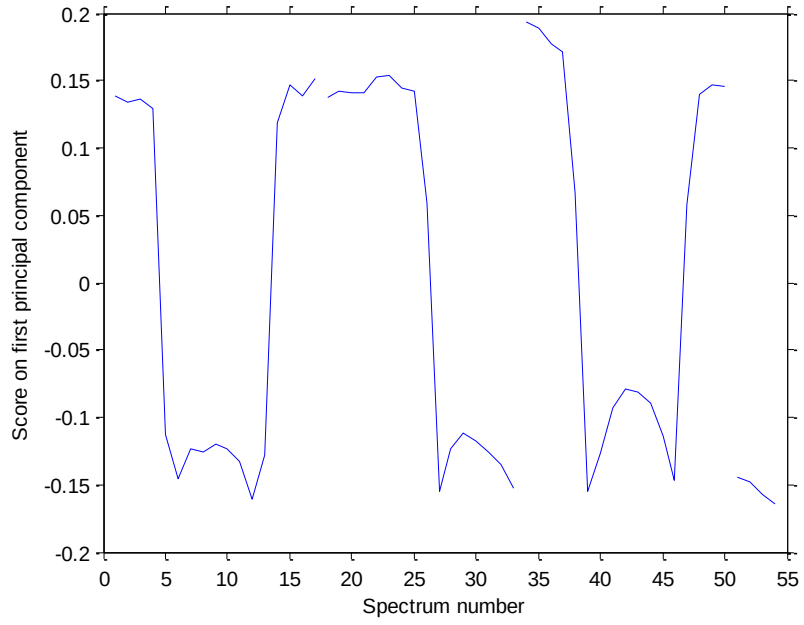

Figure 4.30. Scores on PC1 for the 54 spectra (50 from 0mm, 2mm and 3mm) on the analysis. 50 spectra from The 4 sequences are obtained are 3 for 0mm, 2mm, 3mm fat insert experiment and 1 for 0mm, 2mm, 4mm and 6mm fat insert experiment, reading from left to right.

4.3 Discussion: Discussion of fatty-liver and heart disease analysis.

The focus was on the detection of the fat nodules in the liver and the plaques in the blood vessels of the heart. The spectral results of the fifty-two spectra (12 x 3 and 8 x 2) of the five liver Phantom samples of different thicknesses (8mm, 6.5mm, 4.5mm, 3mm and 3mm). The thickness of the sample was the major consideration in the choice of scan distance (or scan length). Room was made within the pure liver portion before the fat insert and after the fat insert. It was for this reason that the scan length was choosen. For the thirty-one spectra obtained from one liver sample with three different thicknesses (5mm. 6mm and 4mm, a total of 15mm) of fat inserts, with a spacing of 5mm between them. This meant a total of 25mm distance from the back end of 5mm fat insert to the front end of the 4mm fat insert, living 7.5mm of pure liver before the 5mm fat and 7.5mm after the 4mm fat, within a sample holder of 40mm diameter. This explained the geometry behind the choice of scan length of 31mm and implied that only 6mm each of liver at both ends (3mm before 5mm insert and 3mm after the 4mm) was part of the scan length. The same explanation applied to the heart sample of three different thicknesses. The heart sample will be discussed in some details under “Discussion” where the three main experiments are treated in subsections as fatty-liver scanned 1, fatty-liver scanned 2 and heart disease scanned.

The basic considerations are the structure, shape and peak height (PH) of the spectra and the sensitivity of the detection. The sensitivity of detection is the ability of the system to consistently and repeatedly pick up the presence of a particular amount of fat deposit in a given region of interest within the liver or heart sample.

4.3.1 Discussions: Fatty-liver scanned (1)

In a set of 52 spectra where each spectrum refers to a different position across the Phantoms. The thicknesses of the inserted fat are predetermined. The values were indicated as shown in the figures 4.5 to 4.9. The fat inserts in each of the five Phantoms were clearly detected as can be seen in the shape of the spectra. Figure 4.5 showed 12 spectra of Phantom A with an 8mm thickness of fat insert obtained by scanning across 12 mm length, where 1mm thickness represented a spectrum. Looking at the 12 spectra and knowing that an 8 mm thick fat was inserted, spectra, a close look at

spectra numbers 1 to 4, showed some close resemblance. The peak height (PH) increased progressively from number 1 with number 4 being the highest of the four. This is expected as spectrum number 1 is far from the centre of the scattering volume while number 4 is closer. This explains the PH variation. Spectra numbers 5 to 10 nearly equal PH values. The PH values are shown in the data used in plotting the spectra. These spectra are within the scattering volume with the fat sandwiched in between the liver tissue. This explains the closeness in the PH values and the shape. The structure and shape of the spectra numbers 1 and 2 are closely the same and showed they are part of the liver component, whereas the spectra numbers 3 to 10 are similar but different from numbers 1 and 2. Spectra 3 to 10 indicated dual component of fat and liver. Spectra numbers 11 and 12 indicated pure single component, the liver. The closeness in the PH and shape of spectra 1, 2, 11 and 12 spanning a length of 4mm signified pure liver. The similarity in the shape of spectra 3 to 10 spanning the length of 8mm signified the dual component of fat and liver. This equated to the 12mm of the distance scanned from pure liver at one end through liver-fat position to pure liver at the other end.

Similar interpretation can be applied to Figures 4.6 – 4.9. Figure 4.6 showed 12 spectra of the Phantom B with 6mm thickness of fat insert from a scan length of 12mm. Spectra numbers 1 to 4 indicated mostly liver component, numbers 5 to 10 indicated dual component and 11 and 12 indicated a single component. Similarly, in figure 4.7 with 12 spectra of Phantom C with fat insert of 4.5mm thick, spectra numbers 1 to 4 indicated mostly liver, numbers 5 to 9 dual component while numbers 10 to 12 indicated mostly liver.

In figure 4.8 were 8 spectra of sample D with 3mm thick fat insert. Spectra numbers 1, 2 and partly 3 indicated mostly liver, numbers 4, 5 and partly 6 indicated dual component while 7 and 8 indicated mostly liver. There was some distortion. Finally, sample E, figure 4.9 had 8 spectra, where numbers 1 and 2 and partly 3 indicated liver component, numbers 4 to 6, indicated dual component and numbers 7 and 8 the liver.

Figure 4.11 summarized the result of the spectra, showing the estimated fat concentration along Y axis for the five samples, A, B, C, D and E. The X axis had the spectrum number. Sample A spanned from zero to 12 along the X axis, B from 13 to

24, C from 25 to 36, D from 37 to 44 and E from 45 to 52. Through scaling the estimates of the fractional or percentage concentration of fat in each spectrum was established. Looking at the summary plot of the results, the shape for the samples were representative of the size of inserts except for sample D. Samples D and E were 3mm each but there was disparity in the result which could be as a result of some form of Physical deformation of the fat insert within the Phantom. Actually the plots of D and E were supposed to be similar in all forms. The difference could be as a result of the following effects:

- Physical distortion within the sample after insertion
- a shift outside the scattering volume with respect to D, hence making it smaller than expected
- the beam missing out part of the sample (partial beam coverage) or beam covering the entire sample (full beam coverage). Partial beam or smaller beam would give smaller picture.
- Full or bigger beam will give the full size picture. This could be the effect on E

Sample A had expectedly the highest concentration at spectrum number 4 and another at 8 but lower. Sample A had an unusual split as seen in the plot. Some anomaly were observed. Only one peak was expected but two peaks showed up. This could be due to:

- Statistical error in the estimation of the data
- Possible split in the fat insert within the sample
- Displacement from the expected or appropriate position

The drop between 4 and 8 in sample A could be due to some unseen distortion or deformation of the fat insert in the sample. Sample B had its highest concentration at number 19, sample C at 29, sample D at 40 and sample E at 49.

The ability to pick the details of the inserts is explained by Figure 3.5 which showed the contour of the scattering volume with maximum dimension of 7mm x 3.5mm x 1.1mm (length, width and height respectively). This is within position 3 and 17 along X-axis and between about 5.3 to 8.5 (1.6mm) along Y-axis The area of maximum intensity scattering falls between point 6 and 13 along X-axis (3mm long) and between about 5.8 and 7.2 (approximately,0.75mm) along Y-axis.

The samples were therefore positioned appropriately within the scattering volume and the sensitivity and ability of the technique for finding all the fat nodules adequately envisaged.

4.3.2 Discussions: Fatty-liver scanned (2)

This second case which is similar to the result of section 4.3.1 but of a single Phantom containing three fat nodules of different diameters (5mm, 6mm and 4mm) . Scanning the Phantom at 31 different points, 31 diffraction profiles were collected as in figure 4.12. A critical look at the 31 spectral figures spectra 1 and 2 had extra features which could be contribution from the polystyrene structure of the sample holder. Spectra 3 to 6 indicated liver only, 7 to 12 indicated dual components (fatty-liver) and it is within here that 5mm thickness of fat was inserted. Spectra 13 to 18 indicated liver only. Spectra 19 to 25 indicated fatty-liver and within here was 6mm thick fat insert. Spectra 26 to 28 indicated liver only and finally spectra 29 to 30 indicated fatty-liver. The 4mm fat insert was in this portion. Spectrum 31 indicated pure liver. The reduction in the expected size of spectrum for the last 4mm fat was probably due to some distortion, based on the fact that the liver could compress the fat, and thus, reshaping the original geometry of the insert.

Observable differences in the shape of the spectra was seen from position 8 to 12 which peaked at position 10, also between positions 20 to 24 and 28 and 31. This resulted in the analysis figure 4.14, depicting highest concentration of fat at position 10, followed by that at position 22 and then 29, which represented the 6mm, 5mm, and 4mm fat respectively. From the figure 4.14 the percentage concentration at all points are obtained. Estimation of the concentration of fat at every position along the 31 positions was done and percentage worked out as described earlier in section 4.3.2.

The very low concentration of fat could be as a result of the factors discussed in section 4.3.1. The Phantom itself or the position of the fat might not be quite in the scattering volume and so the beam missing most part of it.

Also as explained in section 4.3.1, the scattering volume as plotted in Figure 3.5 enabled good detection.

4.3.3 Discussions: Heart disease scanned

Three Phantoms were used each containing a different sized plaque. Here detectability and sensitivity of the technique to find plaques in blood vessels of the heart were well demonstrated as in figures 4.15 – 4.20. The acquisition time was 50s and the operating potential was chosen to be 40 kV and 2mA.

Three results from the scanned heart data are shown as figures 4.17, 4.18 and 4.19. In the 0mm fat Phantom, spectra 1 to 4 indicated the presence of beeswax for the heart tissue in the spectra with the spectra 4 at the edge, the boundary between the wax and the blood vessel. Spectra number 5 to 13 represented the blood and blood vessel combination, with a shallow curve and 14 is the edge of the blood vessel, another boundary between the blood vessel and the beeswax. Spectra 15 to 17 indicated the beeswax.

Similarly, the heart Phantom with the 2mm of fat exhibited the same characteristics. The shape was almost the same, except for the shift which most probably was as a result of internal shift of the blood vessel in the Phantom. Consequently, spectra 1 to 8 indicated the beeswax, 9 was the edge, the boundary between the wax and the blood vessel, 10 to 16 was the plastic tube (blood vessel), blood and fat combination. The full shape would have come out if the spectra were above 19 or if spectra 1 to 4 were limited to the beeswax as against 1 to 8 which was unnoticed during the scanning.

The 3mm fat result was similar to the two before but more descriptive with well-defined features. As usual spectra 1 to 4 indicated the beeswax, 5, the plastic area, 6 to 13, the blood, fat and plastic combination with a deeper curve, 14 another plastic area and 15 to 17, the beeswax.

Considering the results, it can be seen that they exhibited good level of reproducibility and consistency and the system's ability to see fat nodules/plaques. However, it is easier to detect larger sizes of fat. The ability to see very small ones in a larger body

is subject to some intervening factors such as the magnitude of overlying thicknesses and hence attenuation and the operating conditions. This assessment will be treated in detail in chapter 5.

4.4 Sources of error in the analysis

Errors manifest variously in the experiments leading to expected inaccuracies in the readings and the results. There are obvious errors due to sample positioning and size. The non-uniform size of the samples of the same tissue contributed to the disparity in the obtained values. Most of the contributing factors have been discussed in sub-section 4.3.1

The random process of x-ray production and its detection leads to noise. Noise is proportional to the square root of the number of the x-ray Photon counts, consequently noise contributed to the errors and the degradation of the spectral outputs and results. There is also the possibility of some incoherently scattered photons being detected and the effect of multiple scatter though taken to be less significant.

4.5 Summary

Liver and heart samples are scanned and their spectra obtained. For the liver sample it is assumed that the set of spectra contains at least one pure fat and at least one pure liver. If this is true, these will be the spectra that have the extreme values of either of each component, liver or fat. Thus the fitted spectra corresponding to the extreme values were taken as estimates of the two pure components. The estimates are shown graphically in Figures 4.14 (for the liver), 4.17 – 4.19 (for the heart)

The analysis of results for the liver and heart samples have been done and the outcome very nearly similar. The spectra plots of intensity against energy or momentum transfer showed the differences between the heart or liver tissue, fat (plaque) and water (blood) at different and specific peak positions of momentum transfer values within the energy used. The observed spectra and the expected fitted well.

The PCA plots have showed the spectral difference between the ends of the scans and their middle portions. Also the spectral difference showed a decreased count and a shift in the peak towards higher MT values in the middle portions. All of these represent a difference between the beeswax at the ends and the blood vessel and the contents in the middle. In the heart sample there are really four samples, namely beeswax (heart tissue substitute), fat, blood (water) and the blood vessel. Ideally there are supposed to be four principal components but in the PCA analysis the PC1 explains 97.6% of the total variation, the PC2 explains 1.1% of the total variation, while PC3 explains 0.2%. Therefore extra PC is irrelevant or not significant. Even the PC3 is insignificant. Allowance for sampling variation is given in the interpretation of the spectra.

The point at which the spectra change is where the blood vessel is located. There are also spectral differences, mainly a peak shift further in the direction of higher MT. The system has the ability to detect fat and the blood vessel and its content.

Fat nodules in the liver and plaques in the blood vessels of the heart have been identified and assessed with estimates of their concentrations at various points along the tissue samples. The results demonstrated this EDXRD system's ability to see very small fat deposits from 2mm thick in small tissue Phantoms.

However, there are limitations. It is easier to detect larger sizes of fat in the small samples examined. The ability to see similar sizes of fat or very small ones in a larger body might not be easy due to some intervening factors such as the magnitude of overlying thicknesses of tissues and hence attenuation and the operating conditions. This assessment will be treated in detail with the translation of the system's capability in graduated larger tissue which forms the main subject of the next chapter (Chapter 5).

Chapter 5

Translation to patient-sized examinations of fat in liver and heart tissues

5.1 Introduction

The results in Chapter 4 have been obtained from small sized anthropomorphic phantoms. To investigate the potential of the technique that has been developed for clinical application requires test phantoms of life-sized dimensions. Making measurements on these phantoms would require significant changes to the experimental set-up. The positions of the source and detector would have to be extended to allow for the positioning of the larger phantoms with dimensions ranging from 80mm (for heart) to 300mm (for liver). To overcome this problem it was decided to simulate the larger phantom and the effects of larger phantoms by computing the expected diffraction profiles. The small phantom size was fixed at 30mm for both the liver and heart investigations. The bigger sized sample implies increased attenuation.

Figure 5.1 shows two CT scans of the liver and two of the thorax. The top left image shows a largely fat containing adenoma in the left lobe and the top right image demonstrates severe fatty infiltration of the right lobe of the liver. It can be seen that to make diffraction profile measurements at points within either the left or right lobes of the liver would require the X-ray beam to cross the abdomen and in doing so the incident and exit beam will pass through different relatively dense tissues. The lower two images show sections through the thorax containing the heart and the major blood vessels supplying the heart. Again to study fat deposits in these blood vessels requires the X-ray beam to cross a large section of the patient but in the case of the thorax much of the thorax is filled with low density lung tissue.

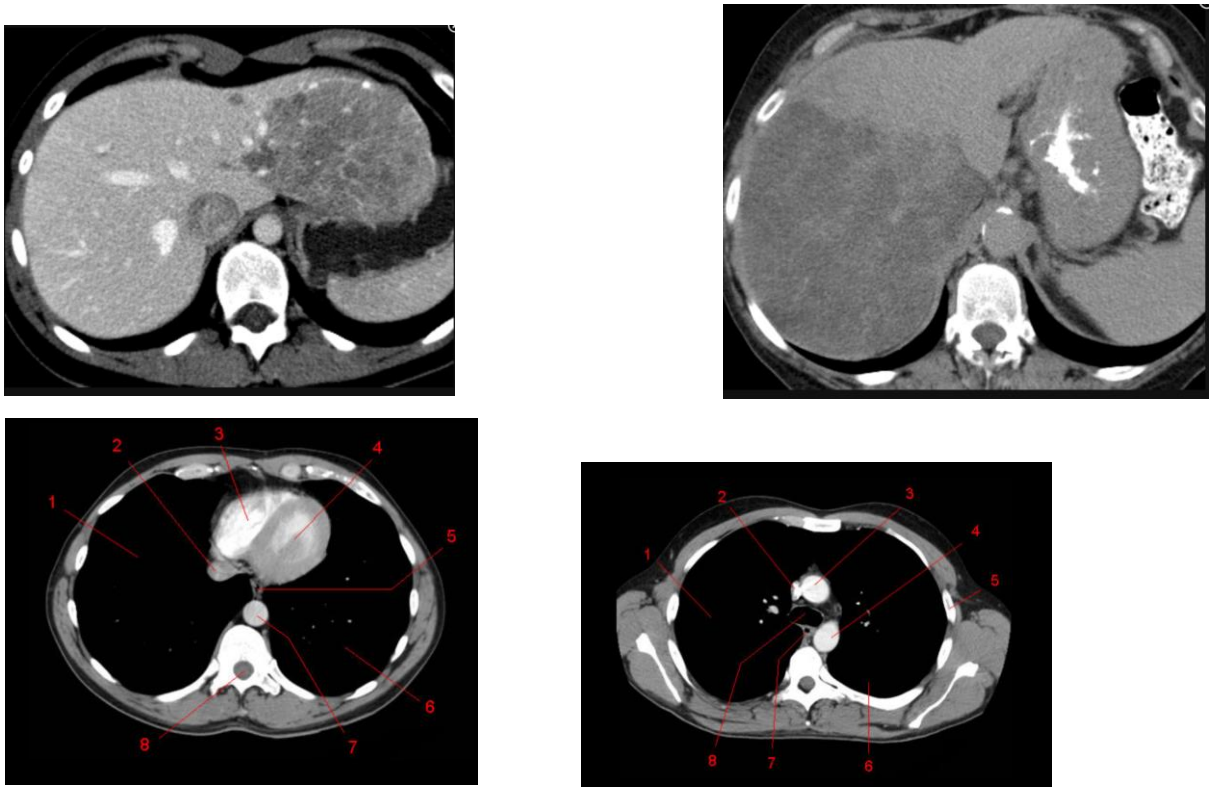

Figure 5.1: Four CT images. The upper images are of liver tissue containing fat. The lower two images are of the thorax demonstrating the heart and the major blood vessels. In the lower left hand figure the ventricles of the heart are labelled 3 & 4 whilst the major blood vessel is 2 and in the lower right hand figure 3 and 4 represent major blood vessels.

In practice there are three important effects taking place due to the attenuation by the additional tissues. Firstly there is a reduced photon flux through the patient. Consequently, the noise on the detected counts will be increased. This could be overcome by operating the X-ray tube at higher tube currents with a consequent increase in patient dose. Secondly there will be a change in the spectral shape due to the preferential attenuation of low energy photons. This is probably the most important change as there is little that can be done to mitigate this change. Finally, there could be an increase in incoherent scatter recorded by the detector. As the incident and exit collimators are limited in cross sectional area, it is thought that this effect should be limited.

5.2 Simulation of attenuation effect on thicker samples

To simulate the spectra from patients the procedure that was followed is outlined in Figure 5.2. In this case the diagram represents an examination of the liver.

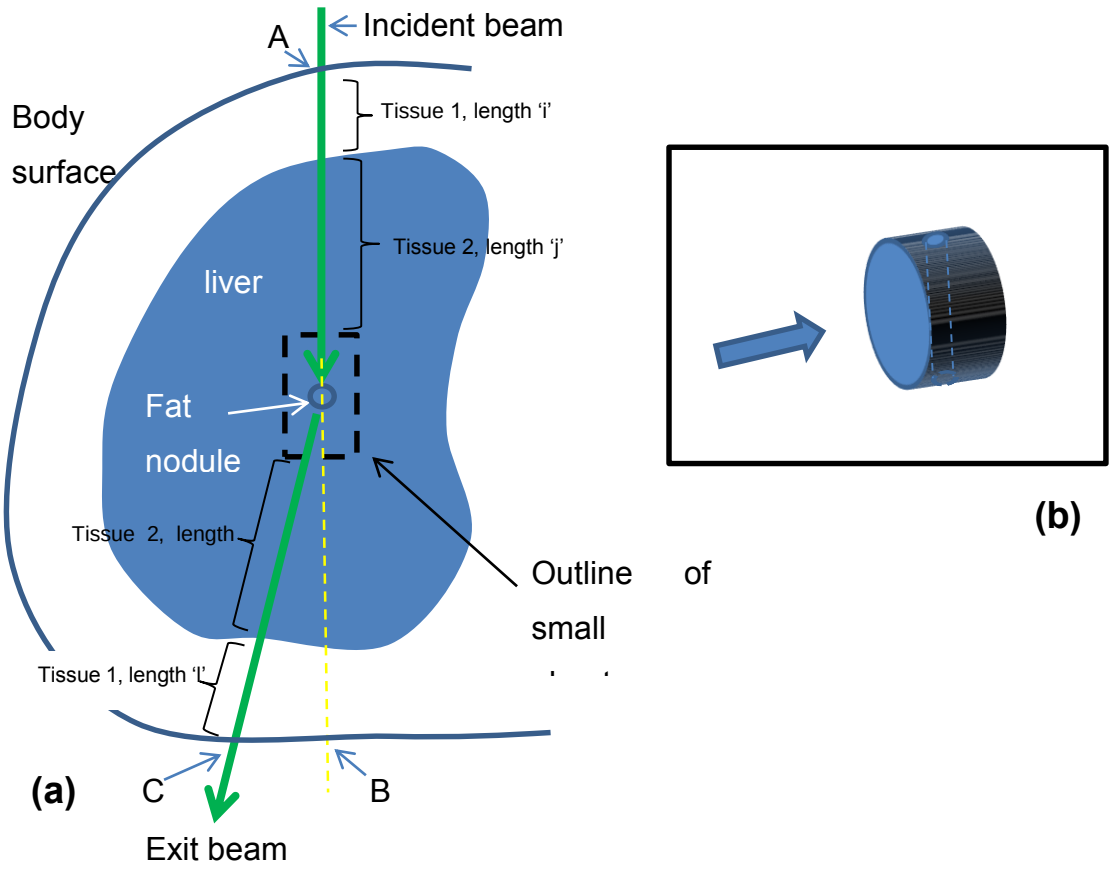

Figure 5.2: Patient study of fat nodules in the liver. (a) The life-sized phantom to be simulated. (b) The small sample phantom on which measurements have been made. Note (a) contains (b) as shown by the dotted line.

Figure 5.2(a) shows the geometry for the scattering measurements. The cross section through the abdomen at a point containing the liver is shown. A fat nodule contained within a small volume of liver, i.e., the small phantom geometry, is shown in the middle of the liver. The measurement geometry for the small phantom is shown in Figure 5.2(b). The spectra that were recorded using the geometry of Figure 5.2(b) need to be corrected for the new geometry shown in Figure 5.2(a) by taking into account the effects of the additional tissue that surrounds the region of interest containing the fat

nodule. To simplify the calculations only two tissue types are considered – additional liver tissue ('tissue 2') and a surrounding layer of adipose tissue ('tissue 1'). Using the distances (i, j, k), as given in Figure 5.2(a) and assuming the measured diffraction profile for the small phantom (Figure 5.2(b)) is given by *S (E)*, the spectrum recorded through the patient-sized phantom would be:

$$\boldsymbol{S'(E) = S(E)\exp\left(-\left(\mu_1(E)(i+l) + \mu_2(E)(j+k)\right)\right)} \qquad 5.1$$

Where, μ_1 and μ_2 in the above equation are the linear attenuation coefficients of tissues 1 and 2 respectively. S (E) is the recorded spectrum of the small phantom. To use equation 5.1 requires knowledge of these attenuation coefficients over a range of energies from 10keV to 70keV. To obtain these coefficients, data have been taken from the National Institute of Standards and Technology (NIST) data tables (www.nist.gov/pml/data/xraycoef/index.cfm) and these are plotted in Figure 5.3. Table 5.1 summarises values of the parameters in equation 5.1 that have been used in the simulations.

Table of parameter values for modelling patient-sized diffraction profiles		
	Fatty liver	Plaques in heart vessels
tissue type 1	adipose tissue	soft tissue
(i+l)	10→40mm	5→10mm
tissue type 2	Liver (soft tissue)	lung
(j+k)	30→160mm	100→300mm

Table 5.1: Parameter values used in the modelling of patient-sized diffraction profiles

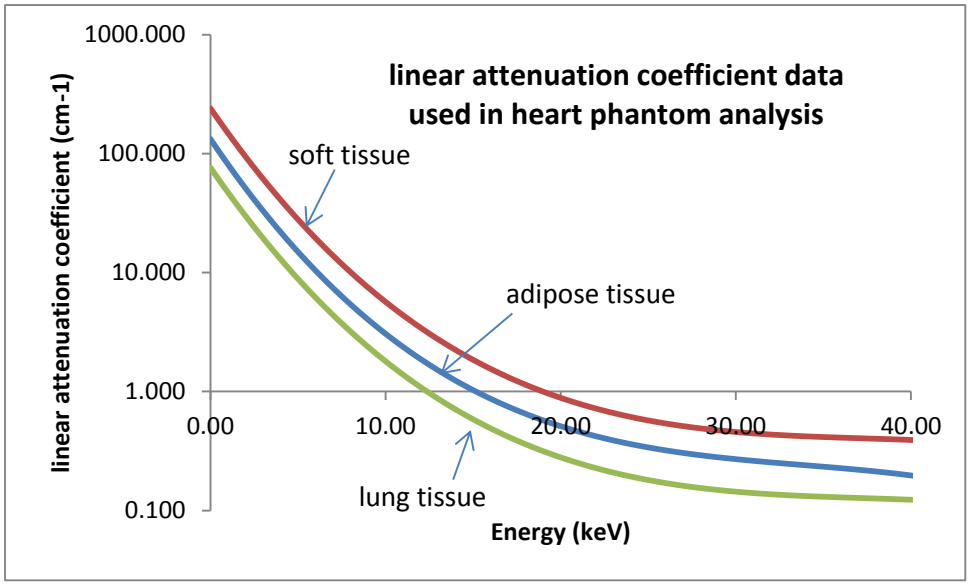

Figure 5.3: Linear attenuation coefficient data relevant to the heart disease problem estimated from NIST data. For the fatty-liver problem only adipose and soft tissue were used but the analysis was extended to 70 keV. Where required additional liver tissue was modelled as soft-tissue.

The NIST data tables give values for mass attenuation coefficients at fixed values of energy. To obtain the full set of data as shown in Figure 5.3 the NIST data was used to obtain a fit over the range of interest. For analysis of the heart phantom the range of interest was from 5 to 40 keV and for the liver phantom it was 5 to 70 keV. To obtain best-fit equations the NIST values were plotted as *log (linear attenuation coefficient) versus photon energy*. A polynomial of curve gave the best fits (with a correlation of 99% fit) and these equations were used to estimate the attenuation coefficients at all required energies for the given range. The attenuation curves (for the heart analysis at 40kV) with polynomial fits have a correlation, R^2 value of a little over 99% for each of the three tissues.

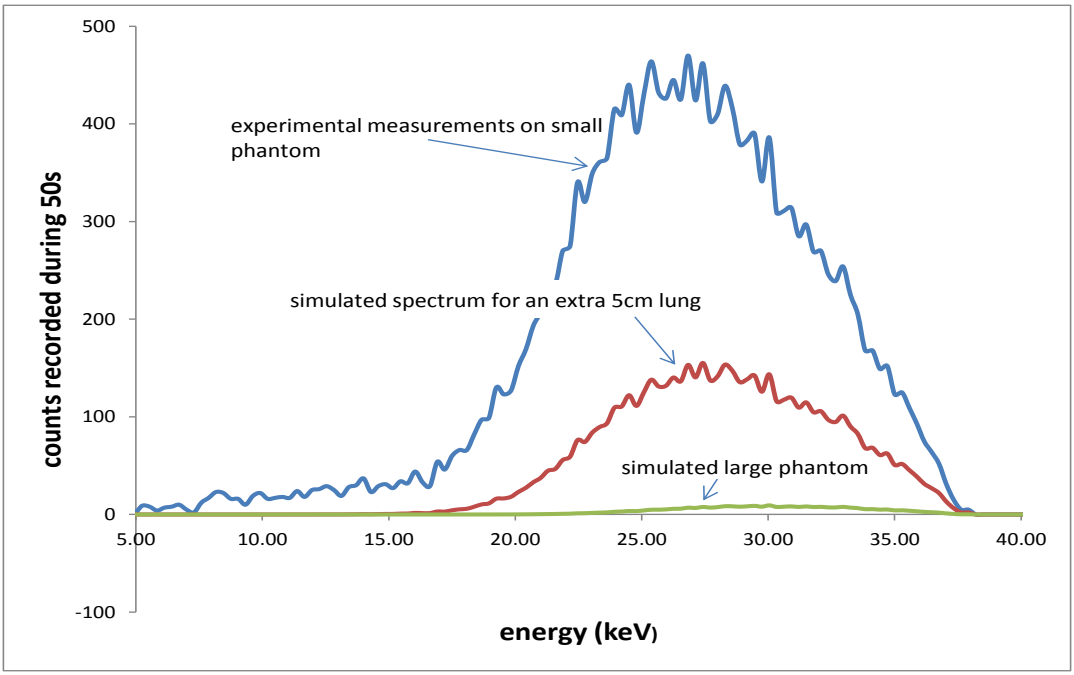

Figure 5.4: Plot of the measured and simulated spectra. Note the changes as the object size is increased. The spectrum changes shape due to filtering of low energy photons and there is significant reduction in recorded events.

Excel spreadsheets were set up to calculate the effects of overlying tissue using the parameters in Table 5.1. An example is shown in Figure 5.4 for the heart phantom with a 2mm plaque present in the blood vessel. The effects of spectral filtering (shift in the peak to higher energies) and attenuation (reduced recorded counts) are clear in Figure 5.4. The spreadsheet also allowed noise to be added as appropriate to the reduced flux. Noise was assumed to follow a Poisson distribution with the mean value, *m,* with a standard deviation, σ, equal to the square root of the mean value, $\sigma = \sqrt{m}$. Hence any count with noise was given by the attenuated count (m*)* + *RAND.f.*σ. Where *f* took on values between 0.1 and 3 (precisely six discrete values, f = 0.1, 0.3, 0.5, 1, 2 and 3) and *RAND* was a random number between -1 and +1

This process of simulating the spectra for larger sized objects was carried out for both the fatty-liver and heart disease conditions, for a range of 'patient' sizes and for a range of noise factors as given in table 5.2. In practice noise factors would be related to dose.

Increase in dose leads to decrease in noise and vice versa. The effect of dose is crucial and will be treated in a separate section.

Models (μ)	1	2	3	4	5
Model Description	Child(1) – Small	Child(2) – Average	Small adult(1)-	Small adult(2)-Average	Large adult
	Heart simulation				
Adipose	5mm	10mm	15mm	15mm	20mm
Soft tissue	30mm	50mm	50mm	80mm	100mm
lung	30mm	30mm	80mm	100mm	120mm
Name	Child(1) – liver	Child(2)-liver	Small adult(1)-liver	Small adult(2)-liver	Large adult-liver
	Liver simulation				
Adipose	5mm	10mm	15mm	15mm	20
Soft tissue (includes liver tissue)	30mm	50mm	50mm	80	100
lung	0	0	0	0	0
Noise factors (f)	0.1,0.3,0.5, 1, 2, & 3	0.1,0.3,0.5, 1, 2, & 3	0.1,0.3,0.5, 1, 2, & 3	0.1,0.3,0.5, 1, 2, & 3	0.1,0.3,0.5, 1, 2, & 3

Table 5.2: The tabulated values of tissue thickness (in mm) and noise factors used for heart and liver simulations. The table also includes the noise factors (*f*) that were used in each case.

5.2.1 Spectral outputs of the simulated patient sized tissues

Typical demonstration of the effects of the extra adipose tissue, soft tissue and noise is seen in the figure 5.5.

In figure 5.5, the blue spectral curve represents the effect of attenuation on the small phantoms, the models of small and average child and the small and average adult. The red spectral curve represents the large adult. The variation in the model sizes are shown in the tabulated values of additional thicknesses in millimetres (mm) coupled with varied noise factors assigned to each model.

Similarly, Figures 5.6 - 5.11 are plots showing how these spectral change with additional thicknesses of tissue and noise due to the effect of attenuation correction. The legends in Figures 5.6 to 5.11 have series 1 (in blue colour) and series 2 (in red colour) shown. Series 1 is indicating the control spectra, that is, the spectra of the small phantom without attenuation correction and series 2 indicating the spectral change with attenuation correction for each of the 5 patient models.

The liver has adipose tissue and extra soft tissue at both sides of the fat nodule under investigation while the heart has the lung in addition to that of soft tissue as shown in Figure 5.2.

These effects were graphically obtained with interactive settings for five different life-size patients (Small child, Average child, Small adult, Average Adult and Large Adult) as in Table 5.2. The graphs in Figures 5.6 -5.11, have the original spectrum obtained from the small phantom without attenuation correction (shown in blue colour) and the second spectrum is reduced according to the attenuating medium (shown in red colour). The thickness values for the adipose tissue, soft tissue and the lung which surround the region of interest are shown below the graphs. The liver examples had extra adipose and soft tissue on both sides of the region of interest and for the heart in addition to the adipose and soft tissue additional lung tissue was added. Noise scaling factors of 0.1, 0.3, 0.5, 1, 2 and 3 were used to obtain these results.

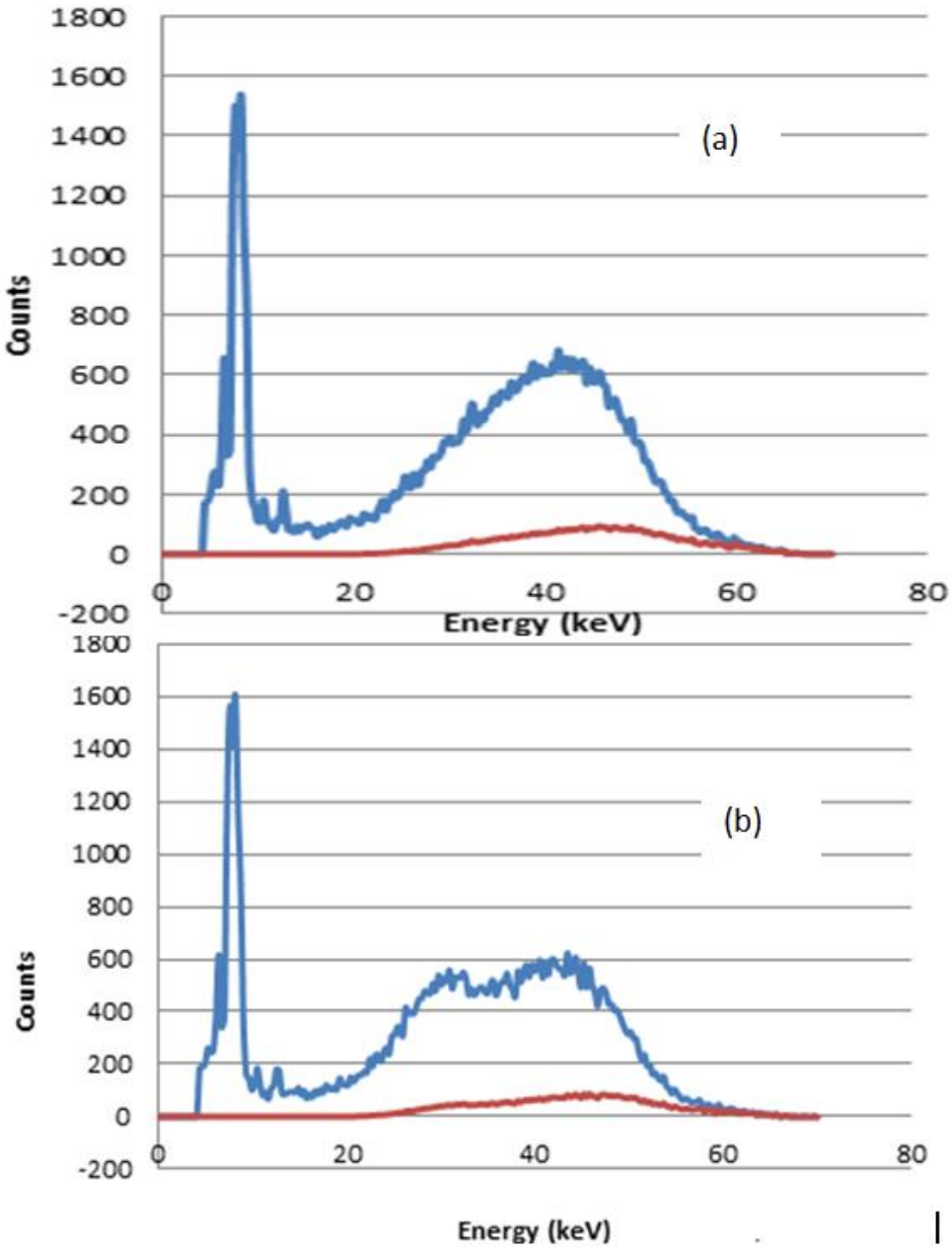

Figure 5.5: Effect of attenuation with attenuation correction for small and large phantom at two special positions (a) at 18 (liver only) and (b) at 10 (fatty liver). The spectra for small phantom in blue and the large phantom in red, which represents the patient-sized model, are plotted together. Other related figures are in the Appendix (Appendix 3) as Figures 5.5b -5.5f.

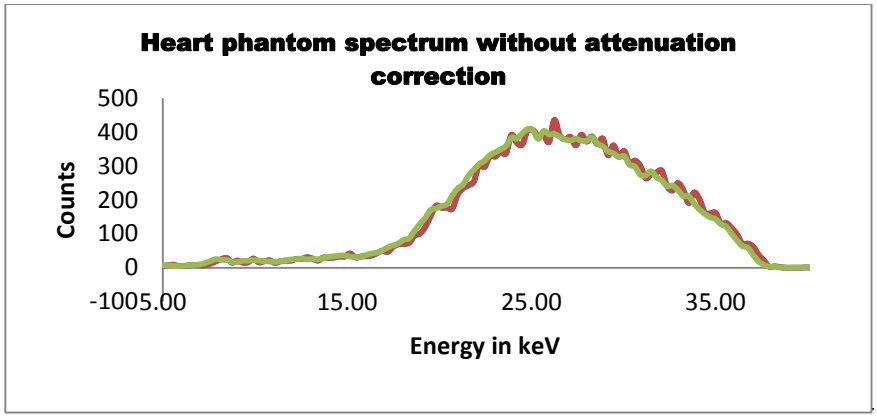

	ADIPOSE	SOFT TISS.	LUNG
Additional tissue thickness in mm	**0**	**0**	**0**

Figure 5.6: This is the control spectra or the small phantom without attenuation correction.

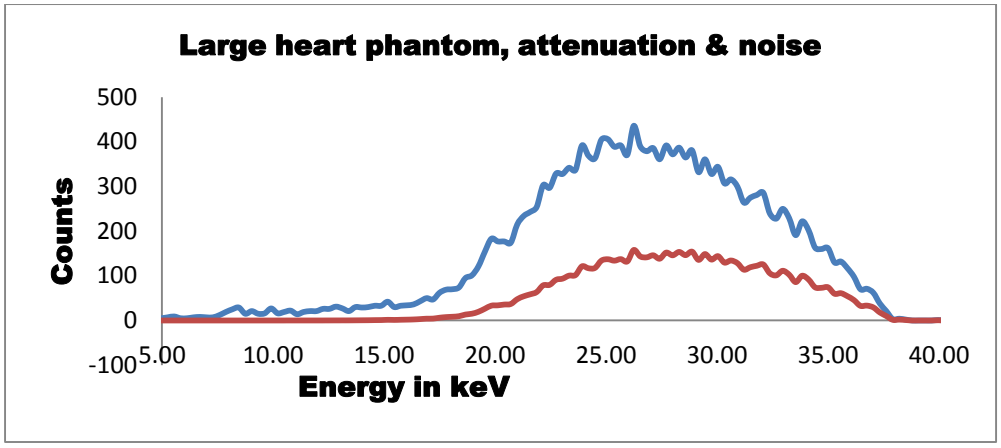

	ADIPOSE	SOFT TISS.	LUNG
Additional tissue thickness in mm	**5**	**30**	**30**

Figure 5.7**:** Spectral change for a very small child (child 1) with extra 5mm, 30mm and 30mm adipose, soft tissue and lung tissue respectively, in red, with attenuation correction. The blue represents the small experimental phantom spectra. The red represents various additional thicknesses of tissue with attenuation.

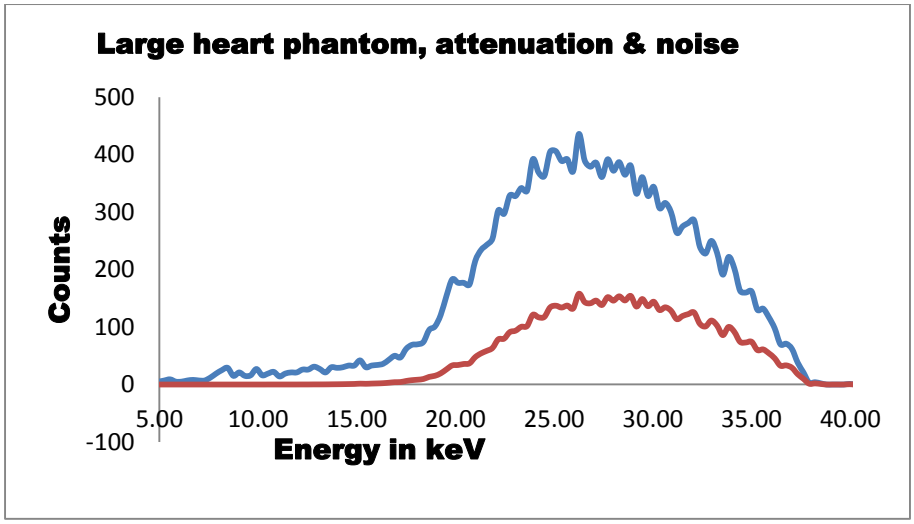

	ADIPOSE	SOFT TISS.	LUNG
Additional tissue thickness in mm	10	50	30

Figure 5.8: Spectral change for an average child (child 2) with extra 10mm, 50mm and 30mm adipose soft tissue and lung tissue respectively, with attenuation correction.

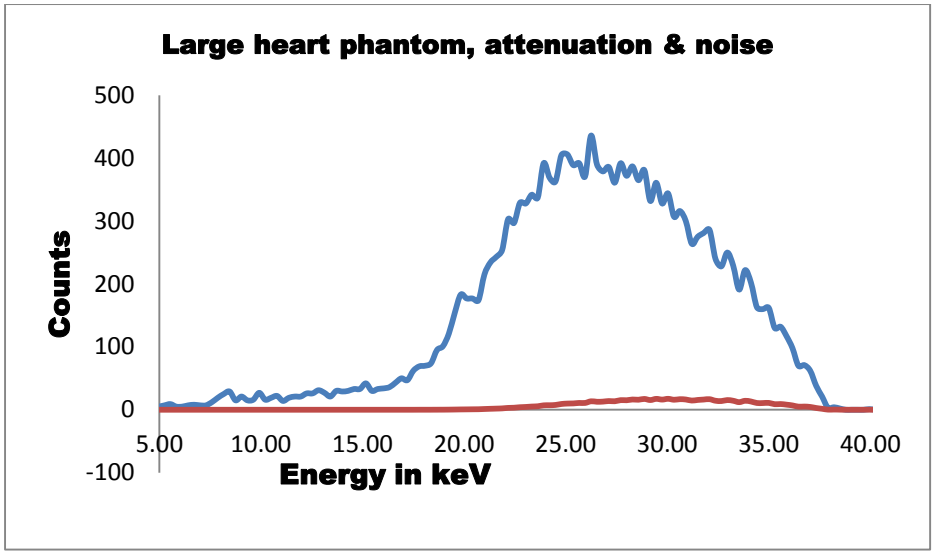

	ADIPOSE	SOFT TISS.	LUNG
Additional tissue thickness in mm	**15**	**50**	**80**

Figure 5.9: Spectral change for a small adult (adult 1) with extra 15mm, 50mm and 80mm adipose, soft tissue and lung tissue respectively in red, with attenuation correction

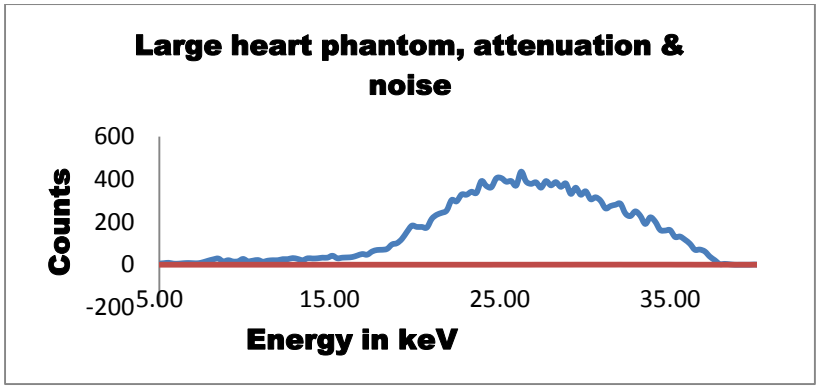

	ADIPOSE	SOFT TISS.	LUNG
Additional tissue thickness in mm	15	80	100

Figure 5.10: Spectral change for an average adult (adult 2) with extra 15mm, 80mm and 100mm, adipose, soft tissue and lung tissue respectively in red, with attenuation correction

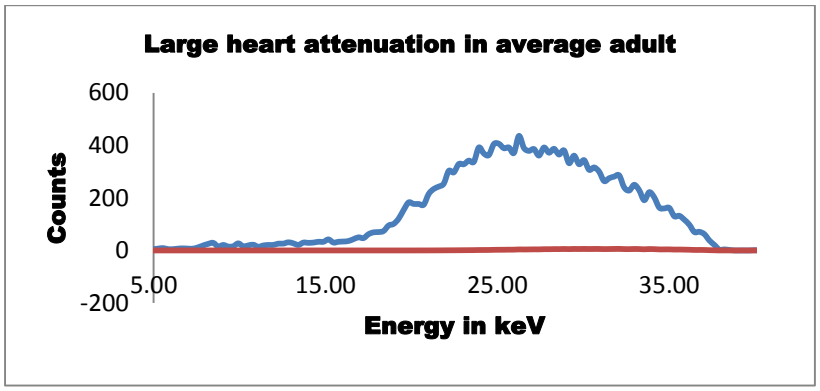

	ADIPOSE	SOFT TISS.	LUNG
Additional tissue thickness in mm	20	100	120

Figure 5.11: Spectral change for a large adult with extra 20cm, 100mm and 120cm adipose, soft tissue and lung tissue respectively in red, with attenuation correction

5.3 Analysis of simulated spectra for large liver tissue

The liver analysis

In the analysis of diffraction data, there are very important parameters of the spectral profile to consider. These include the photon intensity or counts, the spectral shape, the peak or peaks (sharp or broad), peak width and height (amplitude), peak seperation, peak position which depicts the energy or momentum transfer values, quality of the signal and the noise and the integrated counts which gives structural information of the sample. All of these parameters define and characterize the sample(s) under invetigation.

5.3.1 Noise contributions to the diffraction profiles

The diffraction profile from the sample is displayed graphically as intensity against energy or momentum transfer. Momentum transfer is a function of both the energy and scattering angle of the x-ray undergoing coherent scatter. Certain assumptions are made relating to the samples and their scattering. In small sample the scatter is assumed to be less, and more in the bigger sample. Also, along with single Compton scatters, multiple scatter events contributing to the final signal must also be considered. Johns and Cunningham (1983) stated that at 18 keV, photons transfer very little of their energy to the electron during Compton scatter, also that the most likely energy transferred from a 20 keV photon is 0.721 keV and so, the same attenuation coefficients may be assumed for both the first and second scatters in a multiple scatter chain. For a small sample with narrow collimation multiple scatter will be negligible compared to the coherent scatter (Johns and Yaffe, 1983; Owolabi et al, 2005). Therefore, multiple scatter may be considered negligible for this experiment. Endo et al (2001) stated that scattered radiation made a substantial contribution to the noise. However, collimators could improve the signal to noise ratio by decreasing the scattered radiation drastically while keeping the primary radiation at nearly the same level.

5.3.2 Profile analysis of the phantom

The diffraction profiles of the liver phantom were collected at 1mm intervals as the phantom was scanned across the X-ray beam. A total of 31 profiles were collected.

This set of diffraction profiles were subjected to PCA analysis. The residuals, following subtraction of the mean of the diffraction profiles, generated curves that have the same shape but differ in their scales. This is typical behaviour of a two-component (liver and fat), additive system. When PCA models the data, it estimates the shape of the common curve (loading vector) and the multiples of that curve present in each

individual diffraction profile (the scores). This gives useful estimates of the liver –fat contents.

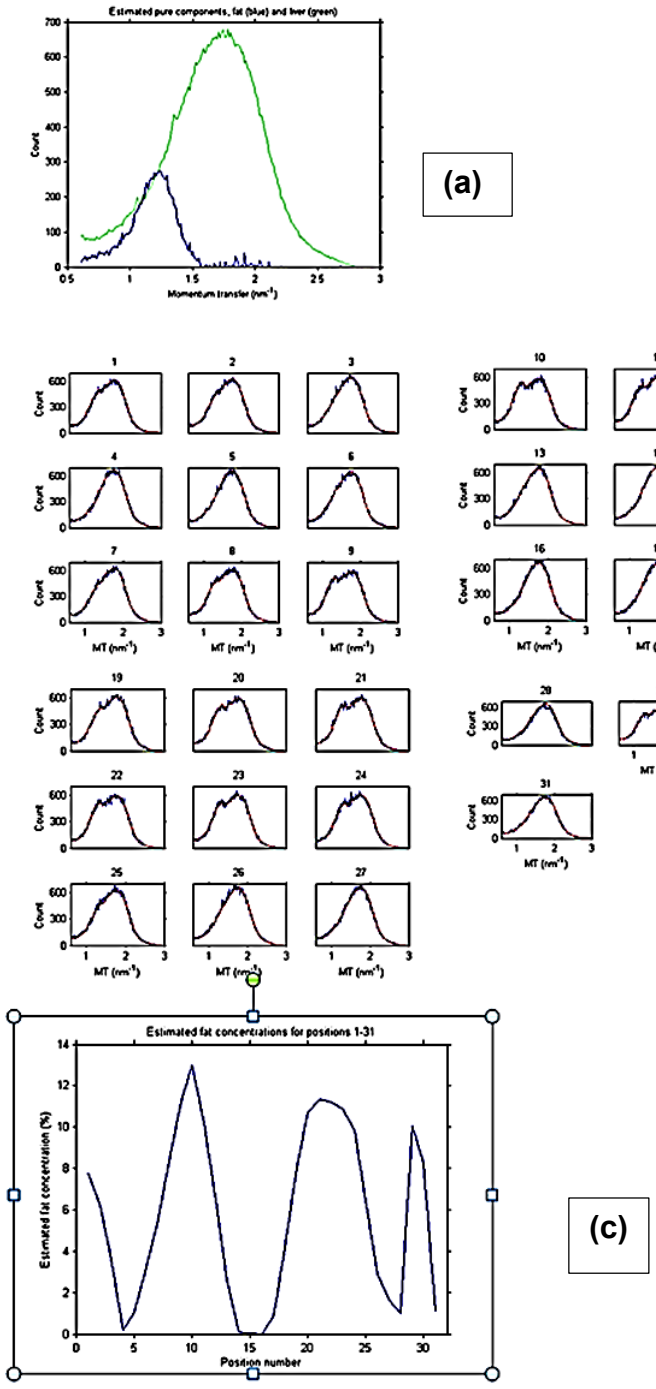

Figure 5.12: Typical output from the liver analysis. (a) is the estimated component spectra, fat in blue and liver in green, see figure 4.13 ; (b) the fitted spectra at each point in the measurement scan and (c) is the estimated fat content at the different positions in the scan, see figure 4.14.

The loading vector and scores were then used to build a model to predict the percentage of fat present at each of the 31 measurement points. The result obtained from these estimations is shown in figure 5.12 above. Figure 5.12a shows the estimated tissue spectra, 5.12b the reconstructed spectra for each measurement point

using the model parameters and 5.12c is the fat content at each measurement point. The fat inclusions of 6, 5 and 4mm are shown as peaks in Figure 5.12c at positions along the x-axis at 10, 22 and 30 respectively. The predicted percentage of fat depends upon the diameter of the insert and the fraction of the scattering volume the insert occupies. For example when fat inclusion is sufficiently large to fully occupy the scattering volume the predicted percentage of fat will be at its largest. When the fat inclusion is smaller so that it only partially occupies the scattering volume the predicted fat signal will be lower. Thus the percentage of fat predicted depends on the amount of fat seen and scanned within the scattering volume created by the collimators. The shapes and widths of the peaks seen in the profile are a convolution of the geometry associated with the fat inclusion and the scattering volume. This genally leads to a 'Gaussian' type profile with a FWHM governed by the size of the fat inclusion for a fixed scattering volume (as is the case in these experiments).

5.3.3 Patient profile analysis

The focus in this chapter is to see whether or not these estimates of fat content could be made in life-sized patients. The diffraction profiles measured with the phantom were used as input to a model that allowed additional tissues to be added as shown in Figure 5.2 and the added noise factors as shown in Table 5.2. For each patient model

(referred to as μ=1, 2, …5 in table 5.2) the diffraction profile set consisting of the 31 profiles was analysed as described in section 5.3

Patient Models (μ)	1	2	3	4	5
Description	Child (1)	Child (2)	adult(1)	adult(2)	Large adult
Adipose tissue thickness added	5mm	10mm	15mm	15mm	20mm
Soft tissue thickness added (includes liver tissue)	30mm	50mm	50mm	80mm	100mm

Table 5.3: The tabulated values of additional tissue thickness (in mm) used for the liver simulations.

Hence the output shown in Figure 5.12c was created for each set of profiles from each patient model. Part (c), hence called the detectability curve, of each set was used to decide if the technique allowed detection of the three peaks seen at positions 12, 22 and 30 and also to see if they are in the correct positions. It was assumed that the 'small child (1) (or μ=1)' set of data with the highest dose demonstrated a clear definition of the three peaks in the correct positions. Hence this response was compared with each of the other sets of data by computing the difference. These

differences are plotted in Figure 5.13, for different sized patients at different radiation doses for the fatty-liver disease problem.

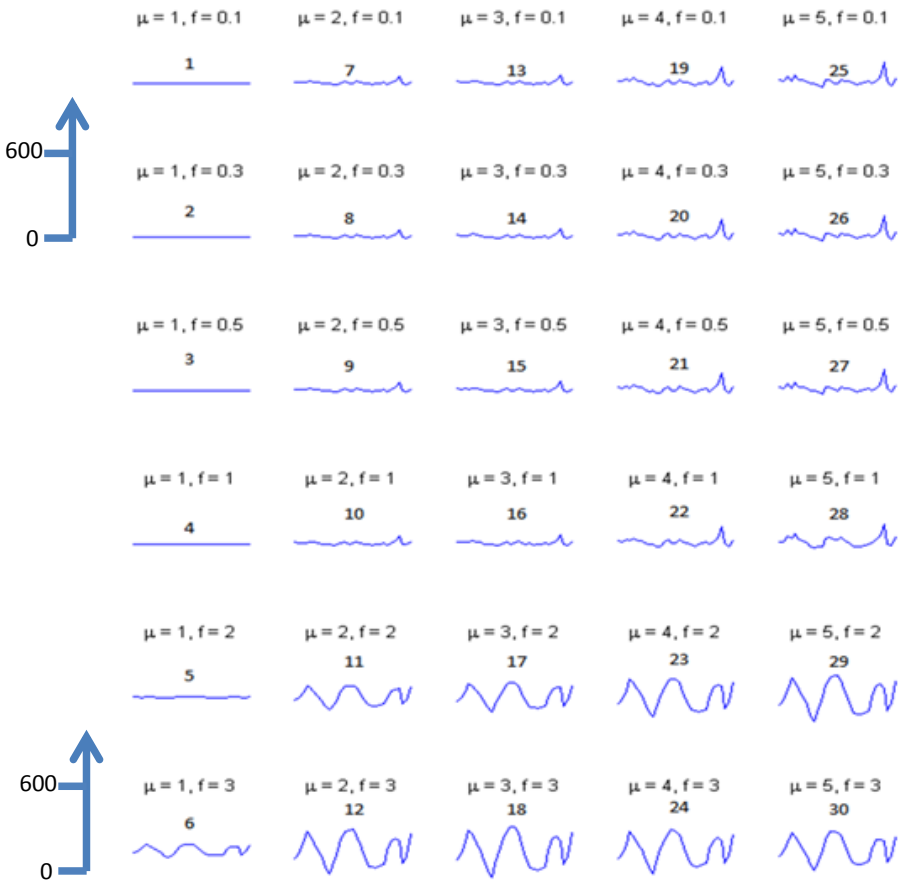

Figure 5.13: Plots (numbered 1-30) of (*Figure 5.12(c), μ, f*) – (*Figure 5.12(c), μ=1, f=0.1*) for 5 different patient sizes (μ = 1→5) and for 6 different noise levels (f=0.1→3). For each plot there are 31 points across the scan. From left to right the patient size increases and from top to bottom the level of noise increases. The axes for each plot are: y-axis = (*Figure 5.12(c), μ, f*) – (*Figure 5.12(c), μ=1, f=0.1*); x-axis = position in scan. Scale bars indicate the magnitude of the differences.

Typical peak values from Figure 5.12 are ~600 counts/s thus the differences can be seen to be ~300 counts/s in the examples in the lower left hand quadrant of Figure 5.13.

5.3.4 Simulating different radiation dose levels

For a given X-ray spectrum the dose to the patient is directly proportional to the number of X-ray photons irradiating the patient. One of the features affecting the

detectability of a feature in a measured diffraction profile is the noise associated with the counts recorded during the irradiation. As the photon count is governed by Poisson statistics the noise will be proportional to the reciprocal of the square root of the number of photons. Thus, for example, increasing the dose to the patient by a factor of 4 will reduce the noise by a factor of 2. Using these ideas different dose levels were simulated by increasing or reducing the noise on a given profile.

The entrance exposure to the small phantom was measured using a Keithly electrometer and ion chamber (see section 5.6). The experimental phantom dose was then used to calculate the dose to larger modelled phantoms of various sizes. To maintain the same statistical quality for any of the larger phantoms the dose used must be increased compared to that used with the small experimental phantom. The increase, or scaling factor has been calculated as the ratio of the detected spectra. Hence,

$$\boldsymbol{D}_{\boldsymbol{phantom}(\boldsymbol{\mu}=\mathbf{1}\rightarrow\mathbf{5})} = \boldsymbol{D}_{\boldsymbol{experi.phantom}} * \frac{\int \boldsymbol{detected\ spectrum\ for\ experi.phantom}}{\int \boldsymbol{computed\ spectrum\ for\ phantom}\ (\boldsymbol{\mu} = \mathbf{1} \rightarrow \mathbf{5})}$$

Where *D* is the entrance dose to the phantom and it is assumed that the same incident spectrum is used in finding the scaling factor.

Alternatively, if the dose is not increased it means less photons will be detected and hence there will be an increase in noise. This effect has been studied by adding noise to the detected spectrum (diffraction profile). Noise has been added assuming a Poisson distribution. Thus the noise for any given channel after computing the effects of attenuation has been calculated by the following steps;

1. Find the counts in any channel, C_i
2. Randomly select the new count (C_n) from a Poisson distribution with mean equal to C_i
3. Compute (C_i - C_n) and use different multiples of this quantity to simulate different doses. Thus *f x* (C_i - C_n) where, f < 1 means the dose has been increased and for *f* > 1 means the dose has been reduced.

The minimum observable feature or signal in a profile is limited by the noise on the signal. The signal-to-noise ratio (SNR) measures the ratio of the signal noise strength relative to the background noise and the visibility of the full signal features. High SNR means greater visibility for the feature. Thus the SNR is improved when the incident intensity is increased, but the maximum allowed dose sets a limit.

A decrease in beam intensity which by implication means a decrease in tube current or tube voltage, reduces the radiation dose but increases the noise.

In the simulation of the 5 patient models (μ = 1 to 5), six (6) different levels of noise (and hence dose) have been used (f = 0.1, 0.3, 0.5, 1, 2, and 3) as shown in Table 5.4.

The issue is to identify acceptable radiation doses needed to achieve detection of the fat nodules.
With a good geometry of an optimized system, low tube current could lead to a substantial reduction in radiation dose and still achieve acceptable quality for the diffraction profile. High radiation dose may not necessarily provide substantially improved profile quality in comparison with moderate, standard or even low radiation dose.

Models (μ)	1	2	3	4	5
Name	Child(1)	Child(2)	Small adult(1)	Small adult(2)	Large adult
Adipose	5mm	10mm	15mm	15mm	20
Soft tissue (includes liver tissue)	30mm	50mm	50mm	80	100
Noise factors (f)	0.1, 0.3, 0.5, 1, 2, & 3	0.1, 0.3, 0.5, 1, 2, & 3	0.1, 0.3, 0.5, 1, 2, & 3	0.1, 0.3, 0.5, 1, 2, & 3	0.1, 0.3, 0.5, 1, 2, & 3

Table 5.4: The tabulated values of the extra tissue thickness (in mm) added to the liver and with the six (6) noise factors, (f = 0.1, 0.3, 0.5, 1, 2, and 3) introduced for the large liver simulations for each of the 5 patient sizes

5.3.5 Detectability of fat nodules in different phantoms

To determine whether or not fat nodules would be detectable in the larger patient sized phantoms the detectability curve (Figure 5.12c) has been plotted in Figure 5.13 for each phantom model (μ=1 to 5) and for different levels of noise (hence dose) as given by the factor *f*. As the smallest phantom when using the highest dose gives the most assured detection of the nodules, all the other conditions (larger phantoms, lower doses) have been compared to the small-phantom, high-dose case. Thus the plots in Figure 5.13 were generated for each phantom and noise condition by subtracting from the resultant detectability curve for a given phantom the equivalent curve for the smallest phantom, i.e., (*Figure 5.12(c), for a given value of μ & f*) – (*Figure 5.12(c), μ=1, f=0.1*).

Thus the subtractions for the Child(1) model with 6 different noise levels are as shown in Table 5.5.

Subtractions of the detectability curves for the Child(1) model	**Profile number in Figure 5.13**
(*Figure 5.12(c), μ=1, f=0.1*) – (*Figure 5.12(c), μ=1, f=0.1*)	**1**
(*Figure 5.12(c), μ=1, f=0.3*) – (*Figure 5.12(c), μ=1, f=0.**1***)	**2**
(*Figure 5.12(c), μ=1, f=0.5*) – (*Figure 5.12(c), μ=1, f=0.**1***)	**3**
(*Figure 5.12(c), μ=1, f=1*) – (*Figure 5.12(c), μ=1, f=0.1*)	**4**
(*Figure 5.12(c), μ=1, f=2*) – (*Figure 5.12(c), μ=1, f=0.1*)	**5**
(*Figure 5.12(c), μ=1, f=3*) – (*Figure 5.12(c), μ=1, f=0.1*)	**6**

Table 5.5: Showing the subtraction configuration of the six (6) variations of Child(1) patient size simulated liver phantom models with the six different noise levels from the small size phantom.

The subtraction configuration of the six variations of Child(1), μ = 1, profile plots are labelled as profile numbers 1-6. The same process was applied to the rest of the four models for (μ = 2 to 5) and noise levels. These are plotted and are labelled as profiles numbers 7-12, 13-18, 19-24 and 25-30 for Child(2), Small adult(1), Small adult(2) and Large adult respectively.

In all 5 patient sizes each has 6 different noise configurations and hence a range of effective doses from 3.2mGys for Child(1) down to 0.32mGys for the large Adult patient.

The top left hand corner of Figure 5.13 is for the smallest sized patient, child(1) with the least of noise and the highest dose. As the resultant curve is a straight and horizontal line it means there are no differences compared to the result in Figure 5.12c which is the small experimental liver phantom. Moving across (patient model horizontal axis) the rows of displayed curves in Figure 5.13, from left to right is moving from a small child patient to a large adult patient (from μ= 1 to μ=5). Also moving vertically down (model noise variation axis) the column of the set of curves the noise factor increases from low level to higher level (**f =** 0.1, 0.3, 0.5, 1, 2, and 3) the dose is reducing (going from an entrance surface dose of (3.2mGy to ~0.32mGy).

In adult and large patients**,** the result demonstrates the existence of large differences in detecting the fat inserts as their locations are incorrectly predicted. However, in the upper left section of Figure 5.13, the small child and small adult region, the curves only show small departures from correctly predicting the location and quantity of fat nodules.

Figure 5.14 has been sectioned into three regions. Region A (curves 1-5, 7-10 and 13-16) is where detection of the fat nodules is deemed to be successful. Region B (curves 19-22, 25-27) demonstrates some success in finding the fat nodules except for the smallest sized insert. Total absence of detection is in region C (curves 6, 11, 12, 17, 18, 23, 24 and 30) where nodules are found in incorrect locations.

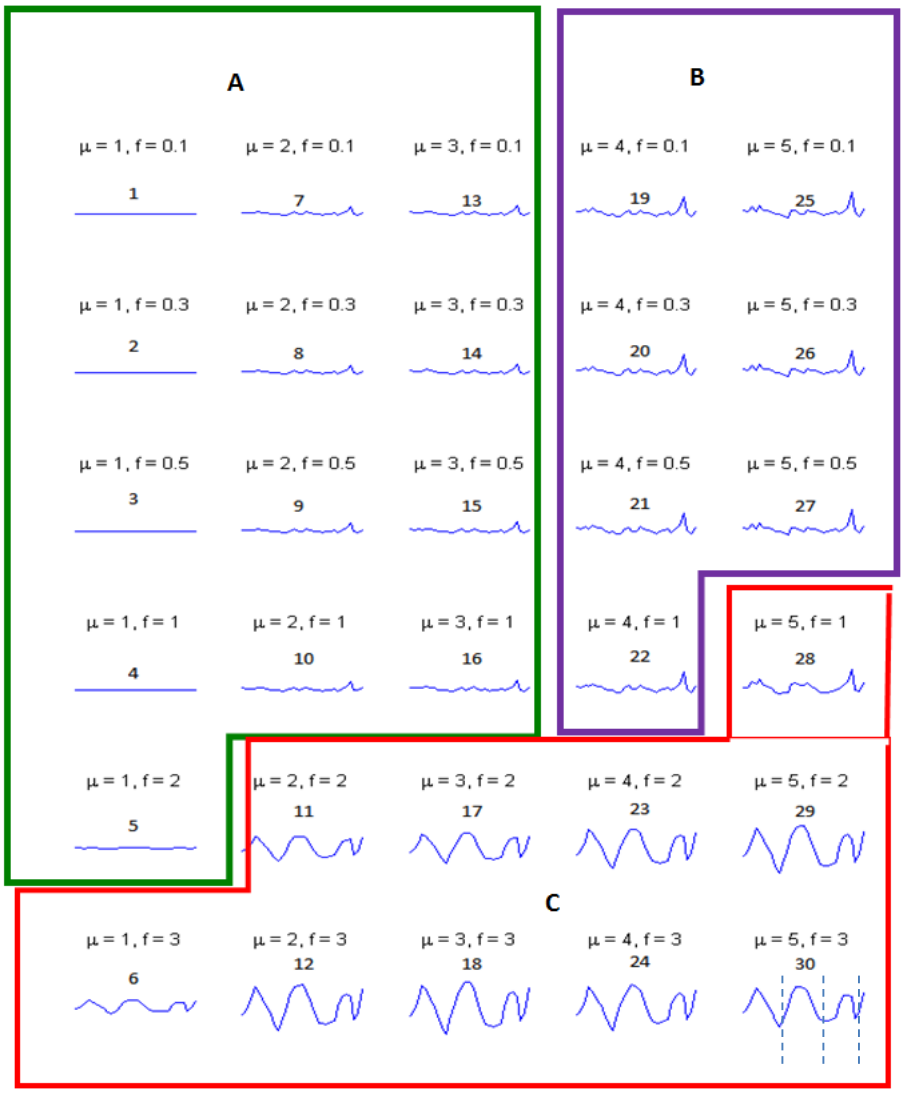

Figure 5.14: Detectability in liver phantoms (patient sized). Profiles within the green colour boundary are detectable and are classified as category A, Those within the purple colour boundary can be fairly detected and fall under category B, while those within the red colour boundary cannot be detected and classified under category C. Expected positions for peaks in the profile are shown for profile 30.

5.4 Scanned Heart Analysis

These spectra were passed through the same analysis package as described in section 4.2. Also the same procedures and analytical processes used on the liver (as described in section 5.3 and its sub-sections) were applied to the heart analysis. For each clinical problem a total of 30 spectra (numbered 1-30) were simulated under the five (5) different patient models, μ(1) to μ(5). Each patient model has also six (6)

different levels of noise, from f(0.1) to f(3), added to the thicknesses as shown in Table 5.6.

5.4.1 Noise contribution

As discussed in sub-section 5.3.1, in a small sample with narrow collimation multiple scatter will be negligible compared to the coherent scatter. The heart sample has increased tissue area than the liver which implied more multiple scatter and noise which may not be considered negligible. Again, considering Endo et al (2001) who stated that scattered radiation made a substantial contribution to the noise. Although as said before, collimators could improve the signal to noise ratio by decreasing the scattered radiation drastically while keeping the primary radiation at nearly the same level, but in the heart noise contribution affected the result more than as seen with the liver.

5.4.2 Profile analysis of the heart phantom

The diffraction profiles of the heart were subjected to PCA analysis as described in sections 4.2.2 and 4.2.3. The analysis used 54 spectra, 50 from the three experiments with the heart phantom with 0, 2 and 3mm fat in the “blood vessel” and 4 extra ones from the 100sec measurements (in the experiment where a range of measuring times were used) on heart phantom with 0, 2, 4, 6mm fat. The extra 4 spectra should fitted into the general pattern of the rest, and indeed should give valuable calibration information, since they include a wider range of fat quantities. The four spectra were made comparable with the others, by dividing the counts obtained from them by 2, to convert the100 sec count to one for 50 sec.

The scores and loading plots for a PCA of these 54 spectra are shown in figures 4.21 and 2. The two principal components shown explain 98.7% of the total variation in the spectra (PC1 97.6%, PC2 1.1%), while the next one (the third) explains only 0.2% with loadings that appear very noisy. After PC1 and PC2 the loadings were down to a noise level in the experiments.

The loading vector and scores were then used to build a model to predict the percentage of fat present at each of the 54 measurement points. The result obtained from these estimations is shown in figure 5.15. Figure 5.12a shows the estimated tissue spectra, 5.12b the reconstructed spectra for each measurement point using the model parameters and 5.12c is the fat content at each measurement point.. The fat inclusions of 6, 5 and 4mm are shown as peaks in Figure 5.12c at positions along the x-axis at 10, 22 and 30 respectively.

5.4.3 Patient profile analysis

The diffraction profiles measured with the phantom were used as input to a model that allowed additional tissues to be added as shown in Figure 5.2 and Table 5.2. For each patient model (referred to as μ=1, 2, …5 in table 5.2) the diffraction profile set consisting of the 31 profiles was analysed as described in sections 5.3 for liver and in 5.4 for the heart.

Hence the output shown in Figure 5.15 was created for each set of profiles from each patient model, hence called the detectability curve used to check if they are in the correct positions. It was assumed that the ‘small child (1) (or μ=1)’ set of data with the highest dose demonstrated a clear definition of the 50 peaks in the correct positions. Hence this response was compared with each of the other sets of data by computing the difference. These differences are plotted in Figure 5.16, for different sized patients at different radiation doses for the heart disease problem.

5.4.4 Simulating different radiation dose levels

The process of simulation for different radiation dose levels for the heart models was the same as in section 5.3.4 for the liver. The dose levels was the same as with the heart. The acceptable radiation doses needed to achieve detection of the plaques in the blood vessels of the heart was also found to be 3.2mGy for Child(1) and reduces as with increase in the patient size and the noise with the minimum for the Large adult as shown in Tables 5.6 (specifications) and 5.10.

Models (μ)	1	2	3	4	5
Model Description	**Child(1)**	**Child(2)**	**Small adult(1)**	**Small adult(2)**	**Large adult**
	Heart simulation				
Adipose	5mm	10mm	15mm	15mm	20mm
Soft tissue	30mm	50mm	50mm	80mm	100mm
Lung	30mm	30mm	80mm	100mm	120mm
Noise factor (f) addition	0.1, 0.3, 0.5, 1, 2, & 3	0.1, 0.3, 0.5, 1, 2, & 3	0.1, 0.3, 0.5, 1, 2, & 3	0.1, 0.3, 0.5, 1, 2, & 3	0.1, 0.3, 0.5, 1, 2, & 3

Table 5.6: The tabulated values of the extra tissue thickness (in mm) added to the heart and with the six (6) noise factors, (f = 0.1, 0.3, 0.5, 1, 2, and 3) introduced for the patient sized simulations for each of the 5 patient sizes.

5.4.5 Detectability of fat (plaques) in the blood vessel of the heart

Figure 5.15 is a typical detectability curve for the heart phantom. This example applies to the child(1) model. As for the liver analysis the detectability curves for all the heart models were evaluated by looking at the difference between the result for a given model and that derived from the smallest, highest dose example. The results of this comparison are shown in figures 5.16.

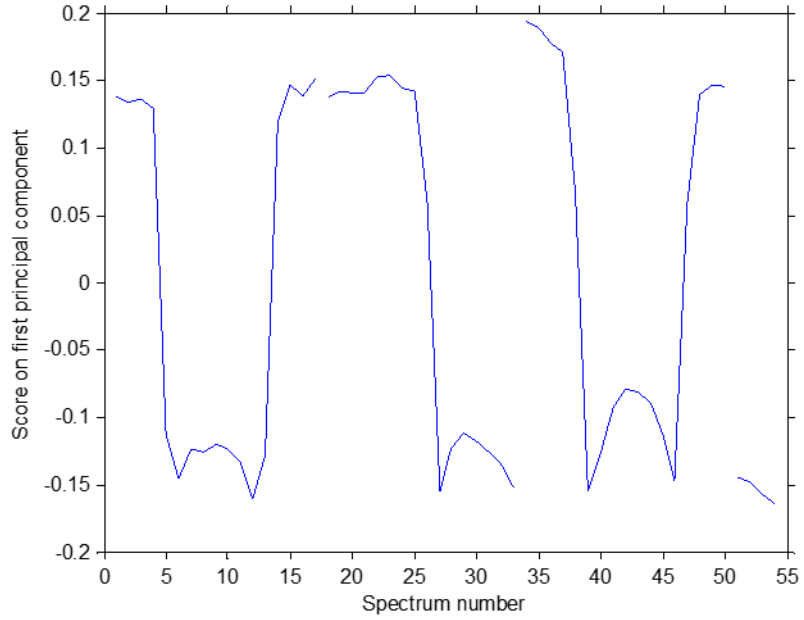

Figure 5.15. Scores on PC1 for the 54 spectra (50 from 0mm, 2mm and 3mm and 4 from 0mm, 1mm, 4mm and 6mm) on the analysis and 4 spectra from the 4 sequences are obtained i.e. 3 (from 0mm, 2mm, 3mm fat insert experiment) and 1 (from 0mm, 2mm, 4mm and 6mm fat insert experiment) reading from left to right. This Figure 5.15 is the heart equivalent of Figure 5.12(c) in liver analysis.

Subtractions of the detectability curves for the Child(1) model	Profile number in Figure 5.16
(Figure 5.15, μ=1, f=0.1) - (Figure 5.15, μ=1, f=0.1)	*1*
(Figure 5.15, μ=1, f=0.3) - (Figure 5.15, μ=1, f=0.1)	*2*
(Figure 5.15, μ=1, f=0.5) - (Figure 5.15, μ=1, f=0.1)	*3*
(Figure 5.15, μ=1, f=1) - (Figure 5.15, μ=1, f=0.1)	*4*
(Figure 5.15, μ=1, f=2) - (Figure 5.15, μ=1, f=0.1)	*5*
(Figure 5.15, μ=1, f=3) - (Figure 5.15, μ=1, f=0.1)	*6*

Table 5.7: Showing the subtraction configuration of the six (6) variations of Child(1) patient size simulated heart phantom models with the six different noise levels from the small size phantom.

The process of the subtraction configuration of the six (6) variations of Child(1) patient size simulated heart phantom models with the six different noise levels from the small size phantom for detectability is shown as tabulated in Table 5.7. The same process applied to the entire patient configurations (all patient models) with the added thicknesses and noise as shown in Table 5.6.

Scanned Heart Analysis: Resultant curves from subtractions

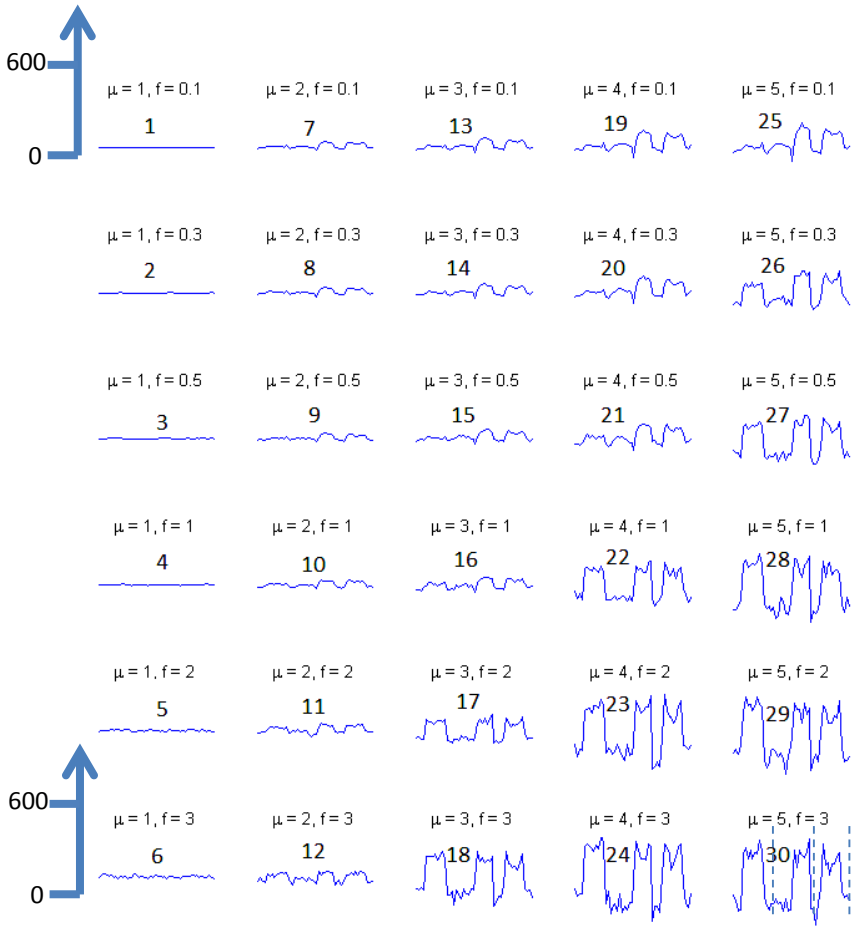

Figure 5.16: The heart equivalent plot to Figure 5.13 for liver. The heart models plot. Plots (numbered 1-30) of (Figure 5.15 μ, f) – (Figure 5.15 μ=1, f=0.1) for 5 different patient sizes (μ = 1→5) and for 6 different noise levels (f=0.1→3). For each plot there are 50 points across the scan. From left to right the patient size increases and from top to bottom the level of noise increases. The axes for each plot are: y-axis = (Figure 5.15 μ, f) – (Figure 5.15 μ=1 to 5, f=0.1 to 3); x-axis = position in scan. Scale bars indicate the magnitude of the differences and dotted lines indicate the expected positions of the peaks in profile 30.

For each plot the individual scans of a phantom have been placed next to each other to form a plot of 50 points across the scan as in Figures 5.15 and 5 16. From left to right the patient size increases and from top to bottom the level of noise increases. Detectability of the fat nodule in the blood system of the heart appeared to be greatly reduced as shown in Figure 5.17.Detectability of all the configurations of Child(1) is good. Reduction in detectability is noticed from Average Child. In small adult and large patients, the result in the heart also demonstrates the existence of large differences in detecting the fat inserts as their locations are most probably incorrectly predicted. In the left section, of Figure 5.17, the small child and small adult region, the curves only show small departures from predicting correctly. The results suggest that in small child and Average child as shown in Figure 5.17, reasonable and useful estimates of fat content could be made. In small size patients, Child(1) and part of Average child belong to category A (10 in number i.e.33%) detection group (with resultant straight and horizontal line and fairly straight lines, numbered, 1-10). Detection in this category is good. as signal to noise ratio (SNR) is high from 1-5 and reduces from 6-10. A fairly detection is possible with category B (17% and numbered, 11, 13-16) and total absence of detection with category C (a total of 15 i.e. 50% and numbered, 6, 11-12, 17 -18 and 19-30). In all there is a detectability of 50%.

Detectability of the fat nodule in the blood system of the heart

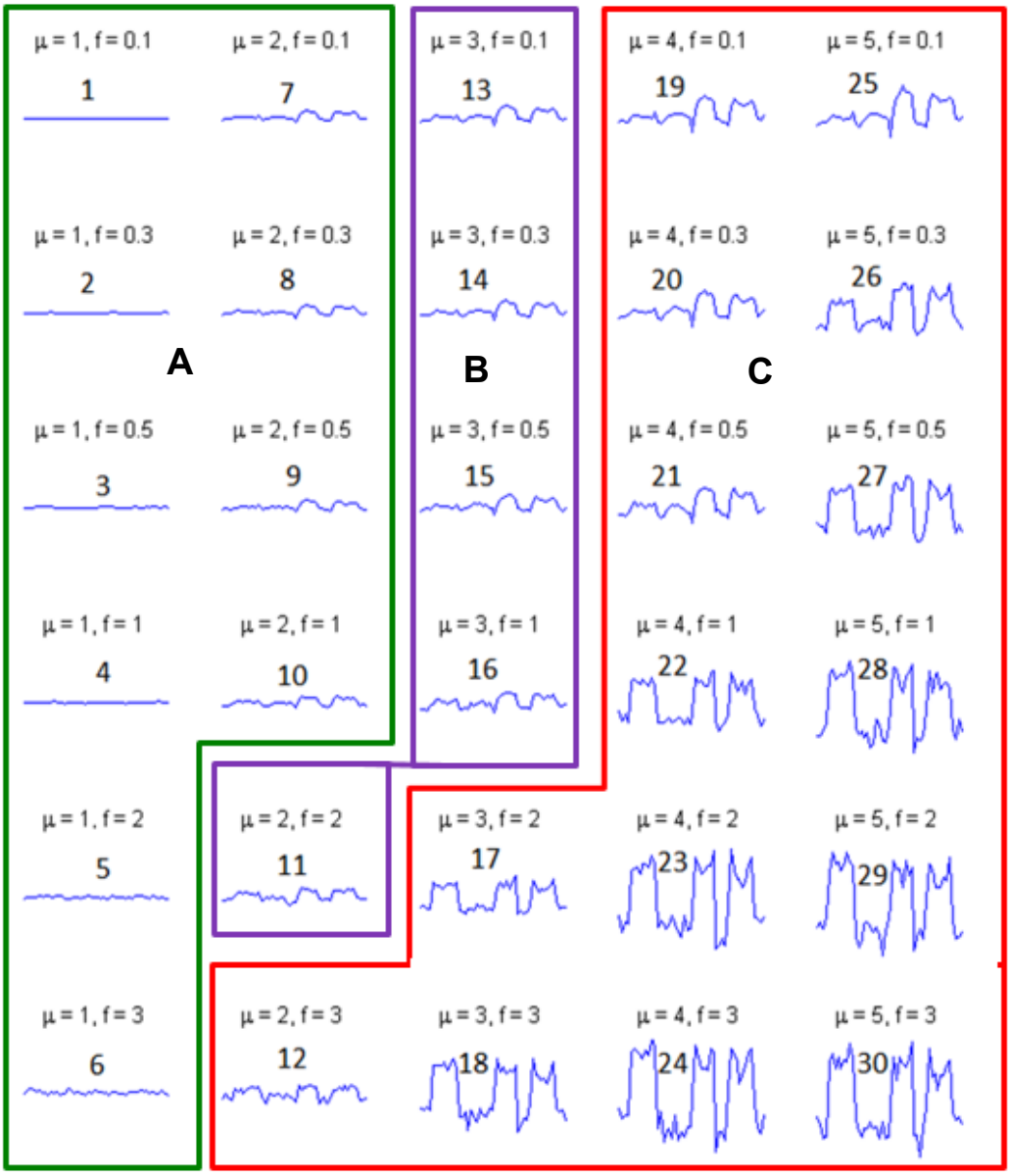

Figure 5.17: Heart detectability (equivalent of Figure 5.13 of liver). Detectability in large heart phantoms (patient sizes). Profiles bounded by the green colour belong to category A, category B, purple and category C, red

5.5 Discussion on simulated spectra analysis

5.5.1 Scanned Fatty-liver analysis

The data that was analysed was derived from scans of the small phantom described in section 3.5.1 and with the analysis in sections 4.2.3. The general effects of increasing the size of the object was to reduce the number of recorded events and to change the spectral shape due to preferential filtering of low energy photons. It would be expected that if increasing the size had no effect upon the analysis technique described in section 4.2.1 the detectability of the fat nodules within the phantom scan would not change. This would mean that the curves in Figure 5.13 would all be straight, horizontal lines. Deviations from this condition indicate that fat nodules are being missed or found in the wrong places, i.e., detectability is being lost.

Looking at Figure 5.13 it can be seen that the curves become less straight as one moves from the top right hand corner to the lower left hand corner, i.e., moving from small object with low noise to large object with more noise conditions. For any given noise condition the detectability degrades as larger objects are scanned. For any given sized object, i.e., a fixed value of μ, the effect of changing the noise factor from 0.1 to 1.0 has little effect on detectability.

However, changes in *f* from 1.0 to 3.0 show significant changes and any combination of $\mu > 1$ and $f > 1$ demonstrate that the analysis has broken down. In these cases the high noise level on low recorded counts means that the spectra related to pure components (cf Figure 5.12(a)) cannot be successfully extracted leading to features being ‘created’ where they do not exist.

However, the geometry of an EDXRD system decides the resolution of the spectral peaks obtained from it. The UCL system was successfully set up for small sized phantoms with the research outcomes validated by Kumari-Maini, 2012. Also, Fenster and Trout (2013) affirmed that such a high-resolution system with a pencil or small size beam gives reliable diffraction results. The UCL system has a reliable detection capability, which can be applied to a larger object. Consequently, the systems evaluation factors, the peak shapes, peak position, peak width, intensity values of the diffraction peaks, photon counts are taken to be accurate. The variability of the intensity depends on the experimental procedure and on the size of the object.

Intensity is small for small size objects and increases with increase in the object size as in Figure 5.12c. This is true under the same operating conditions

Fat detection is confirmed by an established peak position at a momentum transfer value of about 1.1 nm^{-1} (from 0.9 -1.1nm^{-1}) in a spectral plot of intensity against momentum transfer. This value is for pure fat. The amount can be assessed by the value of the peak width. Therefore any presence of fat may not be in doubt. The presence of noise only degrades the peak quality. The noise in the peaks can be filtered for better spectral output.

In absence of fat the peak seen will be that of the object in the diffraction system. Example, if liver only is the sample, the spectrum will have abroad peak for liver which is distinct to it, while fatty-liver has two peaks, one for fat at about 1.1nm^{-1} and the other for liver at about 1.3/1.4nm^{-1} or more depending on the quality of the liver.

Therefore, fat nodules of known values of thicknesses 6mm, 5mm and 4mm were inserted in the liver phantom and the magnitude of the plots and peaks obtained as shown in Figure 5.12(c) are indicative of the presence and correct values of the inserts except for the insert number with a smaller narrow peak. The output of the third peak does not reflect the size as expected. This anomaly could be due to wrong placement in the scattering volume, resulting in partial volume effect.

It is also important to note that peak positions of various test samples are compared with the standard Joint Committee on Powder Diffraction Standards (JCPDS) spectrum and particularly the fat and the caffeine samples used throughout this investigation and found to be in agreement with those of JCPDS. Also, every sample including fat has a diffraction signature (specific peak position, and the corresponding momentum transfer value) unique to it that identifies it. The intensity and the peak width depends on the X-ray tube potential and the amount of the fat within the scattering volume.

.

5.5.2 Scanned heart disease analysis

The analytical process for the heart was similar to that of the liver. The scanned heart data that was analysed was derived from scans of the small heart phantom described in section 3.5.1 and sections 4.2.3. The increase in heart size or its life-size involved the addition of the extra adipose tissue, the soft tissue and the lung and these largely contributed to drastic reduction in the number of recorded events and the change in the spectral shape due to preferential filtering of low energy photons.

5.5.3 Discussion on the scanned heart analysis

Similar to the liver analysis, the data that was analysed was derived from scans of the small heart phantom described in section 3.6 with the analysis technique in section 4.2.3. Also, the general effects in the liver analysis applied to the heart.

As with the liver tissue, it would be expected that if increasing the size had no effect upon the analysis technique described in section 4.2.3, knowing that more tissues are involved in the heart investigation, the detectability of the plaques within the heart phantom scan would not change. This would also mean that the curves in Figure 5.14 would all be straight and horizontal lines. Deviations from this condition indicate that plaques are being missed or found in the wrong places, i.e., detectability is being lost. Looking at Figure 5.14, it can be seen that:

- The curves, numbered 1 to 6 under Child(1) at all levels of noise, are straight and horizontal signifying detection
- The curves numbered 7 to 10 under Child(2) at level of noise from f=0.1 to 1.0 are less straight and horizontal thus signifying a a reduced level of detection
- The curves numbered 11, 12 to 16 under Child(2) at higher level of noise f=2 to 3 and Small Adult(1) at low level of noise f=0.1 to f=1 are losing the straight line character signifying low detection or detection in the wrong location.
- The curves numbered 17 to 30 under Average Adult and Large Adult at all level of noise indicate detection at the wrong locations.
- Thus the outputs become less straight, moving from small object with low noise to large object with more noise conditions, in ascending order of noise and attenuation.

- For any given noise condition the detectability, reduces and the spectrum degrades as larger objects are scanned. It can be seen that for f = 0.1 moving from μ = 1 to μ = 5 features, i.e., even the smallest diameter of plaques, useful information are lost from the scan.
- This shows up as large positive peaks appearing in the right hand side of the resultant spectral subtraction output

5.5.4 Discussion on Detectability

In figures 5.14 and 5.17, the summary of the detectability of fat nodules in the liver and the plaques in the blood vessels of the heart and its translation to real-life patient can be made therefrom. Generally, as already mentioned in section 5.4.3, the horizontal or near horizontal lines in the above figures can be summarized to indicate detectability and the shapes outside that description indicate non-detectability

Therefore, in both scanned liver and heart, detectability of the fat inserts has been categorized in three groups. Group A, as fully seen/detected, that is, being a straight and horizontal line; Group B, mostly or moderately detected, that is, being both nearly straight and horizontal line and Group C, not seen /detected, that is, neither straight nor horizontal. This classification has been undertaken by visual inspection of the difference profiles.

In the liver scans, it can be seen that category A has 13 plots, B has 7 and category C has 10. This means that in liver, 20 out of the 30 conditions are detectable, that is approximately 67% detectability. The heart scan has 10 plots (33%) in category A. Category B has 5 plots (20%) and Category C, has 14. This means that in heart, 15 out of the 30 patient conditions are detectable, that is approximately 50% detectability. A table of this summary is on Table 5.8

For any given sized object, i.e., a fixed value of patient model, μ, the effect of changing the noise factor from 0.1 to 1.0 has little effect on detectability. However, changes in f from 1.0 to 3.0 show significant changes and any combination of $\mu > 1$ and $f > 1$ demonstrate that the analysis has broken down. In these cases the high noise level on low recorded counts means that the spectra related to pure components (cf Figure

5.12(a)) and cannot be successfully extracted leading to features being ‘created’, as with the liver, where they are absent.

Liver	Category A (Detectable)	Category B (Mostly detectable)	Category C (Not detectable)
	13 profiles: **u=1,f=0.1; u=1,f=0.3; u=1,f=0.5 u=1,f=1; u=1,f=2;** **u=2,f=0.1; u=2,f=0.3; u=2,f=0.5; u=2, f=1** **u=3, f=0.1; u=3,f=0.3 ; u=3,f=0.5 ; u=3,f=1**	**7 profiles:** **u=4,f=0.1; u=4,f=0.3 u=4,f=0.5; u=4,f=1** **u=5,f=0.1 ; u=5,f=0.3; u=5,f=0.5**	**10 profiles:** **u=1,f=3;** **u=2,f=2; u=2,f=3; u=3,f=2; u=3, f=3; u=4,f=2;u=4,f=3; u=5,f=1; u=5,f=2; , and u=5,f=3**
Heart	**10 profiles:** **u=1,f=0.1; u=1,f=0.3; u=1,f=0.5 u=1,f=1; u=1,f=2;u=1,f=3** **u=2,f=0.1; u=2,f=0.3; u=2,f=0.5; u=2,f=1;**	**5 profiles:** **u=3, f=0.1; u=3,f=0.3;** **u=3,f=0.5;** **u=3, f=1;** **u=3, f=2**	**15 profiles:** **u =2, f=3;** **u =3,f=2; u =3, f=3; u =4, f=0.1; u=4,f=03; u=4,f=0.5;u=4,f=1; u=4,f=2 ; u =4, f=3 f=0.1; u =4, f=0.1** **u=5, f=0.1; u=5,f=0.3;** **u=5,f=0.5;** **u=5, f=1; u=5, f=2;** **u=5, f=3**

Table 5.8: The table of summary of detectability in large liver and heart patient s models

5.6 Radiation dose measurements

5.6.1 Introduction

The small sized anthropomorphic phantoms used in the experiment were all irradiated and the larger size may relatively absorb higher dose than the small one. Dose is the concentration of energy deposited in the phantom or tissue as a result of an exposure to ionizing radiation, that is the energy absorbed by the phantom or tissue. Increase in dose as well as increase in number of photons will lead to decrease in noise. Low noise or absence of noise is good and ideal but there can be noise which can be filtered out or smoothened. The dose defines the energy deposited per unit mass. The total energy deposited depends on the number of photons, (the photon counts). It is therefore important to know the amount of dose given to the small phantom to ensure that radiation is kept within acceptable limits and as low as reasonably achievable or possible. The dose given to the small phantom can be used to estimate the dose to the simulated larger phantoms of various sizes.

5.6.2 Dose measurement and calculation

The calculation or estimation of the dose for both the fatty liver and heart was done based on the X-ray parameters used to generate the data from the small phantoms. These were tube potential 70 kV, tube current of 2 mA and using a 15cc ion chamber. The measured dose rate was 66.5µGy/sec. However, the X-ray beam diameter at the chamber was estimated to be 2mm diameter whilst the sensitive area of the ion chamber was 1256.64 mm^2. Thus correcting this reading for the area exposed gives the actual dose value as, 83.6mGy/s. To estimate the dose for the large phantoms several steps were considered:

The large phantoms filter out most low energy photons. It was estimated that the effect would be the same as including a 2.5mm Al filter in the beam. Hence dose measurements were repeated with this level of filtration. The dose, when corrected for the area exposed, with the filter present becomes 3.2 mGy/s.

To check that this value did not depend upon the point of measurement in the chamber, profiles of chamber response were measured as shown in Figure 5.18, with 0mm aluminium and with 2.5mm aluminium in figure 5.19.

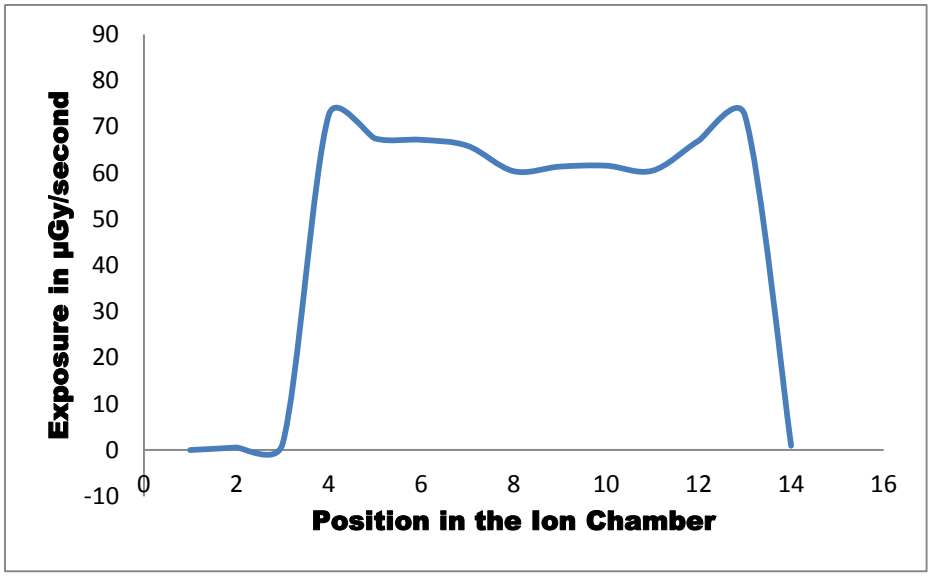

Figure 5.18: A plot of exposure with no filtration against positions in the ion chamber

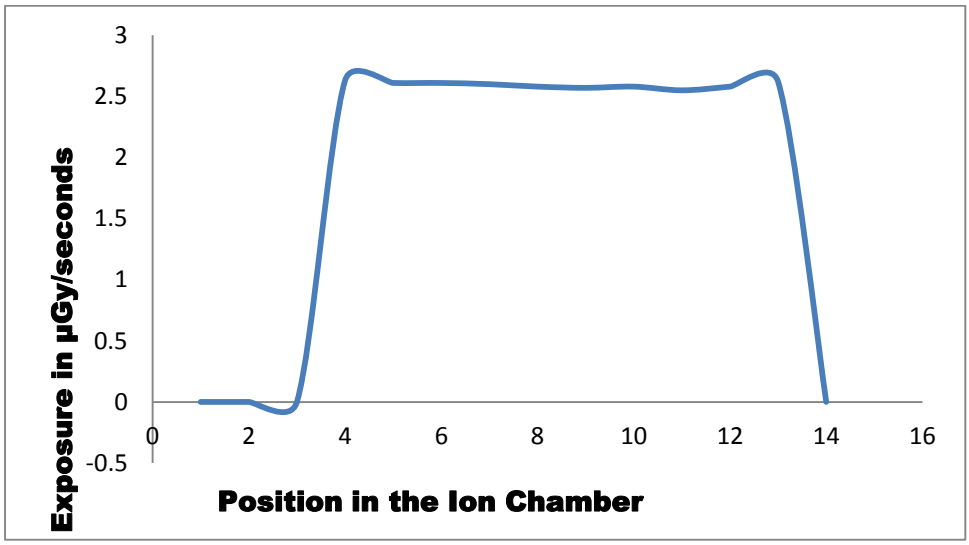

Figure 5.19: A plot of exposure with extra aluminum (2.5mm) filtration against positions in the ion chamber

Clearly the response is reasonably uniform over the chamber area and the estimate of 3.2 mGy/s can be regarded as the dose required for the small phantom experiments.

To consider the large phantoms the integrated counts from the small and large phantom need to be compared. Consider the following example. If the small phantom dose of 3.2 mGy/s gives an integrated count of 'X'. To obtain that statistical quality with the large phantoms means that the ratio of small phantom counts 'X' to large phantom counts, say 'Y' must be used to increase the small phantom dose.

Thus the dose required is obtained by the relation, $\frac{X}{Y}\ x\ 3.2$ mGy/s.

$$\frac{\textbf{integrated count of the small phantom}}{\textbf{integrated count of the patient model}} \text{ x } 3.2 \text{ mGy/s} \qquad \text{.....5.2}$$

With noise factor added the relation below evaluates the dose.

This value is obtained by multiplying the result of equation 5.2 by the inverse square root of the noise factor as in equation 5.3

$$\frac{\textbf{integrated count of the small phantom}}{\textbf{integrated count of the patient model}} \text{ x } 3.2\ \frac{1}{\sqrt{\textbf{Noisefactor}}}\ \text{mGy/s} \qquad \text{.....} \quad 5.3$$

This procedure has been used to calculate the estimated dose for the different phantoms in table 5.9

S/No	Position (number setting on the monitor)	X-ray Exposure (at 70kVp, 2mA) µGy/sec	
		Without extra filter	With 2.5mm thick Aluminum filter
1	9.50	1.3	0
2	10.00	72.6	2.63
3	10.25	67.5	2.61
4	10.50	67.2	2.61
5	11.00	65.9	2.6
6	11.25	60.4	2.58
7	11.5	61.4	2.57
8	12	61.6	2.58
9	12.5	60.5	2.55
10	13	67	2.58
11	13.5	72.5	2.62
12	14	0.93	0

Table 5.9: Table of X-ray exposure without extra filtration and with extra 2.5mm aluminum filtration

The corrected reading is obtained as the ratio of the large chamber over the small area of the aperture multiplied by the measured exposure value.

5.7 The photon counts or flux effect on detection

The change in counts affects the details and the information generated from the phantoms, small or large. It is therefore relevant to evaluate the number of photons or the flux for each model and see how they affect each of the patient models. Table 5.10, has all the details including the integrated counts for both the small and the large phantoms. The heart under the applicable operating parameters had integrated counts of 630,919 photon counts. At this level the fat inserts in the small phantom were

detected. With the 5 different models, representing life-size patients, the number of counts plummeted from 630,919 output count obtained without further increase in the small phantom thickness to 49,797 a reduction of 92% for child(1). The reduction continued as the models got bigger. This resulted in percentage reduction of 97.5, 99, 99.8 and 99.96 respectively, in the number of photons for the remaining 4 models. The implications is that the same number of counts lost or more (or the same percentage of reduction as shown above or more, will be required for the inserted to be detected, that is a minimum of 581,122, 615,480, 624,855, 629,852 and 630,645 photon counts required for detection to be achieved.

The number of photons required is the difference between the integrated number of counts in the main spectrum and the spectrum of the patient models.

Example, for child (1): Heart; 630,919 – 49797 = 581,122

Liver; 2,008,152 – 436,218 = 1,571,934 (see table 5.5).

The same explanation applied to the liver, whose photon reduction was 78% for Child (1), 89, 90, 96 and 98 for the 4 remaining models, with the associated photon requirements of the same percentage with numerical values of, 1,571,934, 1,794,025, 1,809,017, 1,927,380 and 1,962,497 respectively.Taken into account the noise factors, f, the exposures were reduced to the values (in percentage and actual number of photons) as shown in table 5.5, and also showing the values for f = 2 and f =3 noise factors.

Models (μ)	1	2	3	4	5
Model Description	Child(1) – Small	Child(2) – Average	Small adult(1)-	Small adult(2)- Average	Large adult
	Heart simulation @40kVp, 2mA				
Adipose	5mm	10mm	15mm	15mm	20mm
Soft tissue	30mm	50mm	50mm	80mm	100mm
Lung	30mm	30mm	80mm	100mm	120mm
Small heart phantom	630,919: Photon count small heart phantom				
Integrated counts	49,797	15,439	6,064	1,067	274
Reqd.no. of photons	581,122	615,480	624,855	629,852	630,645

Percentage reduction	92	97.5	99	99.8	99.96
Exposure calculated	3.2 mGy/s (rate of exposure for the small liver phantom)				
Exposure large heart model (mGy/s)	16.2@(f=2) 23.5@(f=3)	91.6@(f=2) 75.9@(f=3)	233@(f=2) 193.1@(f=3)	1324.5@(f=2) 1097.5@(f=3)	5157.9@(f=2) 4274@(f=3)
Exposure Reqd. (mGy)	40.5	130.8	332.9	1892.2	7368.4
Liver simulation @ 70kVp, 6mA					
Model Description	Child(1) – liver	Child(2)- liver	Small adult(1)-liver	Small adult(2)-liver	Large adult-liver
Adipose	5mm	10mm	15mm	15mm	20
Soft tissue (includes liver tissue)	30mm	50mm	50mm	80	100
lung	0	0	0	0	0
Small liver phantom	2,008,152 photon counts for small liver phantom				
Int. counts	436,218	214,127	199,134	80,772	45,665
Reqd. no. of photons	1,571,934	1,794,025	1,809,017	1,927,380	1,962,497
Percentage reduction	78	89	90	96	98
Exposure calculated	3.2 mGy/s (rate of exposure for the small heart phantom)				
Exposure large liver model (mGy/s)	10.3 @ f=2 8.5 @ f=3	21 @ f=2 17.4 @ f=3	22.6 @ f=2 18.7 @ f=3	55.7 @ f=2 46.2 @ f=3	98.5 @ f=2 81.6 @ f=3
Exposure Reqd.(Dose)	14.7	30	32.3	79.6	140.7

Table 5.10: Estimates of exposure required dose for detection and the dose with noise factor (f=2 and f=3) added to the patients for various patient models for both heart and liver tissues.

5.8 Parameters that affect dose

The parameters that affect radiation dose include in general, the generator type, exposure (a measure of the charge produced in air by gamma and x-rays), the beam, tube current, the tube voltage (which gives the energy imparted per unit mass of matter by ionization and excitation caused by ionizing radiation), collimation and patient size (McNitt-Gray, 2002). In addition to the parameters already mentioned, the radiation quality factor, multiple scatter, radioactivity, filter-type and its thickness, exposure time and the distances of sample or object from the source and detector involved also affect dose. All these are the major factors of consideration in estimating noise and dose accurately and were taken into account in the simulation and in dose estimation for accuracy and reliability of results.

Multiple scatter by its very nature arises in several uncorrelated scatter interactions and degrades spectrum. The patient size, beam size and the distances from source are amenable to multiple scatter. Tartari et al (1996) in their investigation of spatially resolved photon scattering applications showed that multiple Compton (incoherent) scatter rapidly decreases the photon energy, though, the high-energy region of the coherent scatter spectrum is free from multiple scatter degradation. The components or contributions of multiple scatter can be estimated from the Monte Carlo photon transport simulation programs briefly described in the next section.

It is also of interest to note that decreasing tube potential and current will essentially decrease the radiation dose but the trade-off is usually increased noise (Del Gaizo et al, 2013). Nickoloff and Berman (1993) in their investigation on the effect of tube potential on the x-ray spectra confirmed its output as approximately proportional to the square of the kilo-voltage ($\mathbf{kV_p)^2}$ (precisely in the range of $\mathbf{> kV^{1.8}}$ **to** $\mathbf{< kV^{2.3}}$).

Jacobson (1992) stated that the calculation of dose must be based on actual measurement to make sense from the equipment as tabulated standard measurements are not acceptable as they may not tally with the measured dose in situ. Consequently, real measurements of the relevant geometrical dimensions were made and the actual dose rate measurement was carried out using, Inovision Radiation Dosimeter, model 35050A/CE with an Ion Chamber Input 35080. The

measured data were used in the calculation of the dose and the dose correction as in Table 5.10.

Fajs (2011) described the radiation absorbed dose, as the most important quantity in radiological physics and essentially the value of the energy imparted to matter per unit mass at a point, where it remains to produce any effects attributable to the radiation.

5.8.1 The Monte Carlo simulation technique for the multiple scatter

Monte Carlo simulations aim to simulate each individual x-ray photon and their interactions, in an effort to replicate the results seen in experimentation. If accurate, the simulations provide more information about the properties of the objects under inspection (by the x-rays) than might be possible with experimentation. The simulations approach is as follows in three (3) steps:

1) The technique for the creation of the x ray;
    a. The position and direction of the x-ray is first defined. The position for each photon was set to be a random position on a circle and the direction was set to be straight forward. This means the source was simulated as a true pencil beam, with no divergence. The radius of the pencil beam was 0.5 mm.
    b. The energy of the photon was set by randomly sampling energies from a pre-defined energy spectrum. This distribution was obtained from Spektr, and a 70 kVp spectrum was used. The Spektr energy spectrum was converted to a probability density function (PDF) by normalising by the integral, and then converted to a cumulative distribution function (CDF) by integrating the PDF. The CDF was then randomly sampled, by choosing a random number, r, and finding the first energy bin such that CDF [energy] > r.

2) Transport of the x ray;
    a. The x-ray photon is stepped forward by a certain length, determined by Geant4. During each step the probability of interaction is sampled.

b. If, at a given step, an interaction occurs, Geant4 chooses which interaction (Compton, Rayleigh, Photoelectric, and Pair Production**)** based on the probability of each interaction.
c. The energy loss (if any) and the angular deflection (if any) are sampled based on probability distributions provided by Geant4. These are sampled using random numbers.
d. If no interaction occurs, the photon carries on stepping forward.

3) Detection of the x-ray;

The x-ray photon is detected if it enters the detector volume. The energy of the photon and whether it has been coherently or incoherently scattered is recorded. The table of values is in the Appendix, as Appendix MC, Monte Carlo Simulation.

The above steps are repeated for each individual photon. By simulating a large number of x-ray photons, the simulation should provide a reliable estimate of what occurs in real life experimentation.

The Monte Carlo calculation for the multiple scatter estimation was carried out by Nick Calvert (UCL, Department of Medical Physics & Bio-Engineering).

5.8.2 The effects of multiple scatter

Multiple scattering contribution was estimated from the Monte Carlo simulated phantoms. The numerical simulation generated photons of high scattering order, which made it possible to see the contributions of coherent and incoherent and other possible scattering observed shown as Table 5.11 (in the Appendix) and Figure 5.20 and how they are affected by energy, the structure and properties of a sample. Figure 5.20 shows that multiple scatter (labelled as ‘other’) is significantly less than coherent scatter.

Zustiak et al (2012) found that multiple scattering on fluorescence correlation spectroscopy measurements of particles moving within optically dense media, lead to an increase in apparent illuminated volume and also that multiple scattering is characteristic of many complex biological media such as tissues.

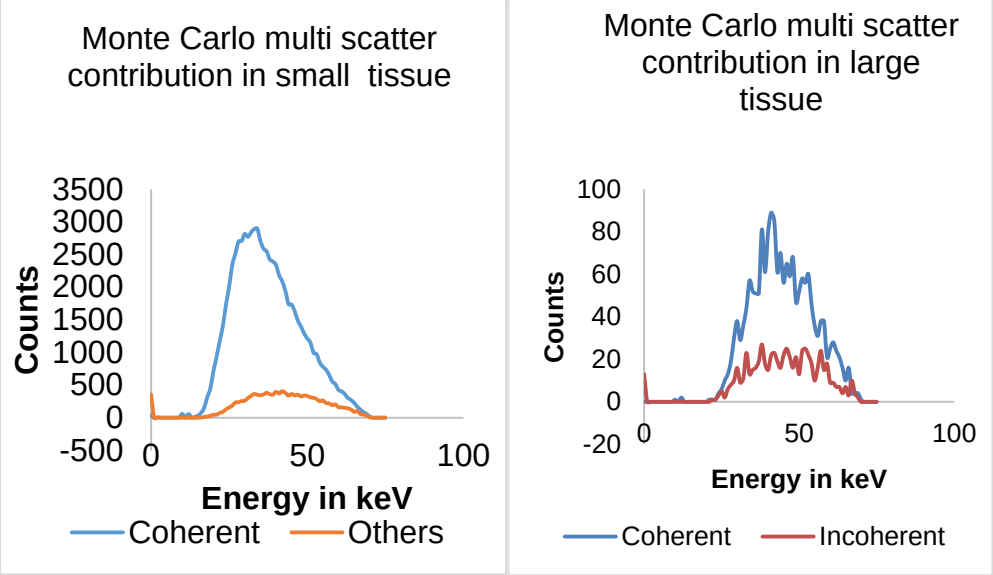

Figure 5.20. The effect of multi scatter contribution in small and large tissue as demonstrated by Monte Carlo simulation process. The large phantom results demonstrate noise due to the low counts.

Aksenova et al (2014) simulated the process of multiple scattering as a random walk of photons in the medium. The parameters of the backscattering peak and the diffusion coefficient they found in the numerical simulation when compared with the experimental data and the result of analytical calculation were found to be consistent.

5.8.3 The limitations of the Monte Carlo simulation

The limitations of simulation in general, include restrictive assumption to make the problem tractable and the need of a computer to execute. In Monte Carlo simulation, the value of a distributed parameter is selected by generation of a random number, with the probability of a given value being determined by the association of random numbers to that variable. The process has to be repeated for a large number of times from which estimates of the parameters of interest may be derived, such as their mean, standard deviations and variances. This is very rigorous and time consuming and therefore may cause credibility problems if the output conflicts with the preconceived. The credibility depends on the number of repeated runs used to produce the output statistics all of which are estimates. It is a purely theoretical tool that can only be a useful guide as to what to expect in a practical experimental procedures.

However, the randomness of its sampling means that it can overestimate or underestimate sample from various parts of the distribution and cannot be totally relied upon to replicate the input distribution's shape unless a very large number of iterations are performed. Multiple scattering will increase the randomness of the scattered photon thereby decreasing the correlation.

In conclusion, Monte Carlo simulations were performed, using Geant4, to estimate the effect that attenuation and Compton/multiple scatter may have when diffraction measurements on the liver in vivo. Simulations were first undertaken with a 70 kVp x-ray beam, 1 mm in diameter, incident upon the end face of a cylinder of adipose tissue measuring 40 mm diameter and 30 mm thick. The photons that scattered through 6 degrees were recorded using a 1 mm diameter detector, which was collimated by a 20 mm thick cylinder of lead. The collimator was placed with a 5 mm distance between the sample and the collimator. The sample was then replaced by a 200 mm diameter cylinder of tissue, and the beam was incident upon the side face of the sample. The detector collimator was placed 5 mm away from the sample, at 6 degrees. For the smaller sample 2.88 billion photons were simulated, whilst 11.52 billion photons were simulated for the larger sample. For the small sample the photon intensity and the effect of multi-scatter, coherent scattering and others recorded was high reaching nearly 3000 counts, also indicating low attenuation, with the energy response at about 17 keV, whereas for large sample there was large effect of multiple scattering, coherent and incoherent scattering, and some noise leading to very low photon intensity, indicating high attenuation with energy response at a point about 24 keV as seen in figure 5.20.

5.9 General Discussion on Translation of the small to patient-sized examinations of fat in liver and heart tissues and the limitations

Translating the results from the small phantom to patient-sized models, theoretical and experimental approaches were employed. The theoretical aspect involved the Monte Carlo simulations, where a model was created, which served as a theoretical guide to

experimental expectations and the experimental work involved the laboratory installed EDXRD system where the real problem was presented for practical observations and solutions.

To investigate the potential of the EDXRD technique that has been developed for clinical application requires test phantoms of life-sized dimensions. Therefore, making measurements on these phantoms would require significant changes to the experimental set-up. Patient sized tissues or real patient dynamics would potentially cause problems for the procedure and it would be cumbersome and too time consuming to image an entire organ.

The positions of the source and detector would have to be extended to allow for the positioning of the larger phantoms with dimensions ranging from 80mm, to accommodate the real life dimensions for heart and up to 300mm, for the liver tissue. The extensions must to be done when real life patients are introduced. This is a matter of engineering physical adjustments of the components while the principles, applications and analysis remain the same.

Monte Carlo was used to analyse multiple scattering in larger phantoms and its effect on the expected diffraction profiles.

The small phantom size was fixed at 30mm for both the liver and heart investigations to fit into the provisions in the laboratory. The small phantom had low attenuation whereas the bigger sized sample implied increased attenuation.

Other factors and the limitations to care for in translating the results of the small phantom to patient sizes include:

- Problem of large tissue mass, shape and variation in the tissue texture (inconsistency). They affect the output but when well observed helps in better analysis of result
- Patient movement in real life investigation can lead to spectral distortions with undesired effects and some filtering and physical control may be advisable
- Physical distortion within the sample after insertion
- Possible shift of the sample outside the scattering volume

- Good beam geometry to rule out error of beam missing out part of the sample (partial beam coverage) and to get the beam covering the entire sample (full beam coverage). Partial beam or smaller beam would give smaller picture. Full or bigger beam will give the full size picture and details
- Control of radiation dose and noise by using appropriate generator type, exposure, tube current, the tube voltage, collimation and patient size. This needs a series of assessment to get optimum values (example, adoption of a tube voltage of 70KVp for both liver and heart investigation because it was found to give better and expected spectral shape, also, limiting the time of data acquisition to 50s for dose reduction) for best results.

5.10 Summary

This chapter dealt on the translation of both results of the small liver and heart phantoms to real patient sized tissues. Using the NIST data the expected diffraction data were computed. Bigger size tissues were found to exhibit greater attenuation, intensity, reduced spectral size, and shape change, multiple scatter effect (observed but not to a very significant amount to lead to distortion) and low energy filtration.

Attenuation effect on the thicker sample simulated using the values of the added thicknesses and the measured values of the small phantom. The simulated spectra of the large tissues were analysed by estimating the amount of the two components of the liver phantom (fat and liver). The components were added together according to the evaluated proportions of the composition to recreate the spectra measured at each point. The simulated and the measured spectra were both compared for similarity and differences. The simulations accounted for the added thicknesses and the noise levels. The resulting spectral figures are the outputs of the small phantom subtracted from the large phantoms with the attenuation and noise in each patient.

In the analysis the thirty (30) resultant outputs obtained showed the levels of detection as:

- The straight lines signify comparatively the best detection of fat
- The near straight lines mean moderate detection.

- The wiggly figures signify no detection of fat and with the analysis broken down.

Radiation dose in the small tissue phantom and the large tissues were assessed and found be at low and acceptable values, which is a major health factor for consideration in an X-ray diffraction investigation system. The discussions in the chapter explained some of the anomalies in the observed and expected results and the problems with simulation and analysis. In addition discussion on the translation of both results of the small liver and heart phantoms to real patient sized tissues with its inherent practical obstacles are discussed with the solution to enable clinical application.

Chapter 6

Conclusions and Future Work with Recommendations

6.1 Introduction

Previous work on X-ray diffraction of human tissue characterisation is predominantly on breast tissue. The purpose of this research was to explore the possibility of applying the UCL EDXRD system in the study of liver and heart disease. The focus was on the detection of fat nodules in the liver and the plaques in blood vessels of the heart. The expectation was to have an alternative method devoid of high doses of radiation, less invasive and at a comparatively low cost.

The aim of the current study was develop a diffraction technique that could identify and quantify small regions (a few millimetres in physical dimension) of fat/plaque within normal tissue. To do this four areas of study were involved – the diffraction system, phantoms to simulate clinical examinations, measurements made on these phantoms and their analysis, and finally the extrapolation of these phantom measurements to life-sized clinical examinations.

6.2 Conclusions

6.2.1 The EDXRD system

The set-up of the EDXRD system for use in the investigation of the fat in the liver and heart has been described in Chapter 2. The system was based around a Philips AGO Industrial X-ray set with a tungsten (W) target. Techniques for the alignment of the system were developed that involved finding the optical axis of the system first. Components were then positioned along this axis and were checked for optimal location by monitoring the transmitted intensity using a flat panel detector. The nominal scattering angle was selected to be 6^0 (taken from previous work) and this was

evaluated using a sample of known characteristics (caffeine). Once optimised the diffraction system would provide detected photon counts over the whole diffraction profile of counts/sec when operated at 70kV and 2mA. The scattering volume was evaluated by moving a small scatterer throughout the volume between source and detector collimators and the sensitive region was found to be approximately 23mm. The system that was built could accommodate volumes up to 100 x 100 x 50mm. Translation slides and appropriate software was developed to position samples within this volume for analysis.

6.2.2 The phantoms

Phantoms were designed to mimic the clinical problem on a small scale. The idea was to establish the viability of the technique in a small scale and then scale the phantoms up to represent human sized objects.

Phantoms were constructed from thin walled Perspex tube. The tube outside diameter was 50mm, with a wall thickness of 5mm. 30mm lengths were used, filled with tissue and positioned so that the axis of the tube was parallel with the incident X-ray beam. Two types of phantom were prepared – single tissue phantoms and those that simulated a real clinical problem, i.e., they were anthropomorphic phantoms. Two versions of these latter phantoms were developed – one representing liver disease and the second simulating heart disease.

6.2.2.1 The liver disease phantom

The anthropomorphic phantoms were to mimic disease conditions and, in the case of liver disease, were prepared by drilling holes across the central diameter for the fat nodule inserts. The procedure was to fill the sample holder with fresh, porcine liver. Lard and pork fat were used as a fat substitute and techniques were developed to insert known quantities of these materials into the liver tissue.

6.2.2.2 Heart disease phantoms

The heart phantom was a more complex structure. The same plastic cylindrical material used for the fabrication of the liver phantom was used to form the outer casing in the heart phantom. Suitable, tissue-mimicking materials were investigated for building the internal structures. Flexible plastic tube, the brand normally used for blood transfusions, was used as a substitute for the blood vessels. Water was used as a substitute for blood, while beeswax was used as a substitute for the heart tissue. The anthropomorphic structure of the phantom was taken from appropriate CT images and porcine fat was used in this investigation to create plaques. Plaques of different thicknesses (1.0mm to 6.0mm) were introduced into the 'blood vessels' before the 'blood' was added and the tubes sealed with silicone.

6.2.3 Diffraction measurements on the anthropomorphic phantoms and their analysis.

The analysis of results for the liver and heart samples have been carried out in a very similar fashion. The spectra of intensity against energy or momentum transfer showed the differences between the heart or liver tissue, fat or plaque and blood at different and specific peak positions of momentum transfer within the range used. Also, in the case of the heart phantom, the spectral differences showed a decreased count and a shift in the peak towards higher MT values in the middle portions. All of these represent a difference between the beeswax, the blood vessel and the other contents. PCA was used to investigate these differences. Plots of the principal components demonstrated that more than 98% of the variation was described by the first two components. Using these components the observed and predicted spectra fitted well and the PCA analysis was used to predict the fat concentrations at different points in the phantoms.

Fat nodules in the liver and plaques in the blood vessels of the heart have been identified and assessed with estimates of their concentrations at various points along the tissue samples. These results have been termed detectability curves. The results demonstrated this EDXRD system's ability to detect very small fat deposits from 2mm thickness upwards in the small tissue phantoms in the correct positions.

6.2.4 Modelled diffraction data from patient examinations and their analysis.

The ability to see similar sizes of fat deposits in a larger body might not be easy due to some intervening factors such as the magnitude of overlying thicknesses of tissues and hence the attenuation of and shape changes to the diffraction profiles. This assessment was treated in detail with the translation of the system's capability to larger volumes of tissue.

The translation of both results of the small liver and heart phantoms was made to real patient sized tissues using narrow beam attenuation models. NIST data were used to compute the effects that overlying tissue would have on the diffraction data. Larger sized models were found to exhibit significant energy dependent attenuation meaning that the intensity and spectral width were reduced. These effects are also accompanied by multiple scatter effects but these were shown to be small. To simulate the effects of taking data at different doses appropriate levels of noise was added to the modelled diffraction profiles.

The analysis developed for the small anthropomorphic phantoms was applied to the modelled diffraction profiles for each sized patient and at each dose/noise level. This led to 30 detectability curves. To determine whether a particular detectability curve demonstrates accurate detection and location all the curves have been subtracted from a known correct result. This demonstrated that for small patients detection of fat deposits was possible even at low doses. However, as the size of the patient increased detection was compromised.

6.3 Summary

6.3.1 General deductions:

- The fat nodules and the plaques in the tissues were identified within the samples.
- Fat deposits as small as 2mm were detected in the liver samples.

- Plaques of thickness from 2mm upwards were identified in the heart phantom.
- Increasing the size of the examined tissue reduced the detectability of the fat deposits but still demonstrate that the technique has clinical potential.

6.4 Future Work and Recommendations

While the EDXRD arrangement has promise as a future for as a tissue characterization system, a number of limitations exist that currently hamper its clinical application. These include its application or trials with real tissue samples and development of its instrumentation to accommodate larger sized objects.

The acquisition and storage of tissue samples is challenging. Availability of real tissue is low. However, scatter signatures obtained from some tissue equivalent materials with the EDXRD system compare well to real tissue. This may offer an easier way forward for future developments on large objects.

The system is yet to be adapted for clinical use.

The core future work shall include:

- Focus on building a clinical EDXRD imaging system.
- Adjusting the present system to get the best field of view of the sample accurately
- An inbuilt algorithm (software for analysis) needs to be incorporated in the EDXRD system for the characterization and statistical analysis. This will usher in a novel liver and heart diffraction imaging modality and will lead to early detection of fatty deposit and early clinical management of the problems of the fatty liver and plaques in the blood vessels of the heart.

References:

Aatandilor, G., Dembo, A., Kormadin, O., Lazarev, P., Paukshto, M., Shkolink, L.and Zayratiyants, O. (2000). Human tissue analysis by small angle x-ray scattering. J.Appl.Cryst.33: 511-514.

Abbas, M. I. (2006). HPGe detector absolute full-energy peak efficiency calibration, including coincidence correction for circular disc sources. J.Phys.D: Appl.Phys. 39: 3952-3958.

Abdelkader, M. H., Alkhateeb, S.M., Bradley, D. A. and Pani, S, (2012). Development and characterization of a laboratory based X-ray diffraction imaging system for material and tissue characterization. Applied Radiation and Isotopes 70 (2012) 1325-1330.

Albertini, V. R. and Paci, B. (2002). Effect of the x-ray beam collimation on the resolution of the energy dispersive diffractometer. Review of Scientific Instruments, Vol.73 No. 9:3160- 3164.

Agostinelli, S., Allison, J., Amako, K., Apostolakis, J., Araujo, H., Arce, P., Asai, M., Axen, D., Banerjee, S., Barrand, G., Behner, F., Bellagamba, L., Boudreau, J., Broglia, L., Brunengo, A., Burkhardt, H., Chauvie, S., Chuma, J. and Zschiesche, D.(2003). GEANT4 – A stimulation kit.

Nuclear Instruments and Methods in Physics Research Section A: Accelerators, Spectrometers, Detectors and Associated Equipment

Volume 506, Issue 3, Pages 250-303.

J. **Allison**, K. Amako, J. Apostolakis, H. Araujo, P. Arce Dubois, M. Asai, G. Barrand, R. Capra, S. Chauvie, R. Chytracek, G. A. P. Cirrone, G. Cooperman, G. Cosmo, G. Cuttone, G. G. Daquino, M. Donszelmann, M. Dressel, G. Folger, F. Foppiano, J. Generowicz, V. Grichine, S. Guatelli, P. Gumplinger, A. Heikkinen, I. Hrivnacova, A. Howard, S. Incerti, V. Ivanchenko, T. Johnson, F. Jones, T. Koi, R. Kokoulin, M. Kossov, H. Kurashige, V. Lara, S. Larsson, F. Lei, O. Link, F. Longo, M. Maire, A. Mantero, B. Mascialino, I. McLaren, P. Mendez Lorenzo, K. Minamimoto, K. Murakami, P. Nieminen, L. Pandola, S. Parlati, L. Peralta, J. Perl, A. Pfeiffer, M. G. Pia, A. Ribon, P. Rodrigues, G. Russo, S. Sadilov, G. Santin, T. Sasaki, D. Smith, N. Starkov, S. Tanaka, E. Tcherniaev, B. Tomé, A. Trindade, P. Truscott, L. Urban, M. Verderi, A. Walkden, J. P. Wellisch, D. C. Williams, D. Wright, and H. Yoshida, 2006. Geant4 Developments and Applications, IEEE TRANSACTIONS ON NUCLEAR SCIENCE, VOL. 53, NO. 1, FEBRUARY 2006.

American College of Radiology (2012). Dose Index Registry: https://nrdr.acr.org/Portal/DIR/Main/page.aspx (Accessed January 28, 2012).

Andrasi, E., Nadasdi, J., Molnar, Z., Bezur, L. and Ernyei, L. (1990). Trace element composition of biological materials. Biological Trace Element Reasearch, Vol. 26-27, No. 1:691-698.

Aksenova, E. V., Kokorin,D. I. and Romanov,.V. P. (2014). Simulation of radiation transfer and coherent backscattering in nematic liquid crystals. Physical Review E 89, 052506-1 – 052506-11.

Brass,W. and Ryan, A. J. (1996). Small angle x-ray scattering and wide angle x-ray scattering combined with thermal and spectroscopic analysis techniques. Journal of Molecular Structure, 33: 309-314.

Ballirano, P., Caminiti, R., Sadun, C. and Caracciolo, G. (2006). The use of energy dispersive x-ray diffraction for the investigation of structural and compositional features of old and modern papers. Microchemical Journal, 88: 107-112.

Barroso, C.R., Oliveira, F.L., Castro, C.R.F., Lima,J.C., Braz, D., Lopes, R.T., Droppa, R., Tromba, G., Mancini, L., Zanini, F., Rigon, L. and Dreossi, D. (2007). Nuclear instruments in physics research Section A: Accelerators, Spectrmeters, Detectors and Associated Equipment, Volume 579, Issue 1: 318-321.

Barts and the London NHS (2005). Research and Development 2004-2005. Clinical Physics Department CPG03175_13.

Batchelar, D. L., Davidson, M.T.M., Dabrowski, W. and Cunningham, I. A. (2006). Bone compositon imaging using coherent scatter computed tomography: Assessing bonehealth beyond bone mineral density. Med. Phys., 33:904-915.

Bhohndiek, S.E., Cook, E.J., Arvantis, C.D., Olivo, A., Royle, G.J., Clark, A.T., Prydderch, M. L., Turchetta, R. and Speller, R.D. (2008). A CMOS active pixel sensor system for laboratory based x-ray diffraction studies of biological tissue. Phys. Med. Biol., 53: 655-672.

Blanton, T., Barnes, C., Putrelo, J., Yeboah, A. and Switalski, S. (2004).

Material characterization using a novel simultaneous near. Infrared/x-ray diffraction instrument. Advances in X-ray Analysis, Vol. 47: 249-255.

British Liver Trust 2011

Cassidy, F. H., Yokoo, T.,Lejla Aganovic, L., Hanna, R. F., Bydder, M., Middleton, M. S., Hamilton, G., Alyssa D. Chavez, A. D.,Jeffrey B. Schwimmer, J. B., Claude B. Sirlin, C. B. (2009). Fatty Liver Disease: MR Imaging Techniques for the Detection and Quantification of Liver Steatosis RadioGraphics, 2009, Vol.29: 231-260, 10.1148/rg.291075123

Catheline JM, Turner R, Champault G.2000. Laparoscopic ultrasound of the liver. Eur J Ultrasound 2000; 12:169–177.

Castro, C.R.F., Barroso, R. C., Anjos, M.J., Lopes,R.T. and Braz, D. (2004). Coherent scattering characteristics of normal pathological breast human tissues. Radiation Physics and Chemistry, 71.

Castro,C.R.F., Barroso, R.C., Oliveira, L.F. and Lopes, R.T. (2005). Coherent scattering x-ray imaging at the Brazilian National Synchrotron Laboratory: Preliminary breasts images. Nuclear Instruments and Methods in Physics Research A 548: 116-122.

Chandawarkar RY, Kakegawa T, Fujita H, Yamana H, Hayabuthi N, 1996. Comparative analysis of imaging modalities in the preoperative assessment of nodal metastasis in esophageal cancer. J Surg Oncol. 1996 Mar; 61(3):214-7.

Changizi, V., Kheradmand, A.A. and Oghabian, M.A. (2008). Application of small angle x-ray scattering for differentiation among breast tumours. J. Med. Phys. 33 (1):19-23.

Chaparian, A., Oghabian, M.A. and Changizi, V. (2009). Acquiring molecular interference functions of x-ray coherent scattering for breast tissues bycombination of simulation and experimental methods. Iran J. Radiat. Res. 7 (2): 113-117.

Chaparian, A., Oghabian, M.A., Changizi, V. and Faquharson, M.J. (2010). The optimization of an energy dispersive x-ray diffraction system for potential clinical application. Applied Radiation and Isotopes, 68: 2237-2245.

Cherry, S.R (2009). Multimodality Imaging: Beyond PET/CT and SPECT/CT. Seminar in Nuclear Medicine, Volume 39, Issue 5, September 2009, Pages 348–353

Cook, E., Fong, R., Horrocks, J., Wilkinson, D. and Speller, R. (2007). Energy dispersive x-ray diffraction as a means to identify illicit materials: A preliminary optimisation study. Applied Radiation and Isotopes, 65:959-967.

Cook, E.J. (2008). Analysis of energy dispersive x-ray diffraction profiles for material identification, imaging and system control. PhD Thesis, University College London.

Davidson,M.T.M., Batchelar, D.L., Velupillai, S., Denstedt, J.D. and Cunningham, I.A. (2005). Analysis of stone components by x-ray coherent scatter: Characterizing composition beyond x-ray diffractometry. Phy. Med. Biol. 50: 3773-3786.

Davies, A.M.C. and Fearn, T. (2005) Back to Basics: The Principles of Principal Component Analysis. Spectroscopy Europe, 16, 20-23.

Andrew J., Del Gaizo, A.J., Fletcher, J.G., Yu, L., Paden, R.G., Spencer, G.C., Leng, S., Silva, A. M., Fidler, J.L., Silva, A.C., Hara, A.K., (2013) Reducing Radiation Dose in CT Enterography RadioGraphics, 2013, Vol.33: 1109-1124, 10.1148/rg.334125074

Desouky, O.S., Elshemey, W. M., Selim, N.S. and Ashour, A.H. (2001). Analysis of low angle scattering peaks from a lyophilized biological samples. Phys. Med. Biol., 46: 2099-2106.

Desgreniers, S. and Largarec, K. (1994). XRDA: A program for energy x-ray diffraction analysis on a PC. J. Appl. Cryst., 27: 432-434.

Dowsett, D., Kenny, P. A. and Johnston, R. E. (2006). Physics of Diagnostic Imaging, 2nd edition, page 227 - 246 CRC Press. ISBN 9781444113396.

Ehman E. C., Yu L., Manduca, A., Hara, A. K., Shiung, M.M., Jondal, D., Lake D. S., Paden R. G, Blezek, D. J., Bruesewitz, M. R., McCollough, C. H., Hough, D. M., Fletcher, J. G. 2014. Methods for clinical evaluation of noise reduction techniques in abdominopelvic CT. Radiographics. 2014 Jul-Aug; 34(4):849-62. doi: 10.1148/rg.344135128.

Elshemey, W. M., Desouky, O. S., Ashour, A. H. (2001). Low angle x- ray scattering from a lyophylized blood constituents. Phys. Med. Biol. 46: 531-539.

Ellmer, K., Mientus, R., Wieb, V. and Rossner, H. (2003). In-situ energy dispersive x-ray diffraction system for time resolved thin-film growth studies. Measurement Science and Technology, 14: 336-345.

Elshemey, W. M., Desouky, O.S., Fekry, M.M., Telaat, S.M. and Elsayed, A.A. (2010). The diagnostic capability of x-ray parameters for the characterization of breast tissue. Med. Phys. 37 (8):4257-4267.

Endo, M., Tsunoo, T., Nakamori, N., and Yoshida, K. 2001. Effect of scattered radiation on image noise in cone beam CT. Med. Phys. **28**, 469; http://dx.doi.org/10.1118/1.1357457

Esbrand, C. (2009). Feature Analysis Methods for Intelligent Breast Imaging Parameter Optimisation using CMOS active pixel sensors. A PhD Thesis, University College London.

Gershman, G. 2012. Practical Pediatric Gastrointestinal Endoscopy. Wiley – Blackwell Publishers Feb 28, 2012 ASIN: B007S7L4LM

Greenberger, N., Blumberg, R. and Burakoff, R. 2009 (Editors). Current Diagnosis & Treatment Gastroenterology, Hepatology, & Endoscopy (Lange Current Series) Paperback – 1 Jun 2009.

Fajs, M. (2011). Dosimetry, University of Ljubljana. mafija.fmf.uni-lj.si/seminar/files/2010_2011/Dosimetry_ver2.3.pdf

Farquharson, M. J. and Speller, R. D.(1996). Measuring bone mineral density in archeological bone using Energy Dispersive Low angle X-ray scattering techniques. Journal of Archeological Science, 24: 765-772.

Farquharson, M. J., AL-Ebraheem, A., Theodorakou, C., Ryan, E., Bradley, D. A., Gurusamy, K. and Davidson, B. (2008). Measurement of K, Fe, Cu, and Zn levels in secondary colorectal liver tissue and surrounding normal liver tissue and their potential as a tissue classifier. X-ray Spectrom, 38: 81-88.

Fernández, M., Keyriläinen, J., Serimaa, R,, Torkkeli, M., Karjalainen-Lindsberg, M. L.,Tenhunen, M., Thomlinson, W., Urban, V., Suortti, P (2002). Small-angle x-ray scattering studies of human breast tissue samples, Physics in Medicine and Biology, **47**(4), 577- 592.

Fewster, P. F. & Andrew, N. L. (1999). Defect and Microstructure Analysis by Diffraction, IUCr Monographs on Crystallography 10, edited by R. L. Snyder, J. Fiala & H. J. Bunge, pp. 346–364. Oxford University Press.

Fewster, P. F. & Trout, D. R. D. (2013). A compact high-resolution X-ray diffractometer. J. Appl. Cryst. **46**, 1626–1639.

Garden, J. O. 2009. Hepatobiliary and Pancreatic Surgery: Companion to Specialist Surgical Practice
https://books.google.com.ng/books?isbn=0702035599

Griffiths, J.A., Royle, G.J., Horrocks, J.A., Hamby, A.M., Pani, S. and Speller, R.D. (2008). Angular dispersive microCT of small breast tissue samples. Radiation Physics and Chemistry, 77: 373-380.

Garcia-Allende, P.B., Krisnaswamy, V., Samkoe, K.S., Hoopes, P.J., Pogue, B.W., Coude, O.M. and Lopez-Higuera, J.M. (2009). Automated interpretation of scattered signatures aimed at tissue morphology identification.Proceedings of SPIE-OSA Biomedical Optics. SPIE, Vol. 7368: 73681C-1.

Gamir, L.P. (1997). A new method for the determination of the entry position of the gamma rays in the high purity germanium detectors by current pulse analysis. PhD Thesis: Cranfield University.

Geraki, K., Farquharson, M. and Bradley, D. (2004). X-ray fluorescence and energy dispersive x-ray diffraction for the characterization of breast tissue. Radiation Physics and Chemistry, Vol.71 Issues 3-4: 969-970.

Geraki, K., Farquharson, M.J., Bradley, D.A., Gundogdu, O. and Falkenburg, G. (2008). The localisation of biologically important metals in soft and calcified tissues using synchrotron x-ray fluorescence technique. X-ray Spectron, 37: 12-20.

Gore RM, Mathieu DG, White EM et al. 1994. Passive hepatic congestion: cross-sectional imaging features. AJR Am J Roentgenol; 162:71–75.

Griffiths, J.A., Royle, G.J., Horrocks, J.A.., Hamby, A.M., Pani, S. and Speller, R.D. (2008). Angular dispersive microCT of small breast tissue samples. Radiation Physics and Chemistry, 77: 373-380.

Griffiths, J.A. 2005. X-ray diffraction measurements for breast tissue analysis. A PhD Thesis. University College London

Grinyer, J., Popovic, M. and Chettle, D.R. (2007). Detection of mecury in kidney via source excited x-ray fluorescence. X-ray Spectrom, 36: 99-103.

Harding, G., Kosanetsky, J. and Neitzel, U. (1987). X- ray diffraction computed tomography. Med. Phys. 14 (4): 515-526.

Harding, G., Newton, M. and Kosanetsky, J. (1989). Energy dispersive x-ray diffraction computed tomography. Med. Phys. Biol., 35(1): 33-41.

He, B.B., Preckwinkel, U. and Smith, K.L. (2000). Fundamentals of two dimensional x-ray diffraction (XRD2). Advances in X-ray Analysis, Vol. 43: 273-280.

Hiller, J.C. and Wess, T.J. (2006). The use of small angle x-ray scattering to study archeologically and experimentally altered bone. Journal of Archaeological Science, 33: 560-572.

Hoyert, Donna L. and Xu Jiaquan, M.D Deaths: Preliminary Data for 2011, National Vital Statistics Repots, Volume 61, Number 6 October 10, 2012

Http://en.wikipedia.org/wiki/animal_fat/fat/#Cite_note-1

Hubbel, J.H. (1999). Review of photon interaction cross section data in the medical and biological context. Phys. Med. Biol. 44: R1-R22.

Hukins, D. W. L. (1981). One dimensional crystals. In X-Ray Diffraction by Disordered and Ordered Systems. Pergamon Press, Oxford. 76 –93.

Ichiro, F., Etsuji, M. and Masachi, K. (2005). Signatures of live fingers extracted from aseries of finger images. Proceedings of SPIE. The International Society of Optical Engineering, Vol. 5677: 177-185.

Imafuku, M. (1997). Developing of fast texture mapping system with energy dispersive x-ray diffraction method. JCPDS-International Centre for Diffraction Data, 1997.

Ioannou, I., Hall, C., Hoff, D.W., Pugsley, D.A. and Jacques, S.D.M. (2005). Synchrotron radiation energy dispersive x-ray diffraction analysis of salt distribution in Lepine limestone. Analyst, 130: 1006-1008.

Ishikawa, T. (2005). Performance of a whole body counter with five high purity germanium detectors. Applied Radiation and Isotopes, 64 (1): 386-389.

Jacbson, D. R. (1992). Radiographic exposure calculator and mammographic dose calculator. Radiology, Volume 182, Issue 2

Jiang, Z. and Hejing, W. 2003. The physical meanings of 5 basic parameters for an X-ray diffraction peak and their application. Chinese Journal of Geochemistry, 2003, Volume 22, Number 1, Page 38

Johns, H. E. and Cunningham, J. R. (1983). The Physics of Radiology, 4th. Ed., Basic interactions between photons and charged particles with matter: 168-173.

Johns, P.C. and Wismayer, M.P. (2002). Medical x-ray imaging with scattered photons. SPIE, TDOI: 355-357.

Johns, P.C. and Wismayer, M.P. (2005). Measurement of coherent scatter form factors for amorphous materials using diffractometers. Phys. Med. Biol. 10(1): 5233-5250.

Johns, P.C. and Yaffe, M.J. (1982). Coherent scatter in diagnostic radiology. Med. Phys. 10 (1): 40-50.

Johns, H. E. and Cunningham, J. R. (1983). The Physics of Radiology, 4th. Ed., Basic interactions between photons and charged particles with matter: 168-173.

Kacperski, K and Nicholas M. Spyrou, N.M. 2004. Three-Gamma Annihilations as a New Modality in PET. IEEE IEEE Trans Med Imaging. 2004 Apr; 23(4):525-9.

Kidane, G., Speller, R.D., Royle, G.J. and Hanby, A.M. (1999). X-ray scatter signatures for normal and neoplastic breast tissues. Phys. Med. Biol., 44: 1791-1802.

King, B.W. and Johns, P.C. (2008). Measurement of coherent scattering form factors using an image plate. Phys. Med. Biol., 53:5977-5990.

King, B.W. and Johns, P.C. (2010). An energy dispersive technique to measure x-ray coherent scattering form factors of amorphous materials. Phys Med. Biol., 55: 855-871.

Kosanetsky, J., Knoerr, B., Hardig, G. and Neitzel, U. (1987). X-ray diffraction measurements of some plastic materials and body tissues. Med. Phys., 14 (4): 526-532.

Kugler, W. (2003). X-ray diffraction analysis in forensic science: The last resort in criminal cases. Advances in X-ray Analysis, Vol. 46.

Kumari-Maini, S. M. (2012). Development of a Breast Tissue Diffraction Analysis System using Energy Dispersive X-ray Diffraction. PhD thesis for UCL.

Kuszyk, B.S., Bluemke, D.A, Urban, B.A., Choti, M.A., Hruban, R. H., Sitzmann, J.V., Fishman, E. K. (1996). Portal-phase contrast-enhanced helical **CT** for the detection of malignant hepatic tumours: Sensitivity based on intraoperative and pathologic findings. Am J Roentgenol. 166: 91–95.

Laine, E. and Lahteenmaki, I. (1980). The energy dispersive x-ray diffraction method: Annotated bibliography, 1968-1978. Journal of Material Science, Vol. 15:269-278.

Leclair, R.J. and Johns, P.C. (2002). Optimum momentum transfer arguments for x-ray forward scatter imaging. Med. Phys., 29 (12): 2881-2889.

Lyman, C. (2003). Energy dispersive x-ray spectrometry in the AEM. (Notes for Lehigh Miroscopy School). Lehigh University, U.S.A.

Machon, G. (2009). Shape identification and ranking in temporal data sets. M.Sc Thesis, University of Maryland.

Maini, S.K. (2012). Breast tissue PhD Thesis, University College London.

Marlene H. McKetty, 1998. X-ray Attenuation, Radiographics. 1998. 18:; 151-163

Matsubara, I. and Millman, B.M. (1974). X-ray diffraction patterns from mammalian heart muscle. Journal of Molecular Biology, Vol. 82 (4):527-530.

Mattson, S. and Thomas, B.J. (2006). Development methods for body composition studies. Phys. Med. Biol., 51: R203-R228.

Manso, M., Carvalho, M.L. and Nunes, M.L. (2007). Characterization of essential and toxic elements in cephalopod tissues by EDXRF and AAS. X-Ray Spectrom, 36: 413-418.

.

McNitt-Gray, M.F. (2002). AAPM/RSNA physics tutorial for residents: topics in CT—radiation dose in CT. RadioGraphics 2002; 22(6):1541–155

Midgley, S. (2006). Angular resolution in magnification radiography and the observation of the x-ray wave interaction signatures. Phys. Med. Biol., 52:5173-5186.

Miller-Keane Encyclopaedia and Dictionary of Medicine, Nursing and Allied Health. 2003. Seventh Edition. Saunders. An imprint of Elsevier Inc.

Mosby's Medical Dictionary, 2000. 8th edition. Elsevier

Nelson, S.A. (2009). X-ray Crystallography. Mineralogy, EENS 211. Tulane University, USA.

Newton, M., Hukins, D.W.L. and Harding, G. (1992). Bone composition measured by x-ray scattering. Phys. Med. Biol., Vol. 37, No.6: 1339-1347.

Nicholas, D. and Hill, C.R. (1975). Acoustic Bragg diffraction from human tissues. Nature, Vol. 257: 305-306.

Nickoloff, E. Land Berman, H. L. (1993). Factors affecting X-ray Spectra, Radiographics, 1993; 13:1337-1348

NIH, 2009. Atherosclerosis. National Institutes of Health, NIH Publication No. 09-7431 August 2009.

Pani, S., Cook, E., Horrocks, J., George, L., Hardwick, S. and Speller, R. (2009). Modelling an energy dispersive x-ray system for drug detection. IEEE transactions on nuclear science, Vol. 56, No. 3:1238-1241.

Pani, S., Cook, E., Horrocks, J.A., Jones, J.L. and Speller, R.D. (2010). Characterization of breast tissue using energy dispersive x-ray diffraction computed tomography. Applied Radiation and Isotopes, Vol. 68, Issue 10: 1980-1987.

Paulson, E.K.,McDermott, V.G., Keogan, M.T. Frederick, M.G. and Nelson, R.C (1998). Carcinoid metastases to the liver: role of triple-phase helical CT. Radiology Volume 206, Issue 1. DOI: http://dx.doi.org/10.1148/radiology.206.1.9423664

Peplow, D.E. and Verghese, K. (1998). Measured molecular coherent scattering form factors of animal tissues, plastics and human breast tissues. Phys. Med. Biol., 43: 2431-2452

Pinheiro, T., Fernandex, R., Maenhaut, W., Hebbretch, G., Watje, U. and Halpern, M.J. (1993). Trace elements in cardiovascular diseases. Nuclear Instruments and Methods in Physics Research, Vol. 75, Issues 1-4: 160-164.

Podgorsak, E. B. (2010) Rdiation Physics for Medical Physicist. 2nd imaging of materials with very similar atomic numbers ISBN 978-3-642-00874-7. Page 448. ISN 1618-7210. Springer

Poletti, M.E., Goncalves, O.D. and Mazzaro, I. (2002). X-ray scattering from human breast tissues and breast equivalent materials. Phys. Med. Biol., 47: 47-63.

Poletti, M.E., Goncalves, O.D. and Mazzaro, I. (2004). Measurement of x-ray scatter signatures for some tissue equivalent materials. Nuclear Instruments and Methods in Physics Research, B 213: 595-598.

Quiroga, S. Sebastià, C., Pallisa, E., Castellà, E., Pérez-Lafuente, M. and Alvarez-Castells, A (2001). Improved Diagnosis of Hepatic Perfusion Disorders: Value of Hepatic Arterial Phase Imaging during Helical CT. RadioGraphics, 21:65–81

Rademaker, J., Widjaja, A. and Galanski, M. (2000). Hepatic hemangiosarcoma: imaging findings and differential diagnosis. Eur. Radiol. 10, 129-133. Springer-Verlag.

Rendle, D.F. (2003). Use of x-ray in the United Kingdom forensic science service. Advances in X-ray Analysis, Vol. 46: 17-24.

Rietveld, H.M. (1967). Line profiles of neutron powder diffraction peks for structure refinement. Acta Cryst. 22: 151-152.

Round, R. A. (2006). Ultra-structural analysis of breast tissue. PhD Thesis. Cranfield Univversity, UK.

Royle, G.J. and Speller, R.D. (1990). Low angle x-ray scattering for bone analysis. Phys. Med. Biol., Vol. 36, No. 3: 383-389.

Royle, G.J., Farquharson, M., Speller, R. and Kidane, G. (1999). Apllication of x-ray diffraction analysis in crystalline and amorphous body tissues. Radiation Physics and Chemistry, 56: 247-258.

Ryan, E.A. and Farquharson, M.J. (2007). Breast tissue classification using x-ray scattering measurements and multivariate data analysis.

Sakellarisa, T., Spyrou, G., Panayiotakis, G, and Tzanakos, G (2010). .A Monte Carlo study of primary electron production inside photoconductors for digital mammography and indications of material suitability, Journal of Instrumentation Volume 5 August 2010: doi:10.1088/1748-0221/5/08/P08004

Santos, J.M.F. and Monteiro, C.M.B. (2001). The response of the high purity germanium detectors to x-rays with energy in the region of the Ge k absorption edge. Applied Radiation and Isotopes. Vol., Issue 3: 331-334.

Sattar,N, 2014. Non-alcoholic fatty liver disease - NCBI - NIH
https://www.ncbi.nlm.nih.gov/pmc/articles/PMC4168663/1

Sauders Comprehensive Veterinary Dictionary, 2007. 3rd Ed., Elsevier Inc

Schmidt J, Strotzer M, Fraunhofer S (2000). Intraoperative ultrasonography versus helical computed tomography and computed tomography with arterioportography in

diagnosing colorectal liver metastases. Lesion-by-lesion analysis. World J Surg; 24:4347.

Sica GT, Ji H, Ros PR. CT and MR imaging of hepatic metastases. AJR Am J Roentgenol (2000); 174:691–698.

Sidhu, S., Siu, K.K.W., Falzon, G., Hart, A.S., Fox, J.G. and Lewis, R.A. (2009). Mapping structural changes in breast tissue disease using x-ray scattering. Med. Phys., 36 (7): 3211-3217.

Silverman, P.M., Brown B., Wray, H., Fox S.H., Cooper, C., Roberts, S. and Zeman, R.K. (1995). Optimal Contrast Enhancement of the Liver Using Helical (Spiral) CT: Value of SmartPrep. AJR 1995; 164:1169 -1171.

Siu, K.K.W., Sidhu, S., Falzon, G., Nazaretian, S., Hart, S.A., Fox, J.G. and Lewis, R.A. (2009). Small angle x-ray scattering signatures for breast cancer detection: Direct comparison of synchrotron and laboratory sources. World Congress on Medical Physics and Biomedical Engineering. ISBN-13: 978-3-642-03878-5: 607-610.

RACGP, 2013. Fatty liver disease – a practical guide for GPs
https://www.racgp.org.au › AFP › 2013 › July

Rajagopal, K 2008. Textbook of Engineering Physics
https://books.google.com.ng/books?isbn=81203366

R.D. **Speller**, *'Blobfinder'*, IDL programme, personal communication, (2002).

Speller, R. D. (2014), Diffractometer collimation schematic, personal communication.

Tamm, E.P., Rong, X.J., Cody, D.D., Ernst, R.D., Fitzgerald, N.D.and K. Kundra, V. (2011). Quality Initiatives: CT Radiation Dose Reduction: How to Implement Change without Sacrificing Diagnostic Quality, RadioGraphics, Vol.31: 1823-1832, 10.1148/rg.317115027

Tani I, Kurihara Y, Kawaguchi A et al. (2000). MR imaging of diffuse liver disease. AJR Am J Roentgenol; 174:965–971

Tartari, A., Bonifazzi, C., Felsteiner, J and Casnati, E. (1996). Detailed multiple-scattering profile evaluations in collimated photon scattering techniques. Nicl. Instrum. Methods B117, 325-332.

Tartari, A., Casnati, E., Bonifazzi, C. and Baraldi, C. (1997). Molecular differential crosssection for x-ray coherent scattering in fat and polymethyl metacrylate. Phys. Med. Biol., 42:2551-2560.

Tartari, A., Taibi, A., Bonifazzi, C. and Baraldi, C. (2001). Updating of form factor tabulations for coherent scattering of photons in tissues. Phys.Med.Biol., 47:163-175.

Theodorakou, C. and Farquharson, M.J. (2008). Human soft tissue analysis using x-ray or gamma ray techniques. Phys. Med. Biol., 53: R111-R149.

Theodorakou, C. and Farquharson, M.J. (2009). The classification of secondary colorectal liver cancer in human biopsy samples using angular dispersive x-ray diffraction and multivariate analysis. Phys. Med. Biol., 54: 4945-4957.

Traub, R.J., Usen, P.C. and McDonald, J.C. (2005). The radiological properties of a novel lung tissue substitute. Radiation Protection Dosimetry, Vol. 121, Issue 2: 202-207.

Tschammler, A. 1998. Statistical inaccuracies in a comparative analysis of imaging modalities in the assessment of nodal metastasis in esophageal cancer. [J Surg Oncol. 1998, 68: 62

Tsuji, T., Yabushita, Y., Tarohda, T., Kanayama, Y., Washiyama, K. and Amano, R. (2003). Elemental concentration of manganese and potassium in brain and other organs of foetal, sucking and developmental mice. Journal of Radio-analytical and Nuclear Chemistry, Vol. 121, Issue 2:202-207.

Vazina, A., Budantsev, A.Y., Bras, W., Deshcherevskaya, N.P., Doldnya, I.P., Gadzhiev, A.M., Koorneev, V.N., Lanina, N.F., Letyagin, V.P., Mayevski, E.I., Matyushin, A.M., Podlsky, I.Y., Samsonova, M.V., Sergienko, P.M., Simonova, N.B., Stankevich, V.G., Trunova, V.A., Vavilov, V.M., Chernyaev, A.L., Sharafutdinov, M.R. and Sheromov, M.A. (2005). X-ray diffraction and spectral studies of biological native and modified tissues. Nuclear Instruments and Methods in Physics Researh, A 543: 297-301.

Van Vliet, E.P.M. Steyerberg, E.W. Eijkemans, M.J.C. Kuipers, E.J and Siersema, P.D. 2007. Detection of distant metastases in patients with oesophageal or gastric cardiac cancer: a diagnostic decision analysis. Br J Cancer. 2007 October 8; 97(7): 868–876.

Washington University School of Medicine, St Louis.2009. "Diabetes, Triglycerides and Cardiovascular disease metabolic risk factors." Science Daily. Science Daily, 24 August 2009.

Christopher D. Williams, Joel Stengel, Michael I. Asike, Dawn M. Torres, Janet Shaw, Maricela Contreras, Cristy L. Landt, Stephen A. Harrison (2011)

Prevalence of Nonalcoholic Fatty Liver Disease and Nonalcoholic Steatohepatitis Among a Largely Middle-Aged Population Utilizing Ultrasound and Liver Biopsy: A Prospective Study

Gastroenterology, Volume 140, Issue 1, January 2011, Pages 124-131

Worbrauschek, P., Pepponi, G., Strli, C., Jokubonis, C., Falkenberg, G. and Osterode, W. (2002). SR- XRF investigation of human bone. Advances in X-ray Analysis, Volume 45: 478-484.

www.webmd.com/digestive-disorders/picture-of-the-liver#1

http://library.med.utah.edu/WebPath/LIVEHTML/LIVER002.html

WHO 2011: The top 10 causes of death. Fact sheet N°310. (Updated June 2011).

www.americanheart.org, Atherosclerosis, American Heart Association, Inc., 2007.

www.americanheart.org, Inflammation, Heart Disease and Stroke: The Role of C-Reactive Protein, American Heart Association, Inc., 2007.

www.americanheart.org. 2007. Metabolic Syndrome, American Heart Association, Inc.

www.hivandhepatitis.com, New Data Suggest that Patients with Chronic Liver Disease are at Increased Risk for Heart Disease, Liz Highleyman, hivandhepatitis.com, 2007.

www.medicalnewstoday.com. May, 2007. Spotlight on Liver Disease: Improving Today's Treatments, MediLexicon International Ltd.

www.umm.edu. 2007.Atherosclerosis, University of Maryland Medical Centre.

www.webmd.com. 2007.The Hard-Liver's Guide to the Liver, WebMD Corporation.

www.nlm.nih.gov/medlineplus/magazine/issues/winter09/articles/
www.mayoclinic.org

Xi Zhang, Xin-Rong Yang, Yu Chen, Hai-Qing Li, Wen-Ya Liu, Qing-Xi Yuan and Shao-Liang Chen, 2010. Diffraction-Enhanced Radiography of Various Mouse Organs. American Journal of Roentgenology; American Roentgon Ray Society. doi:10.2214/AJR.09.4090AJR; Vol. 195 no. 3 545-549.

Yu, L., Bruesewitz, M.R.,• Kristen B., Thomas, K.B., Joel G. Fletcher, J.G., Kofler, J.M., Cynthia H. McCollough, C. H. (2011).Optimal tube potential for radiation dose reduction in paediatric CT: Principles, clinical implementation and pitfalls. RadioGraphics 2011; 31:835–848 • Published online 10.1148/rg.313105079

Zustiak, S Riley,J, Boukari, H, Gand jbakhche, A and Nosai R, (2012). Effects of multiple scattering on fluorescence correlation spectroscopy measurements of particles, moving within optically dense media. J. Biomed. Opt. 17(12), 125004 (Dec 04, 2012). doi:10.1117/1.JBO.17.12.125004

Appendix

Appendix 1: Matlab Programs:

1 SL.mat

```
% This program analyses as one data set all the data from
experiment E12

% Load all the data, previously converted from Excel format to
MATLAB files
load('SL.mat')
% variables loaded
% X  (241 x 31) spectra from positions 1-31
% mt (241 x 1)  momentum stranfer values

% Cut to mt range of 0.6107 to 2.9313  (approx 14.6 - 70 KeV)
X=X(51:end,:);
mt=mt(51:end);    % mt contains the momentum transfer values
(used for the plots)

% transpose so that spectra are in rows
X=X';      % so X is now 31 (spectra) x 190 (mt values)

% dimensions
[n,p]=size(X);  % will give n=31 and p=190 with these data

% find mean spectrum
Xm=mean(X);  % mean spectrum, 1 x 190 row vector

% Principal component analysis (PCA) of X
% S, L, v are scores, loadings and eigenvalues respectively
%  The routine pcatfc uses the MATLAB singular value
decomposition svd(.) to
% carry out a PCA on the centered spectral data
% only a single principal component is calculated, so that S is
an n x 1 vector
% of scores, L an n x 1 vector of loadings, and v (not used) is
a scalar
[S,L,v]=pcatfc(X,1,1);

% calculate the fitted spectra, ie the best (in a least squares
sense)
% approximations to the observed spectra that are provided by a
linear
```

```
% additive model
Xf=ones(n,1)*Xm+S*L';  % Xf, like X, is n x p

% find the most extreme scores
%  smin/smax are the values of the lowest/highest scores,
imin/imax are the
% indices  of the rows they correspond to
[smin,imin]=min(S);
[smax,imax]=max(S);

% the min and max scores are for positions 10 and 16 respectively
% position 10 is clearly a mixture, whereas position 16 could
plausibly
% be a single component so we identify position 16 with "pure"
liver
P1=Xf(imax,:);  % estimated spectrum of liver
 % experimenting with subtracting multiples of P1 from the
spectrum of
% position 10 suggests that it is a mixture of 13% fat, 87%
liver
% (subtract more than 0.87 and the spectrum goes negative,
subtract less
% and there is still a second peak)
livmin=0.87;
P2=Xf(imin,:)- livmin*P1;  % estimated spectrum of fat

% rescale the scores to be percentage of fat
s=100*(1-livmin)*(smax-S)/(smax-smin);

% save the two estimated pure components for use with later
experiments
% save puresL P1 P2 mt

% now plot the results
% all the code below this point is about making the plots

% plot the observed and fitted spectra, by experiment
plotfit=1;
if plotfit==1
    np=4;  % 4 plots with 9 spectra per plot
    for i=1:np
        j0=1+(i-1)*9;
        j1=min(31,9*i);
        jd=j1-j0+1;
        figure

        for j=1:jd
            js=j+(i-1)*9;
            subplot(3,3,j)
```

```
            title(int2str(js))
            hold on
            plot(mt,X(js,:),'-b')
            plot(mt,Xf(js,:),'-r')
            hold off
            set(gca,'XLim',[0.6                    3],'Ylim',[0
700],'TickDir','out','Box','on')
            if j<jd-2
                set(gca,'xtick',[])
            else
                set(gca,'xtick',[1.0 2.0 3.0])
                xlabel('MT (nm^{-1})')
            end
            if round((j+2)/3)*3==j+2
                set(gca,'ytick',[0 300 600])
                ylabel('Count')
            else
                set(gca,'ytick',[])
            end
        end
    end
end

% plot the two estimated pure component spectra
plotpure=1;
if plotpure==1
    figure
    hold on
    plot(mt,P1,'-g')
    plot(mt,P2,'-b')
    set(gca,'Ylim',[0 700],'TickDir','out','Box','on')
    xlabel('Momentum transfer (nm^{-1})')
    ylabel('Count')
    title('Estimated pure components, fat (blue) and liver
(green)')
    hold off
end

% plot the extimated concentration of fat
plotconc=1;
if plotconc==1
    figure
    indx=[1:31];
    plot(indx,s)
    set(gca,'TickDir','out','XLim',[0 32],'Box','on')
    title('Estimated fat concentrations for positions 1-31')
    ylabel('Estimated fat concentration (%)')
    xlabel('Position number')
end
```

2 pcatfc.m

```
function [S,L,v] = pcatfc(X,k,c)
% PCA
% usage [S,L,v] = pcatfc(X,k,c)
% input X - n x p matrix of spectra (in rows)
%       k - number of components to return
%       c - c=1 center X, c=0 do not center
% output S - n x k matrix of scores
%        L - p x k matrix of loadings
%        v - eigenvalues
if c==0
    Xc=X;
else
    Xc = X - ones(size(X,1),1)*mean(X);
end
[U,E,V] = svd(Xc,0);
S = U(:,1:k);
e = diag(E);
e = e(1:k);
v = e.^2;
L = V(:,1:k);
L = L*diag(e);
%S = S*diag(e);
```

3. Prog_scannedheart_Tom_attenuation

```
% This program analyses as one data set all the data from
experiment E12

% Load all the data, previously converted from Excel format to
MATLAB files
load('SH.mat')
% variables loaded
% X  (241 x 31) spectra from positions 1-31
% mt (241 x 1)  momentum stranfer values

% Cut to mt range of 0.6107 to 2.9313  (approx 14.6 - 70 KeV)
X=X(51:end,:);
mt=mt(51:end);     % mt contains the momentum transfer values
(used for the plots)
```

```
% transpose so that spectra are in rows
X=X';       % so X is now 31 (spectra) x 190 (mt values)

SigmaVals = [0.1:0.2:0.5,1:3];

GroupedData = zeros(size(SigmaVals,2),5,31,100);

for iRepeat = 1:100

    iRepeat

    for iAtten = 1:5

        for iSigma = 1:size(SigmaVals,2)

            Xi = X(((iAtten-1)*31 + 1):((iAtten-1)*31 + 31),:);
            XiNoise = zeros(size(Xi,1),size(Xi,2));

            sigma = SigmaVals(iSigma); % changes the value of
sigma for each loop of iSigma

            for iPos = 1:31

                y = Xi(iPos,:);

                for ix = 1:size(mt,1)%-2

                    a = sigma * sqrt(y(ix));
                    b = -(sigma) * sqrt(y(ix));

                    %                 XiNoise(iPos,ix) = ((y(ix)
+ y(ix + 1) + y(ix + 2)) / 3) + (a + (b-a).*rand(1));
                    XiNoise(iPos,ix)   =   y(ix)   +   (a   +   (b-
a).*rand(1));

                end

            end

            %%%%%############       THIS       IS       CORRECT
%%%%%%%%%%%%%%%%%%%%%%%%%%%

            Xi = XiNoise;
            Xi(Xi<0) = 0;

            %%%%%############       THIS       IS       CORRECT
%%%%%%%%%%%%%%%%%%%%%%%%%%%
```

```
            % dimensions
            [n,p]=size(Xi);   % will give n=31 and p=190 with
these data

            % find mean spectrum
            Xm=mean(Xi);  % mean spectrum, 1 x 190 row vector

            % Principal component analysis (PCA) of X
            %  S, L, v are scores, loadings and eigenvalues
respectively
            % The routine pcatfc uses the MATLAB singular value
decomposition svd(.) to
            % carry out a PCA on the centered spectral data
            % only a single principal component is calculated,
so that S is an n x 1 vector
            % of scores, L an n x 1 vector of loadings, and v
(not used) is a scalar
            [S,L,v]=pcatfc(Xi,1,1);

            % calculate the fitted spectra, ie the best (in a
least squares sense)
            % approximations to the observed spectra that are
provided by a linear
            % additive model
            Xf=ones(n,1)*Xm+S*L';  % Xf, like X, is n x p

            % find the most extreme scores
            % smin/smax are the values of the lowest/highest
scores, imin/imax are the
            % indices  of the rows they correspond to
            [smin,imin]=min(S);
            [smax,imax]=max(S);

            % the min and max scores are for positions 10 and
16 respectively
            % position 10 is clearly a mixture, whereas position
16 could plausibly
            % be a single component so we identify position 16
with "pure" liver
            P1=Xf(imax,:);  % estimated spectrum of liver

            % experimenting with subtracting multiples of P1
from the spectrum of
            % position 10 suggests that it is a mixture of 13%
fat, 87% liver
            % (subtract more than 0.87 and the spectrum goes
negative, subtract less
            % and there is still a second peak)
            livmin=0.87;
```

```
            P2=Xf(imin,:)- livmin*P1;   % estimated spectrum of
fat

            % rescale the scores to be percentage of fat
            s=100*(1-livmin)*(smax-S)/(smax-smin);

            % (Sid) Store rescaled scores in a 3D matrix:
            % (1st D) = Attenuation Value
            % (2nd D) = Sigma Value
            % (3rd D) = rescaled scores

            GroupedData(iSigma,iAtten,:,iRepeat) = s;

            % save the two estimated pure components for use
with later experiments
            % save puresL P1 P2 mt

            % now plot the results
            % all the code below this point is about making the
plots

            %  plot  the  observed  and  fitted  spectra,  by
experiment
            % % % % %          plotfit=1;
            % % % % %          if plotfit==1
            % % % % %            np=4;  % 4 plots with 9 spectra
per plot
            % % % % %              for i=1:np
            % % % % %                  j0=1+(i-1)*9;
            % % % % %                  j1=min(31,9*i);
            % % % % %                  jd=j1-j0+1;
            % % % % %                  figure
            % % % % %
            % % % % %                  for j=1:jd
            % % % % %                      js=j+(i-1)*9;
            % % % % %                      subplot(3,3,j)
            % % % % %                      title(int2str(js))
            % % % % %                      hold on
            % % % % %                        plot(mt,Xi(js,:),'-
b')
            % % % % %                        plot(mt,Xf(js,:),'-
r')
            % % % % %                      hold off
            % % % % %                        set(gca,'XLim',[0.6
3],'Ylim',[0 700],'TickDir','out','Box','on')
            % % % % %                      if j<jd-2
            % % % % %                        set(gca,'xtick',[])
            % % % % %                      else
            % % % % %                       set(gca,'xtick',[1.0
2.0 3.0])
```

```
            % % % % %                           xlabel('MT (nm^{-
1})')
            % % % % %                       end
            % % % % %                   if round((j+2)/3)*3==j+2
            % % % % %                      set(gca,'ytick',[0
300 600])
            % % % % %                       ylabel('Count')
            % % % % %                   else
            % % % % %                     set(gca,'ytick',[])
            % % % % %                   end
            % % % % %               end
            % % % % %           end
            % % % % %       end

            % plot the two estimated pure component spectra
            % % % % %       plotpure=1;
            % % % % %       if plotpure==1
            % % % % %           figure
            % % % % %           hold on
            % % % % %           plot(mt,P1,'-g')
            % % % % %           plot(mt,P2,'-b')
            %  %  %  %  %                       set(gca,'Ylim',[0
700],'TickDir','out','Box','on')
            % % % % %               xlabel('Momentum transfer
(nm^{-1})')
            % % % % %           ylabel('Count')
            %  %  %  %  %               title('Estimated pure
components, fat (blue) and liver (green)')
            % % % % %           hold off
            % % % % %       end

            % plot the extimated concentration of fat
% % % % %                   plotconc=1;
% % % % %                   if plotconc==1
% % % % %                       figure
% % % % %                       indx=[1:31];
% % % % %                       plot(indx,s)
% % % % %                       hold on
%             %              %              %              %
plot(indx,squeeze(GroupedData(iSigma,iAtten,:))              -
squeeze(GroupedData(1,1,:)),'r')
% % % % %                   set(gca,'TickDir','out','XLim',[0
32],'Box','on')
% % % % %                       title(['Estimated fat
concentrations    for    positions    1-31.    Attenuation:    '
num2str(iAtten) ', Sigma = ' num2str(sigma)])
% % % % %                       ylabel('Estimated fat
concentration (%)')
% % % % %                       xlabel('Position number')
% % % % %                   end
```

```
        end

    end

% % %     figure
% % %
% % %     for iSigma = 1:size(SigmaVals,2)
% % %         for iAtten = 1:5
% % %
% % %               subplot(size(SigmaVals,2),5,(iSigma-1)*5 +
iAtten)
%                                 %                                 %
plot(indx,squeeze(GroupedData(iSigma,iAtten,:,iRepeat))       -
squeeze(GroupedData(1,1,:,iRepeat)))
% % %             title(['\mu = ' num2str(iAtten) ', \sigma = '
num2str(SigmaVals(iSigma))])
% % %             axis off
%  %  %                        set(gca,'XLim',[0  32],'Ylim',[-15
15],'Box','on')
% % %
% % %         end
% % %     end


end

GroupedDataMean = sum(GroupedData,4) / 100;


figure

for iSigma = 1:size(SigmaVals,2)
    for iAtten = 1:5

        subplot(size(SigmaVals,2),5,(iSigma-1)*5 + iAtten)
        plot(indx,squeeze(GroupedDataMean(iSigma,iAtten,:))   -
squeeze(GroupedDataMean(1,1,:)))
        title(['\mu   =   '   num2str(iAtten)   ',   \sigma   =   '
num2str(SigmaVals(iSigma))])
        axis off
        set(gca,'XLim',[0 32],'Ylim',[-15 15],'Box','on')

    end
end



%         plotfit=1;
```

```
%          if plotfit==1
%              np=4;  % 4 plots with 9 spectra per plot
%              for i=1:np
%                  j0=1+(i-1)*9;
%                  j1=min(31,9*i);
%                  jd=j1-j0+1;
%                  figure
%
%                  for j=1:jd
%                      js=j+(i-1)*9;
%                      subplot(3,3,j)
%                      title(int2str(js))
%                      hold on
%                      plot(mt,Xi(js,:),'-b')
%                      plot(mt,Xf(js,:),'-r')
%                      hold off
%                              set(gca,'XLim',[0.6  3],'Ylim',[0
700],'TickDir','out','Box','on')
%                      if j<jd-2
%                          set(gca,'xtick',[])
%                      else
%                          set(gca,'xtick',[1.0 2.0 3.0])
%                          xlabel('MT (nm^{-1})')
%                      end
%                      if round((j+2)/3)*3==j+2
%                          set(gca,'ytick',[0 300 600])
%                          ylabel('Count')
%                      else
%                          set(gca,'ytick',[])
%                      end
%                  end
%              end
%          end
%
```

4. Prog_scanned_heart.m

```
% This program analyses as one data set all the data from
experiment E12

% Load all the data, previously converted from Excel format to
MATLAB files
load('SH.mat')
% variables loaded
```

```
% X  (241 x 31) spectra from positions 1-31
% mt (241 x 1)  momentum stranfer values

% Cut to mt range of 0.6107 to 2.9313  (approx 14.6 - 70 KeV)
% X=X(51:end,:);
% mt=mt(51:end);    % mt contains the momentum transfer values
(used for the plots)

samples = {'fat0mm', 'fat2mm', 'fat3mm'};

for iSample = 3%!:3

    eval(['X = ' samples{iSample} ';'])

    % transpose so that spectra are in rows
    X=X';       % so X is now 31 (spectra) x 190 (mt values)

    % dimensions
    [n,p]=size(X);  % will give n=31 and p=190 with these data

    % find mean spectrum
    Xm=mean(X);  % mean spectrum, 1 x 190 row vector

    % Principal component analysis (PCA) of X
    % S, L, v are scores, loadings and eigenvalues respectively
    %  The routine pcatfc uses the MATLAB singular value
decomposition svd(.) to
    % carry out a PCA on the centered spectral data
    % only a single principal component is calculated, so that
S is an n X 1 vector
    % of scores, L an n x 1 vector of loadings, and v (not used)
is a scalar
    [S,L,v]=pcatfc(X,1,1);

    % calculate the fitted spectra, ie the best (in a least
squares sense)
    % approximations to the observed spectra that are provided
by a linear
    % additive model
    Xf=ones(n,1)*Xm+S*L';  % Xf, like X, is n x p

    % find the most extreme scores
    % smin/smax are the values of the lowest/highest scores,
imin/imax are the
    % indices  of the rows they correspond to
    [smin,imin]=min(S);
    [smax,imax]=max(S);
```

```
    % the min and max scores are for positions 10 and 16
respectively
    % position 10 is clearly a mixture, whereas position 16
could plausibly
    % be a single component so we identify position 16 with
"pure" liver
    P1=Xf(imax,:);  % estimated spectrum of liver

    % experimenting with subtracting multiples of P1 from the
spectrum of
    % position 10 suggests that it is a mixture of 13% fat, 87%
liver
    % (subtract more than 0.87 and the spectrum goes negative,
subtract less
    % and there is still a second peak)
    livmin=0.87;
    P2=Xf(imin,:)- livmin*P1;  % estimated spectrum of fat

    % rescale the scores to be percentage of fat
    s=100*(1-livmin)*(smax-S)/(smax-smin);

    % save the two estimated pure components for use with later
experiments
    % save puresL P1 P2 mt

    % now plot the results
    % all the code below this point is about making the plots

    % plot the observed and fitted spectra, by experiment
    plotfit=1;
    if plotfit==1
        np=4;  % 4 plots with 9 spectra per plot
        for i=1:np
            j0=1+(i-1)*9;
            j1=min(size(X,1),9*i);
            jd=j1-j0+1;
            figure

            for j=1:jd
                js=j+(i-1)*9;
                subplot(3,3,j)
                title(int2str(js))
                hold on
                plot(mt,X(js,:),'-b')
                plot(mt,Xf(js,:),'-r')
                hold off
                set(gca,'XLim',[0.6                3],'Ylim',[0
700],'TickDir','out','Box','on')
```

```
                if j<jd-2
                    set(gca,'xtick',[])
                else
                    set(gca,'xtick',[1.0 2.0 3.0])
                    xlabel('MT (nm^{-1})')
                end
                if round((j+2)/3)*3==j+2
                    set(gca,'ytick',[0 300 600])
                    ylabel('Count')
                else
                    set(gca,'ytick',[])
                end
            end
        end
    end

    % plot the two estimated pure component spectra
    plotpure=1;
    if plotpure==1
        figure
        hold on
        plot(mt,P1,'-g')
        plot(mt,P2,'-b')
        set(gca,'Ylim',[0 700],'TickDir','out','Box','on')
        xlabel('Momentum transfer (nm^{-1})')
        ylabel('Count')
        title('Estimated pure components, fat (blue) and heart
(green)')
        hold off
    end

    % plot the extimated concentration of fat
    plotconc=1;
    if plotconc==1
        figure
        indx=[1:size(X,1)];
        plot(indx,s)
        set(gca,'TickDir','out','XLim',[0 20],'Box','on')
        title(['Estimated fat concentrations for sample '
samples{iSample} ])
        ylabel('Estimated fat concentration (%)')
        xlabel('Position number')
    end


end
```

5. Prog_scanned_liver.m (Revised prog)

```
% Load all the data, previously converted from Excel format to
MATLAB files
load('SL.mat')
% variables loaded
% X  (241 x 31) spectra from positions 1-31
% mt (241 x 1)  momentum stranfer values

% Cut to mt range of 0.6107 to 2.9313  (approx 14.6 - 70 KeV)
X=X(51:end,:);
mt=mt(51:end);    % mt contains the momentum transfer values
(used for the plots)

% transpose so that spectra are in rows
X=X';      % so X is now 31 (spectra) x 190 (mt values)

% dimensions
[n,p]=size(X);  % will give n=31 and p=190 with these data

% find mean spectrum
Xm=mean(X);  % mean spectrum, 1 x 190 row vector

% Principal component analysis (PCA) of X
% S, L, v are scores, loadings and eigenvalues respectively
%  The routine pcatfc uses the MATLAB singular value
decomposition svd(.) to
% carry out a PCA on the centered spectral data
% only a single principal component is calculated, so that S is
an n x 1 vector
% of scores, L an n x 1 vector of loadings, and v (not used) is
a scalar
[S,L,v]=pcatfc(X,1,1);

% calculate the fitted spectra, ie the best (in a least squares
sense)
% approximations to the observed spectra that are provided by a
linear
% additive model
Xf=ones(n,1)*Xm+S*L';  % Xf, like X, is n x p

% find the most extreme scores
```

```
% smin/smax are the values of the lowest/highest scores,
imin/imax are the
% indices  of the rows they correspond to
[smin,imin]=min(S);
[smax,imax]=max(S);

% the min and max scores are for positions 10 and 16 respectively
% position 10 is clearly a mixture, whereas position 16 could
plausibly
% be a single component so we identify position 16 with "pure"
liver
P1=Xf(imax,:);  % estimated spectrum of liver

% experimenting with subtracting multiples of P1 from the
spectrum of
% position 10 suggests that it is a mixture of 13% fat, 87%
liver
% (subtract more than 0.87 and the spectrum goes negative,
subtract less
% and there is still a second peak)
livmin=0.87;
P2=Xf(imin,:)- livmin*P1;  % estimated spectrum of fat

% rescale the scores to be percentage of fat
s=100*(1-livmin)*(smax-S)/(smax-smin);

% save the two estimated pure components for use with later
experiments
% save puresL P1 P2 mt

% now plot the results
% all the code below this point is about making the plots

% plot the observed and fitted spectra, by experiment
plotfit=1;
if plotfit==1
    np=4;  % 4 plots with 9 spectra per plot
    for i=1:np
        j0=1+(i-1)*9;
        j1=min(31,9*i);
        jd=j1-j0+1;
        figure

        for j=1:jd
            js=j+(i-1)*9;
            subplot(3,3,j)
            title(int2str(js))
            hold on
            plot(mt,X(js,:),'-b')
```

```
            plot(mt,Xf(js,:),'-r')
            hold off
            set(gca,'XLim',[0.6                    3],'Ylim',[0
700],'TickDir','out','Box','on')
            if j<jd-2
                set(gca,'xtick',[])
            else
                set(gca,'xtick',[1.0 2.0 3.0])
                xlabel('MT (nm^{-1})')
            end
            if round((j+2)/3)*3==j+2
                set(gca,'ytick',[0 300 600])
                ylabel('Count')
            else
                set(gca,'ytick',[])
            end
        end
    end
end

% plot the two estimated pure component spectra
plotpure=1;
if plotpure==1
    figure
    hold on
    plot(mt,P1,'-g')
    plot(mt,P2,'-b')
    set(gca,'Ylim',[0 700],'TickDir','out','Box','on')
    xlabel('Momentum transfer (nm^{-1})')
    ylabel('Count')
    title('Estimated pure components, fat (blue) and liver
(green)')
    hold off
end

% plot the extimated concentration of fat
plotconc=1;
if plotconc==1
    figure
    indx=[1:31];
    plot(indx,s)
    set(gca,'TickDir','out','XLim',[0 32],'Box','on')
    title('Estimated fat concentrations for positions 1-31')
    ylabel('Estimated fat concentration (%)')
    xlabel('Position number')
end
```

6. getdataSH.m / getdataSL.m

```
 % read in scanned liver data from spreadsheet and save as .mat
file
[num,txt]=xlsread('HEART PHANTOM SCANNED.xlsx',1);
X=num(2:end,4:end);      % 31 spectra  (241 x 31)
mt=num(2:end,3);     % momentum transfer  (241 x 1)

fat2mm = X(51:end,1:16);
fat3mm = X(51:end,17:33);
fat0mm = X(51:end,34:50);
mt = mt(51:end);
% tidy up
clear num txt

% save as SL.mat
save SH.mat
```

Appendix 2: MONTE CARLO SIMULATION

Table 5.11

Monte Carlo Simulation A (Small tissue)

Energy (keV)	Coherent	Other
0	34	357
1	0	0
2	5	0
3	1	0
4	0	0
5	0	0
6	0	0
7	0	0
8	1	0
9	3	0
10	58	0
11	1	0
12	56	0
13	1	0
14	12	0
15	32	0
16	73	2
17	148	11
18	314	16
19	449	29
20	718	45
21	938	46
22	1178	73
23	1407	90
24	1735	129
25	2004	155
26	2339	185
27	2513	233
28	2698	238
29	2707	255
30	2815	259
31	2771	301
32	2837	332
33	2888	363
34	2896	351
35	2708	344
36	2589	356
37	2547	380
38	2425	360
39	2392	352
40	2338	395

41	2182	370
42	2086	406
43	1940	378
44	1741	339
45	1731	363
46	1628	341
47	1484	351
48	1397	325
49	1290	340
50	1214	332
51	1150	311
52	995	304
53	974	285
54	846	251
55	780	263
56	735	224
57	657	218
58	553	192
59	515	202
60	424	160
61	404	159
62	361	151
63	302	143
64	272	124
65	226	89
66	168	102
67	124	56
68	83	47
69	59	34
70	16	6
71	0	0
72	0	0
73	0	0
74	0	0
75	0	0

Monte Carlo Simulation B (Large tissue)

Energy (keV)	Coherent	Incoherent
0	0	13
1	0	0
2	0	0
3	0	0
4	0	0
5	0	0
6	0	0
7	0	0
8	0	0

9	0	0
10	1	0
11	0	0
12	2	0
13	0	0
14	0	0
15	0	0
16	0	0
17	0	0
18	0	0
19	0	0
20	0	0
21	1	0
22	1	1
23	1	1
24	4	3
25	6	5
26	10	2
27	13	6
28	19	8
29	30	10
30	38	16
31	29	9
32	36	11
33	44	23
34	57	13
35	52	15
36	51	16
37	51	19
38	81	27
39	61	18
40	80	15
41	89	22
42	85	23
43	61	19
44	70	16
45	56	22
46	65	25
47	59	21
48	68	16
49	47	21
50	52	13
51	58	24
52	56	25
53	60	22
54	46	18
55	36	10
56	31	16
57	38	24
58	38	15
59	21	18
60	25	9

61	28	9
62	24	7
63	21	7
64	16	4
65	10	7
66	16	3
67	4	10
68	4	4
69	4	2
70	1	0
71	0	0
72	0	0
73	0	0
74	0	0
75	0	0

Appendix 3: **Effect of attenuation due to large phantom**

Figures 5.5b to 5.5f

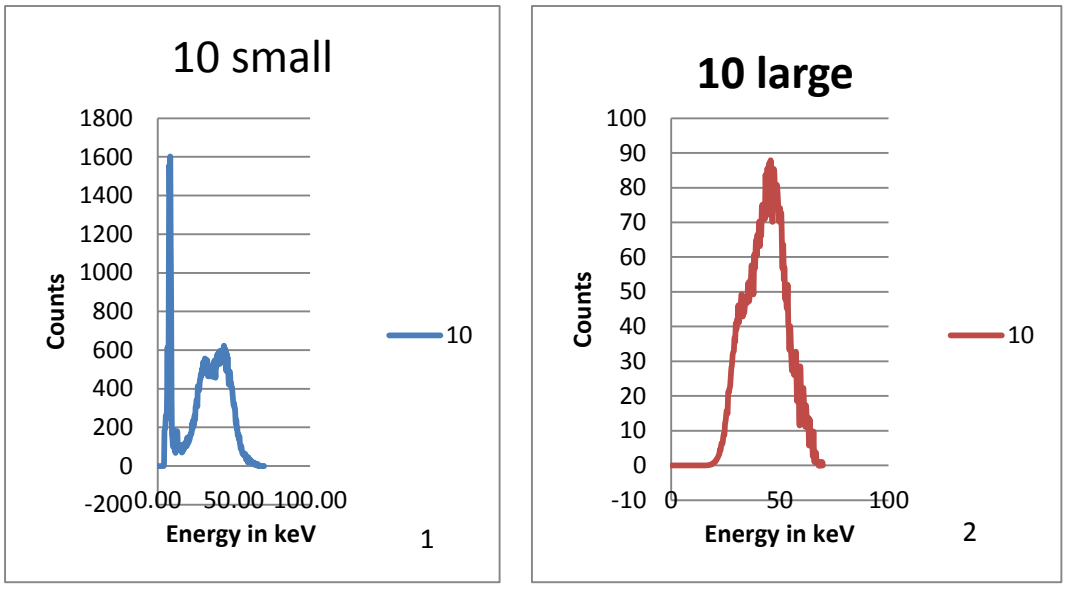

Figure 5.5b: Effect of attenuation due to large phantom (1) Raw spectrum of the small liver phantom at position 10 with (2) the spectrum of patient-sized (large) phantom shown side by side

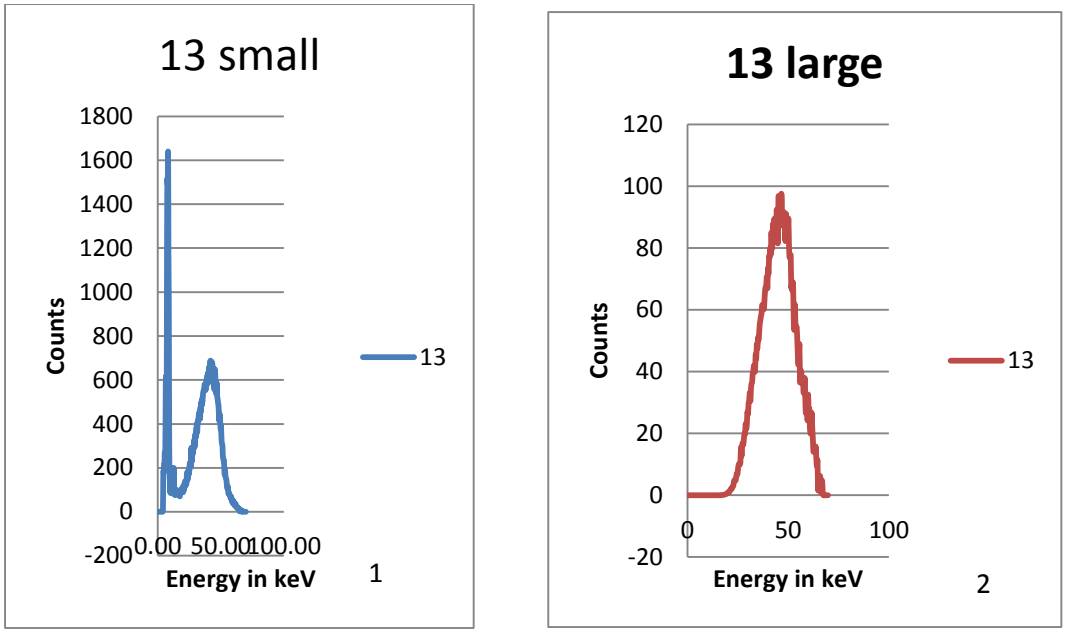

Figure 5.5c: Effect of attenuation due to large phantom (1) Raw spectrum of the small liver phantom at position 13 with (2) the spectrum of patient-sized (large) phantom shown side by side

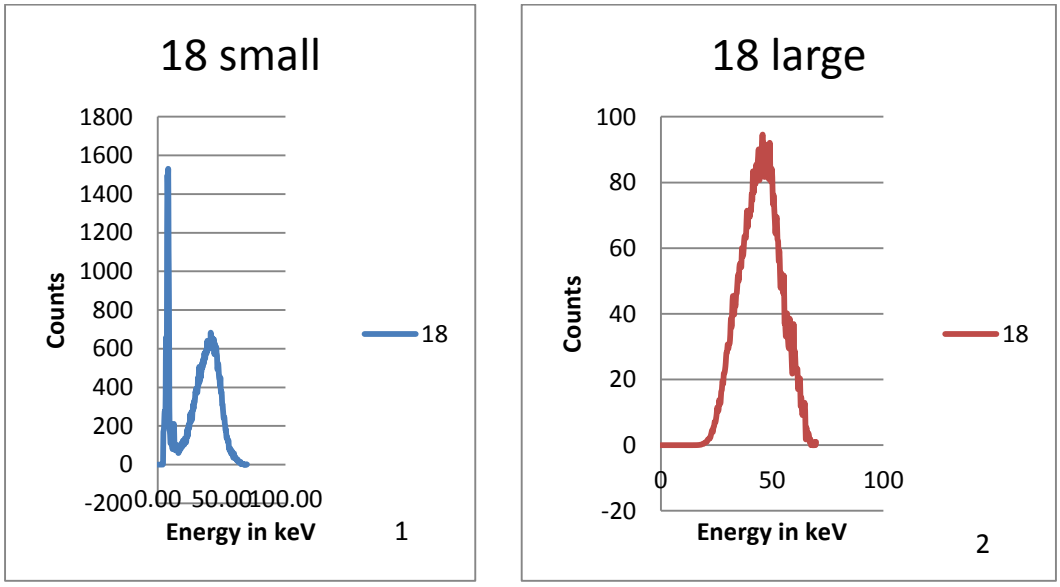

Figure 5.5d: Effect of attenuation due to large phantom (1) Raw spectrum of the small liver phantom at position 18 with (2) the spectrum of patient-sized (large) phantom shown side by side

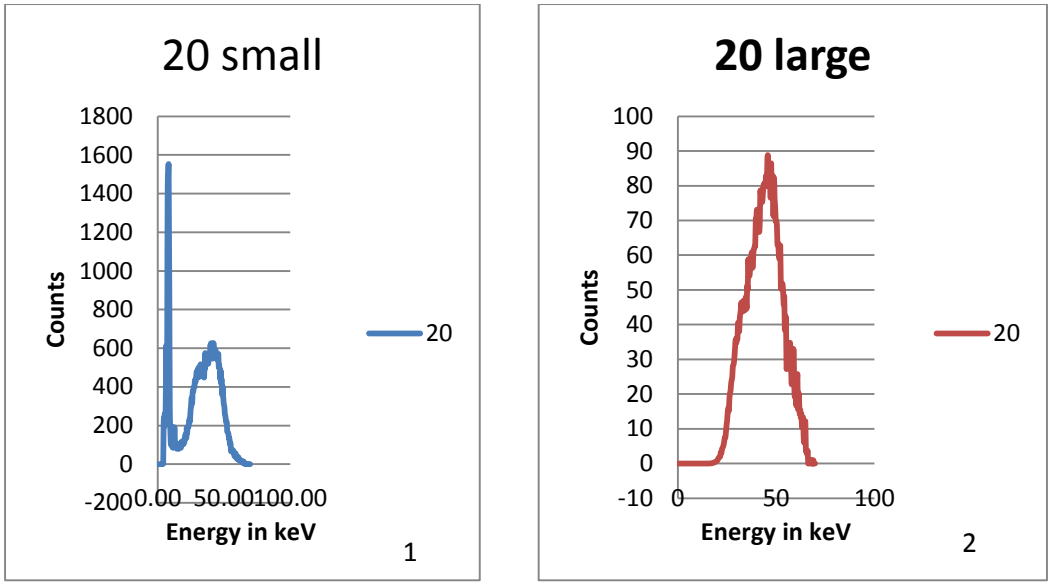

Figure 5.5e: Effect of attenuation due to large phantom (1) Raw spectrum of the small liver phantom at position 20 with (2) the spectrum of patient-sized (large) phantom shown side by side

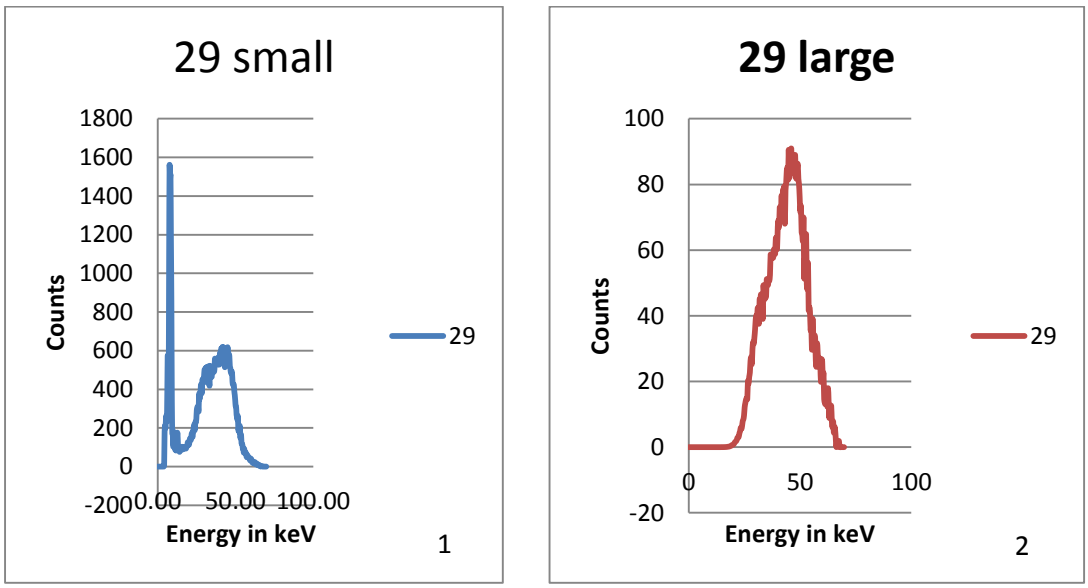

Figure 5.5f: Effect of attenuation due to large phantom (1) Raw spectrum of the small liver phantom at position 29 with (2) the spectrum of patient-sized (large) phantom shown side by side